UNIVERSITÀ
DEGLI STUDI
FIRENZE

DOTTORATO DI RICERCA IN
SCIENZE DELLA TERRA

CICLO XXIX

COORDINATORE Prof. LORENZO ROOK

A FINITE ELEMENT METHOD FOR MAGMA-ROCK INTERACTION DYNAMICS IN VOLCANIC ENVIRONMENT

Settore Scientifico Disciplinare GEO/08

Dottorando
Dott. Garg Deepak
Deepak Garg

Tutore
Prof. Longo Antonella
Antonella Longo

Coordinatore
Prof. Lorenzo Rook

Anni 2013/2016

Acknowledgements

The research work of this thesis was carried out at the National Institute of Geophysics and Volcanology (INGV-Pisa, Italy), from November 2013 to 2016. I gratefully acknowledge the financial support for this research provided by the People Programme (Marie Curie Actions) of the European Union's Seventh Framework Programme (FP7/2007-2013) under the project NEMOH, REA grant agreement n. 289976. A partial funding was also received from the project MED-SUV under the call FP7 ENV.2012.6.4-2.

I would like to acknowledge the efforts and input of my supervisor Dr Antonella Longo, for her supervision, patience and understanding. I also would like to thank her for carefully reading the draft of this thesis and for all the enthusiasm that she has shown in my work and for giving me the freedom and confidence in everything I was doing. I particularly thank Prof. Paolo Papale for his guidance and the continuous motivation. I would like to express my special appreciation of him for being friendly and a tremendous mentor. I want to thank him for the many fruitful discussions concerning the research topic and beyond.

The friendly and enthusiastic environment of my research group was the biggest asset. I thank all members of my research group for sharing their knowledge and experience with me. I want to thank all colleagues and administration staff at INGV-Pisa, in particular, a special thank to everyone I have shared my office with. I express special thanks to Dr Simone Colucci for providing valuable suggestions during the draft of the thesis. I would like to thank every single member of the NEMOH project for so friendly and enjoyable years. A special gratitude to all the lecturers who considerably contributed in enriching my knowledge on the subject. Furthermore, I thank my family, Angela, relatives and friends for their continuous love, support and encouragement.

Abstract

Underground magmatic processes and their effects on the Earth's surface are an issue that requires advanced models to be unrevealed. The comprehension of the mutual link between magma and rock is crucial for the advancement in understanding of the physics of volcanoes and the associated hazard. In this thesis, a numerical method for magma-rock interaction (Fluid Structure Interaction, FSI) problem has been developed in order to understand the processes of magma dynamics in magma chambers. A segregated algorithm by means of finite elements method (FEM) is used to solve the FSI problem, where the fluid and structure domains are interconnected by a standard sequence of transfer of boundary conditions. Multicomponent single-phase flow dynamics is governed by the equations for conservation of mass for each component, and the equations of momentum and energy conservation for the mixture. The thermodynamic variables are computed by a homogeneous mixture model.

The transport equations for the fluid are solved on structured and unstructured grids with the stabilised time discontinuous Galerkin least-squares space-time finite element formulation. The numerical model treats both compressible and incompressible flows simultaneously in a unified way. Differently, from the standard FEM, space and time are dealt in a unified way allowing an implicit consistent treatment of the mesh motion. For time marching problems, constant in time and linear in time predictor-corrector iterative methods of first and third orders are used to solve the non-linear algebraic equations.

The structural model is based on the FEM Lagrangian viscoelastic standard linear solid model formulation. The time-dependent response of a viscoelastic material is included in the constitutive relationship between the stress and the strain tensors. The stress tensor is split into elastic and viscous contributions. The non-linear system of equations obtained from the weak residual formulation is linearised with the Newton method and further solved with a Newmark time marching algorithm. The fluid mesh deformation is computed with the elastic deformation method.

Various standard benchmarks cases for fluid flows on fixed and deforming domains have been validated. The structural model is tested on three numerical examples.

After validation, the numerical algorithm is applied to model the magma flow in chambers. Magma is assumed to have a compressible/incompressible multicomponent single-phase flow. Magma properties are computed as a function of the local P-T-X conditions with the proper constitutive equations. Three simulation cases of natural convection and magma mixing occurring inside magma chambers are presented. The first case studies the Rayleigh-Taylor instability arose between two stratified layers (hot and cold) of a magma in an elliptical chamber. The second case examines the mixing between two heterogeneous magmas placed in the shallower and deeper reservoirs, connected through a vertical dike. The last case analyses the magma mixing in the presence of a seismic excitation. All simulations include the convection driven by buoyancy forces solely. The numerical results reveal that the viscosity of magma plays a crucial role in magma mixing. Depending on the magma viscosity, the time-scale of convection and mixing can vary from a few hours to tens of hours. The simulation results show that the magma mixing caused by the pure buoyant forces causes a decompression in the shallower chamber. The results also illustrate that the impinge of a seismic wave has no influence on the magma mixing, but, it is able to increase the overpressure in the magmatic system.

Contents

Preface

Motivation

The exceptionally fertile soil and the geothermal energy provided by volcanoes have always been advantageous for the humans. On the other hand, volcanoes are a permanent threat to the human life and the infrastructure necessary for living. The ash injected into the atmosphere by an explosive volcanic eruption can damage crops, industrial plants, transportation systems and electrical grids. Moreover, volcanic eruptions can drastically alter land and water for tens of kilometres around the vent, and the sulphur dioxide gas erupted into the stratosphere can change the earth's climate drastically. Historical records indicate that volcanoes have undergone catastrophic eruptions, destroying villages and entire civilisations. Today, millions of people live close to some of the most dangerous volcanoes in the world. Vesuvius and Campi Flegrei (Italy) are among the most dangerous volcanoes in the world; but also Popocatépetl (Mexico), Merapi (Indonesia), Sakurajima (Japan), and many others are included in the list. It is of fundamental importance to get a better knowledge of the current state and the evolution of a volcano.

Our ability to forecast volcanic hazard derives from the knowledge of the physics governing the magmatic and volcanic processes. Volcanologists and geophysicists are interested in predicting the behaviour of volcanoes by understanding the relationship between the observable variables. The constitutive relations among variables allow us to understand the current state of activity, possibly foreseen events and mitigate the volcanic risk. Volcano monitoring for seismicity, ground deformation, gas emission, magnetic, electric and gravity fields is a predominant tool used in eruption forecasting. A change of the seismicity of a volcano may be directly linked to the internal dynamics of the volcano. A volcano in the process of erupting produces strong seismic signals that serve as precursory indicators. Similarly, the ground movements, changes in the electrical, magnetic and gravity fields, and a change in the chemical signature of the gas emitted by fumaroles are good indications of the unrest state of a volcano. The Earth's surface of high inhabited volcanoes is covered by a network of monitoring instruments to gain the precursory indications about the ongoing changes in depth. Despite the fact that these measures can provide invaluable information regarding the changes occurring at the subsurface depth they can not reveal the physical processes behind these. That is where experimental and numerical models serve the purpose.

Experimental studies play a significant role in studying the processes under given conditions. The experiments provide an excellent opportunity to test our hypothesis about a physical process in a controlled environment by using analogue material and natural samples. In engineering applications, a full-scale experiment can provide all the physical characteristics, the relation between the unknowns and clear-cut conclusions under a high level of control with many variations in model parameters. Although recent advancements in laboratory equipment allow us to perform larger scale experiments with great precision, a full-scale experiment is obviously impossible for volcanoes. Therefore, experiments are conducted on small-scale models, and the resulting information is extrapolated to the full scale. One big drawback of this approach is that the small scale models partially loose information that can be gained only with a full-scale system.

An alternative approach to understand the physical processes of a system is to construct a mathematical model based on the fundamental physical laws and then try to solve the model for a given set of conditions by solving the resulting system of equations. The partial differential equations governed by most of the mathematical models are inherently non-linear and time-dependent and are often impossible to be analytically solved except a few simple cases. Therefore, physical-mathematical models are often solved by numerical techniques, where the differential equations governing the system are converted to a set of algebraic equations at discrete points, and then the solution is obtained using digital computers. The big advantage of numerical techniques is to recognise all peculiarities of a physical process of interest. Recent advancement in computing capabilities of computers from the hardware point of view and the programming tools which allow us to run a computer code on multiple processors simultaneously (parallel programming) have played a prominent role in solving complex time-consuming geophysical problems in a short time. Fast processing of new generation computers and the ability of numerical methods to tackle a broad range of challenging problems make the computational modelling an interesting and undoubted choice for volcanology. Nowadays numerical modelling and simulations have become the best alternative tools to supplement experimental study, providing very promising results in improving the understanding of the volcanic processes. Usually, magma dynamics is studied by using the method of computational fluid dynamics (CFD), and the deformation of rock is analysed by the structural mechanics approach. Although the need of computational models is of paramount importance, the numerical models require validation using reliable experimental data before they can be put to good use, which indicates that experimental methods will remain to play a crucial role.

Mainly the numerical techniques are classified into finite difference, finite element and finite volume methods. However, other new techniques such as Lattice Boltzmann method and spectral element method have also gained popularity in recent years. The software implementation of a numerical method is a demanding task, and this is why most people do not write their own programs. A number of commercial and open-source software programs such as (COMSOL Multiphysics, ABAQUS, ANSYS, CodeAster, OpenFoam etc.) are available. Given a particular problem, it is highly likely that one can find open-source software to solve the problem, but it takes the time to understand that before to put to good use. The commercial software programs are often user-friendly and applicable for a range of problems but do not provide the access to the source code. Some software allow to implement the user-specific equation of state but the numerical algorithm to solve the equations is not accessible. In the case of limited time for software training and need of software support, and lack of enough competencies to assess the numerical quality of the results commercial software are recommended. Nonetheless, due to the high cost of commercial software and the need to develop user-specific optimised numerical algorithms motivates researchers to write their own programs. It is useful in the sense that the user has the full control and accessibility to the individual files of the code, which might be modified and extended depending on the problem of interest.

Volcanoes are made by an external structure and a variable number of underground interconnected magmatic reservoirs. Often magma residing inside the reservoirs evolve over a period which can vary from tens to hundreds of years. During the life of a volcano, the magma can crystallise into plutonic rock or can erupt to the surface leaving behind an empty or partially filled reservoir and/or new fresh magma can refill the reservoir itself. Petrological studies indicate that many volcanic eruptions are shortly preceded by injection of new magma into a pre-existing, shallow magma chamber, causing convection and mixing between the incoming and resident magmas. Magma dynamics within the reservoirs generate pressure and deviatoric stress forces, which act along the surrounding rock and might change the shape of a magma chamber. The applied forces may lead to the deformation of rock and overcome the yield strength, making it fail and triggering an eruption. The rock failure and consequently an eruption triggering are determined by the difference between the tensile strength of rock and magmatic forces. The deformation generated at depth as a result of applied magma forces travels through the rock in the form of elastic waves and is detectable at the Earth surface. Early recognition of signals from monitoring networks and diagnosis of ongoing magma dynamics in shallow magmatic systems is critical for developing reliable early warning systems and forecasting of short-term volcanic hazard.

On one side, magmatic forces generated by the dynamics are responsible for the deformation of rock; on the other hand, the dynamics of magma itself is affected by the movement of surrounding rock due to the significant changes in the reservoir domain. In this sense, this is a two-way coupled system, where each part influences the other and is classified as a multi-physics problem and termed in computational mechanics as magma-rock interaction problem. To get the precise information and the understanding of the physics of a volcano, it is of fundamental importance to shed light on the process of interaction between the magma and the rock. A reliable modelling of magma-rock interaction requires a fully two-way coupling. A model that is capable of simulating at the same time the magma fluid-dynamics and rock dynamics would be a substantial advancement in volcanological science. The possibility to compute the mutual effect would be a powerful tool to understand the physics of magma dynamics and to produce more realistic synthetic signals at the Earth's surface. The comparison between the realistic synthetic signals and recorded data from volcano monitoring networks would be helpful to discern the complex magma dynamics precisely ongoing at depth and would be a substantial improvement towards estimating hazard.

Objective of this work

As mentioned before, various commercial finite element software such as COMSOL, ABAQUS and ANSYS are available today to simulate structure analysis and fluid flow problems. In most of these software, the space-time discretisation is performed in a semi-implicit way. In other words, space and time are discretised separately (first space and then time). In this thesis, a novel discontinuous Galerkin space-time finite element method for flow problems is presented, which is accurate, versatile and can alleviate some of the problems commonly encountered with existing methods. From a computational point of view, whereas, most software are based on semi-implicit discretisation approach, the numerical technique developed in the current work discretises space and time simultaneously, providing a consistent and robust tool to tackle various flow problems.

Often the limited access in commercial software restricts us to implement the complex equation of state like the one is required in volcanological applications. In particular, in magma chamber dynamics which is primarily studied in this thesis, magma needs to be modelled as a mixture of liquid melt, dissolved and exsolved volatiles and crystals. In this work, the thermodynamic quantities in the fundamental physical laws are evaluated for the mixture. The densities of individual components (liquid melt, dissolved and exsolved volatiles) are computed by their appropriate equation of state and then after the mixture density is obtained. While the viscosity is computed first for the liquid phase and the effect of gas is added afterwards (details are provided in Chapter 6). Different models have been used to compute the physical properties, which are not straight forward to implement in commercial software programs. The numerical code developed in this work allows to model the requisite user-specific constitutive equations for volcanic applications under a controlled environment.

Over the last few decades, the scientific community dealing with computational geophysical problems has been divided into two parts. One is mainly focused on the rock mechanics, investigating the deformation of rock and stress loading by considering the effects of crustal heterogeneity and anisotropy, and the mechanical properties of faults and layers. Recent models include the non-linear inverse analysis of interferometric synthetic aperture radar (InSAR) data to describe the location of a pressurised magma chamber and uses elastic and viscoelastic rheology of rock to determine the deformation as a consequence of magmatic overpressure [181,182]. The work done in [8,91,143] provides the idea behind the mechanics of large volcanic eruption in terms of change of stress field and mechanical failure of rocks around magma chambers. The other discipline is mainly focused on the dynamics of magma inside the volcanic system. The research work includes the development of numerical techniques to compute the physically accurate solution for magma transport in the crust. The models have been classified by the physics related to magma movement in chambers as well as in conduits [23,87,162,166]. A few attempts have already been made to combine the dynamical behaviour of magma and rock [84,149].

In line, the work presented in this thesis aims to set up a unified multidisciplinary volcano modelling system, based on forward modelling and simulations constrained by geophysical and geochemical data, to relate the observations from the monitoring systems to the dynamics of magma inside the volcano. Such a unified multidisciplinary volcano model will constitute the reference for early warning systems at volcanoes, and a formidable new instrument for exploring the physics of volcanic systems. The research is focused on constructing a two-way coupled numerical model for magma-rock interaction problems, eventually to be embodied in a parallel C++ finite element code to be applied for volcanological applications. The subject needs to develop distinct numerical codes for fluid and structure dynamics and to couple them. Magma is modelled as a fluid which can have compressible/incompressible multicomponent single-phase flow. The dynamics of magma is characterised by solving the Navier-Stokes equations from computational fluid dynamics. Rock are considered to have elastic/viscoelastic rheology and are characterised by solving the elastodynamics/viscoelastodynamics equations from structure mechanics. Both fluid and structural problems are solved separately to utilise the model for individual (fluid-only and structure-only) problems too. A segregated algorithm is employed to solve both systems, and the coupling is done through the boundary conditions at the fluid-structure interface. Considering the multidisciplinary (Geology, Mathematics, Physics and Informatics) nature of this work, a substantial part of the thesis will cover the mathematical formulation of the numerical method and the validation of the employed technique on standard benchmarks. The application of the developed model is not only limited to volcanology rather it covers a broad range of other disciplines including engineering, biomedical and geological sciences. From the point of view of volcanological applications, the principle objectives of the study described in this thesis are as follows:

1. Modelling the natural convection and mixing process inside a magma chamber induced by the difference in temperature of magma.
2. Modelling the magma replenishment from a deeper source to a shallow chamber, in particular, for a magmatic system composed of two chambers (shallower and deeper) connected through a dike. Two different kinds of magmas are assumed to occupy the system and model computes the induced dynamics due to the arrival of volatile-rich magma (Shosonite/Andesite) into a shallow magma chamber (Phonolite/Dacite).
3. Modelling the magma replenishment in the presence of seismic excitation.

All the numerical simulations are performed on two dimensional geometries. The presented technique can be easily extended to 3D with minor changes. The topography for 3D numerical simulation can be imported and modified through a suitable script in order to read the mesh data for the code. The work on numerical code for two-way coupling is nearly completed. Once the code is ready and verified on a number of benchmarks, it will be put in public domain for the use of scientific community.

Thesis outline

Fluid-structure interaction problems are considered among the most severe problems of computational mechanics. Multicomponent nature of magma and elastic/viscoelastic rheology of the rock make the interaction problem even more complicated. The work presented in the thesis evolves through several sequential steps. As a first step, the fluid dynamics model for the stationary domain is developed and validated over several benchmarks. In the second step, the model is extended to deforming domains and tested on some selected benchmark cases. In the third step, the structural model is developed and validated. The final step completes the problem by doing coupling between fluid and structure. All the steps are discussed in detail in the chapters of the thesis. The numerical benchmarks validating the capability of the developed code for fluid flow and structural mechanics problems have been presented in various chapters. Although the theoretical model for two-way fluid-structure interaction has been presented and described in the thesis there was not enough time to implement that in the software program. Therefore, the thesis work does not include any numerical simulations for fluid-structure interaction (FSI) problem. The benchmarking of the two-way FSI problems and its applications to the magma-rock interaction problem is left for the future work. However, the one-way interaction of seismic wave and magma reservoir is presented in Chapter 6 which demonstrates that how a seismic excitation can affect the magma dynamics in a chamber. The thesis outline is as follows.

Chapter 1 presents an introduction to physical-mathematical modelling of magma flow and rock mechanics in volcanology. A general idea of a magma chamber is presented. The role of physical variables which characterise and contribute in any small to substantial changes in the dynamics of magma is discussed. The chapter closes with a brief review of the numerical models for magma flow, rock deformation and magma-rock interaction developed in the past.

In Chapter 2, the physical model for the Fluid-Structure Interaction (FSI) problem is presented. The partial differential equations that govern the fluid and structure mechanics are presented. The fluid flow equations are the Navier-Stokes equations for multicomponent, compressible flows, supplemented with an equation of state. The mixture model is based on the homogenised approach. The structure mechanics equations are for elastic and viscoelastic materials. The mathematical form of FSI problem and the coupling algorithm based on the partitioned approach are presented. Two separate computer codes for fluid and structure have been written and validated, but the coupling between them has not been implemented in the code yet.

Chapter 3 is focused on the solution of fluid flow problem for the fixed domain. The compressible fluid flow equations are written in a compact form and in order to define the incompressibility the solution variable set is transformed from conservation variables to pressure primitive variables. The numerical approach to solve the flow problems is space-time Finite Element Method (FEM). The chapter provides the weak formulation of the FEM, the mapping, the numerical discretization and the evaluation of matrix and vector terms. The numerical scheme is validated on some benchmarks cases at the end of the chapter.

Chapter 4 deals with the flow problem in moving domains. The moving domain problem is discussed in the context of interface tracking and interface capturing techniques. The elastic deformation method for the mesh motion is presented. The method is complemented with the Jacobian based stiffening approach which restricts the excessive deformation of smaller elements. The mesh quality criteria are introduced in order to check the quality of the computational mesh. The mesh motion is tested by two numerical examples. Finally, the mesh velocity is evaluated from the mesh deformation and an algorithm is developed to couple the fluid flow and mesh motion problems. The algorithm is validated on some standard benchmark cases.

Chapter 5 presents the numerical recipe to solve the structural mechanics problems. The weak form is derived from the strong form of a boundary value problem. The constitutive relation for the linear viscoelastic material is derived. The structure structural mechanics problem is solved with the semi-discrete FEM. The matrix-vector equation obtained after the spatial discretization is solved by the generalised α time integration method. The details of the predictor-corrector algorithm and the evaluation of terms at the element level are provided. The numerical method is tested and validated on three benchmark problems.

Chapter 6 presents the applications of the developed numerical technique in volcanology. The numerical simulations are performed to study the natural convection and mixing occurred in magma chambers. Mainly three different cases are investigated: mixing due to temperature contrast, mixing due to different composition and influence of seismic shaking on magma dynamics. The simulation results are discussed at the end of the chapter.

Chapter 7 summarises the contribution of the present work, concluding remarks and avenues for future research.

Chapter 1

Magma-rock dynamics modeling in volcanology: state of the art

Introduction

The aim of this chapter is to introduce the numerical modelling in volcanology. In section 1.1, the formation and shape of magma chambers, and rock failure criteria for generating eruptions are discussed. Section 1.2 presents some selected phyical variables and their influence on the dynamics. Sections 1.3, 1.4 and 1.5 cover the state-of-the-art of the existing numerical models for computations of fluid dynamics, rock dynamics and their mutual interaction.

1.1 Magma chamber

A magma chamber is the engine of every active volcano. A magma chamber forms by the accumulation of partially or totally molten rock located in the crust and is often supplied with new fresh magma from a deeper source. Magmas generated at the depth, ascend through the crust due to relatively low density with respect to the surrounding rock until they reach a buoyancy level where the average density of the overlying crust is equal to or less than the density of the ascending melt. At this level, the magma finds a zone of structural weakness where it can spread laterally. Magma chambers are not directly observable. However, their existence is established by the indirect geophysical observations, in particular, seismic tomography [55] or exposed plutonic bodies that represent exhume magma chambers [38]. Also, large volume volcanic eruptions imply that integrated pools of eruptive magma are periodically present in the crust. For an active volcano, a shallow magma chamber acts as a source for dykes and sills into the crust. Most magma chambers are assumed to develop from sills [7, 32, 52, 183]. The shape of magma chamber can be both regular and irregular. In general, the chambers with irregular shapes are thermally and mechanically unstable due to the thermal gradient between magma and the hosting rock [103, 104]. If the irregular parts of the chamber project into the host rock, those parts have a comparatively large area of contact with the host rock. As normally the host rock is cooler than the magma, heat is transferred rapidly from the magma to the host rock. Consequently, the irregular parts of the chamber tend to cool down quickly and solidify. Conversely, if an irregular part of the host rock projects into the magma chamber, heat is transferred rapidly from the magma into that part of the host rock which, thereby, tends to melt partially. Eventually, the whole part of the host rock may melt when it breaks off from the main part of the roof or the walls and subsides into the chamber. This process gives the tendency of smoothing to the magma chambers. However, in reality, there are many other complex geochemical and physical processes which affect the magma dynamics as well as the domain geometry. Among them, one of the most influential ones is the process of crystallisation. The minerals that constitute igneous rock crystallise at different temperature and liquidus-solidus intervals depending on the mineral phase, volatile content and melt composition. The light crystals usually suspend with the melt while heavier crystals tend to sink down and accumulate at the base of chamber creating an irregular boundary. Magma exerts pressure at the walls of the chamber. Since the rock is not homogeneous and can have irregular shape, the pressure can be higher on the tips in comparison to the other parts. This leads to a further increase in irregularity of the chamber shape. In general for numerical studies, on a larger scales, the chambers are assumed to have a regular shape. It is challenging to construct meshes for irregular geometries. Chambers are presumed to adopt mainly three shapes: spherical, prolate ellipsoidal and oblate ellipsoidal.

The eruption occurs when a magma chamber ruptures and a fracture propagates from the chamber to the surface. In some cases such as Stromboli (Italy) and Sakurajima (Japan), the conduit is continuously open. However, this type of volcanoes is rare in comparison with those where a new fracture

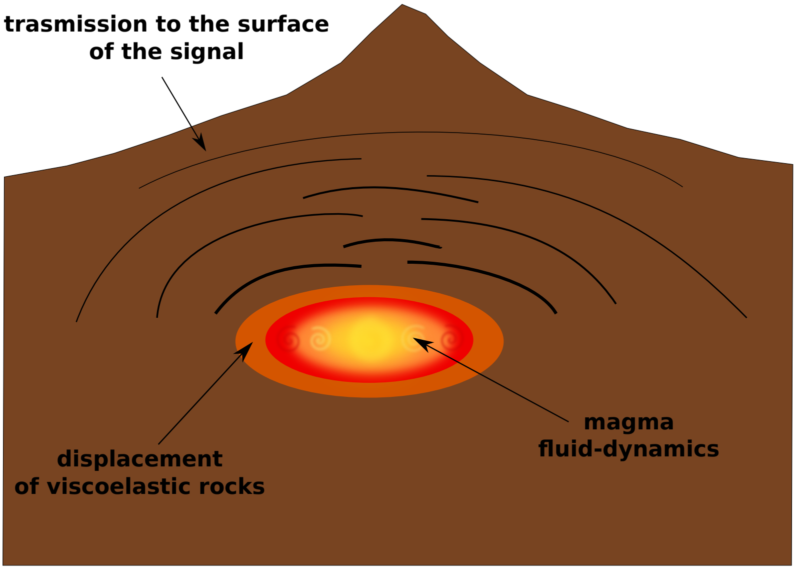

Figure 1.1: Schematic illustration of magma chamber and surrounding rock.

forms during each eruption. The rupture of the magma chamber and the propagation of a dike depend primarily on the magma forces and the tensile strength of rock surrounding the magma chamber. Due to the heat transfer by magma, the surrounding rock behaves like a viscoelastic solid. However, at greater distances, the temperature of magma has no impact on the rock and rock behaves as an elastic material. It is most likely that the magmatic forces applied on the chamber boundary first deform the viscoelastic layer that surrounds it and then further this deformation is transmitted to the elastic rock around, up to the Earth's surface, producing the signals recorded by the monitoring network. A sketch of the processes is shown in Figure (1.1). As regards the viscoelastic shell, once displaced by the forces exerted by magma, it adapts to the new shape and contributes to a change in the magma-dynamics. In the figure, the orange colour represents the shell of the viscoelastic layer of rock. Depending on the type of rock the thickness of the viscoelastic layer can vary up to several meters. The tensile strength of host rock at the boundary of the chamber is limited to $0.5-6MPa$ [9,30,159].

1.2 Physical properties of magma

Magma is a multiphase system constituted by crystals and gas bubbles suspended in a silicate melt. Generally, 99% of any given magma is made up of 11 elements, including Silicon (Si), Titanium (Ti), Aluminum (Al), Iron (Fe), Magnesium (Mg), Magnese (Mn), Calcium (Ca), Sodium (Na), Potassium (K), Hydrogen (H) and Oxygen (O). Volatiles mainly $H_2\mathrm{O}$ and CO_2 can be in liquid or gas phase depending on the system pressure, temperature and composition of the melt. Crystals come from the magma cooling. The way magma behaves in chambers is strongly dependent on its physical properties. In this section, the physical properties of magma and their dependence on pressure, temperature and composition are discussed.

Density
The density of magma is one of the most important factors controlling its physical and chemical behaviour. Density plays a crucial role in controlling the movement of magmas to shallower levels. Moreover, density contrast between silicate melts and minerals plays a role in the differentiation of the magma. Mafic minerals, rich in iron and magnesium such as pyroxenes, olivines and opaque oxides are usually denser than the magma and have a tendency to sink to the bottom of the chamber. Since these minerals are formed in abundance during the first phases of the chemical evolution of magma, their sinking and thus their separation depletes iron and magnesium, contributing to the chemical evolution of magma by fractional crystallisation. On the other hand, minerals like plagioclases and feldspathoids are less dense than the magmatic liquid and usually float at the top. The velocity at which a mineral sinks to the floor of a magma chamber can be estimated by the Stoke's law:

$$v = \frac{2gr^2(\rho_m - \rho_c)}{9\mu} \tag{1.1}$$

Where v is the terminal velocity, r is the radius of the settling crystal (assuming it has a spherical shape), g is the gravitational acceleration, $(\rho_m - \rho_c)$

is the density contrast between the magma and the crystal, and μ is the viscosity of the magma. For a crystal to sink, the gravitational force acting on it must be able to exceed the yield strength of the magma. The density of magma is determined by its temperature, pressure and compositions. Increasing temperature causes magma to expand, which decreases its density while increasing anhydrous pressure causes magma to compress and increase its density. The melt composition plays a fundamental role in controlling magma density. In general, iron, which is relatively abundant in basalts, has a higher mass-to-radius ratio than elements like potassium and silicon, which are enriched in evolved magmas. The density of most magmas ranges from 2.2 to 3.1 g/cm^3, with basalts being densest and rhyolites being least dense. The density of magma can be estimated by

$$\rho = \sum_{i=1}^{N} x_i \rho_i = \sum_{i=1}^{N} \frac{x_i M_i}{V_i} \tag{1.2}$$

Where x_i and ρ_i are the mole fraction and the density of oxide component i. M_i is the molecular mass (also called the molar mass) of oxide i and is usually expressed in units of g/mol. V_i is the fractional volume of oxide i and is usually expressed in units of m^3/mol. N is the total number of oxides in the melt.

Temperature

The temperatures of magmas can be inferred from the direct measurement of the temperature of lavas using optical pyrometers or using thermocouples. The temperature of magma also can be known by using the phase equilibria experiments on crystals and the application of geothermometers. Direct measurement methods yield temperatures in the range of $800 - 1200°C$. The lower temperatures represent those determined for acidic rock or partially crystalline lavas, whereas the higher ones are for basalts. Because most solids have positive slopes i.e. the melting temperature increases by $\approx 3°C/km$, the original temperatures of a magma generated at a depth of $\approx 50km$ will be $150°C$ higher than that determined for the corresponding lava at the surface. In general, the temperature of various magmas is as follows:

- Basalt - 1000 to 1200 $°C$
- Andesite - 950 to 1200 $°C$

- Dacite - 800 to 1100 $°C$
- Rhyolite - 700 to 900 $°C$

Viscosity

The viscosity is a measure of the resistance to the flow of any fluid substance. As a first approximation, the style of the eruptive events depends on the viscosity of the melt. A low-viscosity magma, like basalt, will allow the exsolved gases to migrate rapidly through the magma and escape to the surface. However, if the magma is viscous, like rhyolite, its high polymerization will impede the upward mobility of the gas bubbles. As gas continues to exsolve from the viscous melt, the bubbles will be prevented from rapid escape, thus increasing the overall pressure of the magma column causing fragmentation with the rapid acceleration of the continuous gas. Ultimately, the gas ejects explosively from the volcano. As a general rule, therefore, non-explosive eruptions are typical of basaltic-to-andesitic magmas which have low viscosities and low gas contents, whereas explosive eruptions are typical of andesitic-to-rhyolitic magmas which have high viscosities and high gas contents. The viscosity of magma depends on the temperature, pressure, composition and the amount of volatiles. Viscosity decreases with increasing temperature of the magma thus lower temperature magmas have a higher viscosity than higher temperature magmas. Anhydrous pressure has a small effect on viscosity. Viscosity decreases with increase in pressure. Viscosity depends primarily on the composition of the magma. Higher SiO_2 (silica) content magmas have higher viscosity than lower SiO_2 content magmas. This is simply a function of the percentage of network formers and network modifiers. Acidic magmas are more viscous than basic ones. Thus, basaltic magmas tend to be fairly fluid (low viscosity), but their viscosity is still 10,000 to 1 million times more viscous than water ($\approx$ 1.e-3 Pas). Rhyolitic magmas tend to have an even higher viscosity, ranging between 1 million and 100 million times more viscous than water. Solids also have a viscosity, but it is very high, measured as trillions of times the viscosity of water. Amount and nature of volatiles also affect the viscosity. This is a reflection of the ability of volatile components to act as network modifiers or network formers. The addition of a small amount of H_2O to a magma drastically lowers its viscosity, especially if this magma is acidic or intermediate. On the other hand, the addition of H_2O to an olivine-melt will only have a minor effect on its viscosity. Experimental results demonstrate that viscosity varies on logarithmic scale with respect to temperature and H_2O [113].

Volatiles

Volcanoes release a high amount of H_2O, CO_2, H_2S, SO_2, HCl and HF. In most cases, the volatiles dissolved in the magma play a dominant role in controlling other physical properties of magmas, hence, the volcanic behaviour. Generally, 95-99% of magma is liquid rock. However, the low percentage of gas represents an enormous volume when it expands on reaching atmospheric pressure. Pressure and composition are the most important parameters which affect the dispersion of volatiles in magma. In comparison to other volatiles, water and carbon dioxide are the most abundant volatiles in magma. Magma loses water mainly when it rises to the surface. The solubility of water is higher in rhyolite than basaltic magma. Due to solubility, it is possible to observe the maximum amount of water that might dissolve in magma. If the magma contains less water that it could, then it is undersaturated. Usually, there are not enough water and carbon dioxide in deep crust and mantle, so magma is often undersaturated in these conditions. Magma becomes saturated when it contains the maximum amount of water that can be dissolved in it. If the magma continues to rise to the surface and dissolves more water, then, it becomes oversaturated. At that moment of the process, if other water is dissolved in magma then that will be ejected as bubbles or vapour water. This happens because pressure decreases in the process and velocity increases and the process has to balance also between the decrease of solubility and pressure. As regards the solubility of carbon dioxide in magma, this is considerably less than water, and it tends to exsolve at greater depth. The depth on which carbon dioxide and water are released affects the behaviour of the magmatic system. Due to the low solubility of carbon dioxide, it starts to release bubbles before reaching the magma chamber. The magma at that point is already supersaturated. The magma accompanying carbon dioxide bubbles rise to the roof of the chamber and carbon dioxide tends to leak through cracks. The solubility of volatiles in magma has been investigated by several experiments [47]. In most cases, Henry's law is used to compute the solubility of volatiles in magma. Papale et al. [147] developed a model for H_2O-CO_2 partitioning/solubility in magmas depending on the temperature, pressure, composition and the weight fraction of H_2O and CO_2. The model is considered as the most advanced model to date and is widely used.

1.3 Modelling of magma dynamics: state of the art

Several models have been developed in the past to study the magma dynamics inside a chamber. Often models are applied with simplified assumptions based on the process of interest. The most used simplifications are the steady state flow, 2D or 1D domain, and the state of equilibrium. This section gives a brief review of the models developed to compute the magma chamber dynamics.

Blake [164]
Blake modelled a magma chamber open to an inflow of material from below. He derived a relationship giving the critical volume of added material required to cause an eruption as a function of magma compressibility and the volume by which the chamber expands. The necessary condition to satisfy for an eruption was that the difference between magma pressure and the lithostatic pressure must be greater than the tensile strength of the chamber walls before the contents of the magma chamber reach the thermodynamic and geochemical equilibrium.

Oldenburg et al. [42]
Oldenburg et al. developed a two-dimensional model that considers mixing between incompressible homogeneous magmas induced mainly by the diffusion and thermal-compositional convection. Magma mixing was quantified by the linear scale of segregation corresponding to the length scale of a typical compositional anomaly and the intensity of segregation. Magma chamber walls were considered rigid and insulating. The mass, momentum and energy conservation equations were solved using a Galerkin finite element method with various geologically relevant boundary conditions. The results showed that the mixing occurs quickly in equant bodies than the sill-like bodies where the mixing is inhibited by the formation of multiple cells of different composition in the horizontal direction. Results also showed that the flow reversals cause significant temporal variation in the heat supplied to the roof of the chamber which is important for the episodic phases of hydrothermal alteration. The simulations showed that the dynamics of double-diffusive convection can impart complex patterns of composition through time and space in magma bodies. Bergantz [80] improved the model explicitly taking into account the multiphase fluid dynamics of the magmatic mixture. The

model was applied to study the mixing following magma chamber recharge. This model allowed the study of the convection and mixing following the intrusion of a crystal-bearing magma in a chamber hosting a crystal-free magma. Three distinct flow regimes based on the Reynolds number (Re) were investigated by examples; for $Re \approx 1$, $10 < Re < 100$ and $Re > 100$.

Spera et al. [68]

Spera et al. developed a two-dimensional model and applied to study the origin of compositional and phase heterogeneity in magma bodies undergoing simultaneous convection and phase change. The simulator was applied to binary-component solidification of an initially superheated and homogeneous batch of magma. The model accounted for solidified, mushy (two- or three-phase), and all-liquid regions self-consistently, including latent heat effects, the percolative flow of melt through mush, and the variation of system enthalpy with composition, temperature, and the solid fraction. Phase Equilibria and thermochemical and transport data for the system $KAlSi_2O_6 - CaMgSi_2O_6$ were utilised to address the origin of compositional zonation in model peralkaline magmatic systems. The model equations were solved using a finite difference method for an incompressible fluid with constant viscosity. The simulations were performed over square and rectangular magma chambers to assess the role of thermal boundary conditions, solidification rates, and magma-body shape on the crystallisation history. The model predicted the effect of magma body shape and different thermal boundary conditions on the rate of crystallisation. Spera et al. [69] and Trial et al. [22] improved the model by considering the compositional gradients within the chamber. The magma was treated as an incompressible, single-phase Newtonian fluid with variable properties, such as density and viscosity; the effect of temperature on viscosity was neglected. The equations of conservation of mass and momentum were solved using the Galerkin finite element formulation. As an improvement of this model, Kuritani [178] modelled the magmatic differentiation processes in a cooling magma reservoir using a numerical model that computes crystallisation using multicomponent thermodynamic models.

Bower and Woods [165]

Bower and Woods developed a model for the mass erupted from a magma chamber for a given decrease in chamber pressure, as a function of compressibility of the mixture in the chamber. The erupted mass was modelled to be dependent on the chamber depth, vertical extent and the magma volatile content. The magma chamber was assumed one-dimensional and isothermal. The model considered a homogeneous mixture of liquid, crystals and gas bubbles, accounting for the effect of crystallisation and gas exsolution on mixture density and pressure. The crystal and bubble content were modelled as a function of pressure, temperature and mixture composition. The model implied that in eruptions producing 0.1-1 km^3 of magma either the chamber is shallow of size 1-100 km^3 or the chamber is deep of size 100-10,000 km^3. Model was applied to estimate the volume of deep magma chamber associated with the 1902 eruption of Soufriére and the vertical extent of the shallow chamber associated with the eruption of Nisyros.

Folch et al. [4, 5]
Folch et al. developed an axisymmetrical numerical method to find the temporal evolution of pressure, the position of the exsolution level, the velocity field, the eruption rate, and the amount of erupted material of a shallow, volatile-rich, felsic magma chamber during a Plinian central vent eruption. The overpressure necessary to trigger the eruption was assumed to result from crystallization-driven volatile oversaturation (second boiling). Numerical model solves the Navier-Stokes equations using a finite element method. The algorithm used a fractional step approach that allowed the use of equal interpolation spaces for the pressure and velocity fields and could be used to solve both compressible and incompressible flows. The model considers magma as a homogeneous, incompressible, Newtonian fluid below the exsolution level and as a compressible, homogeneous two-phase mixture of liquid and gas bubbles above that level. The numerical model allowed to solve the flow equations fully implicit, a semi-implicit or a fully explicit way. The standard Galerkin method was used to discretize the space. Regarding the mixture properties, the main assumptions were chemically homogeneous composition of magma, presence of water as the only volatile, and perfect behaviour of gas. The barotropic state law was used as the equation of state. Further assumptions were a constant temperature, the fixed geometry of the system and rigid and erosion-free domain walls. The results showed that the pressure at the conduit entrance decreases exponentially as the eruption proceeds and the shift in exsolution level results in volatile oversaturation in the deeper parts of the magma chamber. The influence of chamber geometry and the physical properties of the magma on the computed parameters was

studied by several examples.

Degruyter and Huber [209]

Degruyter and Huber developed a model that computes the evolution of the thermodynamic state of the chamber (pressure, temperature, gas and crystal content) as new magma is injected into the chamber. The magma chamber was considered to be a homogeneous sphere of volume V and was assumed to remain spherical at all time. A mass was injected at a constant rate into a spherical reservoir with a homogeneous magmatic mixture while it was cooler by a colder, viscoelastic crustal shell. Crystallisation and exsolution took place within the chamber with a variation of the relative quantities of the melt, crystal, and gas phases. The authors followed the evolution of the canonical variables pressure P, temperature T, and gas volume fraction ξ_g, melt density ρ_m, crystal density ρ_Y, and chamber volume V. All other variables were derived from these. The eruption was assumed to occur when overpressure reaches a critical value of 20 MPa and the crystal volume fraction is below 0.5. The primary goal of authors was to investigate the dependence of the frequency of eruptions on the time scale of injection, cooling, and viscous relaxation to place various triggering mechanism such as second boiling crystallisation induced exsolution, mass injection, and buoyancy. Three main timescales were identified:

$$\tau_{\text{in}} = \frac{\rho_0 V_0}{\dot{M}_{in}} \qquad \tau_{\text{cool}} = \frac{R_0^2}{\kappa} \qquad \tau_{\text{relax}} = \frac{\eta_{r0}}{(\Delta P)_c}$$

Where V_0, ρ_0 were the initial volume of the chamber and density of the magmatic mixture respectively, and κ was the thermal diffusivity of the crust. Two other analytical numbers were defined as

$$\theta_1 = \frac{\tau_{\text{cool}}}{\tau_{in}} \qquad \theta_2 = \frac{\tau_{\text{relax}}}{\tau_{in}}$$

The relevance of all the parameters was summarised by the regime diagram (1.2).

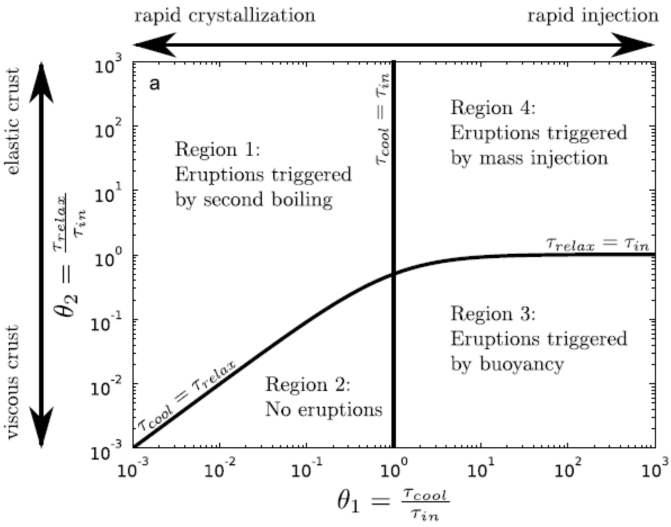

Figure 1.2: The regime diagram can be subdivided into 4 regions according to the dominant timescales. These regions are associated to different eruption triggering mechanism (Adapted from [209]).

1.4 Models for rock deformation: state of the art

Changes to a volcano's ground surface appear as swelling, decompression, or cracking, which can be caused by magma, gas, or water moving underground or by movements in the earth's crust due to motion along faults. Often, this deformation is tiny in magnitude a few centimetres or less and mainly detected and monitored with very sensitive instruments. Precise monitoring and the correct interpretation of the observed data give an insight into the deep processes, and hence crucial for volcanic hazard. Nowadays, development of numerical models to predict the ground deformation of volcanic areas and their verification with the monitoring data has become an active area of research. Over last few decades, many numerical models based on the elastic and inelastic rheology of rock have been proposed. Most of the models attempt to model the surface and rock deformation in response to the magma forces. The majority of rock dynamics models compute the energy propagation and rock deformation within solid materials by solving the equations of continuum mechanics. This section gives a review of some selected models.

Mogi Model [109]

The Mogi model is one of the earliest models developed to infer the ground displacement. Mogi did not derive nor was he the first to use the mathematical expressions relating the surface displacements to hydrostatic inflation or deflation of a small sphere (centre of dilatation) buried in an elastic half-space. Anderson was the first person who solved this problem [60] and applied to volcanoes. The main aim of the model is to understand surface deformation during unrest periods considering the depth and pressure of a magma chamber (modelled as a point source). The applications of Mogi model to surface deformation, are discussed in [127], [148]. Model considers a magma chamber of radius α at depth d under the assumption that $\alpha << d$. The displacements are evaluated as

$$u = \frac{3\Delta p \alpha^3}{4\mu}\frac{x}{R^3} \qquad v = \frac{3\Delta p \alpha^3}{4\mu}\frac{y}{R^3} \qquad w = \frac{3\Delta p \alpha^3}{4\mu}\frac{d}{R^3}$$

where u, v, w are the displacements at the point $(x, y, 0)$, the centre of cavity is at $(0, 0, -d)$ and $R = \sqrt{x^2 + y^2 + d^2}$ is the radial distance from the centre of the cavity to a point on the free surface. Δp and μ are the pressure change in cavity and shear modulus respectively. The formulas are very easy and straightforward, but the Mogi limit bears several limitations. To reproduce the order of magnitude of the observed displacements, the model requires too high pressures, greater than the rock strength to rupture. The model does not provide any information about the stresses around the magma chamber and is constrained to the assumption of the spherical shape of the chamber. Despite these limitations to date, the model has been widely used by various volcanologists. Davis [150] extended the Mogi model for an arbitrary oriented triaxial ellipsoidal shape of the chamber. The surrounding rock was taken as homogeneous, isotropic, elastic half-space, thus neglecting all mechanical layering and heterogeneities. In [180] authors found significant differences between depth estimates for magma chambers placed in homogeneous and isotropic elastic half-spaces and those placed in layered crustal segments. The numerical results indicated that the surface stress and deformation above magma chambers and dikes depend strongly on the mechanical layering of the crustal segments hosting these structures.

Finite element model [105]

This model is focused on observing the differences between vertical and horizontal ground surface deformations near active volcanoes. The authors applied the method to Kilauea, Hawaii. The model computed the deformations for idealised magma reservoirs of various shapes: spheres, horizontal lenses, vertical plugs, sills, and dikes of various inclinations. The model computed the surface deformation of the reservoir with a vertical axis of symmetry and two-dimensional structures that undergo plane strain deformation in a transverse plane. The computations assumed uniform elasticity throughout, the magma reservoir being represented as a cavity in the elastic body. The boundary conditions for the reservoir consisted of stress boundary conditions appropriate to a uniform change of pressure acting normal to the walls of the cavity. The upper surface was assumed to be a planar free surface and represented the surface of the Earth. The sides and bottom were normal and parallel, respectively, to the free surface. The displacements were fixed at zero on the surfaces, the boundaries of the model were placed at large distances from the reservoir and did not affect the results. For the computations, the sides and bottom of the model were kept at greater distances. The numerical results showed a notable variation in the magnitude of stresses. The orientation of the maximum principal compressional stress obtained was vertical.

Viscoelastic models

Bonafede et al. [119] modelled the inelastic rheology of rock. The authors modelled the spherical magma chamber as a point source located at certain depth. The rock surrounding the magma chamber were assumed to have viscoelastic rheology and were modelled by standard linear solid. The deformation of the rock was caused by an instantaneous dilation or the variation in pressure of the magma chamber. The model computed the stress field and static displacement field produced by this centre of dilatation and by the pressure source in the viscoelastic half-space. The model is based on the parameters $\tilde{K}(s)$ and $\tilde{\mu}(s)$

$$\tilde{K}(s) = \lambda + \frac{3}{2}\mu \qquad \tilde{\mu}(s) = \frac{\eta\mu_1 s + \mu_1\mu_2}{\eta s + \mu_1\mu_2}$$

where s is the Laplace variable. μ_1 and μ_2 are the rigidities and η is the viscosity. The relaxation time was modelled as

$$\tau = \frac{(3K + \mu_1)\eta}{3K(\mu_1 + \mu_2) + \mu_1\mu_2}$$

The model was applied to compute the surface deformation at Campi Flegrei (Italy). In the centre of dilation model the initial elastic displacement was noticed to be amplified by 20 percent. In the pressure source model, the initial elastic displacement was noticed to be amplified by a factor of 2 which required unrealistically high-pressure values. Results showed that for a sudden application of pressure, the vertical displacement at the surface grows indefinitely in time, at a rate which approaches a constant value, after a transient phase. The region of seismic signal grows with the applied pressure on the magma chamber surface. The maximum distance from the centre of which the seismogenic region expands was noticed to have the same order as the depth of the magma chamber.

In [122] Dragoni et al. computed the analytical solution for a spherical magma chamber, surrounded by a homogeneous viscoelastic shell (elastic dilatation and Maxwell deviatoric). Outside the shell, the rock was assumed to have elastic rheology. The model illustrated the effects of the pressurisation of a magma chamber surrounded by a thermal metamorphic shell. Assuming the shell as a Maxwell viscoelastic body with respect to deviatoric stresses, displacement and stress fields in the medium were calculated as a function of time. The presence of viscoelastic shell generated an increase in the amplitude of displacements in the surrounding medium, relaxation of shear stress within the shell and stress concentration just outside it. The model showed that the presence of a viscoelastic shell alone is sufficient to avoid unreasonable pressure values in the magma chamber. The presence of a shell with thickness $R_2 - R_1$ amplifies the displacement in the surrounding medium by a factor of $\left(\frac{R_2}{R_1}\right)^3$ with respect to the totally elastic model.

In [2] the numerical solutions for the extended axisymmetric source were calculated by a finite element method and compared with analytical (point source). The model considered different parameters such as size, depth and shape of the chamber, crustal rheology and topography. Rock was considered to have viscoelastic rheology. Analytical solutions for a point source were obtained using the dislocation theory and the propagator matrix technique. The elastic solutions were used together with the correspondence principle of linear viscoelasticity to obtain the solution in the Laplace transform domain. Viscoelastic solutions in the time domain were derived inverting the Laplace transform using the Prony series method. The obtained results showed that neglecting the topographic effects may introduce an error greater than that implicit in the point-source hypothesis. In [97] the authors provided the use and implementation of finite element approach for the computation of volcanic deformation using COMSOL Multiphysics software. Of course, there are many other existing models for ground deformation [82, 95, 102].

1.5 Models for magma-rock dynamics: state of the art

The coupling between the magma and rock is essential to predict the physical processes occurring underneath. Many attempts have been made in the past to join the fluid-dynamics in magma chambers and the rock response, by the application of the magmatic pressure to the chamber walls and its propagation to the ground. However, due to the complex non-linearity of fluid-dynamics equations the models are based on simplifying assumptions. The problems computed with the models include the caldera collapse with rigid rock and magma-rock dynamics for closed and open magma chambers.

Folch et al. [6] Folch and Codina proposed a numerical model to compute the dynamics of magma during caldera-forming eruptions within the frame of fluid-structure interaction problem. This model overcame the assumption of fixed domain considered in their previous models [2, 5]. Magma was modelled as a Newtonian incompressible fluid below the exsolution level and as a compressible gas-liquid mixture above this level. For simplicity, only a single volatile phase was assumed. The gas phase was assumed to behave as a perfect gas. The flow equations were solved by Arbitrary Lagrangian Eulerian formulation in the context of finite element method. The host rock was assumed to subside as a coherent rigid solid. The numerical methodology was based on a staggered algorithm in which the flow and the structural equations were alternatively integrated in time by using separate solvers. The procedure also involved the use of the quasi-Laplacian method to compute the ALE mesh of the fluid. The model was applied to caldera-forming eruption where a piece of rigid rock was subsiding into a magma chamber. Numerical results showed that the velocity of caldera subsidence depends strongly on the magma viscosity. The eruption rate was noticed to increase in beginning and decreasing for later times. The results indicated that for low-viscosity magmas there is a possibility of the formation of vortices beneath the ring fault, which may allow mingling and mixing of parcels of magma initially located at different depths in the chamber. The exsolution level deepened with a velocity similar to that of the subsiding block and numerical results confirmed the exsolution of volatiles as an efficient mechanism to sustain explosive caldera-forming eruptions.

Nishimura and Chouet [185]

Conduit discontinuities play a central role in controlling flow disturbances and also provide specific sites where pressure and momentum changes in the fluid are effectively coupled to the Earth. The model studied the magma dynamics and crustal deformation by finite difference method. The volcanic system consisted of a cylindrical fluid-filled reservoir connected to the surface by a narrow cylindrical conduit with a lid capping its exit. The system was pressurised by the addition of new magma, and an eruption was triggered by the instantaneous removal of the lid or the plug. The magmatic mixture was modelled as a homogeneous, multiphase (liquid + gas), compressible and inviscid fluid and its volume changes were taken into account. The magma dynamics was expressed by the equations of mass and momentum conservation in a compressible fluid, in which fluid expansion associated with depressurization was accounted for by a constitutive law relating pressure and density. The rock properties were assumed perfectly elastic and homogeneous, and the free surface was accounted for through the stress-free condition. The crustal motions were calculated from the equations of elastodynamics. The fluid and solid were dynamically coupled by applying the continuity of wall velocities and normal stresses across the conduit and reservoir boundaries. The free slip was allowed at the fluid-solid boundary. The model predicted the gradual depletion of the magma reservoir, which caused crustal deformation observed as a long-duration dilatational signal. Superimposed on this very-long-period (VLP) signal generated by mass transport were long-period (LP) oscillations of the magma reservoir and conduit excited by the acoustic resonance of the reservoir conduit system during the eruption. The volume of the reservoir, vent size, and magma properties controlled the duration of VLP waves and dominant periods of LP oscillations. The second model predicted that when the magmatic fluid reaches the vent, a high-pressure pulse occurs at this location in accordance with the basic theory of compressible fluid dynamics. The model was applied to compute the shallow conduit dynamics at Stromboli volcano (Italy) [27] and Kilauea Volcano (Hawaii) [28].

Longo [13]

In [13] the model is based on the one-way coupling between magma and rock. The most recent reconstruction of the subsurface magmatic system at Campi Flegrei (Italy) and Etna (Italy) was numerically simulated with a finite element code. Common elements in the two domains were the presence of one or more chambers as well as a feeding dike and the existence of an initial gravitationally unstable interface between the two compositionally different magmas. The denser magma was supposed to fill the swallower chamber, and the lighter magma was set in the dike and lower chamber. The two domains were substantially different in terms of their size, geometrical complexity, depth/confining pressure, employed magma compositions and corresponding physico-chemical properties, and for the resulting density contrast at the interface between the two magma types.

Results showed the initial perturbation of the interface between the two magma types, the formation of a plume that enters the upper chamber, creating vortices and mixing with the resident magma, followed by further plumes each one giving vortexes and mixing. Meanwhile, the dense magma of the upper chamber sinks into the feeding dike with intense mixing between the dense and the light magma filling the dike. This dynamics was associated with an overall decrease of pressure inside the upper chamber, and ULP oscillations (see Figure 1.3). The effect over the rock of this magma dynamics was computed as a first order analysis with the Green's functions. The walls of the magmatic system were assumed fixed, and the stress and magma pressure at the computational grid nodes located at the reservoir walls were considered as point sources for the computation of the Green's functions. The temporal evolution of magmatic forces due to the numerical simulation of magma convection and mixing dynamics was computed at the boundary nodes. The ground displacement resulting from the magmatic force disturbance at the fixed reservoir walls and propagated through the homogeneous rock was registered at the Earth's surface (assumed horizontal) at a series of virtual receivers. The Green's function associated with all the individual source at the reservoir walls were finally integrated. The results showed a trend of displacement that correlates ULP pressure oscillation inside the magmatic reservoir (see Figure 1.3). The model suffered from two main drawbacks: the reservoir walls are fixed, and the magmatic forces were propagated to the Earth's surface with the Green's function. A response of the reservoir walls may significantly alter the magmatic pressure and thus the magma dynamics. The rock surrounding the chamber up to the ground cannot be regarded as homogeneous, instead, they are discontinuous and/or layered. The magmatic forces may propagate along completely different paths in such environment. From this observation stems the aim of this thesis to develop a full two-way coupling of magma and rock, considering the possible motion of the reservoir walls and the non-homogeneities of rock.

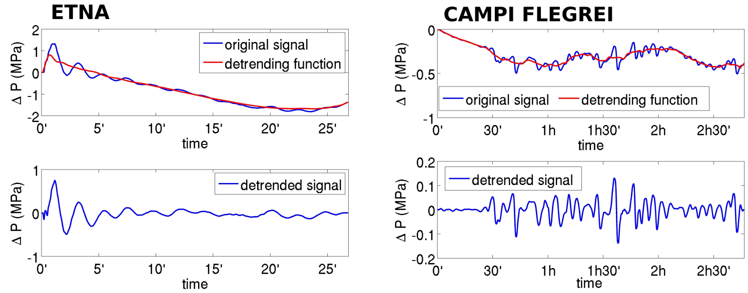

Figure 1.3: Ultra-Long-Period obtained at the Earth's surface (Adapted from [13]).

Chapter 2

Governing equations

Introduction

In this chapter, the physical-mathematical model is presented. In section 2.1 the kinematics is discussed, which is applicable for both fluid and structure. Section 2.2 presents the mass, momentum and energy conservation equations for the compressible/incompressible multicomponent fluid flow followed by the equation of state and the incompressibility of the flow which is determined in terms of the compressibility coefficients. This section is closed with the presentation of homogenised mixture model supplemented with the essential thermodynamics identities. Section 2.3 presents the conservation equations for the structure mechanics followed by the constitutive laws between stress and strain for elastic and viscoelastic material. Elastic and viscoelastic materials are modelled by the Hooke's law and generalised Maxwell model respectively. Finally, the section 2.4 presents the fluid-structure interaction problem, its mathematical form and the algorithms for one-way and two-way coupling.

2.1 Kinematics

In continuum mechanics, a material body is assumed to be completely filled by the matter and the fact that matter is made of discrete atoms on a very fine scale is ignored. Kinematics describes the transformation of a material body from its undeformed to it's deformed state without paying attention to the cause of deformation. The undeformed or reference state is indicated at time $t = 0$. Let Ω_0 be a material body in the reference configuration with boundary Γ_0 and Ω_t be the corresponding domain of material body in the current or deformed configuration with its boundary Γ_t. Let $\mathbf{X} \in \Omega_0$ be a material particle which is moved to a new position $\mathbf{x}$ after some time t and $\mathbf{u}$ is the deformation of the particle $\mathbf{X}$. The deformation is assumed to be time dependent and defined by the continuous function

$$\boldsymbol{u}(\boldsymbol{X}, t) = \boldsymbol{x}(\boldsymbol{X}, t) - \boldsymbol{X} \tag{2.1}$$

This function maps the material points from undeformed to deformed configuration (figure 2.1). In the Eulerian formulation, where observer is fixed in space, all variables are determined in material points which are identified in the deformed state with their current coordinates while, in Lagrangian formulation, where observer follows the material, all variables are determined in material points which are identified in the undeformed state with their initial coordinates. From a theoretical point of view Lagrangian and Eulerian descriptions are equivalent and can be used interchangeably. Eulerian descriptions are more convenient when the spatial distribution of properties are more interested than the properties of a distinct particle. A prominent case for this representation is grid-based fluid dynamics. Structures are often modelled with Lagrangian description, where the dynamics of bodies are studied by tracking position, velocity, and acceleration of the particles.

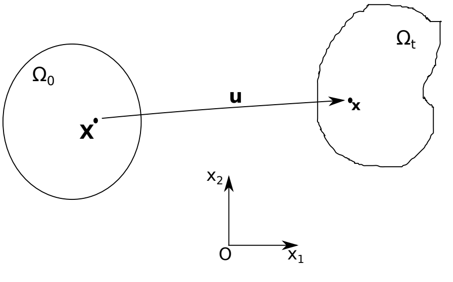

Figure 2.1: Deformation of a material particle $\mathbf{X}$ from reference to current configuration.

From the equation (2.1) the deformation gradient tensor is defined as

$$\boldsymbol{F} = \boldsymbol{x}_{,\boldsymbol{X}} = \boldsymbol{I} + \boldsymbol{\nabla}_{\boldsymbol{X}} \boldsymbol{u} \tag{2.2}$$

To transform the volume of a body from reference to current configuration, the following expression is used

$$d\boldsymbol{\Omega}_t = J \; d\boldsymbol{\Omega}_0 \tag{2.3}$$

where $J = \det \boldsymbol{F}$. For the transformation of the area, the Nanson's relation is used.

$$d\boldsymbol{\Gamma}_t \; \boldsymbol{n} = J \boldsymbol{F}^{-T} \; d\boldsymbol{\Gamma}_0 \; \boldsymbol{N} \tag{2.4}$$

where $\boldsymbol{n}$ and $\boldsymbol{N}$ are the outward normal vector in deformed and undeformed configuration. The Lagrangian strain tensor is defined as

$$\boldsymbol{E} = \frac{1}{2}(\boldsymbol{F}^T \boldsymbol{F} - \boldsymbol{I}) = \frac{1}{2}\Big[\big(\boldsymbol{\nabla}_{\boldsymbol{X}} \boldsymbol{u}\big)^T + \boldsymbol{\nabla}_{\boldsymbol{X}} \boldsymbol{u} + \big(\boldsymbol{\nabla}_{\boldsymbol{X}} \boldsymbol{u}\big)^T \cdot \boldsymbol{\nabla}_{\boldsymbol{X}} \boldsymbol{u}\Big] \tag{2.5}$$

The strain tensor can be understood as measuring the deviation from orthogonality when going from material coordinates to referential coordinates. If no deformation is present then $\boldsymbol{F}^T \boldsymbol{F}$ is $\boldsymbol{I}$ and the strain thus is zero. For small gradient of the deformation ($\boldsymbol{\nabla}_{\boldsymbol{X}} \boldsymbol{u} << 1$) the quadratic term $\big(\boldsymbol{\nabla}_{\boldsymbol{X}} \boldsymbol{u}\big)^T \cdot \boldsymbol{\nabla}_{\boldsymbol{X}} \boldsymbol{u}$ is neglected and the linear strain tensor is defined as

$$\boldsymbol{\epsilon} = \frac{1}{2}(\boldsymbol{F}^T \boldsymbol{F} - \boldsymbol{I}) = \frac{1}{2}\Big[\big(\boldsymbol{\nabla}_{\boldsymbol{X}} \boldsymbol{u}\big)^T + \boldsymbol{\nabla}_{\boldsymbol{X}} \boldsymbol{u}\Big] \tag{2.6}$$

2.2 Fluid Mechanics

Fluid dynamics deals with the calculation of various properties of the fluid (fluid or gas), such as flow velocity, pressure, density and temperature, as functions of space and time. The computations are performed over a domain in the current configuration, considering the Eulerian frame. In fluid dynamics, all the fields of interest like pressure, flow velocity, density and temperature are assumed to be differentiable. Fluid can be composed of either one component or a mixture of several components. The component of fluid can be in either liquid phase or gas phase. The flow of a fluid mixture composed of more than one components in which fluid components have different phases is referred as multicomponent/multiphase fluid flow. The numerical modelling and simulation of a multiphase and multicomponent flow is a very daunting task as compared to a single component or single phase flow. The physical mechanism underlying multiphase and multicomponent flows is very complex. In multiphase and multicomponent flows the phases and/or components can assume a large number of complicated configurations. The modelling and numerical simulations of multiphase and multicomponent flows pose far greater challenges than that of single-phase and single-component flows. These challenges are due to interfaces between phases and large or discontinuous property variations across interfaces between phases and/or components.

Several numerical simulations of multiphase and multicomponent flow have been conducted over the past few years with different modelling approaches. It has been shown that each model and numerical method has limits to their respective capabilities, and there has been a need for improving the technique of modelling multiphase and multicomponent flows. Multicomponent/multiphase problems are mainly solved by two approaches. In the first approach, each phase of the component is considered to occupy a distinct volume and the interfaces between the phases are tracked explicitly by solving the equation of mass for each component and phase, and momentum and energy for each phase [1, 94, 96, 163]. In the second approach, the phases are considered to occupy the same volume leading to a homogeneous mixture [31, 39, 141]. Homogenized-mixture approach is advantageous to the interface-tracking approach because it solves only one set of equations for the momentum, and energy of the mixture, supplemented by equations for the mass of the mixture constituents.

In order to capture most of the physics underlying the flow of a fluid, the model should be able to account the viscous and the transitional nature of the flow. The flow of a fluid can be characterised from compressible to incompressible depending on the flow Mach number. Generally, numerical methods in fluid dynamics for compressible flows like for ideal gases are distinguished from incompressible flows and different kind of solvers have been developed. Sometimes, the inclusion of complex equation of state, necessary to describe the physics of complicated fluids, stems difficulties, as in the case of computations where compressible and incompressible flows can coexist. A natural approach to solve this problem is to start with Navier-Stokes equations for compressible flow and define the variables and suitable conditions for the incompressibility limit. For incompressible flows only mass and momentum equations are solved; the energy conservation equation is of less importance, however, if needed, can be solved separately and solution can be coupled in an explicit way. Whereas, for compressible flows, it is necessary to solve the energy conservation equation and is preferred to solve all the equations in a coupled way.

The conservation equations are defined in the next section. The mathematical model is based on the homogenised mixture approach. The model considers the fluid mixture at mechanical, thermodynamic and chemical local equilibrium. The phases are considered to occupy the same volume and having identical pressure p, temperature T, and velocity $\boldsymbol{v}$. In the description to follow, the mixture is assumed to consist of two phases, namely liquid and gas. The components can undergo an instantaneous phase change. Chemical reactions resulting in component production or consumption are not considered. Variables without subscripts are applicable to the mixture only.

2.2.1 Flow equations

In this section the governing equations for the fluid flows are presented. Let $\Omega_t \in \mathbb{R}^n_{dim}$, $n_{dim} = 1, 2, 3$ be the spatial fluid mechanics domain with boundary Γ_t at time $t \in (0, T)$. The conservation equations are written on $\Omega_t, \ \forall\, t \in (0, T)$. Let $\phi(x, t)$ be any physical quantity in current configuration. By Reynolds transport theorem the time derivative of integration of $\phi(x, t)$ over Ω_t is given as

$$\frac{d}{dt}\int_{\Omega_t}\phi d\Omega = \int_{\Omega_t}\frac{\partial\phi}{\partial t}d\Omega + \int_{\Omega_t}\boldsymbol{\nabla}\cdot(\phi\boldsymbol{v})d\Omega \tag{2.7}$$

$$= \int_{\Omega_t}\frac{\partial\phi}{\partial t}d\Omega + \int_{\Gamma_t}\phi\boldsymbol{v}\cdot\boldsymbol{n}d\Gamma \tag{2.8}$$

where $\boldsymbol{n}$ is the unit outward normal vector, $d\Omega$ and $d\Gamma$ are the volume and surface elements. In above equation, the last term is obtained by using Gauss divergence theorem. All the conservation laws such as conservation of mass, momentum and energy, can be derived from Reynolds transport theorem.

Conservation of Mass

Mass can neither be created nor be destroyed, implies

$$\frac{d}{dt}\int_{\Omega_t}\rho d\Omega = 0 \tag{2.9}$$

Using $\phi = \rho$ in equation (2.7) one gets

$$\int_{\Omega_t}\frac{\partial\rho}{\partial t}d\Omega + \boldsymbol{\nabla}\cdot(\rho\boldsymbol{v})d\Omega = 0 \tag{2.10}$$

This holds for every volume Ω_t. The integrand is assumed to be continuous and equation of mass conservation can be concluded in every spatial point as follows

$$\frac{\partial\rho}{\partial t} + \boldsymbol{\nabla}\cdot(\rho\boldsymbol{v}) = 0 \tag{2.11}$$

For a multicomponent fluid mixture, the equations for conservation of species mass are expressed as the continuity equations for each component

$$\frac{\partial(\rho y_k)}{\partial t} + \boldsymbol{\nabla} \cdot (\rho y_k \boldsymbol{v}) = -\boldsymbol{\nabla} \boldsymbol{\cdot} \boldsymbol{J}^k \tag{2.12}$$

where index k runs from 1 to n (number of components) *i.e.* $k = 1, 2, \dots, n$, and y_k is the weight fraction of kth component. $\boldsymbol{J}^k$ is the mass diffusion flux of kth component and is expressed by the generalized Fick's law for multicomponent fluids by the following expression

$$\boldsymbol{J}^k = -\rho \boldsymbol{D} \boldsymbol{\nabla} y_k \tag{2.13}$$

Here, $\boldsymbol{D}$ is the diffusion coefficient, ρ is the density of the mixture. If ρ_k represents the density of component k, and y_k^π and ρ_k^π represents the weight fraction and density of component k in phase π, then the density ρ of the whole mixture can be written as follows:

$$\frac{1}{\rho} = \sum_{k,\pi} \frac{y_k^\pi}{\rho_k^\pi} = \sum_k \frac{y_k}{\rho_k} \tag{2.14}$$

where the weight fractions y_k satisfy the constraint

$$\sum_k y_k = \sum_{k,\pi} y_k^\pi = 1 \tag{2.15}$$

Conservation of Momentum

The equation for conservation of momentum of the mixture is obtained from the Newton's second law which states that the net rate of outflow of momentum is equal to the net force acting on the volume. This can be expressed as

$$\frac{d}{dt} \int_{\Omega_t} \rho \boldsymbol{v} d\Omega = \int_{\Omega_t} (\rho \boldsymbol{f} + \boldsymbol{\nabla} \boldsymbol{\cdot} \boldsymbol{\sigma}) d\Omega \tag{2.16}$$

where $\boldsymbol{f}$ is the body force per unit mass and $\boldsymbol{\sigma}$ is the Cauchy stress tensor which does not depend on the flow velocity, but on the spatial derivatives of the flow velocity. Applying Reynolds theorem (2.7) with $\phi = \rho\boldsymbol{v}$ and localizing the result at each point gives

$$\frac{\partial(\rho\boldsymbol{v})}{\partial t} + \boldsymbol{\nabla}\cdot(\rho\boldsymbol{v}\boldsymbol{v}) = \rho\boldsymbol{f} + \boldsymbol{\nabla}\cdot\boldsymbol{\sigma} \tag{2.17}$$

Conservation of angular momentum implies the symmetry of stress tensor, $\boldsymbol{\sigma} = \boldsymbol{\sigma}^T$. Cauchy stress tensor splits into pressure tensor $p\boldsymbol{I}$ and deviatoric stress tensor $\boldsymbol{\tau}$. In mathematical expression it is written as:

$$\boldsymbol{\sigma} = \boldsymbol{\tau} - p\boldsymbol{I} \tag{2.18}$$

where $\boldsymbol{I}$ is the identity matrix. For Newtonian isotropic fluid, the linear material law assumes that stress depends on strain linearly. This gives gives

$$\boldsymbol{\tau} = 2\mu\dot{\boldsymbol{\epsilon}} + \lambda tr(\dot{\boldsymbol{\epsilon}})\boldsymbol{I} \tag{2.19}$$

where $\dot{\boldsymbol{\epsilon}}$ is the strain rate tensor and is given by

$$\dot{\boldsymbol{\epsilon}} = \frac{\boldsymbol{\nabla}\boldsymbol{v} + (\boldsymbol{\nabla}\boldsymbol{v})^T}{2} \tag{2.20}$$

λ and μ are the lamé coefficients. μ is called the dynamic viscosity. The value of λ is taken as $\lambda = -\frac{2}{3}\mu$.

Conservation of Energy

According to the first law of thermodynamics, the rate of change of energy is equal to the sum of the net flux of heat and the rate of change of work done due to forces. This can be written as

$$\underbrace{\frac{d}{dt}\int_{\Omega_t}\rho e_t d\Omega}_{\text{Rate of change of energy}} = \underbrace{\int_{\Omega_t}\Big(\boldsymbol{\nabla}\cdot(\boldsymbol{\sigma v}) + \rho \boldsymbol{f v}\Big)d\Omega}_{\text{Work done due to forces}} - \underbrace{\int_{\Omega_t}\Big(\boldsymbol{\nabla}\cdot \boldsymbol{q} + \rho r\Big)d\Omega}_{\text{Net flux of heat}} \tag{2.21}$$

$$\frac{d}{dt}\int_{\Omega_t}\rho e_t d\Omega = \int_{\Omega_t}\Big(\boldsymbol{\nabla}\cdot(\boldsymbol{\sigma v}) - \boldsymbol{\nabla}\cdot \boldsymbol{q} + \rho(\boldsymbol{f v} + r)\Big)d\Omega \tag{2.22}$$

In the above equation, e_t represents the total energy and can be written as

$$e_t = e + \frac{\boldsymbol{v}^2}{2} \tag{2.23}$$

where $e = c_v T$ is the internal energy and $\boldsymbol{v}^2/2$ is kinetic energy. c_v is the specific heat at constant volume and T is the absolute temperature. $\boldsymbol{q}$ is the heat flux vector and by Fourier's law can be expressed as $\boldsymbol{q} = -\kappa\boldsymbol{\nabla}T$. Where κ is the coefficient of thermal conductivity. r is the heat supply per unit mass. Applying Reynolds theorem (2.7) with $\phi = \rho e_t$ and localizing at each point, one obtains

$$\frac{\partial(\rho e_t)}{\partial t} + \boldsymbol{\nabla}\cdot(\rho e_t \boldsymbol{v}) = \boldsymbol{\nabla}\cdot(\boldsymbol{\sigma v}) - \boldsymbol{\nabla}\cdot \boldsymbol{q} + \rho(\boldsymbol{f v} + r) \tag{2.24}$$

2.2.2 Equation of state

In thermodynamics, an equation of state is a relation between state variables. More specifically, an equation of state is a thermodynamic equation describing the state of matter under a given set of physical conditions. It is a constitutive equation $F(\rho, p, T) = 0$ which provides a mathematical relationship between two or more state functions associated with the matter, such as its temperature, pressure, density, or internal energy. The most prominent use of an equation of state is to correlate densities of gases and liquids to temperatures and pressures. One of the simplest equations of state for this purpose is the ideal gas law, which is accurate at low pressures and moderate temperatures. However, the ideal gas equation becomes increasingly inaccurate at very high pressures and lower temperatures and fails to predict condensation from a gas to a liquid. The ideal gas law is the equation of state of a hypothetical ideal gas. Since the ideal gas law neglects both molecular size and intermolecular attractions, it is most accurate for monatomic gases at high temperatures and low pressures. The neglection of molecular size becomes less important for lower densities, i.e. for larger volumes at lower pressures, because the average distance between adjacent molecules becomes much larger than the molecular size. The relative importance of intermolecular attractions diminishes with increasing thermal kinetic energy, i.e., with increasing temperatures. It is a good approximation of the behaviour of many gases under many conditions. The ideal gas law is often written as:

$$pv = n\overline{R}T \tag{2.25}$$

where p is the pressure, v is volume, n is amount of substance of gas, T is temperature and $\overline{R}$ is universal gas constant. Ideal gas law can be written in molar form as follows:

$$p = \rho RT \tag{2.26}$$

Where ρ is the density and R is the specific gas constant defined as the ratio of n and molar mass M. For an ideal gas, the speed of sound is proportional to the square root of the absolute temperature. For ideal gas, the speed of sound can be expressed as

$$c = \sqrt{\frac{\gamma p}{\rho}} = \sqrt{\gamma RT} \tag{2.27}$$

$\gamma = c_p/c_v$. Here c_p is the specific heat at constant pressure.

2.2.3 Incompressible fluid flow

Incompressible fluid flow refers to a flow in which the material density is constant within a fluid parcel-an infinitesimal volume that moves with the flow velocity. Mathematically, this constraint implies that the material derivative (discussed below) of the density must vanish to ensure incompressible flow. This implies that the divergence of the flow velocity is zero. This comes directly from the continuity equations (2.11). Incompressible flow does not imply that the fluid itself is incompressible. Under suitable conditions, compressible fluid flow can be approximated and modelled as an incompressible flow. In order to define the incompressible limit of the flow governed by compressible Navier-Stokes equations, two compressibility coefficients are defined. These are the volume expansivity at constant pressure α_p and the isothermal compressibility at constant temperature β_T, which are defined as

$$\alpha_p = -\frac{1}{\rho}\left(\frac{\partial \rho}{\partial T}\right)_p \qquad \beta_T = \frac{1}{\rho}\left(\frac{\partial \rho}{\partial p}\right)_T \tag{2.28}$$

For incompressible flow the specific heats are equal

$$c_p = c_v \tag{2.29}$$

By definition the compressibility of a flow is the change in density as a result of the pressure and temperature variations. For incompressible flows the compressibility is acceptably small, consequently both α_p and $\beta_T \to 0$. From equation (2.27) one obtains

$$c = \sqrt{\frac{\gamma p}{\rho}} = \sqrt{\frac{1}{\rho \beta_T}} \to \infty \qquad \text{as} \qquad \beta_T \to 0 \tag{2.30}$$

This results in an infinite speed of sound for an incompressible flow of fluid. The compressibility coefficients for ideal gases are defined as

$$\alpha_p = \frac{1}{T} \qquad \beta_T = \frac{1}{p} \tag{2.31}$$

which result in $c_p - c_v = R$.

2.2.4 Homogeneous mixture model

The homogeneous mixture model is based on the notion that quantities associated with a given phase and/or component are averaged to give the corresponding mixture quantity. The mixture density is given by

$$\frac{1}{\rho} = \sum_i \frac{y_i}{\rho_i} = \sum_{i,j} \frac{y_i^j}{\rho_i^j} \tag{2.32}$$

In the above formulation, index i runs for mixture components and index j runs for phase. y_i^j and ρ_i^j are the mass fraction and density of ith component in jth phase. The following constraint must be satisfied.

$$\sum_{i,j} y_i^j = \sum_i y_i = 1 \tag{2.33}$$

Specific heat coefficients c_p, c_v, thermal conductivity k, compressibility coefficients α, β, sound velocity c, viscosity μ, internal energy e, specific enthalpy h and Gibbs free energy g can be averaged as follows: any physical quantity ψ can be written as

$$\psi = \sum_i y_i \psi_i = \sum_{i,j} y_i^j \psi_i^j \tag{2.34}$$

where ψ_i and y_i are the values of ψ and mass fraction of ith component respectively. e_i and h_i for individual components are defined as

$$e_i = c_{v_i} T \qquad\qquad h_i = e_i + \frac{p}{\rho_i} \tag{2.35}$$

The Gibbs free energy of ith component is defined as

$$g_i = g_i^0(T) + RT\ ln\ (px_i) \tag{2.36}$$

where $g_i^0(T)$ is the reference value of Gibbs free energy at temperature T, R is the gas constant, $x_i = n_i/n_t$ is the mole fraction of the ith component in the total mixture, n_i is the number of moles of ith component and n_t is the total number of moles in mixture.

Finally, the conservation equations governing the physics of multicomponent single-phase fluid flow are given by

$$\frac{\partial(\rho y_k)}{\partial t} + \boldsymbol{\nabla} \cdot (\rho y_k \boldsymbol{v}) = -\boldsymbol{\nabla} \boldsymbol{\cdot} \boldsymbol{J}^k \qquad k = 1, \ldots, n \tag{2.37}$$

$$\frac{\partial(\rho \boldsymbol{v})}{\partial t} + \boldsymbol{\nabla} \cdot (\rho \boldsymbol{v}\boldsymbol{v}) = \rho \boldsymbol{f} + \boldsymbol{\nabla} \boldsymbol{\cdot} \boldsymbol{\sigma} \tag{2.38}$$

$$\frac{\partial(\rho e_t)}{\partial t} + \boldsymbol{\nabla}\boldsymbol{\cdot}(\rho e_t \boldsymbol{v}) = \boldsymbol{\nabla}\boldsymbol{\cdot}(\boldsymbol{\sigma}\boldsymbol{v}) - \boldsymbol{\nabla} \boldsymbol{\cdot} \boldsymbol{q} + \rho(\boldsymbol{f}\boldsymbol{v} + r) \tag{2.39}$$

The above system is closed with an equation of state $F(\rho, y_1, \cdots, y_n, p, T) = 0$. The equation of state for the multicomponent flow is obtained from the n equations of states for each component in the form $F(\rho_k, p, T) = 0$ and following two equations

$$\frac{1}{\rho} = \sum_{k=1}^{n} \frac{y_k}{\rho_k} \tag{2.40}$$

$$\sum_{k=1}^{n} y_k = 1 \tag{2.41}$$

The applied boundary conditions are either Dirichlet or Neumann or a combination of both referred as Robin boundary conditions.

2.3 Structure Mechanics

In structure mechanics one is interested in knowing the deformation of a material body under the influence of acting forces. The problems are solved in Lagrangian frame of coordinates on undeformed configuration (see figure 2.1). The deformation $\boldsymbol{u}(\boldsymbol{X},t)$ of a material is given by equation (2.1). The velocity $\boldsymbol{v}(\boldsymbol{X},t)$ is computed as

$$\boldsymbol{v}(\boldsymbol{X},t) = \frac{d\boldsymbol{u}(\boldsymbol{X},t)}{dt} = \frac{\partial \boldsymbol{u}(\boldsymbol{X},t)}{\partial t} \tag{2.42}$$

The deformation is assumed as isothermal. However, if needed the energy conservation equation can be solved explicitly. In the undeformed configuration the density ρ_0, initial deformation $\boldsymbol{u}_0$ and initial velocity $\boldsymbol{v}_0$ are assumed to be known. The physics of a structural body is governed by the conservation of mass and momentum.

2.3.1 Conservation of Mass

The structural density ρ in the current configuration is not known a priori. The structural mass m is defined as

$$m = \int_{\Omega_t} \rho \; d\Omega_t \tag{2.43}$$

The conservation of mass states that the mass of each finite, randomly chosen volume of material points in the continuum body must remain the same during the deformation process. This can be expressed as

$$\frac{d}{dt}\int_{\Omega_t} \rho \; d\Omega_t = 0 \tag{2.44}$$

This can be written as

$$\frac{d}{dt}\int_{\Omega_t} \rho_t \; d\Omega_t = \frac{d}{dt}\int_{\Omega_0} \rho_0 \; d\Omega_0 = \frac{d}{dt}\int_{\Omega_t} \rho_0 \; J^{-1} d\Omega_t \tag{2.45}$$

Here, the relation (2.3) is used. Because Ω_t is arbitrary, result can be localized point-wise

$$\rho = J^{-1}\rho_0 \tag{2.46}$$

Because ρ_0 is known, for a given structural displacement, equation (2.46) may be used to obtain the density at a material point in the current configuration.

2.3.2 Conservation of Momentum

The conservation of momentum can be expressed by

$$\frac{d}{dt}\int_{\Omega_t} \rho_t \boldsymbol{v}\ d\Omega_t = \int_{\Omega_t} (\rho_t \boldsymbol{f} + \boldsymbol{\nabla}\cdot\boldsymbol{\sigma})\ d\Omega_t \tag{2.47}$$

Using equation (2.3) and after simplification the above equation can be written in reference configuration

$$\int_{\Omega_0} \rho_0 \boldsymbol{a}\ d\Omega = \int_{\Omega_0} (\rho_0 \boldsymbol{f} + \boldsymbol{\nabla}\cdot\boldsymbol{P})\ d\Omega \tag{2.48}$$

$$\rho_0 \boldsymbol{a} = \rho_0 \boldsymbol{f} + \boldsymbol{\nabla}\cdot\boldsymbol{P} \tag{2.49}$$

where $\boldsymbol{a} = \dfrac{d\boldsymbol{v}}{dt}$ is the acceleration. $\boldsymbol{P}$ is the non-symmetric first Piola-Kirchhoff stress tensor which is related to symmetric Cauchy stress tensor (in current configuration) by the following relation

$$\boldsymbol{P} = J\boldsymbol{F}^{-T}\boldsymbol{\sigma} \tag{2.50}$$

In structure mechanics, it is necessary only in finite strain theory (large deformations) to specify whether the stresses are measured with respect to the initial configuration (Lagrangian description) or with respect to the deformed configuration (Eulerian description). In this work, the deformations are assumed to be infinitesimal for which the deformed and undeformed configurations coincide. This results in $\boldsymbol{F} = \boldsymbol{I}$ and $J = 1$. In this case Cauchy stress tensor and the first Piola-Kirchhoff tensor become identical, and the density is not variable anymore and the equation for conservation of mass can be skipped. Hence, the only equation required to solve is the equation for conservation of momentum.

$$\rho \boldsymbol{a} = \rho \boldsymbol{f} + \boldsymbol{\nabla} \cdot \boldsymbol{\sigma} \tag{2.51}$$

The above equations are called as linear elastodynamics equations. When the inertial term is not important and neglected the above equation results in

$$\rho \boldsymbol{f} + \boldsymbol{\nabla} \cdot \boldsymbol{\sigma} = 0 \tag{2.52}$$

These are known as linear elastostatic equations. In most of the cases, it is usual to compute the displacements and stresses in a static way (independent of time). However, for viscoelastic materials, the displacements are computed by a quasi-static approach.

2.3.3 Constitutive Laws

Constitutive laws are the relationships between stress and strain. Generally, laws are usually formulated based on empirical observations, and they are material dependent. Moreover, they must be independent of any referential coordinate system that is chosen. In this work, the material under investigation is assumed as isotropic.

Linear Elasticity

Elasticity is the physical property of a material that when it deforms under external force, it returns to its original shape when the force is removed. For an elastic material, the stress-strain curve is the same for the loading and unloading process, and the stress only depends on the current strain, not on its history. A linear elastic material follows Hooke's law, which states that the stress is directly proportional to the strain in small deformations:

$$\boldsymbol{\sigma} = \mathbb{C}\boldsymbol{\epsilon}(\boldsymbol{u}) \tag{2.53}$$

where $\mathbb{C}$ is the elasticity tensor. For isotropic material, the above equation can be rewritten as

$$\boldsymbol{\sigma} = \lambda \; tr(\boldsymbol{\epsilon})\boldsymbol{I} + 2\mu\boldsymbol{\epsilon} \tag{2.54}$$

where λ and μ are lamé coefficients and $\boldsymbol{\epsilon} = \dfrac{\boldsymbol{\nabla u} + (\boldsymbol{\nabla u})^T}{2}$

Linear Viscoelasticity

Viscoelastic materials show time-dependent behaviour. When during a tensile test the stress/strain is prescribed stepwise, the strain/stress will not react immediately, but show a delayed response. Viscoelastic material behaviour is a combination of elastic (see figure 2.2) and viscous behaviour (see figure 2.3) when undergoing deformation. Part of the deformation energy will be dissipated, while the rest is stored as reversible elastic energy. For viscoelastic materials, the relationship between stress and strain depends on time. They possess the following two important properties: stress relaxation (a step constant strain results in decreasing stress) and creep (a step constant stress results in increasing strain) figure 2.4.

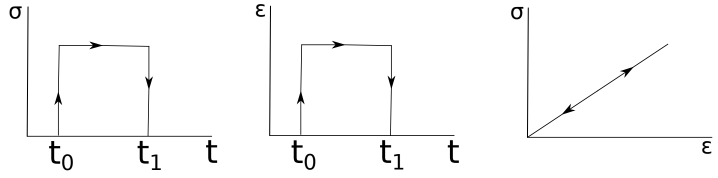

Figure 2.2: Stress-strain curve for elastic material.

The characteristic feature of linear viscoelastic materials is that the stress is linearly proportional to the strain history, and the property of linearity of the response does not refer to the shape of any material response curve. Linear viscoelasticity is usually applicable only for small deformations. Thus, infinitesimal strain theory is employed for this case. Linear viscoelastic materials are generally modelled by the Boltzmann superposition principle, which states that if the origin for time is taken at the beginning of motion

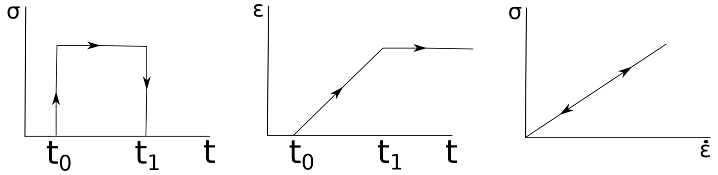

Figure 2.3: Stress-strain curve for viscous material.

and loading (i.e., $\boldsymbol{\sigma}(0) = \mathbf{0}$ and $\boldsymbol{\epsilon}(0) = \mathbf{0}$), then the stress-strain law is given by

$$\boldsymbol{\sigma}(t) = \int_{-\infty}^{t} \boldsymbol{G}(t-s)\frac{d\boldsymbol{\epsilon}(s)}{ds}ds \tag{2.55}$$

where $\boldsymbol{G}(t)$ is the stress relaxation function. Inverse relations may be given where the integral form of stress-strain constitutive relation can be written as

$$\boldsymbol{\epsilon}(t) = \int_{-\infty}^{t} \boldsymbol{J}(t-s)\frac{d\boldsymbol{\sigma}(s)}{ds}ds \tag{2.56}$$

where $\boldsymbol{J}(t)$ is the creep compliance function. There are three main existing mechanical models for viscoelasticity: Maxwell, Kelvin-Voigt and standard solid element. These models are not always useful because the lack of parameters prohibits a good fit of experimental data. In practice, generalised Maxwell or generalised Kelvin-Voigt models are used. All these models can be expressed in the Boltzmann formulation with the suitable choice of parameters. In this work, the generalised Maxwell model is used, which is a combination of springs and dashpots (fig. 2.5) in the one-dimensional case. Experiments show that long past history has less impact on the current stress than recent history. This fading memory property motivates the use of Prony series for $\boldsymbol{G}(t)$ and $\boldsymbol{J}(t)$. The model is followed by computing the

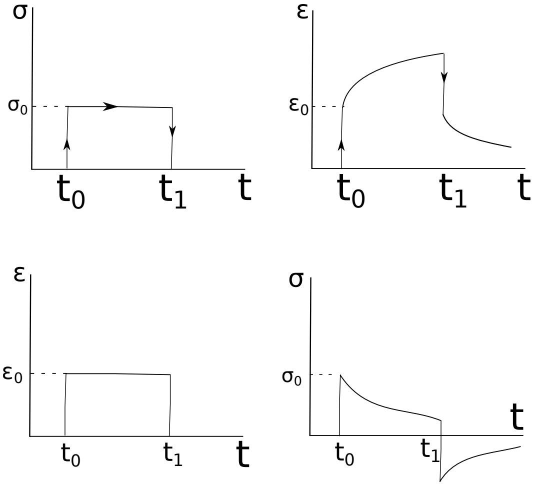

Figure 2.4: Stress-strain curve for linear viscoelastic material. Top figure shows the creep and bottom figure shows the stress relaxation.

$\boldsymbol{\sigma}(t)$ because this is of importance in the finite element model. The stress relaxation function $\boldsymbol{G}(t)$ can be written in the Prony series form:

$$\boldsymbol{G}(t) = \mathbb{C}_\infty + \sum_{i=1}^{n} \mathbb{C}_i e^{\left(\dfrac{-t}{\tau_i}\right)} \tag{2.57}$$

where $\mathbb{C}_\infty$ is the long term modulus once the material is totally relaxed, $\tau_i = \mu_i / E_i$ are the relaxation times; the higher their values, the longer it takes for the stress to relax. Assuming the initial strain to be zero ($\boldsymbol{\epsilon}(0) = 0$) and by substituting (2.57) in (2.55), the stress is split into elastic and inelastic parts.

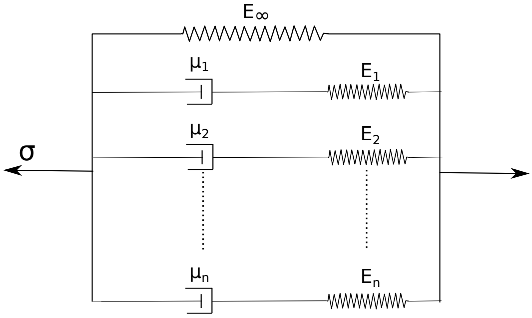

Figure 2.5: Schematic representation of the generalized Maxwell model.

$$\boldsymbol{\sigma}(t) = \boldsymbol{\sigma}^e(t) + \boldsymbol{\sigma}^i(t) \tag{2.58}$$

$$= \int_0^t \mathbb{C}_\infty \frac{d\boldsymbol{\epsilon}(s)}{ds} ds + \int_0^t \sum_{i=1}^{n} \mathbb{C}_i e^{\left(\frac{s-t}{\tau_i}\right)} \frac{d\boldsymbol{\epsilon}(s)}{ds} ds \tag{2.59}$$

$$= \mathbb{C}_\infty \boldsymbol{\epsilon}(t) + \sum_{i=1}^{n} \int_0^t \mathbb{C}_i e^{\left(\frac{s-t}{\tau_i}\right)} \frac{d\boldsymbol{\epsilon}(s)}{ds} ds \tag{2.60}$$

$$= \mathbb{C}_\infty \boldsymbol{\epsilon}(t) + \sum_{i=1}^{n} \boldsymbol{\sigma}_i(t) \tag{2.61}$$

where

$$\boldsymbol{\sigma}_i(t) = \int_0^t \mathbb{C}_i e^{\left(\frac{s-t}{\tau_i}\right)} \frac{d\boldsymbol{\epsilon}(s)}{ds} ds \tag{2.62}$$

$\boldsymbol{\sigma}_i(t)$ represents the inelastic stress which accounts for the strain at all preceding times. Often the viscoelastic behaviour of the material is modelled by the quasi-static approximation, in which the load and deformation are time dependant but the inertia term is neglected. This is equivalent to solving the elastostatic equations with variables depending on the time. However, a complete formulation is provided in chapter 5 in which the generalised alpha-time integration method is employed to solve both elastodynamics and visco-elastodynamics equations.

2.4 Fluid-Structure interaction

Fluid-structure problems are characterised by the kind of coupling between fluid and structure. Generally, the problems are distinguished by one-way coupling and two-way coupling. In one-way coupling problem, there is no feedback between fluid and structure. Furthermore, one-way FSI problems are of two types, one in which the movement of the structure controls the motion of the fluid but the fluid forces have no effect on the structure and the other in which fluid motion affects the structure but structure movement has no effect on fluid dynamics. In two-way coupling, there is a mutual dependence between the fluid and structure mechanics parts. The flow behaviour depends on the shape and the motion of the structure, and the motion and deformation of the structure depend on the fluid mechanics forces acting on the structure. Both one-way and two-way coupling problems are formulated on moving domains. The total domain remains the same but the domains for fluid and structure change with time. This is one of the main difficulties connected with the modelling of FSI problems as well the design of numerical methods for their solution.

In a typical FSI problem, the sets of differential equations and the boundary conditions associated with the fluid and structure domains must be satisfied simultaneously. The domains do not overlap, and the two systems are coupled at the fluid-structure interface. The discretization in FSI can be done in two ways. The first way is to discretize fluid and structure domains separately. This results in non-matching interface meshes. In this case, the solution from one subproblem (fluid or structure) is interpolated at the interface and passed to the other in order to correctly couple the two systems. The another way is to have matching discretization at the interface, which leads to the satisfaction of coupling conditions without any problem. It is necessary to have the compatibility of kinematics and traction boundary conditions at the interface. The structural domain is usually modelled in the Lagrangian frame of coordinates, and its motion follows the material particles. As the structure moves through space, the shape of the fluid subdomain changes to conform to the motion of the structure. The motion of fluid domain is not known a priori and is dependent on the structural displacement which is unknown. In FSI problems the motion of fluid domain is computed as an unknown and is accounted for in the equations and boundary conditions. Mesh updation technique is used to update the fluid domain mesh in the response to changes in the structural domain. In case of significant deformation, a new mesh is generated, and solution is interpolated from the old mesh to the new mesh.

2.4.1 Mathematical form of FSI problem

In this section the coupled fluid-structure interaction problem is described. Let $\Omega_0 \subset \mathbb{R}^n$ be the domain with boundary Γ_0 in reference configuration at time $t = 0$. The domain is split for fluid and structure parts $\Omega_0 = (\Omega_0)_f \cup (\Omega_0)_s$, where $(\Omega_0)_f$ and $(\Omega_0)_s$ are the subsets of Ω_0 occupied by the fluid and structure. Similarly the boundary is split as $\Gamma_0 = (\Gamma_0)_f \cup (\Gamma_0)_s \cup (\Gamma_0)_I$, where $(\Gamma_0)_f$ and $(\Gamma_0)_s$ are the subsets of Γ_0 occupied by the fluid and structure except interface, and $(\Gamma_0)_I$ is the interface between fluid and structure domains (see figure 2.6). Let $\Omega_t \subset \mathbb{R}^n$ be the corresponding deformed domain at time t. Analogously, $\Omega_t = (\Omega_t)_f \cup (\Omega_t)_s$ and $\Gamma_t = (\Gamma_t)_f \cup (\Gamma_t)_s \cup (\Gamma_t)_I$ are split. The FSI problem is stated as: for fluid, solve the Navier-Stokes equations

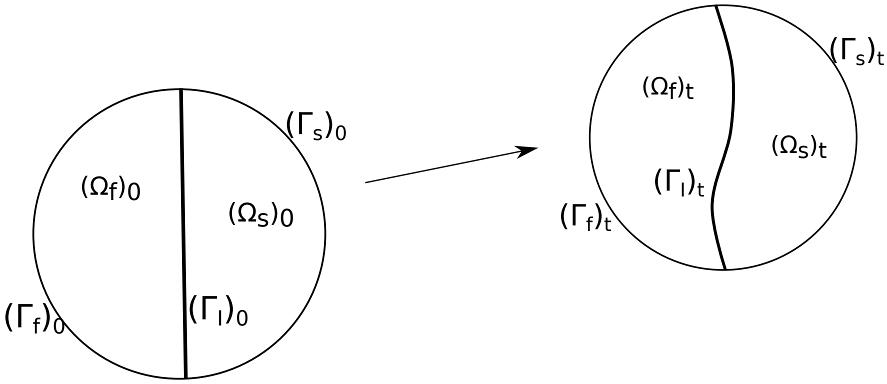

Figure 2.6: Spatial domain for FSI problem in reference and current configuration.

$$\frac{\partial(\rho_f y_k)}{\partial t} + \boldsymbol{\nabla} \cdot (\rho_f y_k \boldsymbol{v}_f) = -\boldsymbol{\nabla} \cdot \boldsymbol{J}^k \tag{2.63}$$

$$\frac{\partial(\rho_f \boldsymbol{v}_f)}{\partial t} + \boldsymbol{\nabla} \cdot (\rho_f \boldsymbol{v}_f \boldsymbol{v}_f) = \rho_f \boldsymbol{f}_f + \boldsymbol{\nabla} \cdot \boldsymbol{\sigma}_f \tag{2.64}$$

$$\frac{\partial(\rho_f e_t)}{\partial t} + \boldsymbol{\nabla} \cdot (\rho_f e_t \boldsymbol{v}_f) = \boldsymbol{\nabla} \cdot (\boldsymbol{\sigma}_f \boldsymbol{v}_f) - \boldsymbol{\nabla} \cdot \boldsymbol{q} + \rho(\boldsymbol{f}_f \boldsymbol{v}_f + r) \tag{2.65}$$

to find y_k, p, $\boldsymbol{v}_f$ and T, and for structure solve

$$\rho_s \boldsymbol{a}_s = \rho_s \boldsymbol{f}_s + \boldsymbol{\nabla} \cdot \boldsymbol{\sigma}_s \tag{2.66}$$

to compute $\boldsymbol{u}_s$ and $\boldsymbol{v}_s$ and for the motion of fluid domain solve

$$\boldsymbol{\nabla} \cdot \boldsymbol{\sigma}_m = 0 \tag{2.67}$$

to find out the deformation of fluid mesh nodes $\boldsymbol{u}_m$. The above equations are linear elastostatic equations with no body forces. The interaction of the fluid with the solid is given by the continuity of the velocity and by a balance of forces:

$$\boldsymbol{v}_f = \boldsymbol{v}_s \qquad \text{and} \qquad \boldsymbol{\sigma}_s \boldsymbol{n}_s = -\boldsymbol{\sigma}_f \boldsymbol{n}_f \qquad \text{on} \qquad (\Gamma_t)_I \tag{2.68}$$

Furthermore, to prevent the fluid and structure meshes from separating at the interface, the following must be satisfied.

$$\boldsymbol{u}_m = \boldsymbol{u}_s \qquad \text{on} \qquad (\Gamma_t)_I \tag{2.69}$$

FSI problems are solved mainly by two approaches: monolithic and staggered which are also known as strongly-coupled and weakly-coupled respectively. In monolithic approach, both subproblems, fluid and structure, are formulated as one combined problem. A single mesh is generated for both fluid and solid, thus, there is no issue of non-matching interface discretization. The equation of fluid, structure and mesh motion are solved simultaneously on the mesh at same time and solution is progressed in time. Examples of monolithic approach can be found in [29, 98, 139]. The solution of the coupled problem via a monolithic scheme is an expensive procedure. Moreover, sometimes the coupling between both problems is in one-way which requires a staggering of the solutions. The staggered approach, also referred as the partitioned approach, is efficient to solve two-way coupling problems. In a staggered algorithm, the fluid, structure and mesh motion problems are solved sequentially with separate solvers. The interaction is taken into account by the boundary conditions. This approach enables the use of existing fluid and structure solvers. The convergence difficulty can be overcome by increasing the number of iterations. For a given time step, a general staggered algorithm computes the solution of fluid with the velocity boundary conditions coming from the extrapolated structural velocities at the interface, followed by the solution of structure with updated fluid traction computed at interface and then followed by the evaluation of mesh motion with the updated structural displacement at the interface. The staggered method has been used in [85, 86, 93, 145].

2.4.2 Algorithms for one-way coupling

As mentioned before in one-way coupling problems, only one problem (fluid or structure) affects the other. One-way coupled problems in which structure affects the fluid but fluid does not affect the structure can be solved by the following general algorithm.

1. Set Δt and initial conditions for fluid and structure at time $t = 0$.
2. Set boundary conditions for structure.
3. Solve the structural problem (2.66) for $\boldsymbol{u}_s$ and $\boldsymbol{v}_s$.
4. Set $\boldsymbol{u}_m = \boldsymbol{u}_s$ on fluid-structure interface $(\boldsymbol{\Gamma}_t)_I$.
5. Solve fluid mesh motion problem (2.67) and update the fluid mesh.
6. Set $\boldsymbol{v}_f = \boldsymbol{v}_s$ as boundary conditions at $(\boldsymbol{\Gamma}_t)_I$.

7. Solve fluid flow problem (2.63)-(2.65) on the updated mesh.
8. Set $t = t + \Delta t$ and go to step 2.

One-way coupled problems in which fluid affects the structure but structure does not affect fluid can be solved by the following general algorithm. In this case, it is preferable to start with the fluid flow problem.

1. Set Δt and initial conditions for fluid and structure at time $t = 0$.
2. Set boundary conditions for fluid.
3. Solve fluid flow problem (2.63)-(2.65).
4. Compute the fluid traction forces $(\boldsymbol{\sigma n})_f$ at $(\boldsymbol{\Gamma}_t)_I$.
5. Set $(\boldsymbol{\sigma n})_s = -(\boldsymbol{\sigma n})_f$ at $(\boldsymbol{\Gamma}_t)_I$.
6. Solve the structural problem (2.66) for $\boldsymbol{u}_s$ and $\boldsymbol{v}_s$.
7. Set $t = t + \Delta t$ and go to step 2.

2.4.3 Algorithm for two-way coupling

Two-way coupled problems in which both subsystems affect each other can be solved by the following general algorithm.

1. Set Δt and initial conditions for fluid and structure at time $t = 0$.
2. Set boundary conditions for fluid.
3. Solve fluid flow problem (2.63)-(2.65).
4. Compute the fluid traction forces $(\boldsymbol{\sigma n})_f$ at $(\boldsymbol{\Gamma}_t)_I$.
5. Set $(\boldsymbol{\sigma n})_s = -(\boldsymbol{\sigma n})_f$ at $(\boldsymbol{\Gamma}_t)_I$.
6. Solve the structural problem (2.66) for $\boldsymbol{u}_s$ and $\boldsymbol{v}_s$.
7. Set $\boldsymbol{u}_m = \boldsymbol{u}_s$ on fluid-structure interface $(\boldsymbol{\Gamma}_t)_I$.
8. Solve fluid mesh motion problem (2.67) and update the fluid mesh.

9. Set $\boldsymbol{v}_f = \boldsymbol{v}_s$ as boundary conditions at $(\boldsymbol{\Gamma}_t)_I$.
10. Set $t = t + \Delta t$ and go to step 2.

In all the above-defined algorithms every subproblem is solved only once per time-step. This can create the problem that interface condition can not be fulfilled exactly. To solve this, the coupling can be done more efficiently by performing several iterations for each time step. The three subproblems can be solved in an iterative manner until the solution does not change anymore. The number of iteration can be determined by defining the convergence criteria. A common convergence criterion is to compute interface residual and bound it to machine double precision (1.e-16).

Chapter 3

Fluid flow for fixed domain

Introduction

In this chapter, the numerical technique to solve the Navier-Stokes equations for multicomponent single-phase fluid flows is provided. In section 3.1, starting with the compact vector equation, the equations are transformed into pressure primitive variables which have the advantage of the simultaneous use for both compressible and incompressible flows. In section 3.2, a brief review on the stabilisation operators is provided, which is necessary to obtain a stable solution. In section 3.3, space-time finite element method, interpolation functions and the associated mapping are introduced with a particular emphasis on moving domain problems. The section also provides the weak formulation of the equations and the discretization schemes along with the detailed calculations of vectors and matrices at the element level. The section is closed with the information on the numerical integration and the discussion on the implementation of boundary conditions. Finally in the section 3.4, the developed numerical technique is validated on several standard benchmark test cases including compressible/incompressible single component and multi-component fluid flows .

3.1 Unified approach for conservation equations

As defined in the chapter (2), the conservation equations for multicomponent single-phase compressible fluid flows are given by

$$(\rho y_k)_{,t} + (\rho v_i y_k)_{,i} = -J^k_{i,i} \tag{3.1}$$

$$(\rho v_j)_{,t} + (\rho v_i v_j)_{,i} = (\sigma_{ji})_{,i} + \rho f_j \tag{3.2}$$

$$(\rho e_t)_{,t} + (\rho v_i e_t + p v_i)_{,i} = \big(\tau_{ij} v_j - q_i - \sum_{k=1}^{n} J^k_i h_k\big)_{,i} + \rho(b_i v_i + r) \tag{3.3}$$

As a first step, the above set of equations is written into a vector form as given below

$$\boldsymbol{U}_{,t} + \boldsymbol{F}^a_{i,i} = \boldsymbol{F}^d_{i,i} + \boldsymbol{\mathcal{F}} \tag{3.4}$$

Where $\boldsymbol{U}$ is the vector of conservation variables. $\boldsymbol{F}^a_i$ is the vector of advective flux. $\boldsymbol{F}^d_i$ is the vector of diffusive flux and $\boldsymbol{\mathcal{F}}$ is the source vector. These vectors are defined as

$$\boldsymbol{U} = \rho \begin{bmatrix} y_1 \\ \vdots \\ y_n \\ \boldsymbol{v} \\ e_t \end{bmatrix} \qquad \boldsymbol{F}^a_i = \rho v_i \begin{bmatrix} y_1 \\ \vdots \\ y_n \\ \boldsymbol{v} + \boldsymbol{\delta_i} p \\ e_t + v_i p \end{bmatrix} \tag{3.5}$$

$$\boldsymbol{F}^d_i = \begin{bmatrix} -J^1_i \\ \vdots \\ -J^n_i \\ \boldsymbol{\tau_i} \\ \tau_{ij} v_j - q_i - \sum_k J^k_i h_k \end{bmatrix} \qquad \boldsymbol{\mathcal{F}} = \rho \begin{bmatrix} 0 \\ \vdots \\ 0 \\ \boldsymbol{b} \\ \boldsymbol{b} \cdot \boldsymbol{v} + r \end{bmatrix} \tag{3.6}$$

Each term in the above vectors is defined in the chapter(2). The above-written equations for multicomponent fluid flows can be easily transformed into the equations for single component flow. In order to achieve that, in weight fraction terms the first component y_1 is kept fixed to 1 and rest all weight fraction terms y_k, $2 \leq k \leq n$ are set to 0. The equation (3.4) can be rewritten in the quasi-linear form as

$$\boldsymbol{U}_{,t} + \boldsymbol{A}_i(\boldsymbol{U})\boldsymbol{U}_{,i} = \left(\boldsymbol{K}_{ij}(\boldsymbol{U})\ \boldsymbol{U}_{,j}\right)_{,i} + \boldsymbol{\mathcal{F}} \tag{3.7}$$

where $\boldsymbol{A}_i(\boldsymbol{U}) = \boldsymbol{F}^a_{i,\boldsymbol{U}}$ is the ith Euler Jacobian matrix and $\boldsymbol{K}(\boldsymbol{U}) = [\boldsymbol{K}_{ij}]$ is the diffusivity matrix with $\boldsymbol{K}_{ij}(\boldsymbol{U})\ \boldsymbol{U}_{,j} = \boldsymbol{F}^d_i$. Using the chain rule, a standard routine of Mathematics, the equation (3.7) can be written for any random independent set of variables, $\boldsymbol{Y}$. The transformed equation can be written as

$$\boldsymbol{A}_0(\boldsymbol{Y})\boldsymbol{Y}_{,t} + \boldsymbol{A}_i(\boldsymbol{Y})\boldsymbol{Y}_{,i} = (\boldsymbol{K}_{ij}(\boldsymbol{Y})\ \boldsymbol{Y}_{,j})_{,i} + \boldsymbol{SY} \tag{3.8}$$

where $\boldsymbol{A}_0(\boldsymbol{Y}) = \boldsymbol{U}_{,\boldsymbol{Y}}$; $\boldsymbol{A}_i(\boldsymbol{Y}) = \boldsymbol{F}^a_{i,\boldsymbol{Y}}$; $\boldsymbol{K}_{ij}\boldsymbol{Y}_{,j} = \boldsymbol{F}^d_i$ and $\boldsymbol{F} = \boldsymbol{SY}$. Here, $\boldsymbol{S}$ is the source matrix. All these matrices are defined in appendix (A). In the work of Hughes et al. [198, 199] the physical entropy variables were used as the independent set of variables for the computation of single component fluid flows, which resulted in the symmetric positive definite $\boldsymbol{A}_0$, symmetric $\boldsymbol{A}_i$ and symmetric positive semi-definite $\boldsymbol{K}_{ij}$ matrices. The entropy variables are denoted by $\boldsymbol{V}$. The set of entropy variables $\boldsymbol{V}$ for single component fluid is defined as

$$\boldsymbol{V} = \frac{1}{T}\begin{bmatrix} g - |\boldsymbol{v}|^2/2 \\ \boldsymbol{v} \\ -1 \end{bmatrix} \tag{3.9}$$

Where, g is the Gibbs free energy per unit mass. The symmetry of the transformed equation (3.8), written in entropy variables, satisfies the Clausius-Duhem inequality which results in basic non-linear stability condition for compressible Navier-Stokes equations. For details see [195], Shakib et al. [64] and [137]. In [72] Hauke and Hughes demonstrated that both compressible and incompressible fluid flows can be solved by the space-time finite element method in a unified way by employing either entropy variables, $\boldsymbol{V}$ or pressure primitive variables, $\boldsymbol{Y} = (p, \boldsymbol{v}, T)$. It was analysed in [74] that for conservative variables, the flux Jacobian matrices were not well defined in the incompressibility limit, *i.e.* when $\alpha_p, \beta_T \to 0$. Several terms in the flux matrices got the value ∞ and $0/0$. Incompressibility limit for entropy and pressure primitive variables was observed to be well defined. The pressure primitive variables for simple fluid compressible-incompressible flows were proved to be a reliable choice in terms of the accuracy, convergence, computational costs and robustness of the numerical technique. Furthermore, it was verified that the pressure primitive variables provide better results than entropy variables for incompressible flows at high Reynolds number and are easier to set in the boundary conditions. Based on the quality features of the pressure primitive variables, in [11] Longo et al. extended the variables vectors to compute the multicomponent/multiphase fluid flows. The vector of pressure primitive variables ($\boldsymbol{Y}$) was extended by including the weight fractions of the components and the entropy variables vector ($\boldsymbol{V}$) was extended by including the specific Gibbs free energies of the components.

$$\boldsymbol{Y} = \begin{bmatrix} y_1 \\ \vdots \\ y_{n-1} \\ p \\ \boldsymbol{v} \\ T \end{bmatrix} \quad \text{and} \quad \boldsymbol{V} = \frac{1}{T} \begin{bmatrix} g_1 - k \\ \vdots \\ g_{n-1} - k \\ g_n - k \\ \boldsymbol{v} \\ -1 \end{bmatrix} \tag{3.10}$$

The numerical technique applied in [11] to solve the compressible/incompressible multicomponent/multiphase fluid flows was based on the stabilised space-time Galerkin least square finite element method for the fixed domains. In the next sections, the numerical technique is extended to account for the moving boundary problems. The spatial and time dependence Navier-Stokes equations are needed to be discretized in both space and time. In the context of finite element methods, there are mainly two approaches proposed in the literature; semi-discrete and space-time method. In the semi-discrete approach, the spatial domain is discretized by the Galerkin finite element method and the solution is progressed in time by discretizing the time domain by the finite difference method. While in the space-time finite element method both space and time are discretized simultaneously generating the space-time slabs. In the latter technique, time is considered as an extra dimension and treated in the same way as space.

It has been studied and verified by many researchers in the past that the discontinuous Galerkin finite element methods are better than continuous

Galerkin finite element methods in terms of stability and consistency. Although there is a requirement of more degrees of freedom in the discontinuous discretization, it generally offers more flexibility and accuracy. The discontinuity can be imposed in both space and time. Some of the earlier published papers on the time-discontinuity are [35, 146]. The time-discontinuous Galerkin method was studied in [40,212]. The space-time least square method was proposed by Nguyen and Reynen [81]. In [78] Hulbert et al. applied the space-time method for the second-order hyperbolic equation, in particular for elastodynamics. Space-time discontinuous Galerkin/Least-squares algorithms for fluid flow problems were developed by Shakib and Hughes [64].

3.2 Stabilisation operators

In the computational fluid dynamics, for several flow problems the stabilisation operators play a key role to acquire the best accurate solutions. Specifically, in the case of the advection dominated flows the numerical techniques require the additional stabilisation operators to attain a stable solution. In last few decades, a number of stabilisation operators have been developed for compressible and incompressible flows. For incompressible flows see [128, 129, 133, 137, 177, 187, 192, 193] and in the context of compressible flows see [62, 76, 77, 112, 114, 172, 173]. The upwind scheme in the finite elements was attempted in [108, 123, 124, 130, 138] to enhance the stability in advection-dominated flow problems. The idea was to add the artificial numerical diffusion corresponding to the upwind methods in the central finite differences. In this section, some of the stabilisation operators are reviewed.

SUPG method. The SUPG method is a residual-based upwind technique, which stabilises the Galerkin finite element method for equal-order interpolations. The first stabilised method streamline upwind Petrov-Galerkin (SUPG) was developed for the advection-diffusion equations and the incompressible Navier-Stokes equations [24]. The method possesses the streamline upwind to restrict the excessive crosswind diffusion and the Petrov-Galerkin weighted residual formulation to remove the artificial diffusion. Hughes and Tezduyar [201, 202] generalised the SUPG operator to the Navier-Stokes equations for the compressible flows. To review it, equation (3.7) is considered with zero diffusion *i.e.* $\boldsymbol{F}_i^d = 0$.

$$\boldsymbol{U}_{,t} + \boldsymbol{A}_i(\boldsymbol{U})\boldsymbol{U}_{,i} - \boldsymbol{\mathcal{F}} = 0 \tag{3.11}$$

The semi-discrete variational formulation of the above equation with the SUPG method will result in

$$\int_{\Omega} \boldsymbol{W}^h \left(\boldsymbol{U}^h_{,t} + \boldsymbol{A}_i(\boldsymbol{U}^h)\boldsymbol{U}^h_{,i} - \boldsymbol{\mathcal{F}} \right) + \text{ SUPG}(\boldsymbol{W}^h, \boldsymbol{U}^h) = 0 \tag{3.12}$$

With

$$\text{SUPG}(\boldsymbol{W}^h, \boldsymbol{U}^h) = \sum_e \int_{\Omega_e} \tau_e \boldsymbol{A}_i^T(\boldsymbol{U}^h) \cdot \nabla \boldsymbol{W}^h \left(\boldsymbol{U}^h_{,t} + \boldsymbol{A}_i^h(\boldsymbol{U}^h)\boldsymbol{U}^h_{,i} - \boldsymbol{\mathcal{F}} \right) \tag{3.13}$$

Where, the spatial domain is discretized in elements with $\Omega = \cup_{e=1}^n \Omega_e$ and the Dirichlet boundary conditions are embedded in the test and trial spaces. The parameter τ_e was designed in according to a temporal or a spatial criterion. The tested definitions are:

$$\tau_e = \alpha \Delta t \qquad \text{(Temporal criteria)} \tag{3.14}$$

$$\tau_e = \alpha h / a \qquad \text{(Spatial criteria 1)} \tag{3.15}$$

$$\tau_e = \alpha h_i / a_i \qquad \text{(Spatial criteria 2)} \tag{3.16}$$

Where, a_i is the spectral radius of $\boldsymbol{A}_i$, and $a = (a_i a_i)^{1/2}$. α is the algorithmic constant and set to $1/2$. h_i and h are defined as

$$h_i = 2\left((x_{i,\xi})^2 + (x_{i,\eta})^2 \right) \tag{3.17}$$

$$h = h_i \frac{a_i}{a} \tag{3.18}$$

In [201] the authors presented a detailed analysis of SUPG stabilisation on the stability and order of convergence for a class of predictor/multi-corrector time integrators adopted in the computations. The numerical results showed good performance of the method in the case of steady shocks and noisier results in the case of transient shocks.

GLS method. In [197] Hughes et al. generalised the SUPG into Galerkin least/squares (GLS) stabilisation method and applied to the advection-diffusion problems. Shakib et al. [64] tested GLS on space-time formulation of the compressible Navier-Stokes equations. The GLS stabilization term for (3.8) in entropy variables can be written as

$$\mathrm{GLS}(\boldsymbol{W}^h, \boldsymbol{V}^h) = \sum_e \int_{\Omega_e} \boldsymbol{\mathcal{L}}(\boldsymbol{W}^h) \boldsymbol{\tau_V} \left(\boldsymbol{\mathcal{L}}(\boldsymbol{V}^h) - \boldsymbol{\mathcal{F}} \right) \tag{3.19}$$

Where the differential operator $\boldsymbol{\mathcal{L}}$ is defined as

$$\boldsymbol{\mathcal{L}} = \boldsymbol{A}_0 \frac{\partial}{\partial t} + \boldsymbol{A}_i \frac{\partial}{\partial x_i} - \frac{\partial}{\partial x_i} (\boldsymbol{K}_{ij} \frac{\partial}{\partial x_j}) \tag{3.20}$$

For the compressible Navier-Stokes equations written in the pressure primitive variables, the GLS stabilisation term is defined as

$$\mathrm{GLS}(\boldsymbol{W}^h, \boldsymbol{Y}^h) = \sum_e \int_{\Omega_e} \boldsymbol{\mathcal{L}}^T (\boldsymbol{W}^h) \boldsymbol{\tau_Y} \left(\boldsymbol{\mathcal{L}}(\boldsymbol{Y}^h) - \boldsymbol{\mathcal{F}} \right) \tag{3.21}$$

With

$$\boldsymbol{\mathcal{L}}^T = \boldsymbol{A}_0^T \frac{\partial}{\partial t} + \boldsymbol{A}_i^T \frac{\partial}{\partial x_i} - \frac{\partial}{\partial x_i} \left(\boldsymbol{K}_{ij}^T \frac{\partial}{\partial x_j} \right) \tag{3.22}$$

$\boldsymbol{\tau_V}$ and $\boldsymbol{\tau_Y}$ are the stabilization matrices for entropy and pressure primitive variables, related by the relation $\boldsymbol{\tau_Y} = \boldsymbol{Y}_{,\boldsymbol{V}} \boldsymbol{\tau_V}$. The matrix $\boldsymbol{\tau_V}$ is obtained as the solution of an eigenvalue problem, which is complicated and CPU time consuming. To remedy this problem, in [71] Hauke introduced two simplified forms of the tau matrices $\boldsymbol{\tau}_d$ and $\boldsymbol{\tau}_{nd}$ for pressure primitive variables defined as

$$\boldsymbol{\tau}_d = \mathrm{diag}(\tau_c, \tau_m, \tau_m, \tau_e) \qquad \text{in 2D} \tag{3.23}$$

with

$$\tau_c = \min \left(\frac{|\boldsymbol{v}| h^e}{2} \right) \tag{3.24}$$

$$\tau_m = \min\left(\frac{\Delta t}{2\rho}, \frac{h^e}{2\rho(|\boldsymbol{v}|+c)}, \frac{(h^e)^2}{12\mu}\right) \tag{3.25}$$

$$\tau_e = \min\left(\frac{\Delta t}{2\rho c_v}, \frac{h^e}{2\rho c_v(|\boldsymbol{v}|+c)}, \frac{(h^e)^2}{12\kappa}\right) \tag{3.26}$$

Where, $|\boldsymbol{v}|$ is the absolute value of velocity, c is the sound speed, $[g^{ij}]$ is the element metric tensor, h^e is the element size in streamline direction and computed as

$$(h^e)^2 = \frac{4v_i g^{ij} v_j}{|\boldsymbol{v}|^2} \qquad \text{with} \qquad g^{ij} = \frac{\partial x_i}{\partial \xi_k}\frac{\partial x_j}{\partial \xi_k} \tag{3.27}$$

$\boldsymbol{\tau}_{nd}$ is defined as

$$\boldsymbol{\tau}_{nd} = \boldsymbol{Y}_{,\boldsymbol{U}}\hat{\boldsymbol{\tau}} \qquad \hat{\boldsymbol{\tau}} = \text{diag}(\hat{\tau_c}, \hat{\tau_m}, \hat{\tau_m}, \hat{\tau_e}) \tag{3.28}$$

with

$$\hat{\tau_c} = \min\left(\frac{\Delta t}{2}, \frac{1}{\lambda^e}\right) \tag{3.29}$$

$$\hat{\tau_m} = \min\left(\frac{\Delta t}{2}, \frac{1}{\lambda^e}, \frac{\rho(h_d^e)^2}{12\mu}\right) \tag{3.30}$$

$$\hat{\tau_e} = \min\left(\frac{\Delta t}{2}, \frac{1}{\lambda^e}, \frac{\rho c_v(h_d^e)^2}{12\kappa}\right) \tag{3.31}$$

where,

$$(\lambda^e)^2 = \frac{4}{\Delta t^2} + \alpha_1(\boldsymbol{v}^2 + c^2) + \frac{\alpha_2 c^2}{2} + \frac{c\sqrt{c^2\alpha_2^2 + 16\alpha_1^2\boldsymbol{v}^2}}{2} \tag{3.32}$$

$$\alpha_i = n_l^{s_i} g_{lm} n_m^{s_i} \qquad \text{and} \qquad (h_d^e)^2 = 4\left(\frac{1}{\alpha_1} + \frac{1}{\alpha_2}\right) \tag{3.33}$$

After performing a number of test cases it was concluded that with both $\boldsymbol{\tau_d}$ and $\boldsymbol{\tau_{nd}}$ the accuracy and stability of the method was good. Based on the results of Hauke [71], in [11] Longo et al. constructed the stabilized matrices for multicomponent fluid flows. In the extension authors proposed a stabilization term for each component of the fluid mixture. The structure of composed matrix is given as:

$$\boldsymbol{\tau}_{\boldsymbol{Y}}^{nd} = \boldsymbol{Y}_{,\boldsymbol{U}} \boldsymbol{\tau}_{\boldsymbol{U}} \tag{3.34}$$

$$\boldsymbol{\tau}_{\boldsymbol{U}} = \operatorname{diag}(\tau_{\rho y_1}, \cdots, \tau_{\rho y_k}, \tau_{\rho v_1}, \tau_{\rho v_2}, \tau_{\rho e_t}) \qquad \text{in 2D} \tag{3.35}$$

with

$$\tau_{\rho y_k} = \min\left(\frac{\Delta t}{2}, \frac{1}{\lambda^e} + \frac{h_d^e}{2|\boldsymbol{v}|}, \frac{(h_d^e)^2}{12 d_{kk}}\right) \tag{3.36}$$

$$\tau_m = \min\left(\frac{\Delta t}{2}, \frac{1}{\lambda^e} + \frac{h_d^e}{2|\boldsymbol{v}|}, \frac{\rho (h_d^e)^2}{12 \mu}\right) \tag{3.37}$$

$$\tau_e = \min\left(\frac{\Delta t}{2}, \frac{1}{\lambda^e} + \frac{h_d^e}{2|\boldsymbol{v}|}, \frac{\rho c_v (h_d^e)^2}{12 \kappa}\right) \tag{3.38}$$

Where d_{kk} is the diffusion coefficient for component k and rest of the terms are the same as defined in (3.32)-(3.33). The authors found that analogous to the $\boldsymbol{\tau}$ matrix for single component fluids, the extended tau matrix provide the stable solutions.

DC operator. For compressible flows in the presence of shock waves, it is necessary to add the discontinuity capturing operator as a dissipation mechanism to remove the oscillations present near the sharp boundary layers or internal interfaces. The shock waves can also exist in low-speed incompressible fluid flows. One standard example is the water hammer phenomenon, where both pressure and velocity changes very rapidly. The shock can be detected by the exact calculation of Mach number. The shock waves are generated for the flow with a Mach number greater than one. This can be checked by computing the entropy generation in the flow. In the context of compressible Navier-Stokes equations, shocks are termed as discontinuities. Hughes et al. [200] developed a discontinuity capturing operator based on the projector in the direction of solution gradient computed in entropy variables for compressible Navier-Stokes equations. In [74] Hauke and Hughes used the following simple discontinuity capturing term DC for the generalised set of variables.

$$\mathrm{DC}(\boldsymbol{W}^h, \boldsymbol{Y}^h) = \sum_{e=1}^{n_{el}} \int_{\Omega_e} \nu_{\mathrm{HM}} g^{ij} \boldsymbol{W}^h_{,i} \cdot \boldsymbol{A}_0 \boldsymbol{Y}^h_{,j} \tag{3.39}$$

With

$$\nu_{\mathrm{HM}} = \max \left(0,\ \left(\frac{(\boldsymbol{\mathcal{L}} \boldsymbol{Y} - \boldsymbol{\mathcal{F}}) \cdot \boldsymbol{V}_{,\boldsymbol{U}} (\boldsymbol{\mathcal{L}} \boldsymbol{Y} - \boldsymbol{\mathcal{F}})}{g^{ij} \boldsymbol{Y}_{,\boldsymbol{i}} \cdot {\boldsymbol{V}_{,\boldsymbol{Y}}}^T \boldsymbol{U}_{,\boldsymbol{Y}} \boldsymbol{Y}_{,j}} \right)^{\frac{1}{2}} - \frac{(\boldsymbol{\mathcal{L}} \boldsymbol{Y} - \boldsymbol{\mathcal{F}}) \cdot \boldsymbol{\tau_V} (\boldsymbol{\mathcal{L}} \boldsymbol{Y} - \boldsymbol{\mathcal{F}})}{g^{ij} \boldsymbol{Y}_{,\boldsymbol{i}} \cdot {\boldsymbol{V}_{,\boldsymbol{Y}}}^T \boldsymbol{U}_{,\boldsymbol{Y}} \boldsymbol{Y}_{,j}} \right) \tag{3.40}$$

Where, $\boldsymbol{\tau_V} = \boldsymbol{V}_{,\boldsymbol{U}} \boldsymbol{\tau_U}$ is the stabilization matrix for entropy variables. $\boldsymbol{\tau_U}$ is defined in (3.35). The same discontinuity capturing operator term was used by Longo et al. [11] for the multicomponent flows. $\boldsymbol{V}_{,\boldsymbol{U}}$ and $\boldsymbol{V}_{,\boldsymbol{Y}}$ for the multicomponent flows are defined in appendix (A).

3.3 Space-time finite element method

The space-time finite element method is very efficient in providing the numerical discretization for problems with deforming meshes. For the moving domain problems, discretization of equation (3.8) by FEM requires the movement of mesh point at each instant of time in order to account for the boundary movement. Generally at the new position data is not available and requires the projection of the data from the old mesh to the new mesh. This interpolation process is generally non-conservative and can introduce substantial errors. The space-time finite element method is an alternative to solve this problem. The discontinuous Galerkin space-time FEM has been applied successfully for the inviscid compressible flows described by the Euler equations of gas dynamics [83, 107]. Extensions of the method to the advection-diffusion equation are given in [106] and for the compressible Navier-Stokes equations in [15,16,41]. In this section, the space-time Galerkin least square finite element method is presented for moving domains to solve the equation (3.8) in pressure primitive variables $\boldsymbol{Y}$. The numerical technique is time-discontinuous and uses the same interpolation functions for all solution variables. This method is well suited to deal with the time-dependent flow domains with moving boundaries and dynamic meshes. The method performs an implicit discretization using the space-time elements which is globally conservative on deforming meshes and prevents the inaccuracies of data interpolation between the various meshes. The next section begins with the concept of space-time domain and defines the mapping from a space-time reference element onto a space-time physical element. The weighted residual formulation of the equation (3.8) is presented, supplemented with the GLS and DC stabilisation operators. This is followed by the discretization schemes and the algorithms to solve the system of algebraic equations.

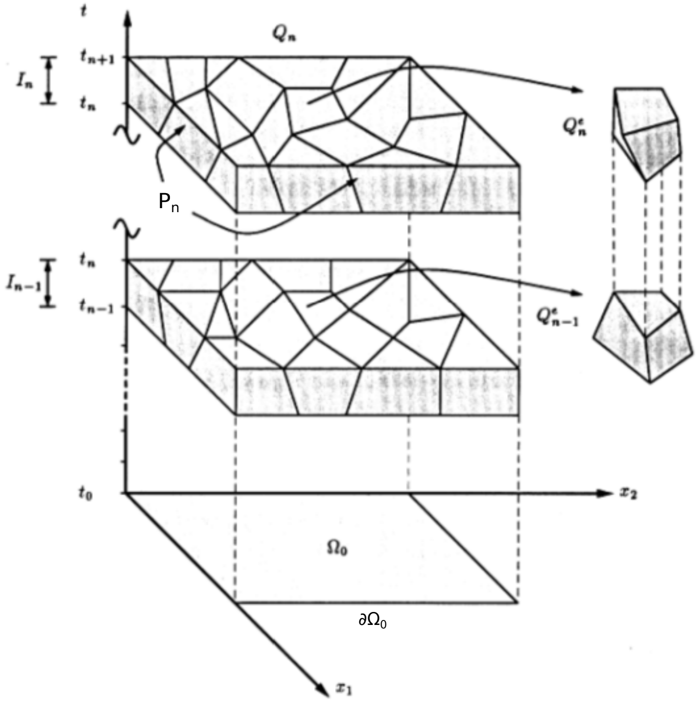

Figure 3.1: Illustration of two consecutive space-time slabs with unstructured finite element meshes in space-time, adapted from [16].

In space-time finite element method both space and time are discretized simultaneously by taking a tensor product of basis functions for the spatial domain and one-dimensional basis function in time direction. A piecewise continuous approximation in space and discontinuous approximation in time is considered. Discontinuous approximation in time allows to solve independently for each time slab instead of solving a global problem over the whole time domain. A space-time domain is defined as $Q = \Omega_t \times (0, T)$ with boundary $P = \partial\Omega_t \times (0, T)$, where Ω_t is the spatial domain with boundary $\partial\Omega_t$. The space-time formulation requires the introduction of space-time slab and elements. Let the time interval $(0, T)$ be subdivided into an ordered series of time levels $0 = t_0 < t_1 < \cdots < t_n < t_{n+1} < \cdots < t_N = T$. Denoting the nth time interval as $I_n = (t_n, t_{n+1})$ with $T = \cup_n I_n$. The length of I_n is defined as $\Delta t_n = t_{n+1} - t_n$. Let Ω_n is the spatial domain at time $t = t_n$ then for time interval I_n a space-time slab is defined as $Q_n = \Omega_n \times (t_n, t_{n+1})$ with boundary $P_n = \partial\Omega_n \times (t_n, t_{n+1})$. Each space-time slab is divided into $(n_{el})_n$ elements Q_n^e having boundary P_n^e with discontinuous basis functions across the slab boundaries in time-direction. The space-time elements are constructed by splitting the spatial domain Ω_n into $(n_{el})_n$ spatial elements at time t_n and then mapping the vertices of elements to their new position at time t_{n+1}. Each space time element Q_n^e is obtained by connecting the spatial elements Ω_n^e and Ω_{n+1}^e using linear interpolation in time. Figure (3.1) illustrates the concept. Note that the mesh is unstructured in space. In a typical space-time computation all the nodes of the space-time slab would be on the time plane n or $n + 1$ or in between, not necessarily on time planes parallel to the n and $n + 1$ but without requiring a space-time mesh that is unstructured in time. It is usual to consider that the space-time slab would simply be deformed versions of each other. The mesh on the upper surface of the slab at t_{n+1} is obtained from the deformation of the mesh nodes at the lower surface t_n. Galerkin least/squares stabilized space-time method for moving domain is named as deforming-spatial-domain/stabilized space-time (DSD/SST) by Tezduyar and colleagues [111, 190, 191, 213].

3.3.1 Space-time mapping

The geometry of a space-time element can be defined by introducing the mapping $\boldsymbol{\phi}$. The mapping connects each space-time element $Q_n^e(x, y, t)$ in the physical domain to a master element $\hat{Q}_n^e$ in the reference domain with coordinates $(\xi, \eta, \theta) \in [-1, 1]^3$. As defined in [191], the space-time shape functions are defined as

$$N_a^\alpha = N_a(\xi, \eta) T^\alpha(\theta) \qquad a = 1, 2, \ldots, n_{el_{nodes}} \qquad \alpha = 1, 2 \tag{3.41}$$

Here, $n_{el_{nodes}}$ is the number of element nodes; 3 for a triangle and 4 for a quadrangle. In this thesis, only 2D flow test cases are studied with quadrangle elements. However, the extension from 2D to 3D is straightforward. $N_a(\xi, \eta)$ is the bilinear spatial shape functions for node a of the element and $T^\alpha(\theta)$ are the temporal shape functions defined at lower part of slab corresponding to $\alpha = 1$ and at upper part of slab corresponding to $\alpha = 2$. The spatial and temporal shape functions are defined as

$$N_a(\xi, \eta) = \frac{1}{4}(1 - \xi_a \xi)(1 - \eta_a \eta) \tag{3.42}$$

$$T^\alpha(\theta) = \frac{1}{2}\left(1 + (-1)^\alpha \theta\right) \tag{3.43}$$

Where (ξ_a, η_a) are the nodal coordinated of node a in the reference domain. The space-time mapping $\boldsymbol{\phi}$ is defined as $\boldsymbol{\phi} : [-1, 1]^3 \to \mathbb{R}^2 \times \mathbb{R}$. The figure (3.2) displays the space time mapping from a reference element onto a physical element. The right image in figure(3.2) is taken from [191] and represents the geometry of a general space-time element in the physical domain. The space-time mapping $\boldsymbol{\phi} : (\xi, \eta, \theta) \to (x, y, t)$ is defined as follows:

$$x = \sum_\alpha \sum_a N_a^\alpha x_a^\alpha \tag{3.44}$$

$$y = \sum_\alpha \sum_a N_a^\alpha y_a^\alpha \tag{3.45}$$

$$t = \sum_\alpha \sum_a N_a^\alpha t_a^\alpha = \sum_\alpha T^\alpha t^\alpha \tag{3.46}$$

Here, x_a^α and y_a^α are the spatial-coordinates of node a at time level α; t_a^α is the temporal coordinate vector of mesh element nodes in the physical space-time domain. The above defined mapping is sufficiently smooth, orientation preserving and invertible. Therefore (x, y, t) are continuously differentiable with respect to (ξ, η, θ). This gives

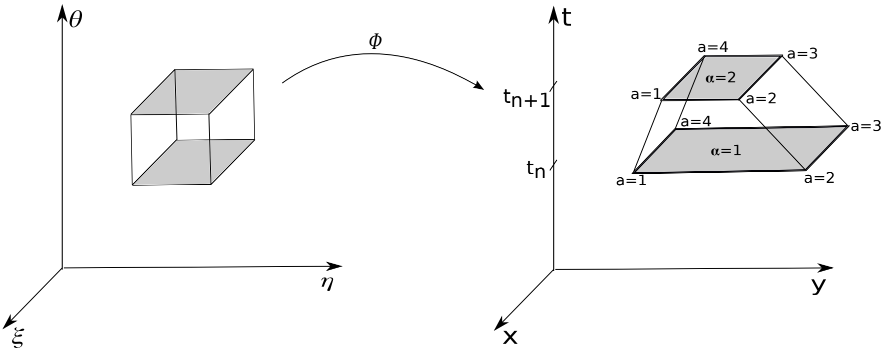

Figure 3.2: Space-time mapping

$$\begin{bmatrix} dx \\ dy \\ dt \end{bmatrix} = \begin{bmatrix} x_{,\xi} & x_{,\eta} & x_{,\theta} \\ y_{,\xi} & y_{,\eta} & y_{,\theta} \\ t_{,\xi} & t_{,\eta} & t_{,\theta} \end{bmatrix} \begin{bmatrix} d\xi \\ d\eta \\ d\theta \end{bmatrix} = \boldsymbol{J}^{ST} \begin{bmatrix} d\xi \\ d\eta \\ d\theta \end{bmatrix} \tag{3.47}$$

The matrix $\boldsymbol{J}^{ST}$ of the space-time mapping is called the space-time Jacobian matrix. Each component of the Jacobian matrix is computed by performing the partial derivative on equations (3.44)-(3.46) as follows:

$$x_{,\xi} = \sum_{\alpha} \sum_{a} N^{\alpha}_{a,\xi} x^{\alpha}_{a} \qquad y_{,\xi} = \sum_{\alpha} \sum_{a} N^{\alpha}_{a,\xi} y^{\alpha}_{a} \qquad t_{,\xi} = \sum_{\alpha} \sum_{a} T^{\alpha}_{,\xi} t^{\alpha} = 0 \tag{3.48}$$

$$x_{,\eta} = \sum_{\alpha} \sum_{a} N^{\alpha}_{a,\eta} x^{\alpha}_{a} \qquad y_{,\eta} = \sum_{\alpha} \sum_{a} N^{\alpha}_{a,\eta} y^{\alpha}_{a} \qquad t_{,\eta} = \sum_{\alpha} \sum_{a} T^{\alpha}_{,\eta} t^{\alpha} = 0 \tag{3.49}$$

$$x_{,\theta} = \sum_{\alpha} \sum_{a} N^{\alpha}_{a,\theta} x^{\alpha}_{a} \qquad y_{,\theta} = \sum_{\alpha} \sum_{a} N^{\alpha}_{a,\theta} y^{\alpha}_{a} \qquad t_{,\theta} = \sum_{\alpha} \sum_{a} T^{\alpha}_{,\theta} t^{\alpha} = \frac{\Delta t}{2} \tag{3.50}$$

Since the temporal shape functions are independent of ξ and η, therefore the partial derivative results zero. The spatial-coordinates x_a^2 and y_a^2 are computed by adding the contribution coming from the mesh deformation to the spatial-coordinates x_a^1 and y_a^1. The values of $x_{,\theta}$ and $y_{,\theta}$ are evaluated as

$$x_{,\theta} = \sum_{\alpha}\sum_{a} N_{a,\theta}^{\alpha} x_a^{\alpha} = \sum_{a} N_a \frac{(x_a^2 - x_a^1)}{2} = \sum_{a} N_a \frac{u_{x_a}^m}{2} = \frac{\Delta t}{2}\sum_{a} N_a v_{x_a}^m \tag{3.51}$$

$$y_{,\theta} = \sum_{\alpha}\sum_{a} N_{a,\theta}^{\alpha} y_a^{\alpha} = \sum_{a} N_a \frac{(y_a^2 - y_a^1)}{2} = \sum_{a} N_a \frac{u_{y_a}^m}{2} = \frac{\Delta t}{2}\sum_{a} N_a v_{y_a}^m \tag{3.52}$$

Where, for node a, $u_{x_a}^m$, $u_{y_a}^m$ and $v_{x_a}^m$, $v_{y_a}^m$ are the x and y component of mesh deformation and mesh velocity respectively. In case of no mesh motion, these values are set to zero. The spatial Jacobian matrix $\boldsymbol{J}^S$ is defined as

$$\boldsymbol{J}^S = \begin{bmatrix} x_{,\xi} & x_{,\eta} \\ y_{,\xi} & y_{,\eta} \end{bmatrix} \tag{3.53}$$

By substituting the above relations in space-time Jacobian matrix, the determinant can be computed as

$$|\boldsymbol{J^{ST}}| = \frac{\Delta t}{2}|\boldsymbol{J^S}| = \frac{\Delta t}{2}(x_{,\xi}y_{,\eta} - y_{,\xi}x_{,\eta}) \tag{3.54}$$

The inverse of space-time Jacobian matrix is computed as follows:

$$(\boldsymbol{J}^{ST})^{-1} = \begin{bmatrix} \xi_{,x} & \xi_{,y} & \xi_{,t} \\ \eta_{,x} & \eta_{,y} & \eta_{,t} \\ \theta_{,x} & \theta_{,y} & \theta_{,t} \end{bmatrix} = \frac{1}{|\boldsymbol{J^S}|} \begin{bmatrix} y_{,\eta} & -x_{,\eta} & \dfrac{2(x_{,\eta}y_{,\theta} - y_{,\eta}x_{,\theta})}{\Delta t} \\ -y_{,\xi} & x_{,\xi} & \dfrac{2(y_{,\xi}x_{,\theta} - x_{,\xi}y_{,\theta})}{\Delta t} \\ 0 & 0 & \dfrac{2}{\Delta t} \end{bmatrix} \tag{3.55}$$

The spatial and temporal derivatives of shape functions in the physical domain can be linked to the derivatives of shape functions in the reference domain as follows:

$$\begin{bmatrix} N_{a_{,x}} \\ N_{a_{,y}} \\ N_{a_{,t}} \end{bmatrix} = \begin{bmatrix} \xi_{,x} & \eta_{,x} & \theta_{,x} \\ \xi_{,y} & \eta_{,y} & \theta_{,y} \\ \xi_{,t} & \eta_{,t} & \theta_{,t} \end{bmatrix} \begin{bmatrix} N_{a_{,\xi}} \\ N_{a_{,\eta}} \\ N_{a_{,\theta}} \end{bmatrix} \tag{3.56}$$

Where, the terms in matrix can be evaluated from relation (3.55). This can be rewritten as

$$\begin{bmatrix} N_{a_{,x}} \\ N_{a_{,y}} \\ N_{a_{,t}} \end{bmatrix} = (\boldsymbol{J}^{ST})^{-T} \begin{bmatrix} N_{a_{,\xi}} \\ N_{a_{,\eta}} \\ N_{a_{,\theta}} \end{bmatrix} \tag{3.57}$$

3.3.2 Weak formulation

The weighted residual formulation of equation (3.8) is derived by multiplying with an arbitrary test function $\boldsymbol{W}^h$ and integrate it over the space-time domain, which is divided into the space-time slabs, and which are further divided into the space-time elements. The numerical solution is computed on only one slab at a time and taken as the initial conditions for the next slab. The enforcement of initial conditions is done weakly as in discontinuous Galerkin method, which is equivalent to maintain the continuity of the solution between two consecutive slabs. Two functional spaces are defined, one for trial functions and the other for weighting functions. The trial function space in each space-time slab Q_n is denoted by $\mathscr{T}_n^h$ and the test function space is denoted by $\mathscr{W}_n^h$. Within each space-time element, the trial solution and weighting functions are approximated by kth order polynomials $\mathscr{P}_k$. Since the discontinuity is considered only in time, the functions are assumed C^0 continuous within each space-time slab, and are discontinuous across the interfaces of the slabs. The finite element spaces are defined as

$$\mathscr{T}_n^h = \Big\{\boldsymbol{Y}^h |\ \boldsymbol{Y}^h \in (C^0(Q_n))^m,\ \ \boldsymbol{Y}^h_{|Q_n^e} \in (\mathscr{P}_k(Q_n))^m,\ g_1(\boldsymbol{Y}^h) = g \text{ on } P_n\Big\} \tag{3.58}$$

$$\mathscr{W}_n^h = \Big\{\boldsymbol{W}^h |\ \boldsymbol{W}^h \in (C^0(Q_n))^m,\ \ \boldsymbol{W}^h_{|Q_n^e} \in (\mathscr{P}_k(Q_n))^m,\ g_2(\boldsymbol{W}^h) = 0 \text{ on } P_n\Big\} \tag{3.59}$$

Where m is the number of degrees of freedom. $g_1, g_2 : \mathbb{R}^m \to \mathbb{R}^i$, are the boundary condition transformation functions and g is the prescribed boundary condition. It is possible that not all components of $\boldsymbol{Y}$ have imposed boundary conditions, it depends on the case of interest. The continuity over Q_n implies the continuity in space but does not require a continuous interpolation between the time slabs. Although, $\mathscr{P}_k$ indicates the space of polynomials of total degree $\leq k$ the degree of the polynomials in space and time can be chosen independently. The space-time finite element weighted residual formulation of equation (3.8) is written as follows: Given a trial function space $\mathscr{T}_n^h$ and weighting function space $\mathscr{W}_n^h$, within each Q_n, $n = 0, 1, \cdots N-1$, find $\boldsymbol{Y^h} \in \mathscr{T}_n^h$ such that $\forall\ \boldsymbol{W^h} \in \mathscr{W}_n^h$ the following relation is satisfied

$$\int_{Q_n} \Big(\boldsymbol{W}^h\cdot\boldsymbol{U}_{,t}(\boldsymbol{Y}^h)+\boldsymbol{W}^h\cdot\boldsymbol{F}^a_{i,i}(\boldsymbol{Y}^h)-\boldsymbol{W}^h\cdot\boldsymbol{F}^d_{i,i}(\boldsymbol{Y}^h)-\boldsymbol{W}^h\cdot\boldsymbol{S}\boldsymbol{Y}^h\Big)dQ_n \tag{3.60}$$

$$+\int_{\Omega(t_n^+)} \Big(\boldsymbol{W}^h(t_n^+)\cdot\boldsymbol{U}\big(\boldsymbol{Y}^h(t_n^+)\big) - \boldsymbol{W}^h(t_n^+)\cdot\boldsymbol{U}\big(\boldsymbol{Y}^h(t_n^-)\big)\Big)d\Omega \tag{3.61}$$

$$+\sum_{e=1}^{(n_{el})_n}\int_{Q_n^e}\boldsymbol{\mathcal{L}}^T\boldsymbol{W}^h\cdot\boldsymbol{\tau}\left(\boldsymbol{\mathcal{L}}\boldsymbol{Y}^h-\boldsymbol{S}\boldsymbol{Y}^h\right)dQ_n+\sum_{e=1}^{(n_{el})_n}\int_{Q_n^e}\nu g^{ij}\boldsymbol{W}^h_{,i}\cdot\boldsymbol{A}_0\boldsymbol{Y}^h_{,j}\,dQ_n \tag{3.62}$$

$$=0 \tag{3.63}$$

In the above formulation, (3.61) is the jump term to weakly enforce the continuity of the solution between consecutive slabs and is the mechanism by which the information is propagated from one slab to another. The discontinuity of finite element functions at the space-time slab interfaces allows the possibility to change the spatial discretization from one space-time slab to the next. This feature is very useful in the moving domain problems where the mesh is deforming. In case, if the mesh distortion exceeds a predetermined specific threshold then a new mesh can be generated and the solution obtained from the mesh at previous space-time slab can be projected to the new mesh. This process is facilitated by the jump term. In the above formulation, the stabilisation operators are added to ensure the well known Ladyženskaja-Bebuška-Brezzi (LBB) condition, which is necessary and sufficient for the well-posedness of the discretization via Galerkin method. In (3.62) the first integral is the least-square stabilization term where $\boldsymbol{\mathcal{L}}$ is the differential operator and $\boldsymbol{\mathcal{L}}\boldsymbol{Y^h}-\boldsymbol{S}$ represents the residual of the equations. $\boldsymbol{\tau}$ is the stabilisation matrix for primitive variables. In this study, the following diagonal tau matrix $\boldsymbol{\tau}^d_{\boldsymbol{Y}}$ is used for multicomponent fluid flows.

$$\boldsymbol{\tau}^d_{\boldsymbol{Y}}=\mathrm{diag}(\tau_{c_1},\cdots,\tau_{c_k},\tau_m,\tau_m,\tau_e)\qquad\text{in 2D} \tag{3.64}$$

with

$$\tau_{c_k}=|\boldsymbol{v}|^2\mathrm{min}\left(\frac{\Delta t}{2},\frac{1}{\lambda^e},\frac{\rho(h^e_d)^2}{12d_{kk}}\right) \tag{3.65}$$

$$\tau_m=\min\left(\frac{\Delta t}{2\rho},\frac{1}{\rho\lambda^e},\frac{(h^e_d)^2}{12\mu}\right) \tag{3.66}$$

$$\tau_e=\min\left(\frac{\Delta t}{2\rho c_v},\frac{1}{\rho c_v\lambda^e},\frac{(h^e_d)^2}{12\kappa}\right) \tag{3.67}$$

The notations are defined in (3.32)-(3.33). The second integral in (3.62) denotes the discontinuity capturing operator. The discontinuity capturing operator is defined in (3.39). The weak form of equations is obtained by performing the integrating by parts in weighted residual formulation. The integration by parts of the flux term of equation (3.60), gives

$$\int_{Q_n} \boldsymbol{W}^h \cdot \boldsymbol{U}_{,t}(\boldsymbol{Y}^h)\, dQ_n = \int_{Q_n} \Big(\boldsymbol{W}^h \cdot \boldsymbol{U}(\boldsymbol{Y}^h)\Big)_{,t}\, dQ_n - \int_{Q_n} \boldsymbol{W}^h_{,t} \cdot \boldsymbol{U}(\boldsymbol{Y}^h)\, dQ_n \tag{3.68}$$

By applying the Gauss divergence theorem for time, one gets

$$\begin{aligned}\int_{Q_n} \boldsymbol{W}^h \cdot \boldsymbol{U}_{,t}(\boldsymbol{Y}^h)\, dQ_n =& \\ & \int_{P_n} \boldsymbol{W}^h \cdot \boldsymbol{U}(\boldsymbol{Y}^h)\hat{n}_t\, dP_n + \int_{\Omega(t^-_{n+1})} \boldsymbol{W}^h(t^-_{n+1}) \cdot \boldsymbol{U}(\boldsymbol{Y}^h(t^-_{n+1}))\, d\Omega \\ & - \int_{\Omega(t^+_n)} \boldsymbol{W}^h(t^+_n) \cdot \boldsymbol{U}(\boldsymbol{Y}^h(t^+_n))\, d\Omega - \int_{Q_n} \boldsymbol{W}^h_{,t} \cdot \boldsymbol{U}(\boldsymbol{Y}^h)\, dQ_n\end{aligned} \tag{3.69}$$

Applying the Gauss divergence theorem on spatial flux terms and substituting (3.69) in the weighted residual equation, results in

$$\begin{aligned}&\int_{Q_n} \Big(- \boldsymbol{W}^h_{,t} \cdot \boldsymbol{U}(\boldsymbol{Y}^h) - \boldsymbol{W}^h_{,i} \cdot \boldsymbol{F}^a_i(\boldsymbol{Y}^h) + \boldsymbol{W}^h_{,i} \cdot \boldsymbol{F}^d_i(\boldsymbol{Y}^h) - \boldsymbol{W}^h \cdot \boldsymbol{S}\boldsymbol{Y}^h \Big) dQ_n \\ &+ \int_{\Omega(t^-_{n+1})} \boldsymbol{W}^{\boldsymbol{h}}(t^-_{n+1}) \cdot \boldsymbol{U}(\boldsymbol{Y}^{\boldsymbol{h}}(t^-_{n+1}))\, d\Omega - \int_{\Omega(t^+_n)} \boldsymbol{W}^{\boldsymbol{h}}(t^+_n) \cdot \boldsymbol{U}(\boldsymbol{Y}^{\boldsymbol{h}}(t^-_n))\, d\Omega \\ &+ \sum_{e=1}^{(n_{el})_n} \int_{Q^e_n} \mathscr{L}^T \boldsymbol{W}^{\boldsymbol{h}} \cdot \boldsymbol{\tau} \left(\mathscr{L}\boldsymbol{Y}^{\boldsymbol{h}} - \boldsymbol{S}\boldsymbol{Y}^{\boldsymbol{h}}\right) dQ_n + \sum_{e=1}^{(n_{el})_n} \int_{Q^e_n} \nu g^{ij} \boldsymbol{W}^h_{,i} \cdot \boldsymbol{A}_0 \boldsymbol{Y}^h_{,j} dQ_n \\ &\quad = - \int_{P_n} \boldsymbol{W}^h \cdot \boldsymbol{U}(\boldsymbol{Y}^h)\hat{n}_t\, dP_n + \int_{P_n} \boldsymbol{W}^h \cdot \Big(\boldsymbol{F}^d_i(\boldsymbol{Y}^h) - \boldsymbol{F}^a_i(\boldsymbol{Y}^h)\Big)\hat{\boldsymbol{n}}_i\, dP_n\end{aligned} \tag{3.70}$$

In the above equation, the Neumann boundary conditions are imposed weakly in the boundary integral terms. The Dirichlet boundary conditions are applied explicitly during the solution process of the system of algebraic equations, resulted from the discretization schemes.

Computation of $\hat{n}_t$

In equation (3.70), in boundary integral terms the first term contains the time unit vector $\hat{n}_t$, which must to be computed on P_n. For any point $P(x, y, t)$ on P_n the spatial coordinates x and y can be interpolated from the spatial coordinates by the relations (3.44)-(3.45). Time t can be interpolated by (3.46). The tangent vectors at point $P(x, y, t)$ can be computed as

$$t_1 = (x, y, t)_{,\xi} = (x_{,\xi}, y_{,\xi}, t_{,\xi}) = (x_{,\xi}, y_{,\xi}, 0) \tag{3.71}$$

$$t_2 = (x, y, t)_{,\eta} = (x_{,\eta}, y_{,\eta}, t_{,\eta}) = (x_{,\eta}, y_{,\eta}, 0) \tag{3.72}$$

$$t_3 = (x, y, t)_{,\theta} = (x_{,\theta}, y_{,\theta}, t_{,\theta}) \tag{3.73}$$

Let $\hat{\boldsymbol{n}}(\hat{n}_x, \hat{n}_y, \hat{n}_t)$ be the space-time unit normal vector at point $P(x, y, t)$. Where, $\hat{n}_x$ and $\hat{n}_y$ are the spatial unit normal vectors and $\hat{n}_t$ is the temporal unit normal vector. By definition $\hat{\boldsymbol{n}}$ must be perpendicular to the tangent vectors (3.71)-(3.73). $\hat{\boldsymbol{n}} \cdot t_1 = 0$ and $\hat{\boldsymbol{n}} \cdot t_2 = 0$ follow directly from the definition of spatial unit normal vectors. $\hat{\boldsymbol{n}} \cdot t_3 = 0$ implies

$$\hat{n}_x x_{,\theta} + \hat{n}_y y_{,\theta} + \hat{n}_t t_{,\theta} = 0 \tag{3.74}$$

This results in

$$\hat{n}_t = \frac{-\hat{n}_x x_{,\theta} - \hat{n}_y y_{,\theta}}{t_{,\theta}} = -2\frac{(\hat{n}_x x_{,\theta} + \hat{n}_y y_{,\theta})}{\Delta t} \tag{3.75}$$

Where $x_{,\theta}$ and $y_{,\theta}$ are evaluated from equations (3.51) and (3.52). The above equation can be rearranged as

$$\hat{n}_t = -\hat{n}_x v_x^m - \hat{n}_y v_y^m \qquad \text{with} \qquad v_x^m = \frac{u_x^m}{\Delta t} \quad \text{and} \quad v_y^m = \frac{u_y^m}{\Delta t} \tag{3.76}$$

Here, v_x^m and v_y^m are the components of mesh velocity. In case of fixed domain problems $\hat{n}_t$ results zero. Consequently the first boundary integral in equation (3.70) becomes zero.

3.3.3 Space-time discretization

This section presents the discretization schemes in the context of space-time finite element method. There are two discretization schemes proposed by Shakib et al. in [64]; constant in time and linear in time. In constant in time the interpolation functions are considered piecewise linear in space and constant in time, while in linear in time interpolation functions are linear in space and time both. Being computationally less expensive and having good stability properties constant in time is usually preferred for steady problems. Linear in time is often used for the transonic problems. In linear in time within the nth space-time slab Q_n, the finite element trial solution $\boldsymbol{Y}^h$ and weighting function $\boldsymbol{W}^h$ are defined as

$$\boldsymbol{Y}^h = \sum_{A=1}^{(n_{np})_{(n)}} N_A^2 \boldsymbol{Y}_A^2 + N_A^1 \boldsymbol{Y}_A^1 \tag{3.77}$$

$$\boldsymbol{W}^h = \sum_{A=1}^{(n_{np})_{(n)}} N_A \left(\boldsymbol{W}_A^2 + (T^1 - T^2) \boldsymbol{W}_A^1 \right) = \sum_{A=1}^{(n_{np})_{(n)}} N_A \boldsymbol{W}_A^2 - \theta N_A \boldsymbol{W}_A^1 \tag{3.78}$$

Where, $\boldsymbol{Y}_A^2$ and $\boldsymbol{Y}_A^1$ are the vectors of unknown at node A at time t_{n+1}^- and t_n^+ respectively. Analogously, $\boldsymbol{W}_A^2$ and $\boldsymbol{W}_A^1$ are the vectors of nodal weighting function at time t_{n+1}^- and t_n^+ respectively. $(n_{np})_{(n)}$ is the number of nodal points in nth space-time slab. The structure of weighting function is different from the trial solution due to the imposition of pre-conditioner. The reason for this is to enhance the stability of predictor multi-corrector method and has been discussed in [63]. The value of weighting function at time t_{n+1}^- and t_n^+ is evaluated as

$$\boldsymbol{W}^h(t_{n+1}^-) = \sum_{A=1}^{(n_{np})_{(n)}} N_A \left(\boldsymbol{W}_A^2 - \boldsymbol{W}_A^1 \right) \tag{3.79}$$

$$\boldsymbol{W}^h(t_n^+) = \sum_{A=1}^{(n_{np})_{(n)}} N_A\left(\boldsymbol{W}_A^2 + \boldsymbol{W}_A^1\right) \tag{3.80}$$

The temporal and spatial derivatives of weighting function are evaluated as

$$\boldsymbol{W}_{,t}^h = \sum_{A=1}^{(n_{np})_{(n)}} N_{A,t}\boldsymbol{W}_A^2 - (\theta N_A)_{,t}\boldsymbol{W}_A^1 = \sum_{A=1}^{(n_{np})_{(n)}} N_{A,t}\boldsymbol{W}_A^2 - \left(\theta N_{A,t} + \theta_{,t} N_A\right)\boldsymbol{W}_A^1 \tag{3.81}$$

$$\boldsymbol{W}_{,i}^h = \sum_{A=1}^{(n_{np})_{(n)}} N_{A,i}\boldsymbol{W}_A^2 - (\theta N_A)_{,i}\boldsymbol{W}_A^1 = \sum_{A=1}^{(n_{np})_{(n)}} N_{A,i}\boldsymbol{W}_A^2 - \theta N_{A,i}\boldsymbol{W}_A^1 \tag{3.82}$$

To simplify the notations the subscript A is dropped. Substituting the equations (3.78)-(3.82) into weighted residual formulation equation (3.70) and assuming there are no essential boundary conditions, one gets two systems of non-linear algebraic equations for variables vectors $\boldsymbol{Y}_A^2$ and $\boldsymbol{Y}_A^1$.

$$\boldsymbol{G}_2\left(\boldsymbol{Y}^2, \boldsymbol{Y}^1, \boldsymbol{Y}_{(n)}^2\right) = 0 \tag{3.83}$$

$$\boldsymbol{G}_1\left(\boldsymbol{Y}^2, \boldsymbol{Y}^1, \boldsymbol{Y}_{(n)}^2\right) = 0 \tag{3.84}$$

To reduce the systems of non-linear algebraic equations into linear, an implicit/explicit third order predictor multi-corrector algorithm was proposed in [64]. In this work, implicit method is used. Let $Y^{2^{(i)}}$ and $Y^{1^{(i)}}$ be the ith iterative approximation of Y^2 and Y^1 respectively. The residual vectors $\boldsymbol{R}_2^{(i)}$, $\boldsymbol{R}_1^{(i)}$ and tangent matrix $\boldsymbol{M}^{(i)}$ are defined as

$$\boldsymbol{R}_2^{(i)} = \boldsymbol{G}_2\left(\boldsymbol{Y}^{2^{(i)}}, \boldsymbol{Y}^{1^{(i)}}, \boldsymbol{Y}_{(n)}^2\right) \tag{3.85}$$

$$\boldsymbol{R}_1^{(i)} = \boldsymbol{G}_1\left(\boldsymbol{Y}^{2^{(i+1)}}, \boldsymbol{Y}^{1^{(i)}}, \boldsymbol{Y}_{(n)}^2\right) \tag{3.86}$$

$$\boldsymbol{M}^{(i)} = \frac{\partial \boldsymbol{G}_2\big(\boldsymbol{Y}^{2^{(i)}}, \boldsymbol{Y}^{1^{(i)}}, \boldsymbol{Y}^2_{(n)}\big)}{\partial \boldsymbol{Y}^{2^{(i)}}} \tag{3.87}$$

The residual vectors and tangent matrix are computed locally element wise and then assembled into global vectors and matrix. This process can be written as follows:

$$\boldsymbol{R}_2^{(i)} = \mathbf{A}_{e=1}^{n_{el}} \boldsymbol{R}_2^e \ , \qquad \boldsymbol{R}_2^e = \{\boldsymbol{R}_{2_a}^e\} \ , \quad a = 1, 2, \cdots, n_{en} \tag{3.88}$$

$$\boldsymbol{R}_1^{(i)} = \mathbf{A}_{e=1}^{n_{el}} \boldsymbol{R}_1^e \ , \qquad \boldsymbol{R}_1^e = \{\boldsymbol{R}_{1_a}^e\} \ , \quad a = 1, 2, \cdots, n_{en} \tag{3.89}$$

$$\boldsymbol{M}^{(i)} = \mathbf{A}_{e=1}^{n_{el}} \boldsymbol{M}^e \ , \qquad \boldsymbol{M}^e = \{\boldsymbol{M}_{ab}^e\} \ , \quad a, b = 1, 2, \cdots, n_{en} \tag{3.90}$$

Here, n_{el} denotes the number of elements and n_{en} denotes the number of element nodes. $\boldsymbol{R}_2^e$ and $\boldsymbol{R}_1^e$ are the residual vectors for element e. Similarly, $\boldsymbol{M}^e$ is the tangent matrix for element e. The finite element assembly operator is denoted by $\mathbf{A}$. In third order predictor multi-corrector algorithm, for each iteration, the following systems of equations are solved.

$$\boldsymbol{M}^{(i)} \Delta \boldsymbol{Y}^{2^{(i)}} = -\boldsymbol{R}_2^{(i)} \tag{3.91}$$

and

$$\boldsymbol{M}^{(i)} \Delta \boldsymbol{Y}^{1^{(i)}} = -\boldsymbol{R}_1^{(i)} \tag{3.92}$$

Here, $\Delta \boldsymbol{Y}^{2^{(i)}}$ and $\Delta \boldsymbol{Y}^{1^{(i)}}$ are the correction factors for $\boldsymbol{Y}^{2^{(i)}}$ and $\boldsymbol{Y}^{1^{(i)}}$ respectively for the ith iteration. The systematic algorithm defined in [64] to solve the above system of equations, is stated in the appendix (A). In the predictor phase, for each time step the solution obtained from the previous time slab is consider as the initial solution for the current slab. In the corrector phase, the solution is updated with the correction factor computed implicitly by setting several iterations per time step. In order to solve the large sparse systems of linearised equations (3.91)-(3.92) for each iteration, a preconditioned block GMRES solver is applied. The solution is approximated by building a Krylov search space of 200 basis functions with 5 restarts. The total number of iterations are set to maximum, which is one less than the number of degrees of freedom. The performance of GMRES iterative solver is measured on how quickly the iterates converge within an acceptable tolerance. The convergence rate of GMRES is strongly dependent on the condition number of the assembled matrix. A suitable pre-conditioner effectively lowers the condition number of the matrix and accelerate the convergence of the solver. Therefore, an ILU preconditioner is employed, which is cheap, and provides a good approximation to the exact system of equations and lead to an efficient solution technique. The GMRES solver and the associated ILU preconditioner are used from the Belos package of Trilinos software. Details on the iterative solver and the pre-conditioner can be found in [56, 134].

3.3.4 Evaluation of vectors and matrices

This section presents the individual terms of the residual vectors $\boldsymbol{R}^e_{2_a}$ and $\boldsymbol{R}^e_{1_a}$, and of the tangent matrix $\boldsymbol{M}^e_{ab}$. The finite element trial function $\boldsymbol{Y}^h$ is localized over an element and is denoted by $\boldsymbol{Y}^e$.

$$\boldsymbol{Y}^e = \sum_{a=1}^{n_{en}} N^2_a \boldsymbol{Y}^2_a + N^1_a \boldsymbol{Y}^1_a \tag{3.93}$$

Where, $\boldsymbol{Y}^2_a$ and $\boldsymbol{Y}^1_a$ are the vectors of unknown at node a of the element e at time t^-_{n+1} and t^+_n respectively. In this study, the quadrangle elements *i.e.* $n_{en} = 4$ are used. At time levels t_{n+1} and t_n the values of θ are 1 and -1 respectively. Substituting the value of θ in temporal shape functions, the value of $\boldsymbol{Y}^e$ at time t_{n+1} and t_n is evaluated as

$$\boldsymbol{Y}^e(t^-_{n+1}) = \sum_a N_a \boldsymbol{Y}^2_a \tag{3.94}$$

$$\boldsymbol{Y}^e(t^+_n) = \sum_a N_a \boldsymbol{Y}^1_a \tag{3.95}$$

The temporal derivative of trial function is calculated as

$$\boldsymbol{Y}^e_{,t} = \sum_a N^2_{a,t} \boldsymbol{Y}^2_a + N^1_{a,t} \boldsymbol{Y}^1_a$$

$$= \sum_a \left(N_{a,t} T^2 + N_a T^2_{,t}\right) \boldsymbol{Y}^2_a + \left(N_{a,t} T^1 + N_a T^1_{,t}\right) \boldsymbol{Y}^1_a \tag{3.96}$$

The time derivative of temporal shape functions is obtained by using the value of $\theta_{,t}$ from the relation (3.55)

$$T^{\alpha}_{,t} = \frac{(-1)^{\alpha}\theta_{,t}}{2} = \frac{(-1)^{\alpha}}{\Delta t} \tag{3.97}$$

By substituting (3.97) in (3.96), one yields

$$\boldsymbol{Y}^{e}_{,t} = \sum_{a} N_{a,t}\left(T^{2}\boldsymbol{Y}^{2}_{a} + T^{1}\boldsymbol{Y}^{1}_{a}\right) + \frac{N_a}{\Delta t}\left(\boldsymbol{Y}^{2}_{a} - \boldsymbol{Y}^{1}_{a}\right) \tag{3.98}$$

The spatial derivatives of trial function are evaluated as

$$\boldsymbol{Y}^{e}_{,i} = \sum_{a} N^{2}_{a,i}\boldsymbol{Y}^{2}_{a} + N^{1}_{a,i}\boldsymbol{Y}^{1}_{a} = \sum_{a} N_{a,i}T^{2}\boldsymbol{Y}^{2}_{a} + N_{a,i}T^{1}\boldsymbol{Y}^{1}_{a} \tag{3.99}$$

Temporal and spatial derivatives of spatial shape functions N_a are computed from the transformation from the reference to the physical coordinates, equation (3.57).

$$N_{a,i} = N_{a,\xi}\xi_{,i} + N_{a,\eta}\eta_{,i} \tag{3.100}$$

$$N_{a,t} = N_{a,\xi}\xi_{,t} + N_{a,\eta}\eta_{,t} + N_{a,\theta}\theta_{,t} \tag{3.101}$$

Where, the values can be directly substituted from (3.55). The integration over the finite element domain is performed element-wise. Substitution of all the above relations in weak form equation (3.70) gives the primary residual vectors $\boldsymbol{R}^{e}_{2_a}$ and secondary residual vector $\boldsymbol{R}^{e}_{1_a}$. The primary residual vectors $\boldsymbol{R}^{e}_{2_a}$ is computed corresponding to the nodal weighting functions $\boldsymbol{W}^{2}_{a}$ and is evaluated as

$$\boldsymbol{R}^{e}_{2_a} = \int_{Q^{e}_{n}} \Big(- N_{a,t}\boldsymbol{U}(\boldsymbol{Y}^{e}) - N_{a,i}\boldsymbol{F}^{a}_{i}(\boldsymbol{Y}^{e}) + N_{a,i}\boldsymbol{F}^{d}_{i}(\boldsymbol{Y}^{e}) - N_{a}\boldsymbol{S}\boldsymbol{Y}^{e}\Big) dQ_n$$

$$+ \int_{\Omega(t^{-}_{n+1})} N_a\boldsymbol{U}\left(\boldsymbol{Y^{e}}(t^{-}_{n+1})\right) d\Omega - \int_{\Omega(t^{+}_{n})} N_a\boldsymbol{U}\left(\boldsymbol{Y^{e}}(t^{+}_{n})\right) d\Omega$$

$$
\begin{aligned}
&+\int_{Q_n^e} \Big(N_{a,_t}\boldsymbol{A}_0^T + N_{a,_i}\boldsymbol{A}_i^T\Big)\cdot\boldsymbol{\tau}\left(\boldsymbol{A}_0\boldsymbol{Y}^e_{,t} + \boldsymbol{A}_i\boldsymbol{Y}^e_{,i} - \boldsymbol{S}\boldsymbol{Y}^{\boldsymbol{e}}\right)dQ_n \\
&+\int_{Q_n^e} \nu^e\left(N_{a,_\xi}\boldsymbol{A}_0\boldsymbol{Y}^e_{,\xi} + N_{a,_\eta}\boldsymbol{A}_0\boldsymbol{Y}^e_{,\eta}\right)dQ_n + \int_{P_n^e} N_a\boldsymbol{U}(\boldsymbol{Y}^a)\hat{n}_t\ dP_n \\
&+\int_{P_n^e} N_a\Big(\boldsymbol{F}_i^a(\boldsymbol{Y}^a) - \boldsymbol{F}_i^d(\boldsymbol{Y}^a)\Big)\hat{\boldsymbol{n}}_i\ dP_n \qquad (3.102)
\end{aligned}
$$

The secondary residual vectors $\boldsymbol{R}^e_{1_a}$ is computed corresponding to nodal weighting functions $\boldsymbol{W}^1_a$ and is evaluated as follows:

$$
\begin{aligned}
\boldsymbol{R}^e_{1_a} = &\int_{Q_n^e}\Big(\big((\theta N_a)_{,t}\boldsymbol{U}(\boldsymbol{Y}^e) + \theta N_{a,_i}\boldsymbol{F}_i^a(\boldsymbol{Y}^e)\big) - \theta N_{a,_i}\boldsymbol{F}_i^d(\boldsymbol{Y}^e) + \theta N_a\boldsymbol{S}\boldsymbol{Y}^e\Big)dQ_n \\
&-\int_{\Omega(t^-_{n+1})} N_a\boldsymbol{U}\left(\boldsymbol{Y}^{\boldsymbol{e}}(t^-_{n+1})\right)d\Omega - \int_{\Omega(t^+_n)} N_a\boldsymbol{U}\left(\boldsymbol{Y}^{\boldsymbol{e}}(t^+_n)\right)d\Omega \\
&-\int_{Q_n^e}\Big((\theta N_a)_{,t}\boldsymbol{A}_0^T + \theta N_{a,_i}\boldsymbol{A}_i^T\Big)\cdot\boldsymbol{\tau}\left(\boldsymbol{A}_0\boldsymbol{Y}^e_{,t} + \boldsymbol{A}_i\boldsymbol{Y}^e_{,i} - \boldsymbol{S}\boldsymbol{Y}^{\boldsymbol{e}}\right)dQ_n \\
&-\int_{Q_n^e}\nu^e\theta\left(N_{a,_\xi}\boldsymbol{A}_0\boldsymbol{Y}^e_{,\xi} + N_{a,_\eta}\boldsymbol{A}_0\boldsymbol{Y}^e_{,\eta}\right)dQ_n - \int_{P_n^e}\theta N_a\boldsymbol{U}(\boldsymbol{Y}^a)\hat{n}_t\ dP_n \\
&+\int_{P_n^e}\theta N_a\Big(\boldsymbol{F}_i^d(\boldsymbol{Y}^a) - \boldsymbol{F}_i^a(\boldsymbol{Y}^a)\Big)\hat{\boldsymbol{n}}_i\ dP_n
\end{aligned}
$$

The tangent matrix is computed at time t_{n+1} and is written as

$$
\begin{aligned}
\boldsymbol{M}^e_{ab} = &\int_{Q_n^e}\Big(-N_{a,t}\boldsymbol{A}_0N_b - N_{a,_i}\boldsymbol{A}_iN_b + N_{a,_i}\boldsymbol{K}_{ij}N_{b,_j} - N_a\boldsymbol{S}N_b\Big)dQ_n \\
&+\int_{Q_n^e}\Big(N_{a,_t}\boldsymbol{A}_0^T + N_{a,_i}\boldsymbol{A}_i^T\Big)\cdot\boldsymbol{\tau}\left(N_{b,_t}\boldsymbol{A}_0 + N_{b,_i}\boldsymbol{A}_i - N_b\boldsymbol{S}\right)dQ_n
\end{aligned}
$$

$$+\int_{\Omega(t_{n+1}^-)} N_a \boldsymbol{A}_0 N_b \; d\Omega + \int_{Q_n^e} \nu^e \left(N_{a,\xi} \boldsymbol{A}_0 N_{b,\xi} + N_{a,\eta} \boldsymbol{A}_0 N_{b,\eta} \right) dQ_n$$

$$+\int_{P_n^e} N_a \boldsymbol{A}_0 N_b \; \hat{n}_t \; dP_n + \int_{P_n^e} N_a \left(\boldsymbol{A}_i N_b - \boldsymbol{K}_{ij} N_{b,j} \right) \hat{\boldsymbol{n}}_i \; dP_n \qquad (3.103)$$

In finite elements, it is usual to perform the integration numerically. This is done in two steps. In the first step, the variables are transformed from a space-time element in physical domain to a master element in reference domain and in the second step the integral over the master element $\hat{Q}_n^e$ with boundary $\hat{P}_n^e$ is computed by applying the Gaussian quadrature rule. For all element integrals over Q_n^e the following apply

$$\begin{aligned}
\int_{Q_n^e} f(x,y,t) \; dQ_n &= \int_{\tilde{Q}_n^e} f\big(x(\xi,\eta,\theta), y(\xi,\eta,\theta), t(\theta)\big) \; |\boldsymbol{J}^{\boldsymbol{ST}}(\xi,\eta,\theta)| \; d\hat{Q}_n \\
&= \int_{-1}^{1} \int_{\hat{\Omega}_n^e} g\left(\xi,\eta,\theta\right) \; |\boldsymbol{J}^{\boldsymbol{ST}}(\xi,\eta,\theta)| \; d\hat{\Omega}_n d\theta \\
&= \int_{-1}^{1} \int_{-1}^{1} \int_{-1}^{1} g\left(\xi,\eta,\theta\right) \; |\boldsymbol{J}^{\boldsymbol{S}}(\xi,\eta,\theta)| \frac{\Delta t}{2} \; d\xi d\eta d\theta \\
&\approx \sum_{i=1}^{2} \sum_{j=1}^{2} \sum_{k=1}^{2} g\left(\xi_i,\eta_j,\theta_k\right) \; |\boldsymbol{J}^{\boldsymbol{ST}}(\xi_i,\eta_j,\theta_k)| \; w_i w_j w_k \qquad (3.104)
\end{aligned}$$

Where, ξ_i, $,\eta_j$ and θ_k are the quadrature points. w_i, w_j and w_k are the quadrature weights. Here, two point quadrature rule is used which is exact up to the cubic polynomials. The boundary integrals are computed by computing the surface normal vector. The surface area is computed as a vector oriented in the direction normal to the surface P_n^e. At boundary surface one of the coordinate (say η) is constant. Then, the surface normal vector is computed as

$$\int_{P_n^e} f(x,y,t) \hat{\boldsymbol{n}}_i \; dP_n = \int_{\tilde{P}_n^e} f\big(x(\xi,\theta), y(\xi,\theta), t(\theta)\big) d\boldsymbol{P}_n \qquad (3.105)$$

Where $\boldsymbol{dP_n}$ is given by the following cross product

$$d\boldsymbol{P_n} = \begin{pmatrix} x_{,\xi} \\ y_{,\xi} \\ 0 \end{pmatrix} \times \begin{pmatrix} 0 \\ 0 \\ 1 \end{pmatrix} \frac{\Delta t}{2} d\xi d\theta \tag{3.106}$$

For the jump term, the integrals are evaluated as

$$\int_{\Omega(t_{n+1}^-)} f(x,y,t)\ d\Omega = \int_{\tilde{\Omega}_{n+1}} f\big(x(\xi,\eta,1), y(\xi,\eta,1), t(1)\big)\ |\boldsymbol{J^S}(\xi,\eta,1)|\ d\tilde{\Omega} \tag{3.107}$$

$$\int_{\Omega(t_n^+)} f(x,y,t)\ d\Omega = \int_{\tilde{\Omega}_n} f\big(x(\xi,\eta,-1), y(\xi,\eta,-1), t(-1)\big)\ |\boldsymbol{J^S}(\xi,\eta,-1)|\ d\tilde{\Omega} \tag{3.108}$$

In equations (3.107) and (3.108), the integrals are over the spatial domain at specific times and the function is dependent on only ξ an η. To evaluate these integrals the Gaussian quadrature is applied with ξ_i and η_j.

In linear in time the solution depends on the both time labels t_n and t_{n+1}. Correspondingly, in the third order predictor multi-corrector algorithm, one has to solve two discretized linear systems of equations for the solution increments at both time labels. In [64] authors also proposed one another discretisation scheme called as constant in time, in which the solution does not vary along the time axis in space-time slab. This discretization scheme is computationally less expensive in comparison to the linear in time approach as it generates only one linear set of equations. In constant in time, within an element the trial functions and weighting functions are taken as

$$\boldsymbol{Y}^e = \sum_{a=1}^{n_{en}} N_a \boldsymbol{Y}_a^2 \tag{3.109}$$

$$\boldsymbol{W}^e = \sum_{a=1}^{n_{en}} N_a \boldsymbol{W}_a^2 \tag{3.110}$$

By substituting the above functions in weak form equation, and following the similar procedure as defined in subsection 3.3.3, one gets only one set of linearised equations (3.91). Where, $\boldsymbol{R}^e_{2_a}$ and $\boldsymbol{M}^e_{ab}$ are defined in (3.102) and (3.103) respectively. In order to solve the non-linear discretized system of equations, the proposed first order predictor multi-corrector algorithm is summarized in appendix (A).

Like ordinary finite element method, it is easy to implement the boundary conditions in ST-FEM. The Neumann boundary conditions are applied directly to the boundary integral terms of the weak formulation. Whereas, the Dirichlet boundary conditions are applied strongly in the linear algebraic system. The linear system was built by substituting the constrained degrees of freedom (dof) in element vectors and matrices. In order to apply the Dirichlet boundary conditions, in globally assembled matrix, the rows corresponding to the constrained dofs are filled with zeros and value 1 on the main diagonal. In parallel computing systems, the non-zero value is repeated as many times as the dof is shared among the processors. Similarly, the corresponding value on the right-hand side, in assembled residual vector, is set to zero. This way, the constrained dof gets the zero correction value upon the solution of the system and does not affect the solution of other dofs.

3.4 Numerical Examples

This section presents a series of benchmark cases and discusses the numerical results obtained with the proposed formulation to verify and validate the numerical code. The test cases covered in this section are for stationary (non-moving) bodies. All the test cases are computed with the constant in time discretization scheme and the first-order predictor multi-corrector algorithm. In order to solve the fixed domain flow problems presented in this section, the mesh velocity $\boldsymbol{v}^m$ is set to zero. In this case $\Omega(t^-_{n+1})$ is simply equal to $\Omega(t^+_n)$ for each space-time element. The benchmarks for moving domain problems are discussed in the next chapter.

The presented benchmark cases can be divided into four different categories. In the first category of problems, the accuracy and ability of the numerical method are validated for compressible viscous fluid flows. For the purpose, the code is tested on several standard benchmarks including the normal shock, oblique shock, shock reflection, flat plate and the compression corner. Here the case of flow over a flat plate is presented. This test case is a classical benchmark case for the shock generation along with a boundary layer. In the second category, the numerical simulation benchmark cases are computed for the natural convection. The buoyancy driven flow and Rayleigh-Benard convection are tested at different Rayleigh numbers. Here, the buoyancy-driven flow problem is presented. The third category of problems deals with the incompressible fluid flows including driven cavity flow, the flow around the fixed cylinder and the backward facing step problem. Here, the unsteady lid driver cavity flow and the transient flow over backward facing step are presented at various Reynolds number. Finally, the fourth category deals with the multicomponent fluid flow. The simulations are performed for the mixing of two different fluids, broken dam and driven cavity with stripes. Here, broken dam and driven cavity with stripes of different fluids are presented. The results obtained with the proposed technique are compared with the pre-existing ones available in the literature.

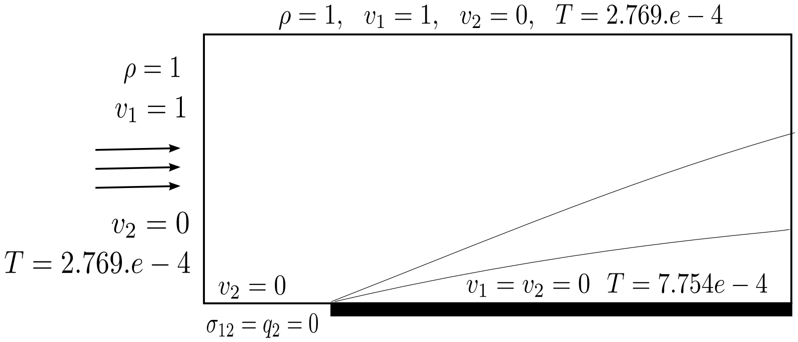

Figure 3.3: Flat plate: domain and boundary conditions.

3.4.1 Flat plate

The problem consists of a Mach 3 ($M = \boldsymbol{v}/c = 3$) viscous flow sliding over a thin plate. The flow direction is parallel to the axis of the plate. Since the flow is viscous and there is a viscous boundary layer, the flow generates a subsonic boundary layer, a transonic region and a curved induced shock starting from the leading edge of the plate, which is a singular point. The shock layer is the region between the plate surface and the boundary layer. For this simulation, the Reynolds number, $Re = \boldsymbol{v}L/\nu$ is fixed to 1000 and the Sutherland viscosity law $\mu = 0.0906T^{1.5}/(T + 0.0001406)$ is employed. This corresponds to the free stream temperature of 216.7 K. The computational domain extends $-0.2 \leq x \leq 1.2$ and $0 \leq y \leq 0.8$, with the leading edge of the plate at $x = 0$. The problem statement and boundary conditions are illustrated in figure (3.3). Ideal gas law is used as the equation of state. The conservative variables ρ of the reference case is transformed through the equation of state into the primitive variables p in order to prescribe initial and boundary conditions. At inflow and top boundaries pressure, velocity and temperature are assigned. On the symmetry line vertical velocity, tangential viscous stress and heat flux are set to zero. The wall is no-slip and at stagnation temperature. On the outlet, no boundary condition is assigned. To solve this problem, an unstructured mesh is composed of 6993 elements and 7168 nodes. For the time marching procedure the size of the time step $\Delta t = 0.001$ is chosen.

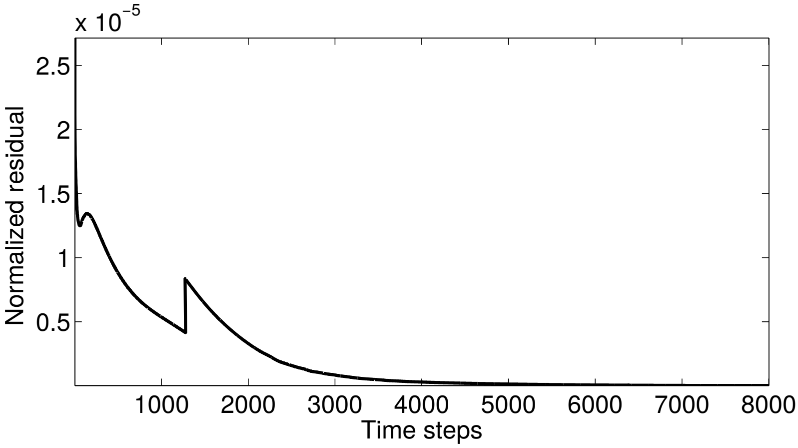

Figure 3.4: Flat plate: time history of GMRES iterations with ILU preconditioner.

At each predictor step, the linear system of algebraic equations is solved using GMRES iterative solver. Convergence of the solver is defined if the residual norm becomes less than 1.e-8. Residual norm is computed as the difference of norm between the two consecutive iterations. The convergence behaviour of the computation is shown in Figure (3.4). After around 1300 time steps there is a little increase in the normalised residual, which is due to the change in time step. The time step was changed from $\Delta t = 0.001$ to $\Delta t = 0.002$ to obtain the result quickly. Steady state is achieved after around 5000 time steps, which is corresponding to $t = 5s$ when the residual norm decreases below 1.e-8. Figure (3.5) shows the temporal development of shock in density. Starting from time 0.001 the shock starts to develop and by $5s$ the shock is completely developed. From the figure the boundary layer is apparent. The accuracy of obtained results is tested by computing the pressure coefficient $C_p = p - p_\infty / \frac{1}{2}\rho_\infty u_\infty^2$ and the wall friction coefficient $C_f = \tau_w / \frac{1}{2}\rho_\infty u_\infty^2$. The coefficients are compared with [74] and are shown in Figure (3.6). The contours of pressure and Mach number are shown in Figure (3.7). The similarity of current computed results with [74] validates the accuracy of the numerical technique for compressible viscous fluid flows.

3.4.2 Buoyancy Driven flow

This test case presents the fluid flow in a differentially heated closed square cavity. The left and right wall of the cavity are isothermal and kept at temperatures T_2 and T_1 respectively with $T_2 > T_1$. The horizontal walls are considered adiabatic, meaning that there is no heat transfer through these walls. The fluid inside the cavity is assumed to be incompressible, Newtonian and Boussinesq-approximated. In the Boussinesq approximation, the density differences are neglected from the Navier-Stokes equations, except in the body force terms where they appear in terms multiplied with the acceleration due to gravity. The density variations are assumed to have a fixed part and another part that has a linear dependence on temperature

$$\rho = \rho_0 - \beta \rho_0 (T - T_1) \tag{3.111}$$

Where ρ_0 and T_1 are the reference density and temperature respectively. β is the coefficient of expansion, defined in previous chapter. The body force is defined as

$$\boldsymbol{b} = \Delta \rho \boldsymbol{g} = -\beta \rho_0 \boldsymbol{g} (T - T_1) \tag{3.112}$$

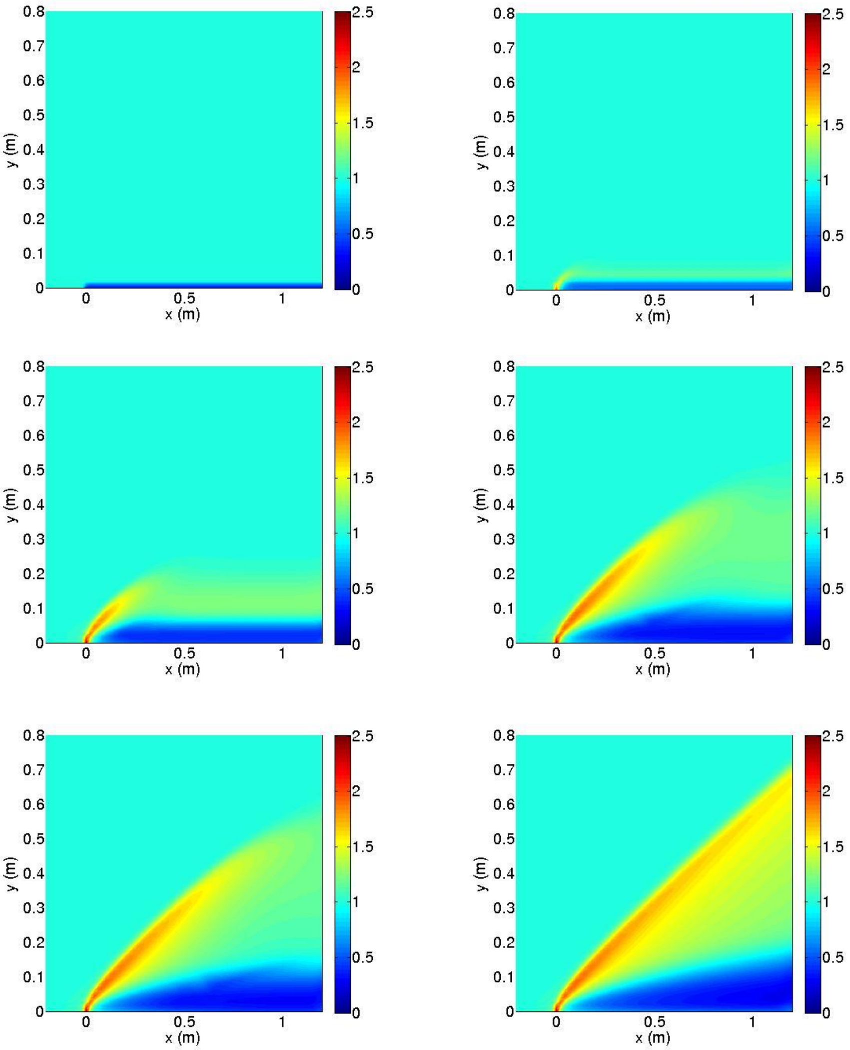

Figure 3.5: Flat Plate: temporal evolution of shock in ρ (kg/m^3). Row wise from left, at time t = 0, 0.1, 0.4, 1, 1.3, 5 *s*.

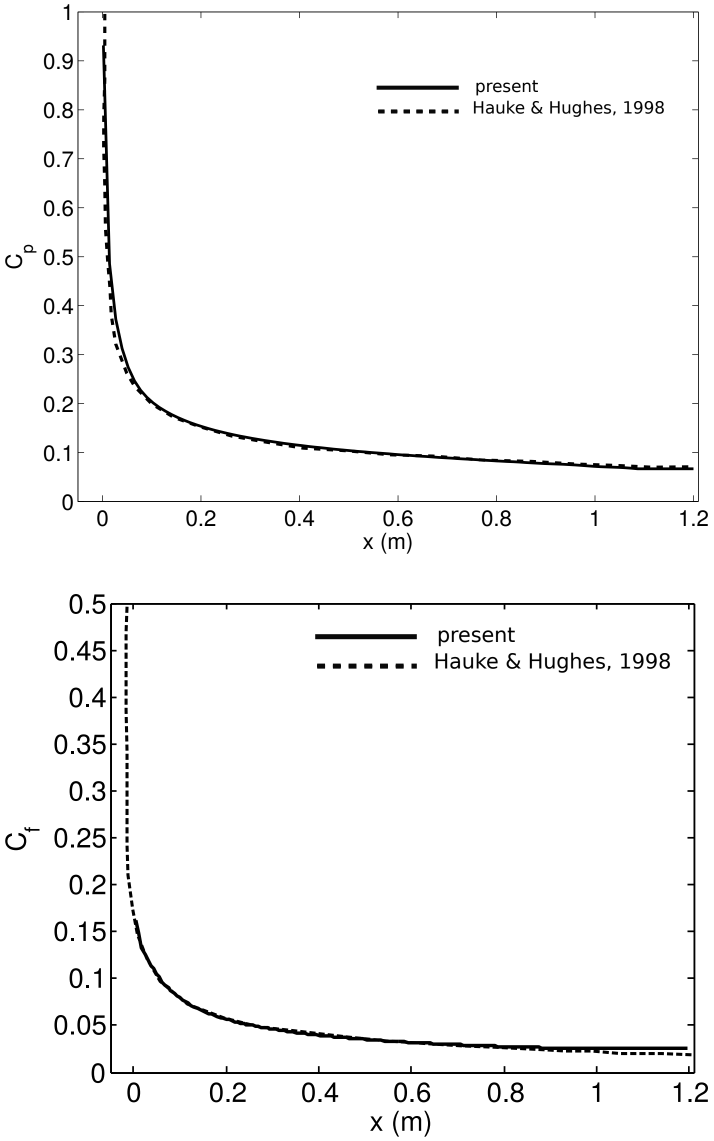

Figure 3.6: Flat plate: pressure coefficient C_p and friction coefficient C_f. Solid line: present work, dashed line: Hauke et al. [74].

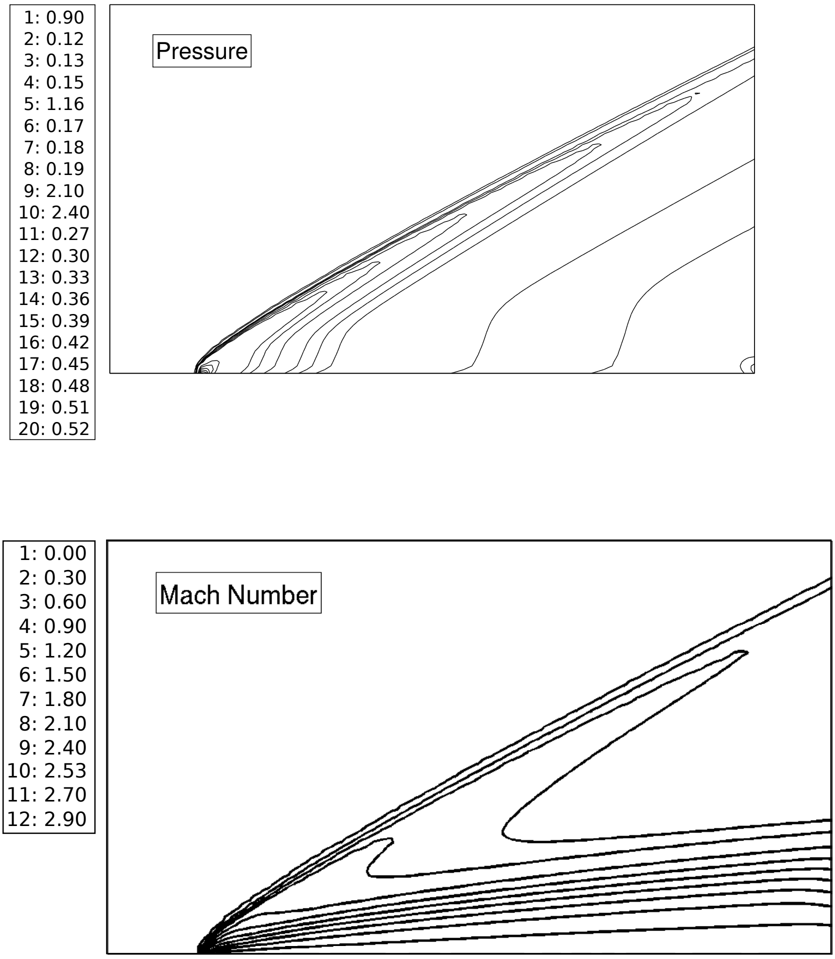

Figure 3.7: Flat plate: pressure (Pa) and Mach contours.

The density variation is directly proportional to the thermal gradient. Consequently, the body forces are largely affected by the increase or decrease in temperature. In this test case, the behaviour of the systems depends on upon the magnitude of the buoyancy force, which is the only cause of motion. To implement the Boussinesq-approximation in only the source matrix $\boldsymbol{S}$ need to be changed. The source matrix with appropriate changes is defined in the appendix (A). The geometry and boundary conditions for the problem are depicted in figure (3.8). T_2 and T_1 are set to 2 and 1 K respectively. On all the walls, no slip boundary condition is imposed and pressure is fixed to zero at left bottom corner. As initial conditions, the fluid is set at temperature T_1 with velocity 0.

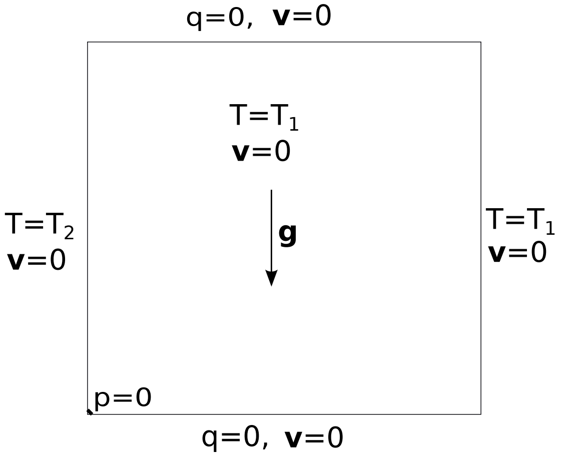

Figure 3.8: Buoyancy driven flow: domain and boundary conditions.

This problem is characterized by three non-dimensional numbers: Prandtl (Pr), Rayleigh (Ra) and Nusselt (Nu) defined as

$$Pr = \frac{\mu c_p}{\kappa} \qquad Ra = \frac{|\boldsymbol{g}|\beta \Delta T L^3}{\alpha \nu} \qquad Nu = \frac{hL}{\kappa} \tag{3.113}$$

Where μ is the dynamic viscosity, c_p is the specific heat at constant pressure, κ is the thermal conductivity, g is the acceleration due to gravity, β is the coefficient of expansion, $\Delta T = T_2 - T_1$, L is the characteristic length, α is the thermal diffusivity, ν is the kinematic viscosity and h is the coefficient of heat transfer. The Prandtl number represents the ratio of the momentum diffusivity and thermal diffusivity. Rayleigh number is viewed as the ratio of buoyancy and viscosity forces multiplied by the ratio of momentum and thermal diffusivity. The Rayleigh number quantifies the coupling between the momentum and energy equations. Nu is viewed as the ratio of convective to conductive heat transfer across the boundary. For constant Pr, the convection-free source term becomes dominant as the Rayleigh number Ra is increased, leading to a set of coupled stiff partial differential equations. In the present study, the Pr is fixed to 1. The problem is solved over four different values of $Ra = 1.e3, 1.e4, 1.e5, 1.e6$. For simulation, an unstructured mesh made of quadrangles is generated consisting 5566 elements. Δt is set to 0.01.

At left hot wall the fluid receives the heat from the wall and due to the increase in buoyancy forces the fluid tend to rise upwards. At right cold wall fluid loses some of its heat and move downwards. Figures (3.9)-(3.11) show the contours for v_1, v_2 and the absolute value of velocity, $|\boldsymbol{v}|$ for different values of Ra number. In the v_1-velocity contours there are two horizontal eddies, one below the other, for $Ra = 1.e3$. For higher values of Rayleigh number, these two eddies move closer to the two adiabatic walls. Similarly, two dominant circulations are prominently visible in the vertical iso-velocity contours (on the left and right zones of the cavity) for $Ra = 1.e3$. These two eddies subsequently move closer to the hot wall and the cold wall with an increase in the Rayleigh number. This illustrates that the boundary layer gets thinner as a function of Rayleigh number. From the contours of velocity norm, it is depicted that at $Ra = 1.e3$ the flow is completely symmetric. With the increase in Rayleigh number, the symmetry of the flow is disturbed. Figures (3.12)-(3.13) displays the streamlines and isothermal contours. In the figures of streamlines, it is illustrated that only a single circulating eddy persists for Ra=1.e3 and $Ra = 1.e4$. For $Ra = 1.e5$, the innermost zone of the main recirculation splits into two smaller counter-rotating eddies in the core region. These two small inner eddies are stretched toward the top left and bottom right corners, retaining the dominance of the main circulation. For $Ra = 1.e3$, the isotherm contours are almost vertical with a little bend. With the increase in Ra the isotherms gradually achieve a horizontal pattern. Nevertheless, the contours are normal to the horizontal adiabatic walls, which demonstrate that there is no movement of heat flux through this boundary.

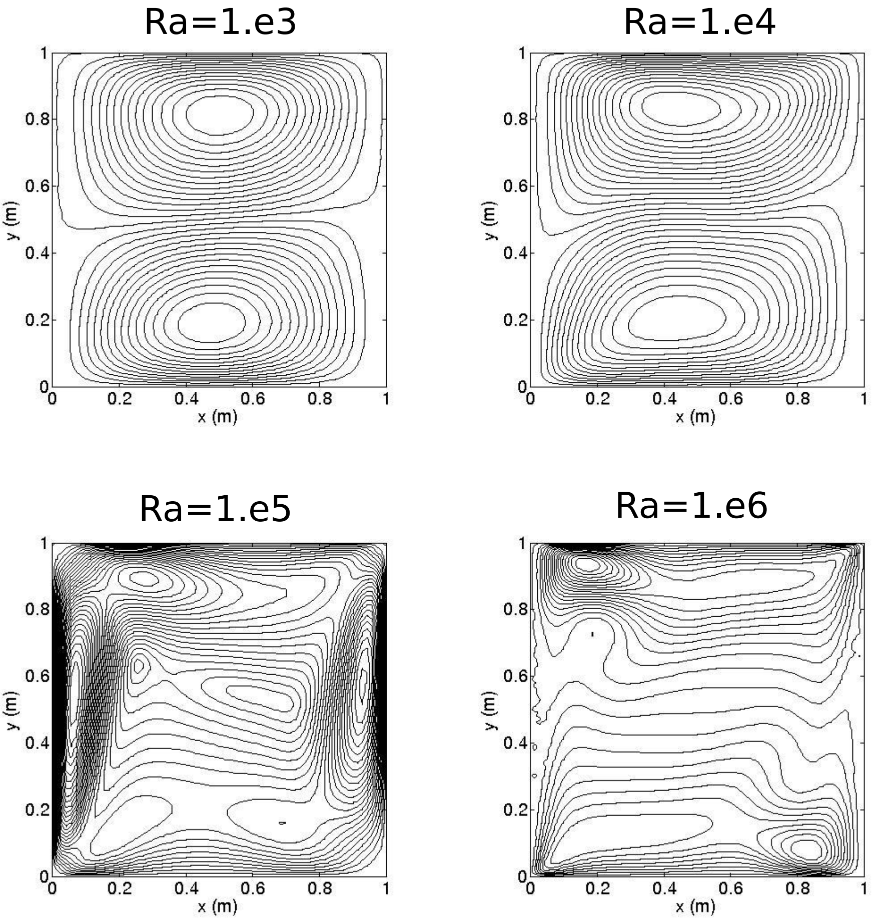
Ra=1.e3

Ra=1.e4

Ra=1.e5

Ra=1.e6

Figure 3.9: Buoyancy driven flow: steady state iso-velocity contours of v_1 (m/s) for different Rayleigh numbers.

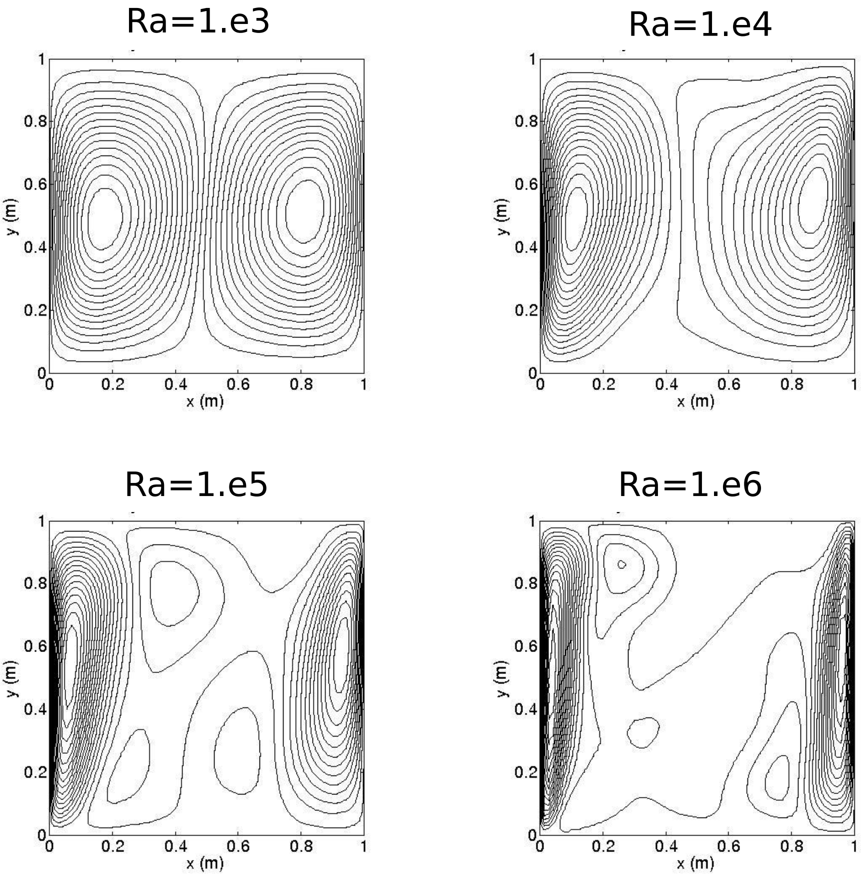

Figure 3.10: Buoyancy driven flow: steady state iso-velocity contours of v_2 (m/s) for different Rayleigh numbers.

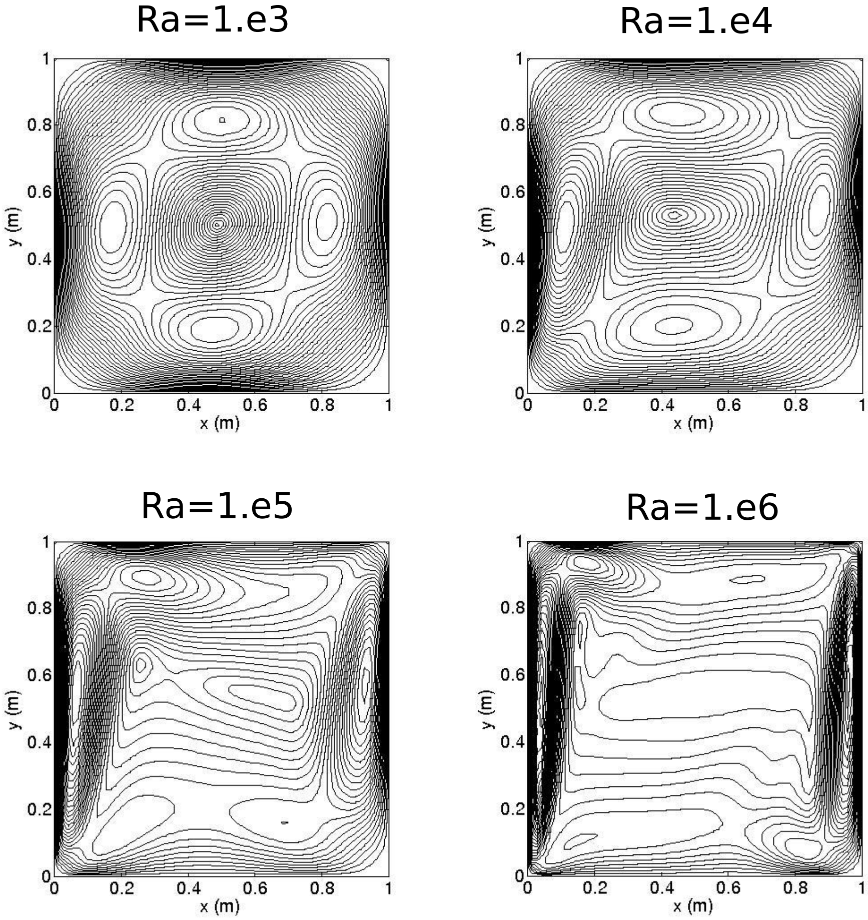

Figure 3.11: Buoyancy driven flow: steady state iso-velocity contours of $|\boldsymbol{v}|$ (m/s) for different Rayleigh numbers.

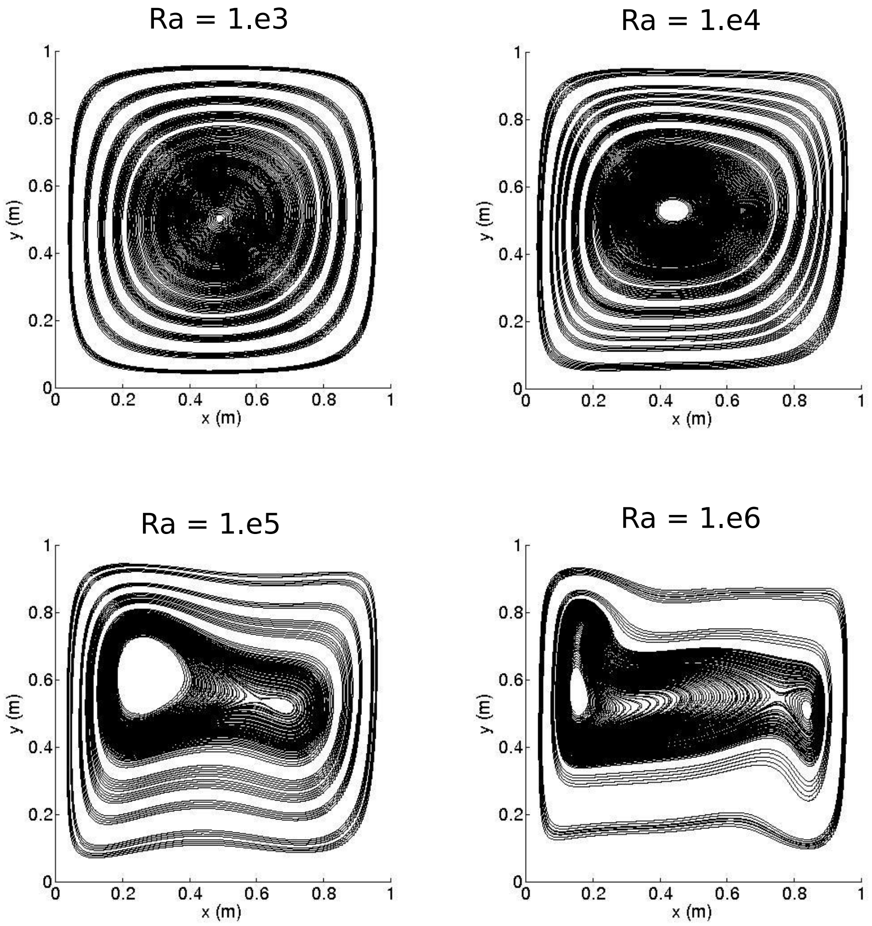

Figure 3.12: Buoyancy driven flow: steady state streamlines (m^2/s) patterns for different Rayleigh numbers.

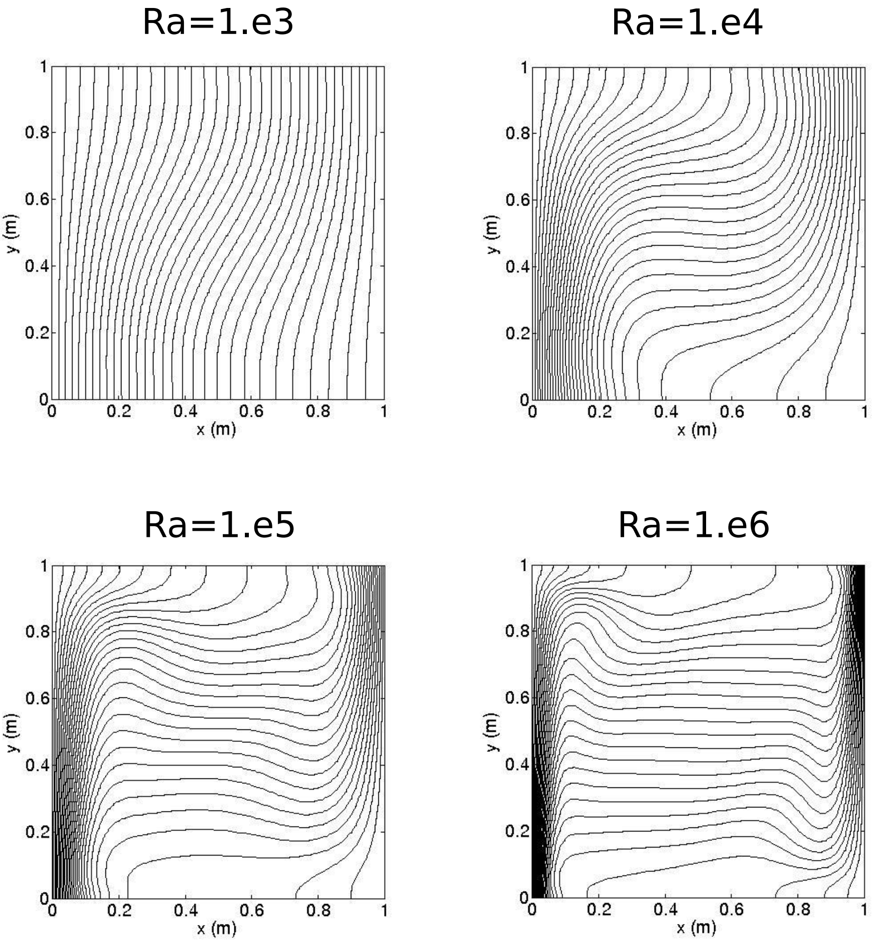

Figure 3.13: Buoyancy driven flow: steady state isotherm contours (K) for different Rayleigh numbers.

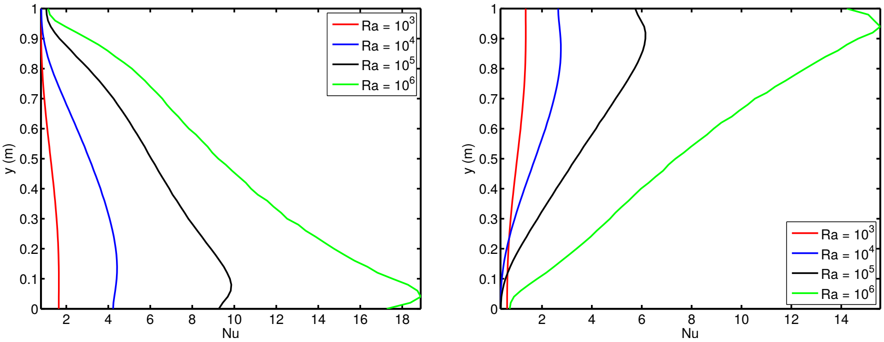

Figure 3.14: Buoyancy driven flow: computed local Nusselt number for different Rayleigh numbers. Left: hot wall; Right: cold wall

In the immediate neighbourhood of the hot and cold walls, the contours remain parallel to the isothermal vertical walls. For high Ra number, a very dense set of isothermal contour lines is seen near the vertical walls. In natural convection case, it is valuable to compute the heat transfer coefficient along the hot and cold walls. In order to compute that the local Nusselt number Nu_l is defined as

$$Nu_l = -T_{,x} \tag{3.114}$$

The relation represents the local Nusselt number, which is defined at each boundary element on the considered wall. The Nusselt number is non-zero only on the isothermal walls. The interpretation of the local Nusselt number is different for the hot and the cold wall. At the hot wall, the Nusselt number represents the heat transfer from the wall to the fluid, and at the cold wall from the fluid to the wall. Figure (3.14) shows the computed local Nusselt number at the hot and the cold wall for various Rayleigh numbers. For the higher Ra-range, where the effect of convection is more significant, the Nusselt number is increasing with the Rayleigh number, as expected. There is greater heat transfer from the lower part of the hot wall to the fluid and from the fluid to the upper part of the cold wall. There is an anti-symmetric distribution of the local Nusselt number between the hot and cold wall. This

Ra	Present	[51]	[50]
1.e3	1.1357	1.115	1.117
1.e4	2.2962	2.259	2.254
1.e5	4.6981	4.483	4.598
1.e6	8.9360	8.881	8.976

Table 3.1: Buoyancy driven flow: the average local Nusselt number for different values of Ra.

is as expected due to the antisymmetric distribution of the steady fluid flow and the isotherms. The average Nusselt number is computed by the following expression

$$\overline{Nu} = \int_0^1 Nu_l \; dy = \frac{1}{L} \sum_i Nu_i \; dy_i \tag{3.115}$$

Table (3.1) shows the average Nusselt numbers for different Rayleigh numbers along with the results from [50, 51] for comparison. A good correspondence is obtained in the average Nusselt number values computed with the present computation and with other available results. This validates the numerical results.

3.4.3 Lid driven cavity

This test case computes the physics of an incompressible flow driven by the lid movement in a cavity. The problem geometry is simple and applying numerical method with boundary conditions is easy and straight forward. The computational domain is a unit square with upper part of the boundary sliding towards right direction at a constant velocity of $1m/s$. The domain geometry and boundary conditions are displayed in figure (3.15). At left, bottom and right walls velocities are fixed to zero. At upper wall v_1 and v_2 are fixed to 1 and 0 respectively. Since only Dirichlet boundary conditions are imposed on all parts of the domain, pressure is determined only up to an arbitrary constant. in order to define the pressure uniquely, the pressure is fixed at one point in the middle of the bottom part of the cavity. The upper sliding part generates shear forces which cause the recirculation inside the cavity. The main characteristic of the flow is the creation of a primary vortex at the centre of the cavity. Depending on the Re, other secondary vortices can appear at the right bottom, left bottom and left upper corners of the cavity. Upper corners, where the velocity field is discontinuous, are the singular points. Here the flow problem is investigated for $Re = 1, 100, 400, 1000, 2000, 3200$, $5000, 7500$ and 10000. In [57] Erturk et al. solved the stream functions and vorticity equations separately to obtain the steady state solution for driven cavity flow at high Re. In that paper, the authors used a 601 × 601 fine grid mesh to resolve the flow field. The mesh used in the present computations is much coarser than the one used in [57].

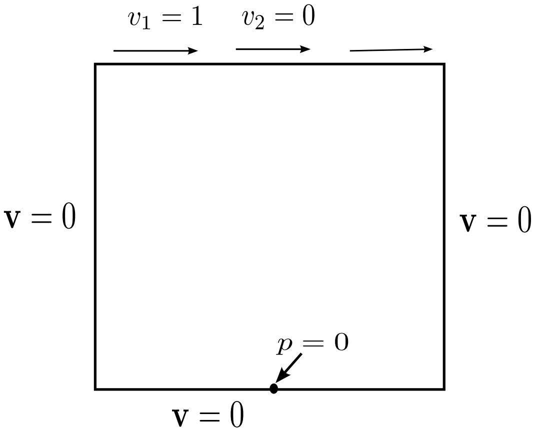

Figure 3.15: Driven cavity: domain and boundary conditions.

To study the flow, a non-uniform grid is used. The mesh is more concentrated at the corners of the cavity. Mesh composed of 9316 elements and 9563 nodes is displayed in figure (3.16). The mesh is sharply refined at the upper corners due to the singular points and at the bottom corners to capture the vortices. To compute the solution up to the final value of $Re = 10000$, the steady solution obtained from the previous Re is used as the initial conditions for the next one.

The steady solution for $Re = 1$ is obtained by using the predictor-corrector algorithm, and passed to $Re = 100$ as initial conditions. The same process

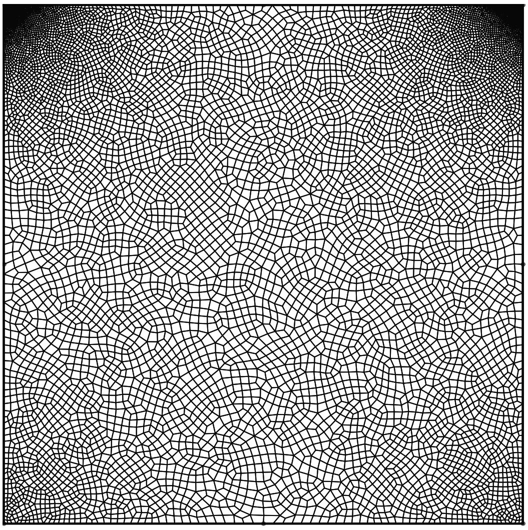

Figure 3.16: Driven cavity: the computational mesh

is followed for the subsequent Reynolds numbers. A constant time step $\Delta t = 0.01s$ is set for all the test cases. Figures (3.17) and (3.18) show the pressure and norm of velocity contours for various Reynolds numbers. Figure (3.19) displays the streamlines plot for the various values of Re in whole domain including corners. In all cases, within a few seconds, a primary vortex forms next to the lid and start to grow. The shape and size of the vortex depend on the value of Re.

As the Re increases, the primary vortex gradually moves towards the right upper corner and continue to broaden until it achieves the steady state. This tendency of movement of the primary vortex stems other recirculation regions near the bottom corners. Starting from $Re \geq 400$ a secondary vortex appears in the lower right corner of the cavity, moving anticlockwise. For $Re \geq 1000$, one another eddy is seen in the left bottom corner of the cavity. From $Re \geq 3200$, a small eddy appears in the upper left corner. The size of vortices continues to grow with an increase in Re. From $Re = 7500$ the flow momentum is sufficient to generate additional vortices. A small

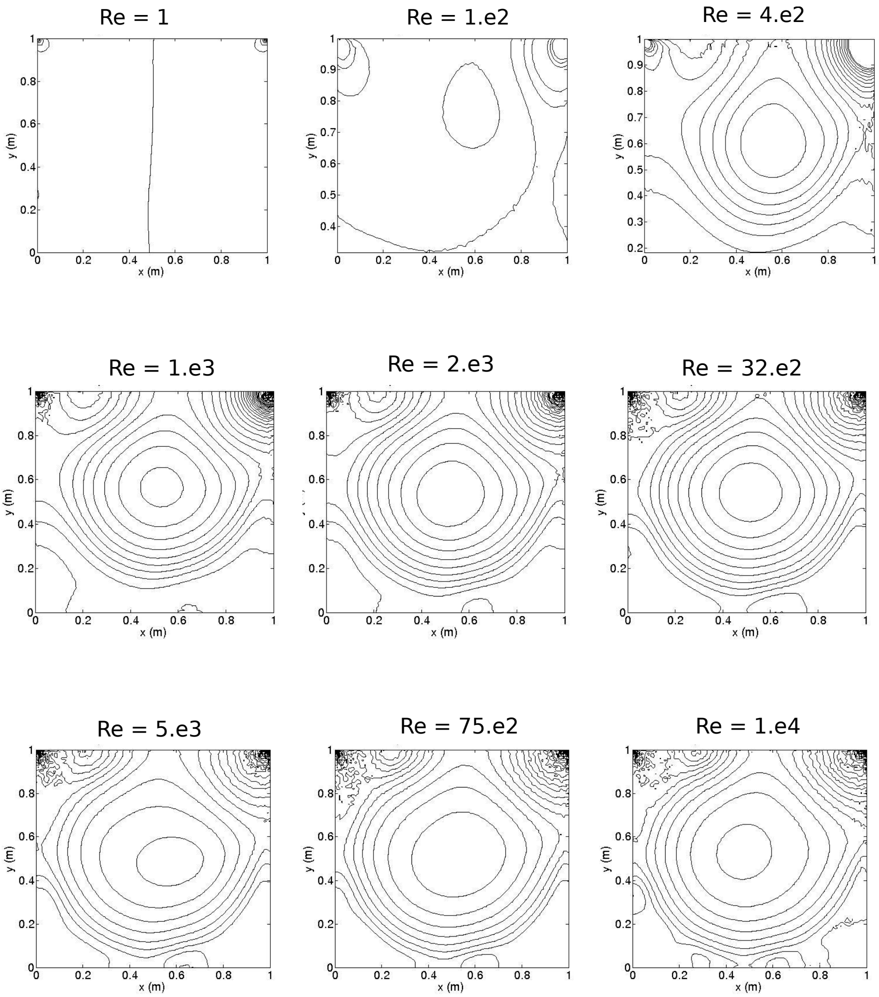

Figure 3.17: Driven cavity: pressure (Pa) contours at various Reynolds number

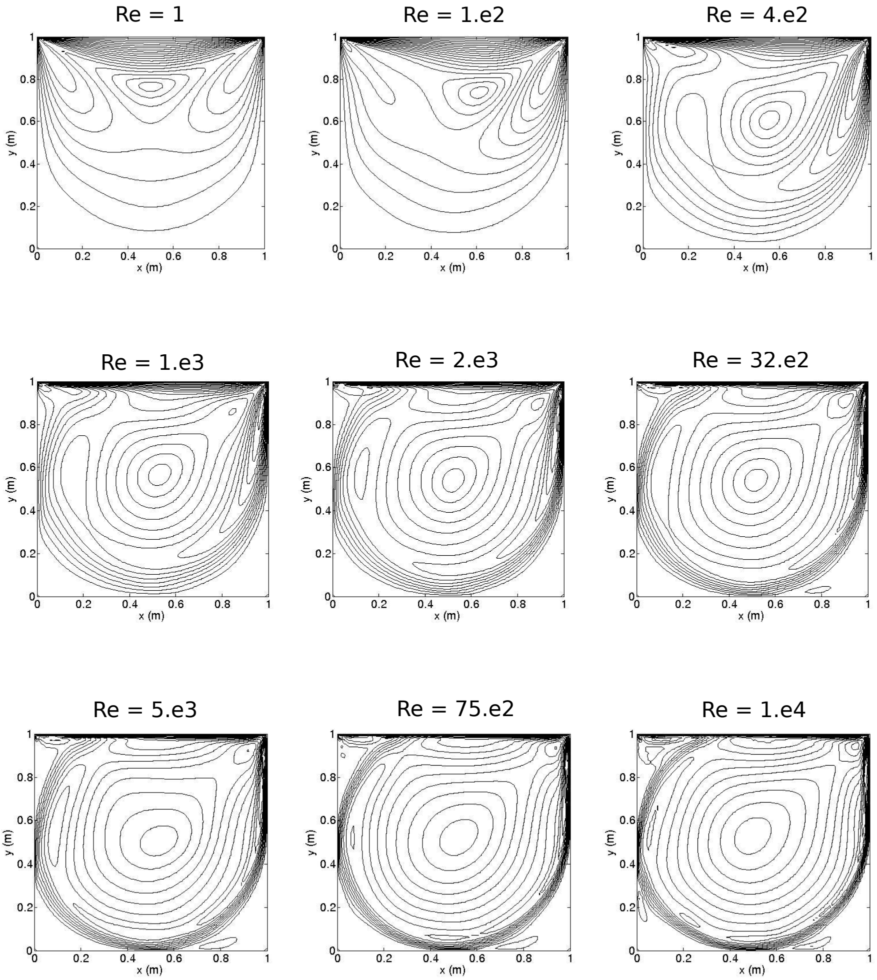

Figure 3.18: Driven cavity: absolute velocity (m/s) contours at various Reynolds number

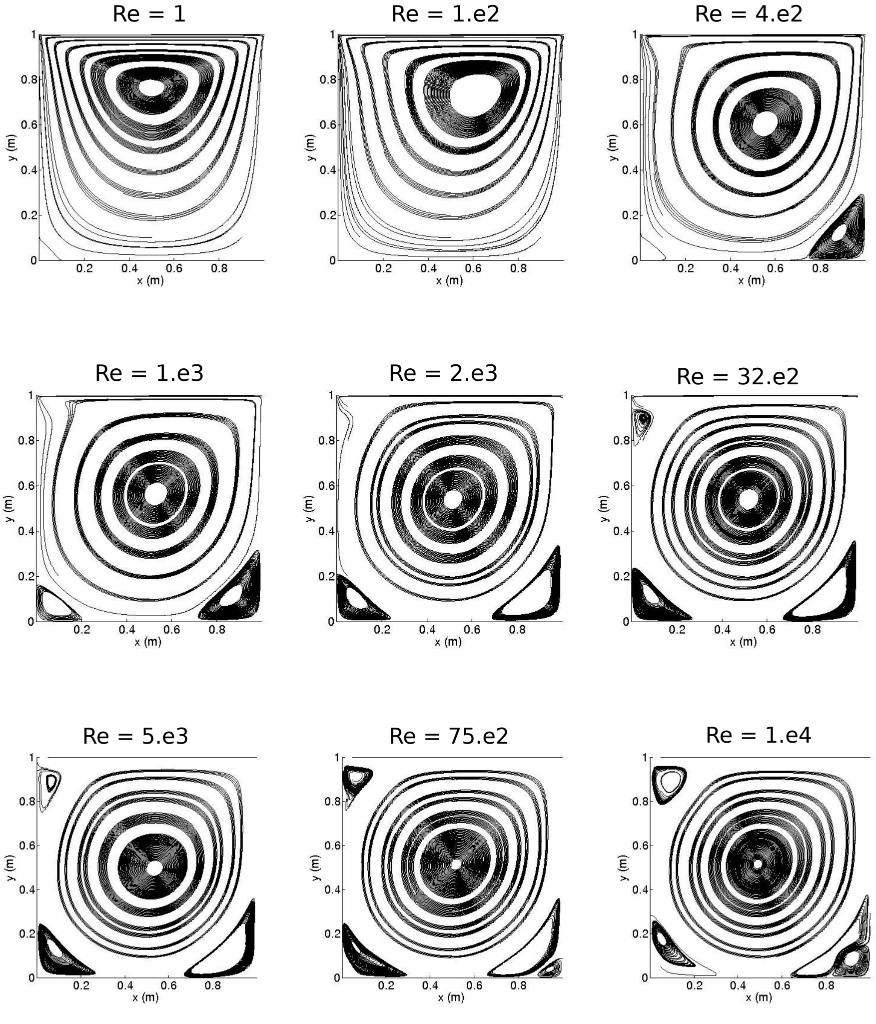

Figure 3.19: Driven cavity: streamlines (m^2/s) at various Reynolds number

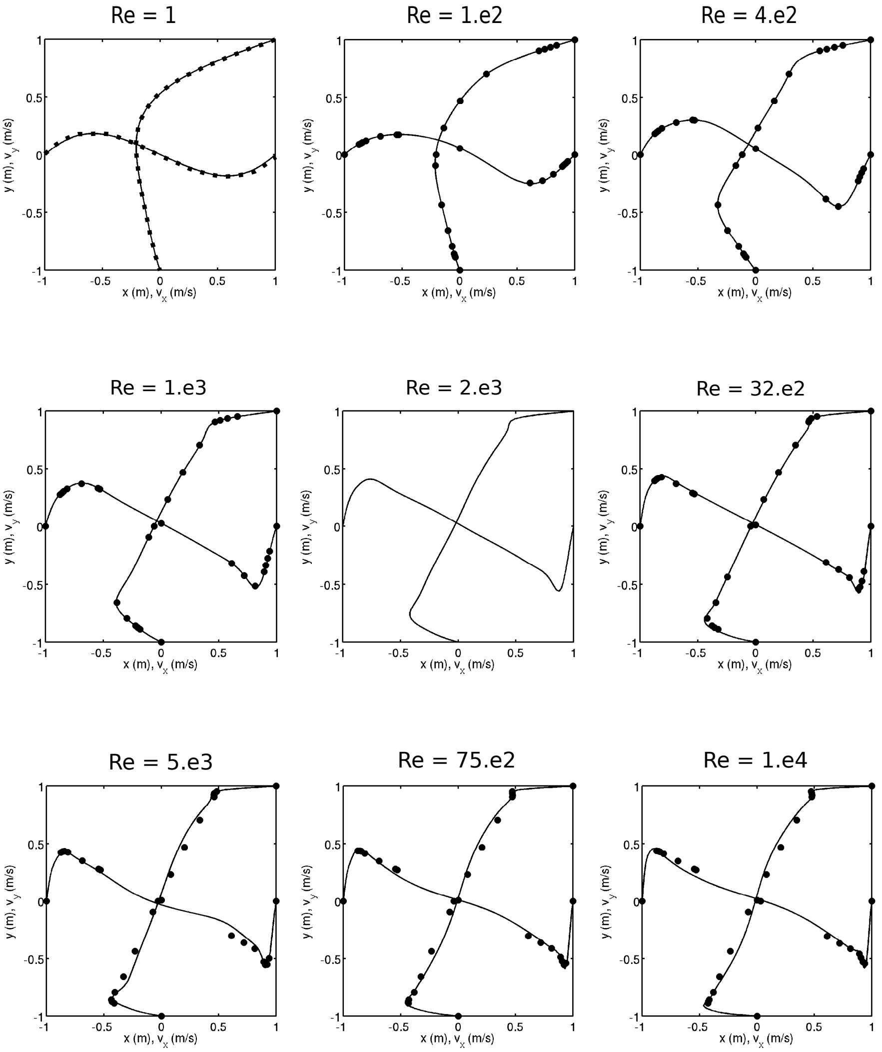

Re = 1

Re = 1.e2

Re = 4.e2

Re = 1.e3

Re = 2.e3

Re = 32.e2

Re = 5.e3

Re = 75.e2

Re = 1.e4

Figure 3.20: Driven cavity: comparison of v_1 (m/s) and v_2 (m/s) along the vertical and horizontal centrelines. For Re 1 dashed lines are from Hauke [74], in the other cases reference dots are from Ghia et al. [205]

eddy appears in the right bottom corner, immediately next to the secondary vortex, moving in the clockwise direction, as does the primary vortex. The computed results show good agreement with the aforementioned works in terms of velocity, shape and the location of the vortices for all values of *Re*. The computation results are validated by plotting the horizontal and vertical profile of velocities along centre vertical and centre horizontal lines respectively, and are shown in Figure (3.20). For $Re = 2000$ no reference experimental data is available. Nevertheless, the accuracy of the flow can be checked by interpolating the solution obtained at $Re = 1000$ and $Re = 3200$. Computed profile for $Re = 2000$ does not differ much from $Re = 1000$. As can be seen in figures with an increase in *Re*, both horizontal and vertical velocity curves get steeper near the end points. For small Re numbers up to $Re \leq 3200$, computed results with current numerical model match perfectly with the results obtained by Ghia et al. [205]. For $Re > 3200$ there is a small difference between the current results and [205], which is primarily due to the coarseness of the mesh. Overall, the present method provides adequate results for *Re* up to 10000 using much coarser grid (9316 elements) compared to that of 129×129 up to 257×257 used by Ghia et al. [205] and 601×601 used by Erturk et al. [57].

3.4.4 Backward facing step

The backward-facing step flow is a popular benchmarking and validation test for computational fluid dynamics simulations owing to its simple geometry and the availability of a good number of quality experimental data [61]. The schematic view of the case is shown in the Figure (3.21). The main characteristic of the flow is the separation and the recirculation eddies. The unstable shear layer carrying large vertical structures just behind the step splits at the reattachment zone and a significant part of the flow is reversed to supply the recirculation stream. The strong recirculation flow produces a small counter-rotating corner eddy (X_1) just behind the step. Depending on the *Re* number, a secondary separation appears in the form of another recirculation eddy in the vicinity of the upper surface. The secondary separation starts at (X_2) distance from the step and reattaches up to (X_3). The length of vortices grows almost linearly with the increase in *Re* number. In this case, flow is strongly dependent upon the *Re* and the expansion ratio. The expansion ratio is defined as the ratio of the outlet channel height to the inlet channel height. Based on the step height h, the Re is defined as $Re = \bar{U}h/\nu$, where $\bar{U}$ is the inlet mean velocity and is given by two third of the maximum inlet velocity. ν is the kinematic viscosity. In [151] authors concluded that the flow remains laminar, stable and computable up to $Re = 800$. Keskar et al. investigating the flow problem at $Re = 800$ with the spectral domain decomposition method [99]. Barkley et al. [46] computed the flow problem for an extended range of Re number demonstrating that even up to Re 1500 the flow remains stable, provided that the spatial mesh is sufficiently refined. In the present study, the simulations are performed for Re in the range of 100-800 for a fixed expansion ratio 2.0 in order to directly compare the present results with the numerical and experimental solutions found in the literature.

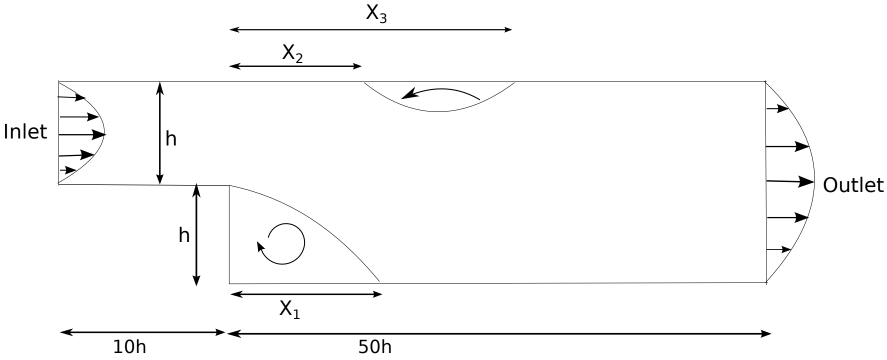

Figure 3.21: Backward-facing step: sketch of the flow field.

In the simulations, the effect of Re variations is explored on the primary and secondary reattachment lengths. The velocity profiles computed at the different locations are compared with the laboratory data. The adopted geometry for the simulation case is shown in Figure (3.21) with step height $h = 1m$. The inlet length and the downstream length are set to $10h$ and $50h$ respectively. The mesh consists of 156684 nodes composing 154614 quadrilateral elements. At the inlet and outlet, a fully developed parabolic velocity profile is assigned. The implemented boundary conditions are given as below:

$$\text{At Inlet} \qquad v_1 = -\frac{4}{h^2}(y-h)(y-2h), \qquad v_2 = 0 \tag{3.116}$$

$$\text{At Outlet} \qquad v_1 = -\frac{y(y-2h)}{2h^3}, \qquad v_2 = 0 \tag{3.117}$$

At all other parts of the boundary, no-slip boundary conditions are imposed. A constant time step of 0.01 is used for all *Re* numbers.

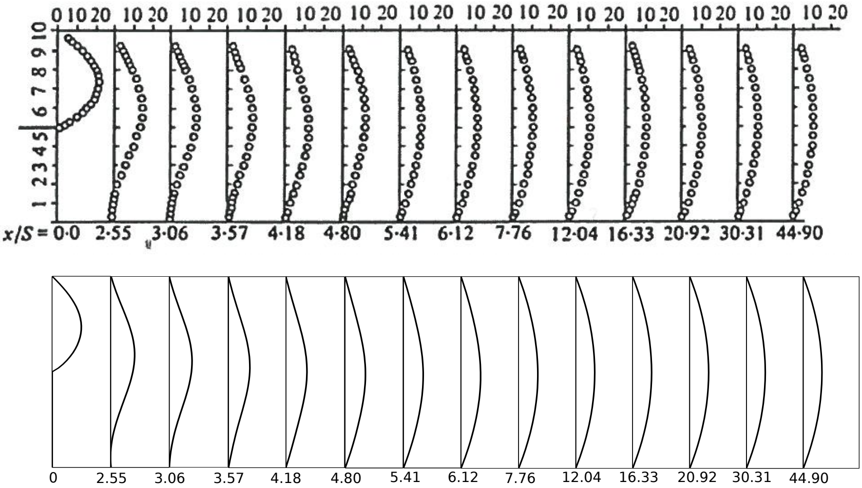

Figure 3.22: Backward-facing step: horizontal velocity (m/s) profile along various locations for Re 100. Top: Armaly et al. [61], Bottom: Present result.

Figure (3.22) shows a comparison of the stream-wise velocity profiles at various locations downstream for Re 100. The top part of the figure shows the experimental solutions of Armaly et al. [61] and the bottom part displays the

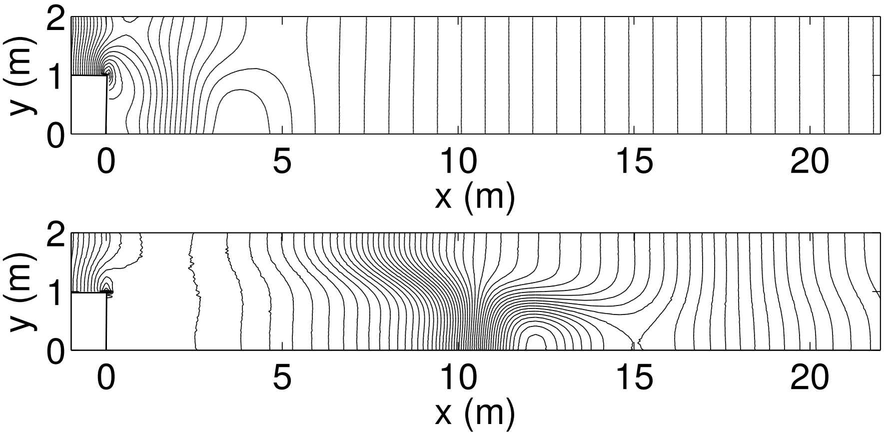

Figure 3.23: Backward-facing step: steady state flow pressure (Pa) contours. Top: Re=100 and Bottom: Re=800

results obtained from the present computation. The comparison results show a good agreement between the current results and the experimental data. Figure (3.23) shows the pressure contours at Re 100 and 800. Figure (3.24) shows the v_1 distribution in the whole domain. For small Re the viscous forces are more dominant over the inertial forces, consequently, immediately after the step the flow stream gradually bend downwards and then continue horizontally straight-wards in downstream. With the increase in Re number the inertial forces holds the tendency to keep the flow field horizontal up to some distance after the step and then bend downwards sharply resulting in the formation of vortices. In figures (3.25,3.26) the streamlines in the whole including the recirculation area are plotted for various Re. Recirculation point coordinates are calculated starting from x=0, beginning of the step. A different scale in x and y directions is used to clearly identify the different details present in the flow for the whole rank of Re. The streamline figures illustrate that the local shear induced vortices are affected by the dissipative nature of the fluid viscosity and convect downstream.

Bounded to the inlet high momentum flux depending on flow Re, the vortices move downward in their subsequent evolution. Starting from the step, the flow curves towards the upper part of the channel and forms convex stream-

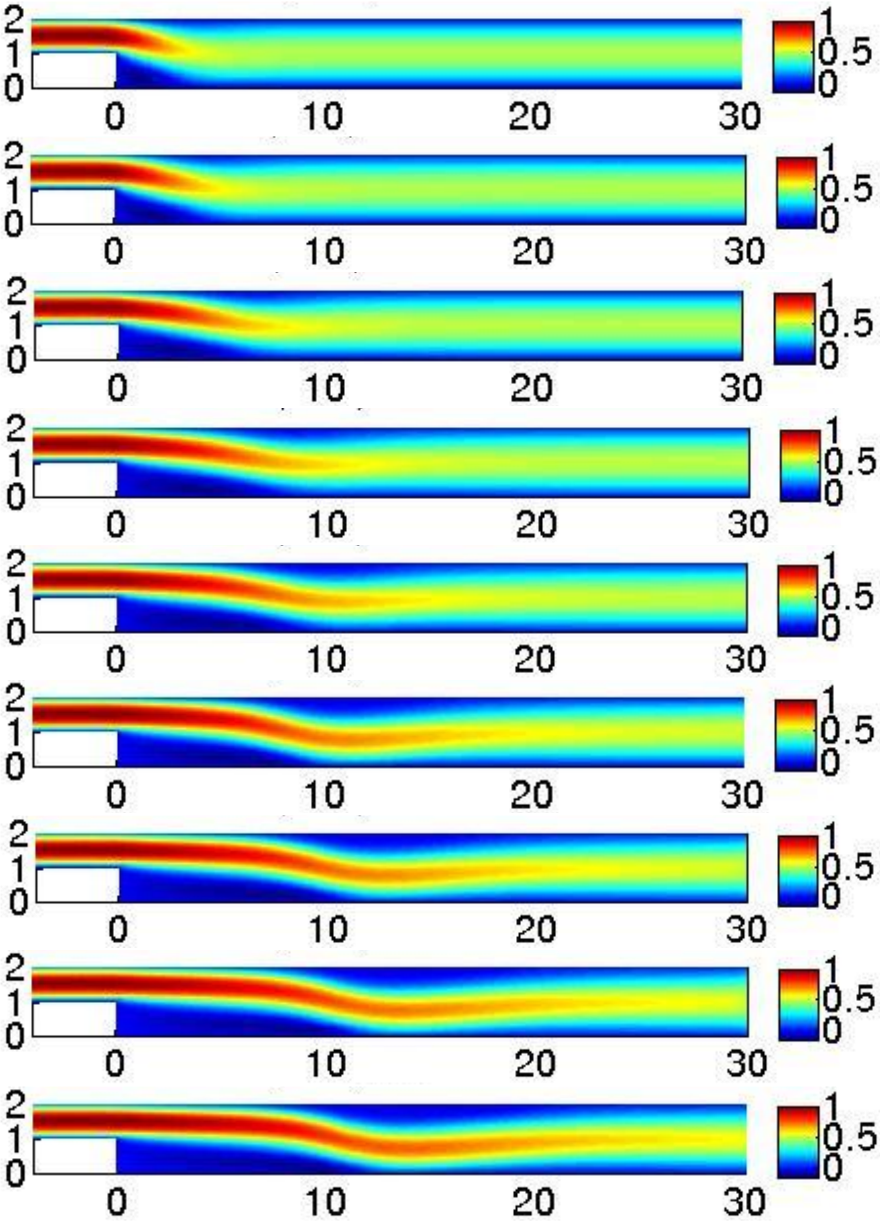

Figure 3.24: Backward-facing step: v_1 (m/s) distribution (from top) at $Re =$ 100, 150, 250, 350, 450, 550, 650, 750 and 800.

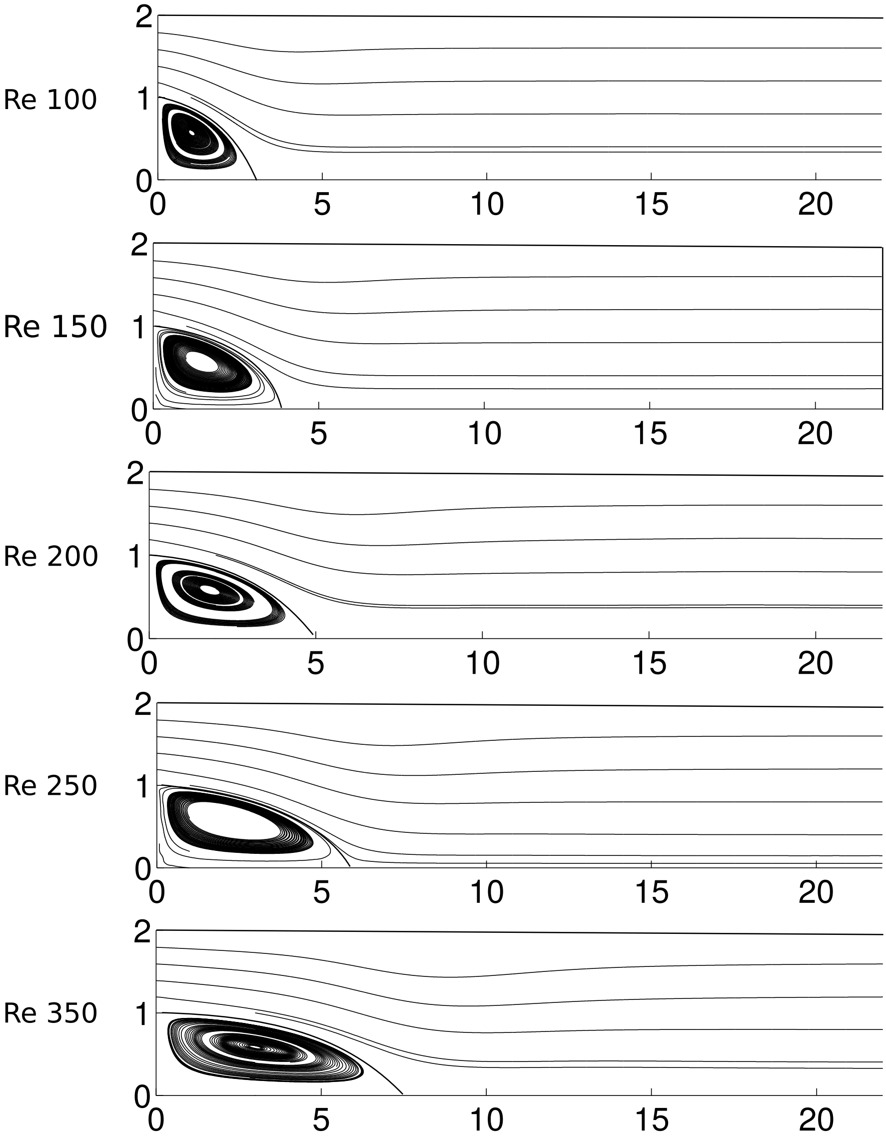

Figure 3.25: Backward-facing step: streamlines (m^2/s) along recirculation regions (from top) at Re = 100, 150, 200, 250, 350

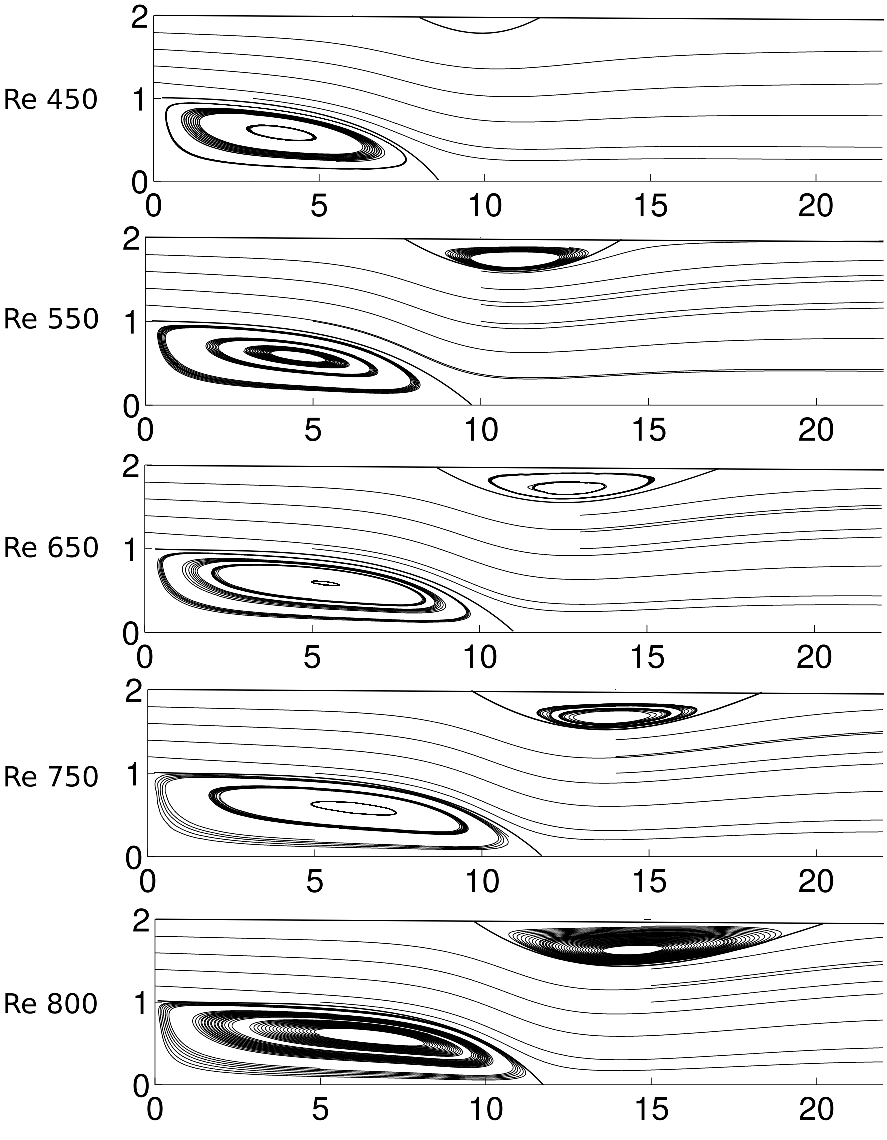

Figure 3.26: Backward-facing step: streamlines (m^2/s) along recirculation regions (from top) at Re = 450, 550, 650, 750 and 800.

Re	X_1	X_1^* []	X_2	X_2^* []	X_3	X_3^* []
100	2.920	2.922	-	-	-	-
150	3.993	3.962	-	-	-	-
200	4.998	4.982	-	-	-	-
250	5.731	5.872	-	-	-	-
350	7.512	7.507	-	-	-	-
450	8.867	8.843	7.762	7.769	11.631	11.633
550	9.903	9.885	8.011	8.190	14.397	14.478
650	10.709	10.71	8.552	8.663	17.108	17.011
750	11.426	11.44	9.890	9.145	19.129	19.361
800	11.882	11.834	9.979	9.476	20.223	20.553

Table 3.2: Backward-facing step: locations of detachment and reattachment of the flow. Present computation: X_1, X_2, X_3 Rouizi et al. [214]: X_1^*, X_2^*, X_3^*

lines. The bend in the flow generates a new separation zone. The direction of the secondary vortex formed at the channel roof is anticlockwise, unlike the primary one, which is just after the step in the clockwise direction. In current computations, the separation-reattachment flow pattern is not observed for $Re < 450$. With an increase in Re, at $Re = 450$, the recirculating region attached to the channel roof becomes visible. As shown in Figure (3.26) for $Re \geq 550$, this eddy is clearly revealed. The results for the whole range of Re are compared to numerical and experimental ones obtained by other authors. Table 3.2 lists the length of recirculation regions in terms of X_1, X_2, X_3. Columns X_1, X_2, X_3 show the results coming from the current study and X_1^*, X_2^*, X_3^* show the results reported in [214]. The comparison between the computed results and aforementioned in literature validates the accuracy of the obtained solutions.

3.4.5 Driven cavity with stripes of different fluids

This simulation presents the test case for incompressible multicomponent fluid flows. In this simulation, for simplicity, the multicomponent fluid is considered to consist of a mixture of two liquids with identical physical properties, identified by two different colours. The physical problem description, domain

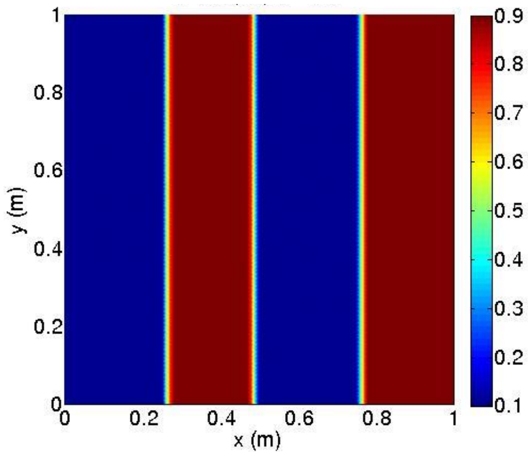

Figure 3.27: Multicomponent driven cavity flow: initial conditions for weight fractions.

geometry and initial and boundary conditions for pressure and velocity are same as those for the single component driven cavity flow (3.4.3). The *Re* number for the flow is 1. The initial condition for composition consists of four stripes of two different liquids parallel to the vertical sides of the cavity, as shown in figure (3.27). In order to set the total weight fraction equal to one, the red stripes are set to contain the 90% weight of the whole mixture and blue stripes are set to have 10% weight. The walls of the cavity are considered impermeable. For simplicity, it is assumed that there is no diffusion between red and blue liquids, and there is a very small value of diffusion among red and blue liquids themselves. The value of diffusion coefficient in diffusion matrix $d_{kk},\ k = 1, 2$ is set to $1.e$-6. Due to this setting of diffusivity, the components are able to maintain a sharp interface amongst each other when the inertial forces are not dominant. In this case, the molecular forces do not play a big role in mixing and the convective forces are the main forces those are responsible for the mass transfer by utilising the bulk motion (bulk flow).

Figure (3.28) shows the temporal evolution of the mixing process. The movement of the lid bends the upper part of the stripes towards right. This is evident from the second image in the first row of the figure. In the second row of the figure this is clearly visible that due to the strike with the right

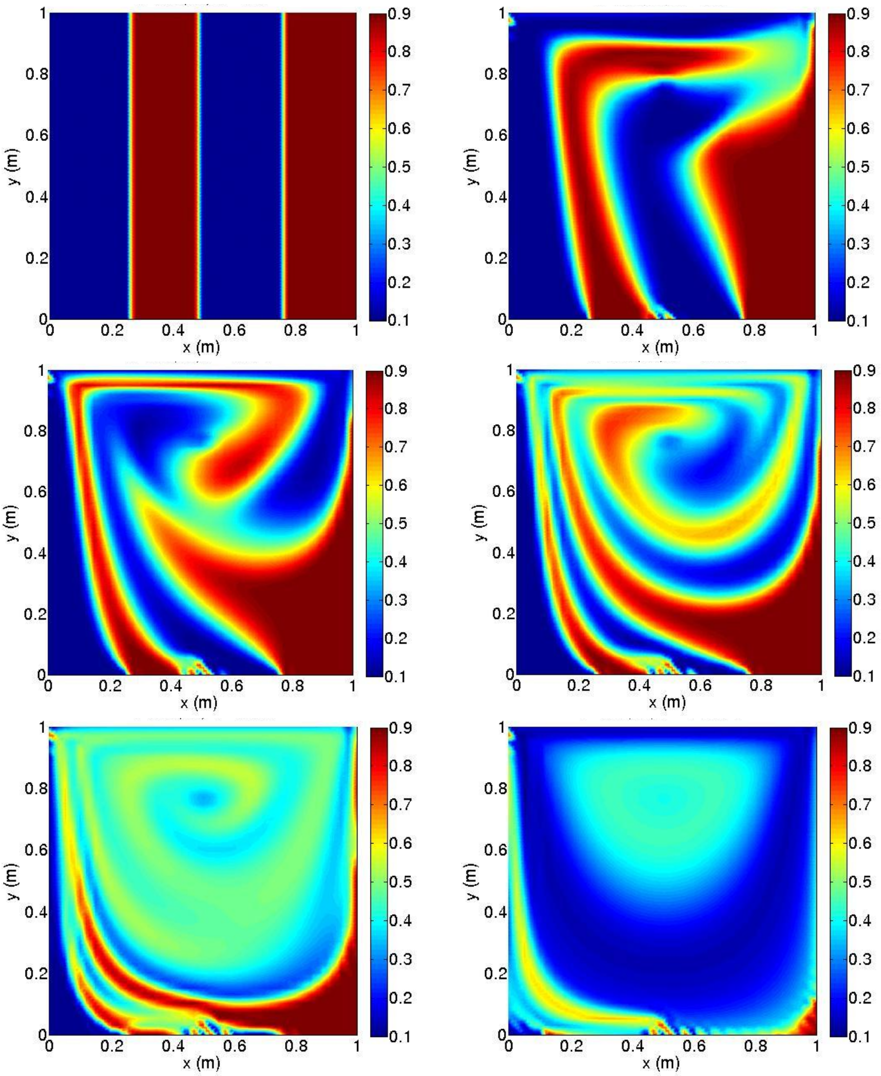

Figure 3.28: Multicomponent driven cavity flow: temporal evolution of movement of stripes in the process of formation of homogeneous mixture. Row wise from left, at time t = 0, 1, 5, 10, 30 and 1680s.

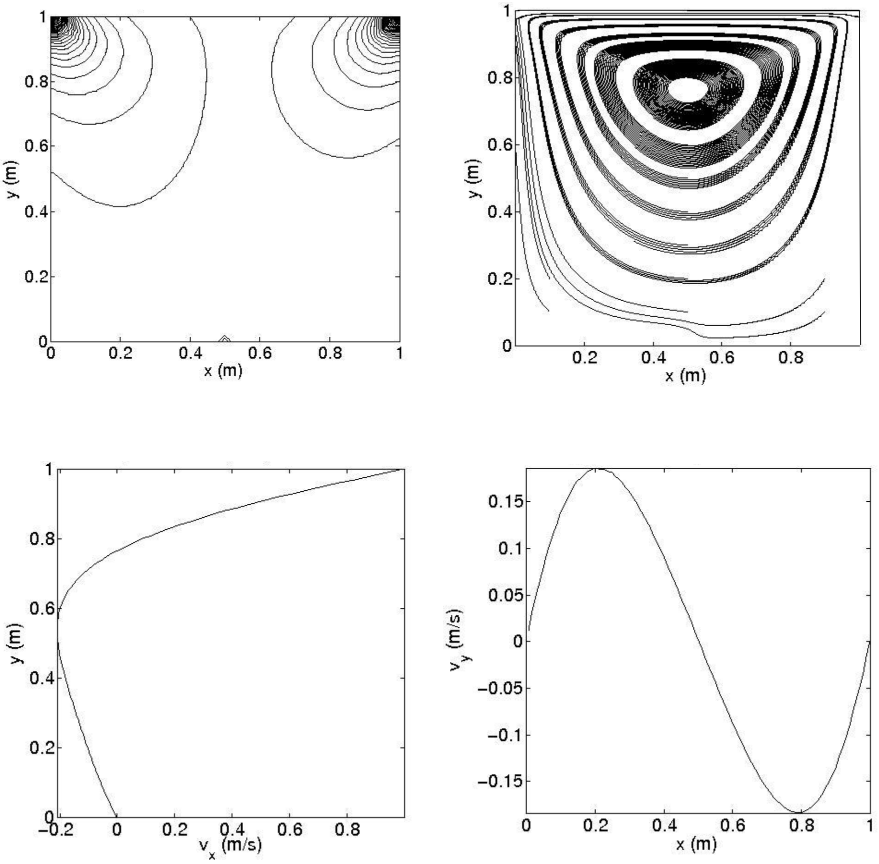

Figure 3.29: Multicomponent driven cavity flow: (row wise from left) pressure contours (Pa), streamlines, v_1 (m/s) along centre vertical line and v_2 (m/s) along centre horizontal line.

wall and in the process of formation of a primary vortex, the lower part of the right stripes bends toward the left and start moving upwards. At time $t = 10s$ the stripes move along the primary vortex and form a spiral shaped pattern. By time $t = 30s$ the shape of stripes is almost lost and in the last image of the figure at time $t = 1680s$ the mixture proceeds towards the uniform composition. Since the Reynold number of the flow is low, the convection does not affect the fluid at bottom corners and they retain their respective composition even after the uniform composition is reached in the middle of the cavity. Figure (3.29) shows the steady state pressure contours, streamlines pattern, the profile of horizontal velocity along the centre vertical line and the profile of vertical velocity along the centre horizontal line. The results are coincident with the case of single-component driven cavity flow (3.4.3), demonstrating that the model works well for multicomponent fluid flows.

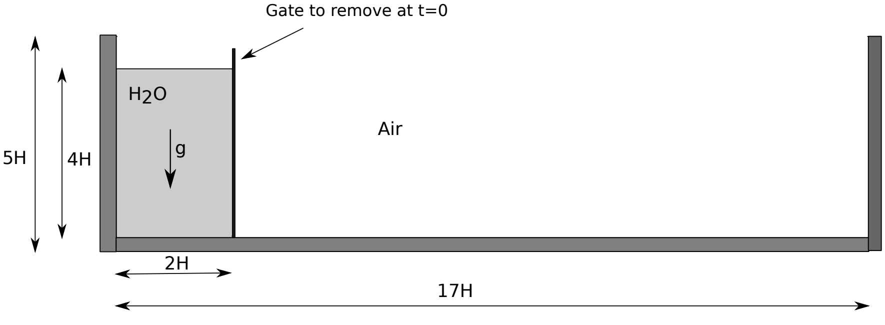

Figure 3.30: Broken dam: problem definition and schematic.

3.4.6 Broken dam

This problem represents a test for the capability of simultaneous computation of compressible-incompressible multicomponent flows. This case involves the incompressible behaviour of the falling water and the subsonic compressible behaviour of the air, within the same computational domain. The test case consists of the gravitational force and the advection of interface between water and air. For this problem the initial flow configuration is simple and the experimental data is available which will be used for the comparison. Advancement of the waterfront and re-treatment of the free surface make this problem very challenging and enables one to test the free surface-tracking technique more thoroughly. The problem is defined and illustrated in figure (3.30). A rectangular column of water in hydrostatic equilibrium is confined between a vertical wall and the gate. The gate is suddenly removed at time t = 0 and the water column starts to collapse under the influence of gravity, forming an advancing water wave to the right. The dam is chosen to have 2H×4H rectangular column with H=0.03. At all walls the slip boundary conditions ($\boldsymbol{v} \cdot \hat{\boldsymbol{n}} = 0, \;\; \hat{\boldsymbol{t}} \cdot \boldsymbol{\sigma}\hat{\boldsymbol{n}} = 0$) are applied. Here $\hat{\boldsymbol{n}}$ and $\hat{\boldsymbol{t}}$ are unit normal and tangential vectors respectively.

The velocities are set to zero as the initial condition. The initial pressure for air is set to 1.e5 and for water, a hydrostatic pressure profile is assigned. The gravity is assumed to act with a magnitude of 9.81. For water, the density and the viscosity are fixed to 1.e3 and 1.e-3 respectively. For air, the viscosity is set to 1.e-5, and density is computed from the ideal gas law with fixed absolute temperature $298K$. The diffusion coefficient for water and air is set to 1.e-10. A mesh consist of 6037 elements is composed of quadrangle elements. A constant time step of 1.e-4 is used for the simulation. As soon as the gate is removed, the water column starts to collapse from the upper right corner and the water wave accelerates rapidly along the floor as time elapses. Figure (3.32) shows the temporal evolution of the water wavefront. Figure (3.31) shows the pressure and $|\boldsymbol{v}|$ contours at various time levels. The results are noticed to be smooth in overall domain demonstrating the good stabilisation of the numerical technique. Figure (3.31) shows the comparison of water wavefront of free surface with the numerical results obtained in [17] and the experimental results. The non-dimensional length and time are calculated as $x/2H$ and $t\sqrt{g/H}$ respectively. As seen the computed results are in good agreement with the reported experimental and numerical ones.

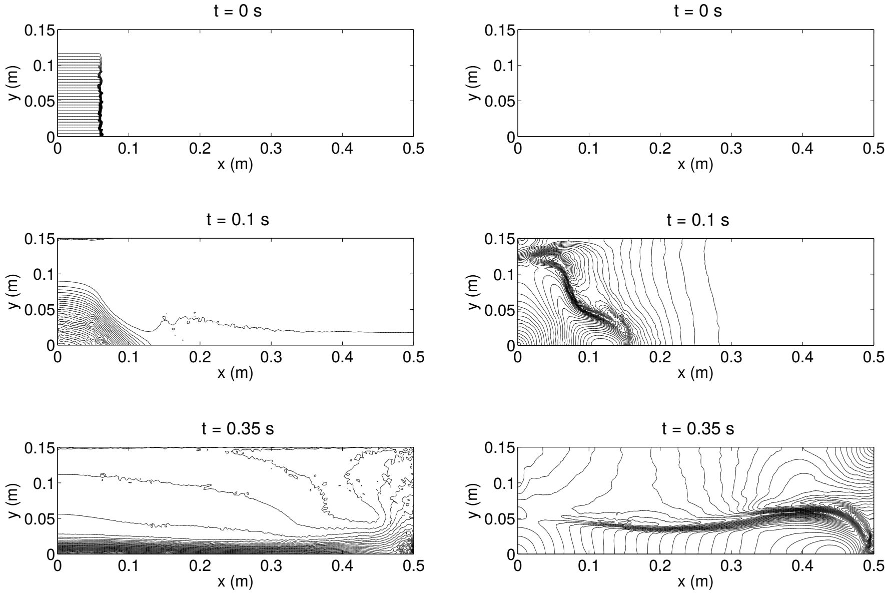

Figure 3.31: Broken dam problem: pressure (Pa) and $|\boldsymbol{v}|$ (m/s) contours on left and right respectively.

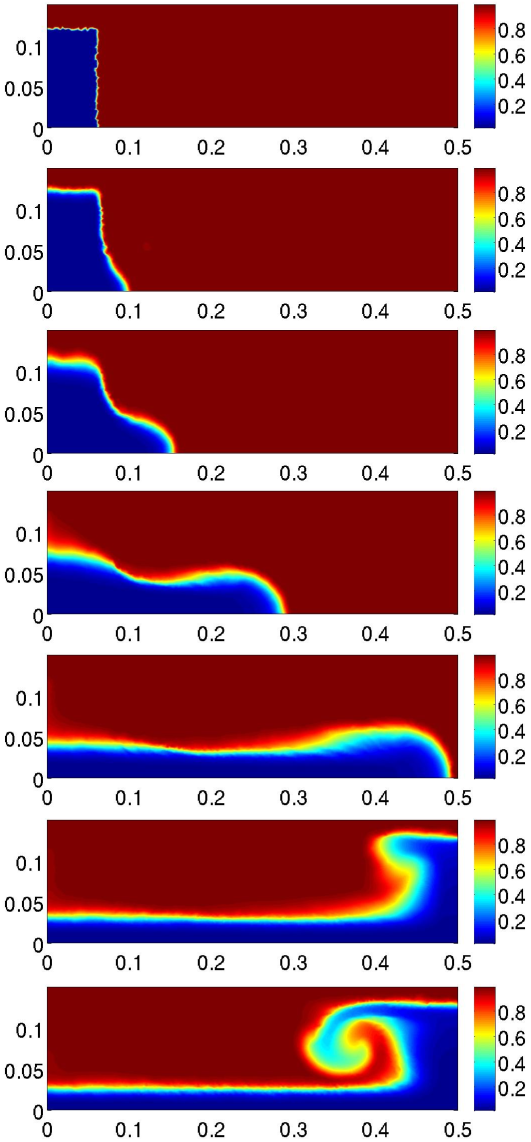

Figure 3.32: Broken dam problem: the temporal evolution of the water front (from top) at time t= 0, 0.05, 0.1, 0.2, 0.35, 0.45 and 0.55s.

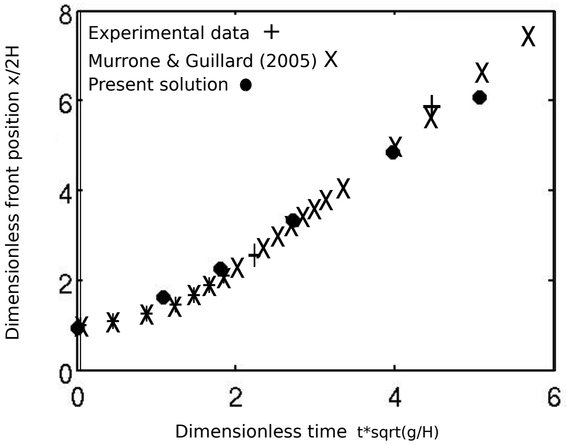

Figure 3.33: Broken dam problem: comparison of present numerical results with experimental data and result from Murrone and Guillard [17].

Chapter 4

Fluid flow for moving domain

Introduction

This chapter covers the numerical technique for the moving domain problems. In section 4.1 the interface-capturing and interface-tracking methods are discussed for moving domain problems. In section 4.2, starting with an overview of the mesh deformation methods, the details on the elastic deformation method are given. The Jacobian based stiffening approach is presented in order to control the rigidity of the mesh elements followed by the definitions of mesh quality criteria. In section 4.3, two numerical examples are provided to check the employed mesh deformation method. In section 4.4, the mesh velocity is discussed and a segregated algorithm is presented to couple the mesh deformation with the fluid flow problem. In section 4.5, the algorithm is verified over four fluid flow problems with moving boundaries.

4.1 Numerical techniques for moving domain problems

Moving domain problems can be solved with either interface-capturing or interface-tracking techniques. Interface capturing methods do not define the interface as a sharp boundary. A fixed grid extends beyond the moving surface over which the computation is performed. In interface capturing methods, the fraction of each cell near the moving boundary is computed. Usually, an artificial scalar field is used for an implicit description of the interface. The most common representatives of this class of approaches are the level set [101, 215] and the volume of fluid method [45, 155]. These approaches are inherently able to consider the problems where the interface is subjected to severe motion even topological changes can be considered. This flexible interface description provides challenges regarding the mass conservation and the treatment of discontinuities across the interface. Nonetheless, in many cases, interface-capturing techniques, which do not normally require costly mesh update steps, could be used with the understanding that the interface will not be represented as accurately as it would be with an interface-tracking technique. On the other hand, in interface tracking methods the moving boundary is explicitly described by the computational mesh. Hence, the movement of the interface has to be accounted for by adjusting the position of the nodes on the interface. Generic front tracking [53], volume tracking [67, 184] and immersed boundary method [135] fall in this category. These methods have the tremendous advantage that the boundary conditions are treated neatly and resolved very accurately because the moving boundary coincides with one line of the numerical grid. Interface tracking approaches are known to provide great accuracy, yet their applicability is limited in the case of severe interface motion. In complex problems such as in the computation of two-fluid flows, sometimes it becomes difficult to track the interface while keeping the frequency of remeshing at an acceptable level. Not being able to reduce the frequency of remeshing might introduce overwhelming mesh generation and projection costs, making the computations with the interface-tracking technique no longer feasible. Nevertheless, the interface tracking methods are preferred over the interface capturing methods and widely used for moving domain problems.

The deforming-spatial-domain/stabilised space-time (DSD/SST) formulation, discussed in the previous chapter, is an interface-tracking method. In the previous chapter, the finite element formulation was presented for Navier-Stokes equations over the space-time domain. This automatically took into account the motion of the boundaries and interfaces. At each time step of a computation, the locations of the boundaries and interfaces were calculated as part of the overall solution. In the previous chapter, the flow problems were computed on fixed domain by setting the mesh velocity equal to zero, which eventually removed all the terms associated with the movement of the mesh elements from the formulation. However, in a typical moving domain problem at each time step, the mesh velocity need to be evaluated to update the mesh.

Often the locations of the moving boundaries and interfaces are unknown within the fluid mechanics problem and must be determined together with the solution of the Navier-Stokes equations. In order to evaluate the new location of mesh nodes, mesh updation technique is used.

4.2 Mesh updation

In general, the mesh updation has two components: moving the mesh as long as it is possible, and perform remeshing by generating fully or partially a new set of nodes and elements when the element distortion becomes too high. Remeshing includes the projection of the solution from the old mesh to the new mesh, which is computationally an expensive process and contains the unavoidable projection errors. In mesh updation techniques the main aim is always to reduce the frequency of remeshing, which can be done by adopting a powerful mesh deformation technique. In general, the mesh can be moved in any desirable way with only one requirement is to match the normal velocity of the mesh with the normal velocity of the moving interface. This is needed to prevent the fluid domain and the boundary from separating. In certain cases, it is better to match both normal and tangential components of velocities. It is common to use the automatic mesh moving methods which automatically move the mesh nodes in order to keep the mesh elements in good shape for accurate flow computations. The deformation of the mesh depends on the overall domain geometry, the complexity of interface and the starting mesh. Mesh deformation can be handled arbitrary in several ways. Different methods typically compromise between the amount of boundary deformation that can be tolerated and the computational expense of the procedure.

In order to move the mesh, many methods have been proposed in the literature including the Laplacian [154], the biharmonic [186], the spring [33,90,142,208], transfinite interpolation [75] and the elastic deformation methods [54, 189, 194]. Laplacian and biharmonic method use the laplacian operator ∇^2 and biharmonic operator ∇^4 respectively. The spring methods are divided into tension spring and torsion spring methods. In tension spring method, each edge of the mesh is represented by a spring whose stiffness is proportional to the reciprocal of the length of the edge. By replacing the edges with springs, a deformation of the boundary translates into a deformation of the spring network, which adjusts its shape to the equilibrium position of the network. The displacements in each direction are decoupled and the equation that updates the position of the nodes is relatively easy to solve. A disadvantage of this method is that, for highly distorted meshes, collapsed or negative volume cells may appear, especially on high-aspect-ratio cells like the ones used for viscous flows. The torsion spring method consists of adding a torsional spring to the tension spring technique. The stiffness of the torsional spring is related to the angle between the edges. As the angle tends to zero, the stiffness tends to infinity, thus preventing vertices from crossing over edges and avoiding negative volume cells. The disadvantage of this method is the higher complexity and computational cost, compared to the tension spring analogy. The transfinite interpolation mesh deformation technique is based on the linear interpolation of the boundary motion. The motion of a node located between a moving and a fixed boundary is equal to the motion of the moving boundary times a scale factor. This scale factor, assigned to each node of the mesh, depends on the distances from the node to the moving and the fixed surfaces. The scale factor is 1 for nodes on the moving boundary and 0 for nodes on the fixed boundary. The method guarantees a smooth transition between the moving boundaries and the fixed boundaries. One disadvantage of this method is that it cannot guarantee the mesh orthogonality at deforming surfaces, a condition that is important for viscous flows. In mesh moving method based on the linear elasticity, the mesh is modelled as an elastic solid using the equations of linear elasticity. The deformed grid is obtained by solving the equilibrium equations for the stress field subject to the Dirichlet boundary conditions imposed on the moving boundaries. In this work, the elastic deformation method is applied to deform the mesh nodes.

4.2.1 Elastic deformation method

The elastic deformation method was proposed by Tayfun Tezduyar and his colleagues [19, 188]. The elastic deformation method for mesh motion treats the mesh as an elastic body and solves a simplified form of the standard linear elastostatic equations to compute the displacements of the inner vertices subject to the applied boundary conditions. The formal statement for the standard linear elastostatic problem is as follows. Let $\Omega \subset \Re^n$ be the computational domain bounded by Γ, where n is the space dimension. $\Gamma =$

$\Gamma_g \cup \Gamma_h$ and $\Gamma_g \cap \Gamma_h = \phi$, where Γ_g and Γ_h are the parts of boundary domain corresponding to Dirichlet and Neumann type boundary conditions. The governing equations of elastostatic are:

$$\boldsymbol{\nabla} \cdot \boldsymbol{\sigma} = \boldsymbol{f} \quad \text{ on } \Omega \tag{4.1}$$

Where, $\boldsymbol{f}$ is the body force, and $\boldsymbol{\sigma}$ is the Cauchy stress tensor dependent upon the strain tensor $\boldsymbol{\epsilon}$. The following Hooke's law for isotropic homogeneous medium expresses the stress tensor $\boldsymbol{\sigma}$ as a function of the strain tensor $\boldsymbol{\epsilon}$ in case of plane stresses:

$$\boldsymbol{\sigma} = \lambda \ \mathrm{tr}(\boldsymbol{\epsilon})\boldsymbol{I} + 2\mu\boldsymbol{\epsilon} \tag{4.2}$$

or

$$\boldsymbol{\epsilon} = \frac{1+\nu}{E}\boldsymbol{\sigma} - \frac{\nu}{E} \ \mathrm{tr}(\boldsymbol{\sigma})\boldsymbol{I} \tag{4.3}$$

Where, λ and μ are the Lamé coefficients, E is the Young's modulus that represents the stiffness of the material. Large values of E indicate more rigidity. ν is the Poisson ratio representing the measure of how much the material shrinks in the lateral direction as it expands in the axial direction. The kinematic law relating the strain tensor $\boldsymbol{\epsilon}$ and the displacements $\boldsymbol{u}$ is:

$$\boldsymbol{\epsilon} = \frac{\boldsymbol{\nabla}\mathbf{u} + \boldsymbol{\nabla}\boldsymbol{u}^T}{2} \tag{4.4}$$

and measures the change in length for elastic materials. The Dirichlet and Neumann boundary conditions are written as:

$$\boldsymbol{u} = \boldsymbol{g} \quad \text{on } \Gamma_g \tag{4.5}$$

$$\boldsymbol{\sigma} \cdot \boldsymbol{n} = \boldsymbol{h} \ \text{ on } \Gamma_h \tag{4.6}$$

The trial and weighting function spaces for the Galerkin finite element formulation are:

$$\mathcal{T}^h = \left\{ \boldsymbol{u}^h | \boldsymbol{u}^h \in H^h(\Omega)^n, \boldsymbol{u}^h = \boldsymbol{g}^h \text{ on } \Gamma_g \right\} \tag{4.7}$$

$$\mathcal{V}^h = \left\{ \boldsymbol{w}^h | \boldsymbol{w}^h \in H^h(\Omega)^n, \boldsymbol{w}^h = 0 \text{ on } \Gamma_g \right\} \tag{4.8}$$

Where, $H^h(\Omega)$ is a finite dimensional functional space on Ω. The finite element problem can be written as: find $\boldsymbol{u}^h \in \mathcal{T}^h$ such that $\forall\ \boldsymbol{w}^h \in \mathcal{V}^h$

$$\int_\Omega \boldsymbol{\epsilon}(\boldsymbol{w}^h) : \boldsymbol{\sigma}(\boldsymbol{u}^h)\ d\Omega = \int_\Omega \boldsymbol{w}^h \cdot \boldsymbol{f}^h\ d\Omega + \int_{\Gamma_h} \boldsymbol{w}^h \cdot \boldsymbol{h}^h\ \ d\Gamma \tag{4.9}$$

Simplifications adopted for the elastic mesh deformation method consist in neglecting the body forces and assigning only Dirichlet boundary conditions, which can be enforced strongly on the linear system. The interface must satisfy the kinematic boundary condition of equality of displacements (velocities). Therefore, Neumann boundary conditions are not considered and only the Dirichlet boundary conditions are imposed over the mesh boundary including deforming and stationary parts. The finite element discretization of equation (4.9) and the imposition of Dirichlet boundary conditions results in the following matrix form

$$\boldsymbol{K}\boldsymbol{u} = \boldsymbol{g} \tag{4.10}$$

Where, $\boldsymbol{u}$ and $\boldsymbol{g}$ are the vectors of unknowns and the given displacements on boundary, and

$$\boldsymbol{K} = \int_\Omega \boldsymbol{B}^T \boldsymbol{C} \boldsymbol{B}\ d\Omega \tag{4.11}$$

Here, $\boldsymbol{B}$ and $\boldsymbol{C}$ are the strain-displacement and elastic tensor matrices and defined as

$$\boldsymbol{B} = \begin{bmatrix} N_{a,1} & 0 & 0 \\ 0 & N_{a,2} & 0 \\ 0 & 0 & N_{a,3} \\ 0 & N_{a,3} & N_{a,2} \\ N_{a,3} & 0 & N_{a,1} \\ N_{a,2} & N_{a,1} & 0 \end{bmatrix} \qquad \boldsymbol{C} = \begin{bmatrix} \lambda+2\mu & \lambda & \lambda & 0 & 0 & 0 \\ \lambda & \lambda+2\mu & \lambda & 0 & 0 & 0 \\ \lambda & \lambda & \lambda+2\mu & 0 & 0 & 0 \\ 0 & 0 & 0 & \mu & 0 & 0 \\ 0 & 0 & 0 & 0 & \mu & 0 \\ 0 & 0 & 0 & 0 & 0 & \mu \end{bmatrix} \tag{4.12}$$

Jacobian based stiffening

In mesh moving problems, the major issue is to maintain the appropriate quality of the elements situated near the moving boundaries. In deforming domain problems, the presence of moving boundaries requires high refinement in their neighbourhood. As boundaries move, the consequent displacement of these neighbourhood nodes may lead to severe distortion with vertices getting closer with crossing edges and production of negative element areas. These kind of elements are error prone to the exact fluid flow computations. One solution to avoid this problem is to increase the rigidity of the smaller elements in comparison to the bigger ones. This can be done by altering the values of λ and μ in the elasticity matrix. In [19] the authors investigated the effect of λ/μ on the changes of aspect ratio for the elements of the domain of interest. In this direction, the Jacobian based stiffening method was proposed in [19, 189]. The Jacobian based stiffening is an extension of elastic deformation technique relevant in finite element formulations for the purpose of preserving mesh quality. It is based on a selective treatment of the elements deformation based on their size which decreases mesh distortion by increasing the rigidity of smaller elements with respect to the larger ones. This is obtained by solving the simplified form of the standard linear elasticity equation (4.1) with a change of the Jacobian of transformation from reference to the current element. A stiffening power is introduced to set the degree by which the smaller elements are rendered stiffer than the larger ones. Starting from the standard weak formulation of the simplified linear elasticity equations (4.9), the Jacobian is modified as:

$$\int_{\Omega}[..]d\Omega = \sum_{e}\int_{\mathcal{E}}[..]^e J^e d\mathcal{E} \rightarrow \sum_{e}\int_{\mathcal{E}}[..]^e J^e \left(\frac{J^0}{J^e}\right)^{\chi} d\mathcal{E} \tag{4.13}$$

Where, $\mathcal{E}$ is the finite element reference domain, [..] represents the quantity to be integrated, J^e is the Jacobian for element e, χ is the degree by which the smaller elements are rendered stiffer than the larger ones, and J^0 is an arbitrary scaling parameter inserted into the formulation to make the alteration dimensionally consistent and is set equal to one. This method stiffens each element by the factor $(J^e)^{-\chi}$. If the stiffening power is 0, the method reduces back to an elasticity model with no Jacobian-based stiffening. The stiffening increases with increasing χ. The Jacobian stiffening method is a powerful automatic mesh motion technique that depends on a minimum number of arbitrarily adjustable parameters. The best values of the stiffening factor have been discussed in [110].

4.2.2 Mesh quality criteria

A mesh with good element quality is necessary for obtaining a finite element solution that converges to the analytical solution of the mathematical model. A poor quality mesh can display results that are more mesh dependent than the model itself. In extreme cases, when the elements are of very poor quality, computations may not converge. Several geometrical measures are available to evaluate the mesh quality. A good quality criterion should be neither too restrictive nor too loose in detecting the state of mesh deterioration. Such criteria should have an intermediate level of quality definition, in order to avoid remeshing when the grid is still able to sustain further deformation maintaining convergence and accuracy of the fluid solution. The quality criteria considered are the angle, length ratio, the element area change and the element shape change. The angle criterion f_a considers the maximum and minimum element's angles that must belong to the interval $[15° - 165°]$. The length ratio criterion is defined as:

$$f_l = \max_e \left(\frac{l^e_{\text{max}}}{l^e_{\text{min}}} \right) \tag{4.14}$$

Where, l^e_{max} and l^e_{min} are the maximum and minimum edge lengths of the element e. The best f_l value is 1, in correspondence to a square element, and the maximum threshold is assumed to be 7. The area change, f_A, and the shape change, f_{AR} are defined as:

$$f^e_A = \max_e \left| \log \left(\frac{A^e}{A^e_0} \right) \right|, \quad f^e_{AR} = \max_e \left| \log \left(\frac{AR^e}{AR^e_0} \right) \right| \tag{4.15}$$

where the subscript “0” refers to the undeformed mesh and AR^e is the element aspect ratio, defined as

$$AR^e = \frac{(l^e_{\text{max}})^2}{A^e}, \tag{4.16}$$

For both criteria the best value is 0, corresponding to no change either in area or aspect ratio, the worst value is assumed to be 0.8, corresponding to a change of ∼6.

4.3 Numerical Examples

In this section, the automatic mesh deformation method is tested on two numerical examples: squeezing can and rotating circle. The test cases are in 2D and cover the deformation of meshes, with bending, translational and rotational motion. The pre-determined displacement functions are applied on the moving parts to impose the Dirichlet boundary conditions. In order to avoid the deformation of small mesh elements the Jacobian based stiffening approach is used with $\chi = 0.8$ and the quality of each mesh element is determined by the quality criteria. The details of test cases are as follows.

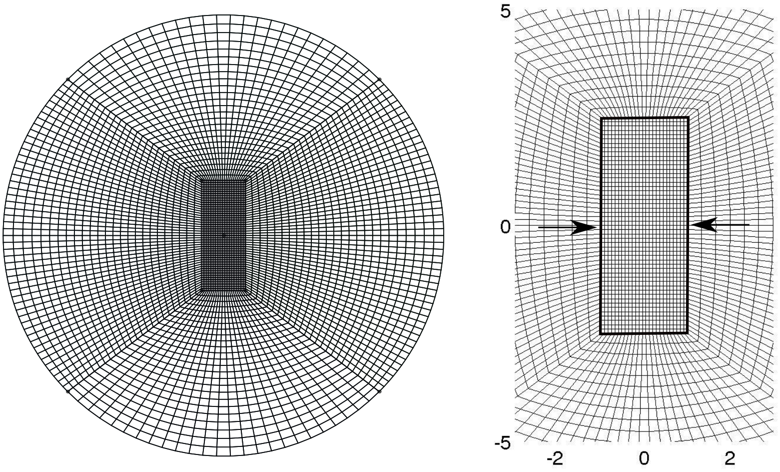

Figure 4.1: Squeezing can: on left the whole mesh and on right the zoomed view of can mesh. The arrow show the direction of prescribed displacement (m).

4.3.1 Squeezing can

This numerical example regards a can with deformable geometry [140]. This test case checks the capability of the mesh moving technique in case of bending. A can is taken inside a large circular domain and the time-dependent deformation function is applied on the vertical sides of the can. Subject to the applied deformation on the boundary nodes the interior nodes move to keep the mesh elements in good shape. The length and breadth of the cylinder are set to 5 and 2 units respectively inside a circular domain of radius 10 units. The can is placed at its centre with y as the longitudinal axis of the cylinder. The domain is discretized with a structured mesh of 8780 nodes and 8699 elements. Figure (4.1) shows the zoomed view of the can mesh along with the exterior elements. The simulation is carried out up to 1 s with 10 steps of motion. On time dependant vertical sides of the can the following boundary conditions are assigned.

$$\text{if}\, |y(0)| < 2 \quad \text{then} \quad \mathbf{x}(t) = \begin{cases} y(t) = y(0) \\ x(t) = (\alpha + (1-\alpha)(1-t^2))x(0) \end{cases} \tag{4.17}$$

where

$$\alpha = \frac{1}{2.2}\left(1.2 - \cos\left(\frac{\pi}{2}\,|y(0)|\right)\right) \tag{4.18}$$

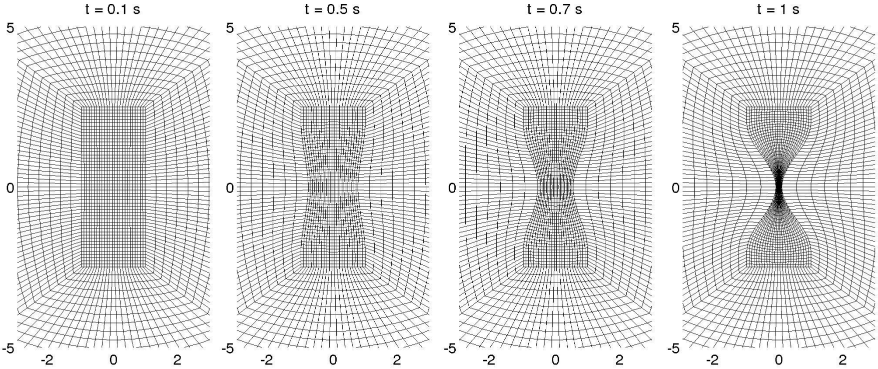

Figure 4.2: Squeezing can: temporal evolution of the mesh at various times.

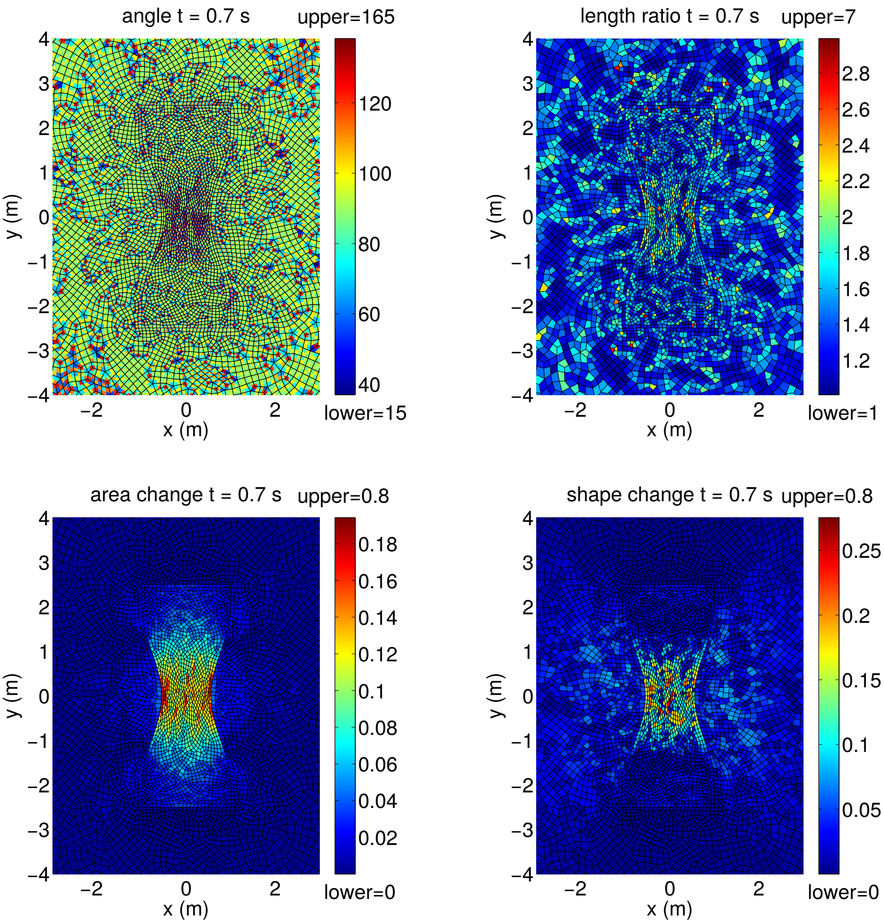

Figure 4.3: Squeezing can: quality criteria at t = 0.7 *s*.

Figure (4.2) shows the mesh at different times. At time 1 *s* the mesh elements which are situated at the centre of the can, become completely distorted. Figure (4.3) shows the quality of mesh elements at time t = 0.7 *s* with different criteria. The mesh elements are noticed to remain in the acceptable quality range up to t = 8 *s*. After this, the mesh becomes completely distorted and there is the strict need of remeshing.

4.3.2 Rotating circle

This simulation consists of an expanding and rotating circle inside another circle with fixed external boundary, thus combining the translational and rotational motions. The mesh is structured in a broad sense, composed of 3811 nodes and 3750 elements, with radial and orthogonally circular lines. The inner circle rotates first anticlockwise upto angle $\pi/4$ and its radius elongates sinusoidally of 0.5 m. Afterwards, the motion is inverted, with clockwise rotation down to $-\pi/4$ and with a total radius contraction of 0.5 m, crossing the state corresponding to the initial set up. Finally the motion is inverted again until the initial position is recovered. The total simulation time is $T = 4$ s, and each rotation of $\pi/4$ is subdivided into 10 steps. The function describing this motion written in polar coordinates (r, θ) is:

$$\mathbf{r}(t) = \mathbf{r}(t=0) + \hat{\mathbf{r}} A \sin\left(\frac{\pi}{2}t\right) \qquad \text{for} \quad t = 0-4 \text{ s} \tag{4.19}$$

$$\begin{cases} \theta(t) = \theta(t=0) + \dfrac{\pi}{4}t & \text{for} \quad t = 0-1 \text{ s} \\[2ex] \theta(t) = \theta(t=0) + \dfrac{\pi}{4} - \dfrac{\pi}{4}(t-1) & \text{for} \quad t = 1.1-3 \text{ s} \\[2ex] \theta(t) = \theta(t=0) - \dfrac{\pi}{4} + \dfrac{\pi}{4}(t-3) & \text{for} \quad t = 3.1-4 \text{ s} \end{cases} \tag{4.20}$$

Where, $|\mathbf{r}(t=0)| = 1$ m is the initial radius of the inner circle, and $A = 0.5$ m is the maximum radius expansion/contraction. In figure (4.4) the mesh is shown at maximum expansion (t = $1s$), with anticlockwise rotation of the internal circle and the mesh at maximum contraction (t = $3s$), with clockwise rotation of the internal circle. During the compression and expansion phases, the radial lines between the internal and external circles maintain a fixed position on the external circle and rotate leftward and rightward, dragged by the rotation of the internal circle. Figure (4.5) shows the quality of mesh elements at time t = 3 s with different criteria. This case shows that with elastic deformation method the mesh translates and rotates in a good way.

4.4 Mesh velocity

In the previous chapter, the detailed formulation of space-time finite element method was written. The whole space-time domain was split into space-time

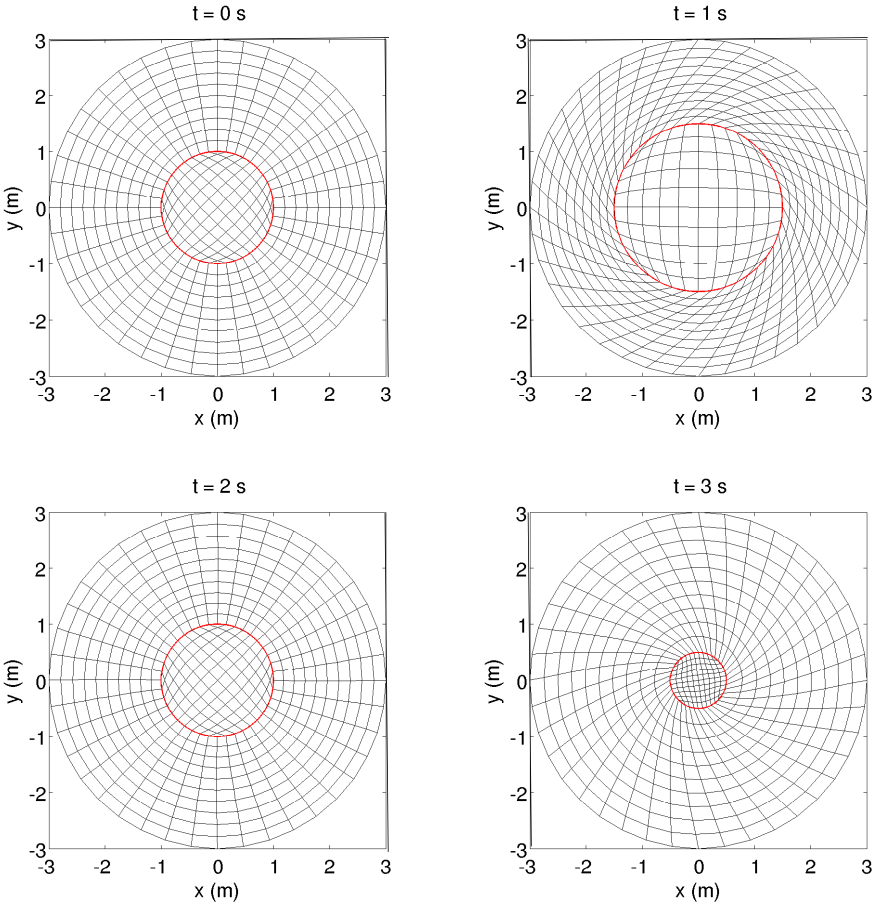

t = 0 s

t = 1 s

t = 2 s

t = 3 s

Figure 4.4: Rotating circle: mesh at different times.

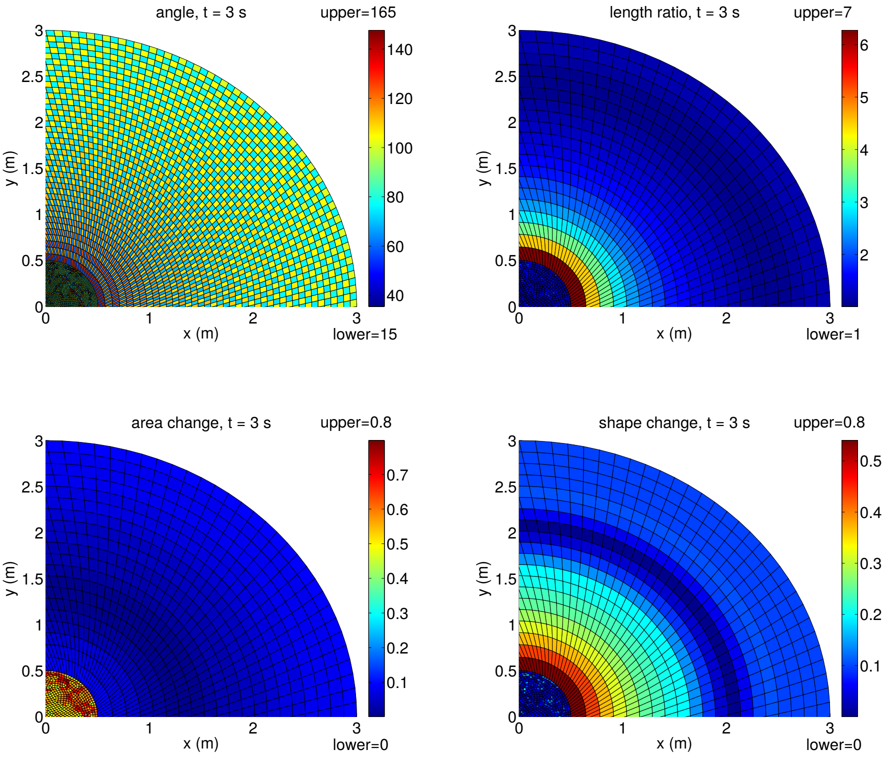

Figure 4.5: Rotating circle: quality criteria at t $= 3$ s. Due to the symmetry of the domain, only a quarter is shown.

slabs which were composed of space-time elements. A typical nth space-time slab lies in time interval (t_n, t_{n+1}). In the case of moving domain problems, the position of mesh nodes at time t_{n+1} is not known and need the mesh velocity to be defined. This became clear with the definition of the mapping. For each space-time element in the physical domain, a mapping was defined, which mapped it onto a reference element. While defining the space-time mapping, it was noticed that in the computation of $x_{,\theta}$ and $y_{,\theta}$ in equations (3.51) and (3.52) the mesh velocity $\boldsymbol{v}^m$ was needed to complete the space-time mapping. Also in the weighted residual formulation in equation (3.70) to compute the surface integral, the formulation of the temporal unit normal vector $\hat{n}_t$ was needed. In equation (3.76), the $\hat{n}_t$ was formulated, which ultimately, was computed in terms of mesh velocity. For moving domain problems, within nth space-time slab the fluid mesh displacement is computed by solving the equation (4.9) with $\Omega = \Omega(t_n)$. Fluid mesh velocity $\boldsymbol{v}^m$ can be obtained by differentiating the fluid mesh displacement with respect to time. Once the mesh velocity is known the space-time slab can be constructed by knowing the position of mesh nodes at time t_{n+1} with the following relation

$$(x, y)(t_{n+1}) = (x, y)(t_n) + (v_x^m, v_y^m)\ \Delta t \tag{4.21}$$

Here, $(x, y)(t_{n+1})$ and $(x, y)(t_n)$ are the node coordinates at time levels t_{n+1} and t_n respectively, (v_x^m, v_y^m) is the mesh velocity and $\Delta t = t_{n+1} - t_n$. In the context of the deforming domain, the problems are divided into two categories. The first one deals with the problems in which the fluid domain movement is affected by some solid object. Fluid-structure interaction problems fall in this category. The second category deals with the free surface flow problems, in which the movement of boundary nodes situated at the free surface is driven by the internal dynamics of the fluid. A segregated algorithm is employed to solve the fluid flow and the mesh deformation problems separately at each time step. To begin the procedure, it is considered that for a general nth space-time slab Q_n, $n = 0, 1, \ldots, N-1$, the flow domain $\Omega(t_n)$ and flow variables are known at time t_n. The following algorithm is followed.

Step 1. Calculate the mesh deformation at the moving boundaries. In case of fluid-structure interaction, this comes directly from the structure (specified/ computed) and in case of free flows, it is computed from the fluid velocities.

Step 2. Solve the elasticity equations for the mesh velocity $\boldsymbol{v}_n^m$ by specifying the deformation, computed in step 1, as Dirichlet boundary conditions.

Step 3. Obtain the new domain $\Omega(t_{n+1})$ by transforming the vertices of the domain $\Omega(t_n)$ via equation (4.21) and generate the space-time slab.

Step 4. As explained in the previous chapter, solve the Navier-Stokes equations by space-time finite element method by substituting the value of $\boldsymbol{v}_n^m$. The computations are performed over the domain $\Omega(t_{n+1})$. Compute the fluid flow variables pressure, velocity, temperature and composition (in case of multicomponent fluid flows) at time t_{n+1}.

Step 5. Check if $n = N - 1$, otherwise go to Step 1 with n = n+1.

The above-defined algorithm is valid for both single and multi-component fluid flows. In the next section, the algorithm is tested on a number of benchmark cases.

4.5 Numerical Examples

To show the accuracy and efficiency of the space-time finite element method for deforming domain problems, three numerical benchmarks are presented. The first numerical example, the horizontal moving cylinder is for rigid translational motion. The next two numerical examples: broken dam and solitary wave propagation present the free surface flows. For the finite element basis functions, the bilinear functions in space and linear functions in time are used. For all test cases, the spatial meshes are made of the unstructured quadrilateral elements and time slabs are formed simply by moving the spatial meshes in time. As pointed out earlier, the domain velocity is computed with the elastic deformation method and the problems are solved with the above defined segregated algorithm. The problems with detailed description are given below.

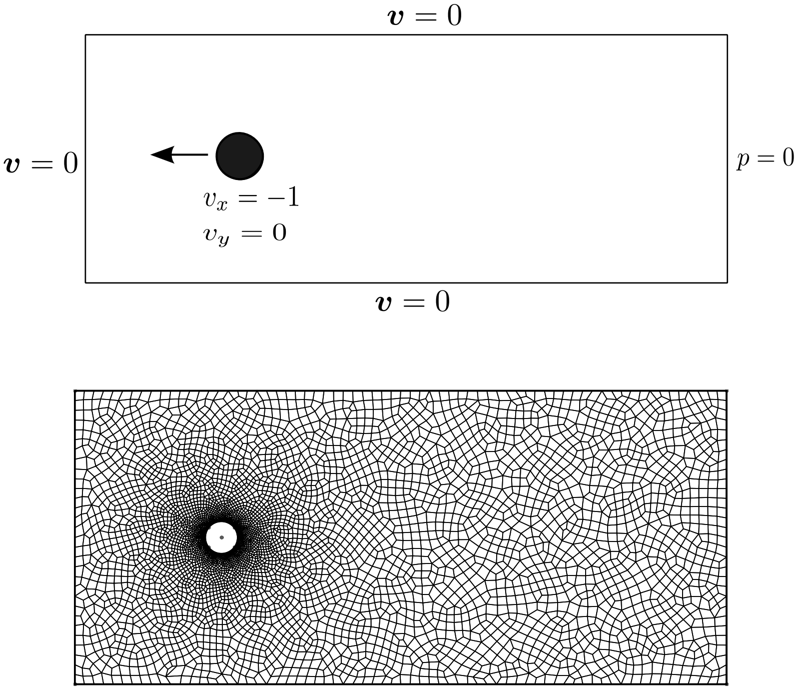

Figure 4.6: Horizontal moving cylinder: problem description and computation mesh

4.5.1 Horizontal moving cylinder

In this problem, the algorithm is tested on a rigid moving object and compared with the problem in which the mesh is stationary but subject to a uniform flow. This test case represents one-way coupled fluid-structure interaction problem, in which the fluid flow is affected by the movement of the solid object but the fluid flow has no impact on the solid. This problem has been formulated in [16, 188, 193]. In this test case, a circular rigid cylinder moving at Mach 0.01 and Reynolds number 40 is introduced in a stationary fluid domain at time t = 0. The problem is displayed in figure (4.6). The Reynolds number is based on the mean stream density of the fluid and the velocity and diameter of the cylinder. The computational domain covers an area $-4.5 \leq x \leq 15.5$ and $-4.5 \leq y \leq 4.5$, with a unit diameter cylinder centred at x = 0 and y = 0. An unstructured mesh comprising 5353 elements is generated to solve this problem, figure (4.6). In order to capture the accuracy and details of the flow, the mesh is more refined in the vicinity of the boundary of the cylinder. The mesh is being moved rigidly with the cylinder. At left and horizontal walls, velocity is set to zero. At the surface of cylinder the no-slip condition $v_1 = -1$ and $v_2 = 0$ is prescribed. At the right wall, zero pressure is imposed. A constant time step of 1.e-2 is set for this simulation. Figure (4.7) shows the temporal evolution of mesh deformation and the horizontal component of velocity at time t = 0, 1 and $2s$. Flow streamlines and v_2 at time t = 0, 1 and $2s$ are displayed in figure (4.8). To validate the results, the numerical solution is compared with the steady-state flow past a fixed cylinder at Reynolds number 40. In Figure (4.9) the pressure contours are compared at time t = 1 and 2 s. It is evident that the two solutions are in very close agreement.

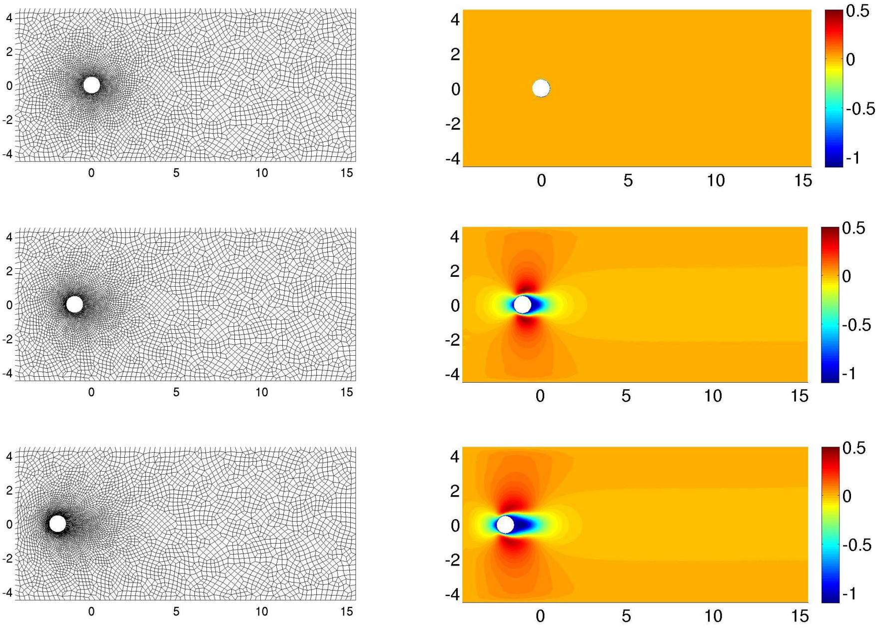

Figure 4.7: Horizontal moving cylinder: the deforming mesh and v_1 (m/s) at time t = 0, 1 and $2s$.

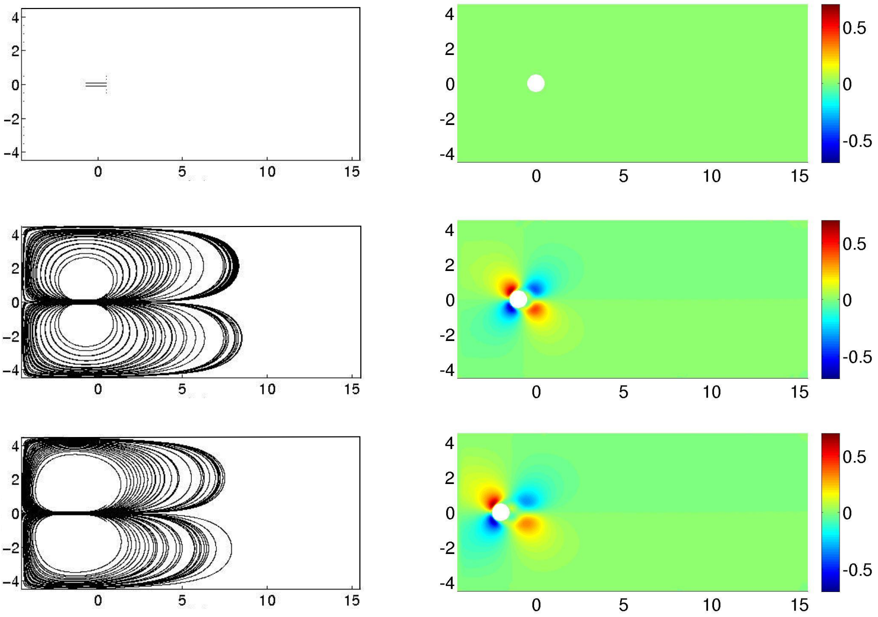

Figure 4.8: Horizontal moving cylinder: streamlines and v_2 (m/s) at time t = 0, 1 and 2s.

4.5.2 Broken dam

This problem is solved in [66] using an Arbitrary Lagrangian Eulerian (ALE) finite element method. In [144] authors used a characteristic -based split algorithm and solved the flow problem in the Lagrangian coordinate system. In [207] a splitting method for the time discretization is used and the technique is similar to the volume of fluid (VOF) method. In the last chapter, this test case was discussed with a column of standing water and air inside a container. The problem was solved with a multicomponent fluid flow model in which the constitutive equations for the flow field were written in the Eulerian form. The numerical solution was computed on a fixed mesh and the interface between the water and air was tracked by solving the mass conservation equations for both components. Here, the same problem is solved from ALE point of view with moving mesh. In this problem, only water is considered as a fluid with the free surface on two sides of the domain boundary. As soon as the water column changes its shape and boundary nodes start to

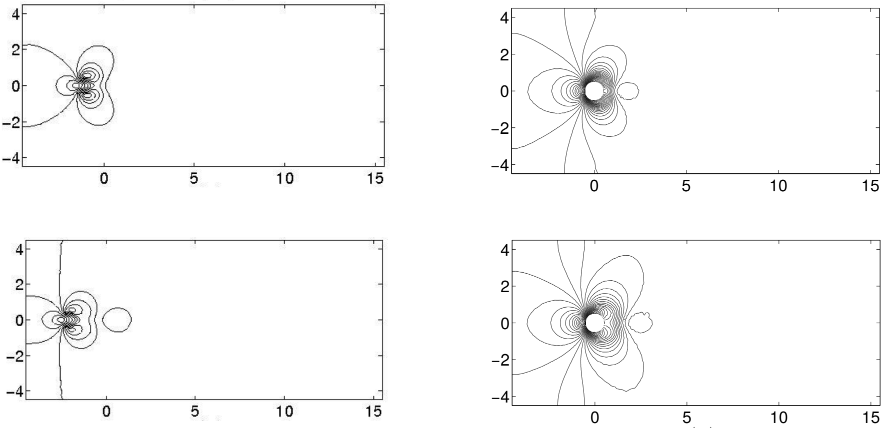

Figure 4.9: Horizontal moving cylinder: the pressure (Pa) contours (row wise) at time t = 1 and 2 *s*. On left hand side the current results with moving mesh and on right hand side the steady state solution of the fixed cylinder.

move, the respective changes are updated for the rest of the computational mesh by employing the mesh updation technique. The boundary mesh nodes are moved in the Lagrangian way while the interior mesh nodes follow an arbitrary Eulerian fashion.

To begin with the problem, once again, a block of water is kept at rest in a container in the initial stage using a thin paper film. In this case, both top and right side walls of the container are removed to provide the infinite space to the fluid flow. Instantaneously, at time t = 0, the paper film is removed and the water spreads out under the influence of gravity. The geometry of the solution domain is shown in figure (4.10). In the Figure, Γ_h and Γ_v represent the horizontal and vertical walls of the container, where the fluid is allowed to slip. Whereas, Γ_f represents the free surface boundary of the water column. The base length and height of the block of water are set to 3.5 m and 7 m respectively. The computational mesh used to solve this problem consists 7004 elements and is displayed in figure (4.10). The top-right and bottom-right corners are critical regions where mesh deforms very rapidly. To keep the mesh in reasonable shape for later time steps and to avoid remeshing, the initial mesh is constructed by refining the both right corners. The density of water is taken to be $\rho = 1$ kg/m^3, and the dynamic

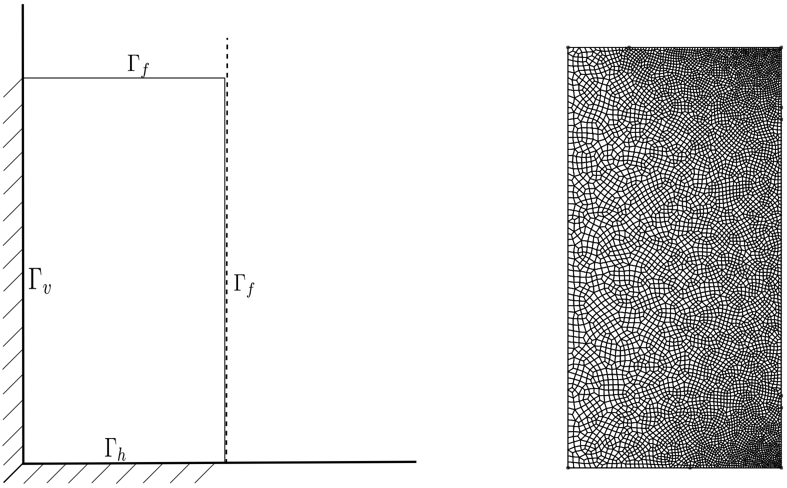

Figure 4.10: Broken dam: the problem description and computational mesh.

viscosity is $\mu = 0.01$ kg/ms. The gravity is set to 1m/s^2. For fluid as initial conditions a gravitational pressure profile was set and velocity is set to zero. The temperature is kept constant at 298 K throughout the simulation. For the fluid flow, at Γ_h and Γ_v the slip boundary conditions are applied and at free surface Γ_f the traction free conditions are prescribed. The latter may be changed to the fixed pressure and zero normal gradients of the velocities. For the elastostatic problem, the initial displacements are set to zero and at Γ_f the domain velocity is set equal to the fluid velocity. At Γ_h the vertical displacement and at Γ_v the horizontal displacement is set to zero. The time step for the numerical simulation is set to 1.e-3.

The gravity causes the water column to the left of the reservoir to seek the lowest possible level of potential energy. Thus, the column will collapse and eventually come to rest. The initial stages of the flow are dominated by inertia forces with viscous effects increasing as the water comes to rest. On such a large scale, the effect of surface tension forces is unimportant and therefore not considered in the model. Figure (4.11) shows the mesh and v_2 at various time levels. It is clear from the figure that mesh is moving very smoothly in response to the fluid velocity at the boundaries. No remeshing was done during this simulation and computations were performed up to

5s. Despite a large distortion of mesh elements, the flow was accurately computed. Figure (4.12) shows the pressure and horizontal component of the velocity at various time levels.

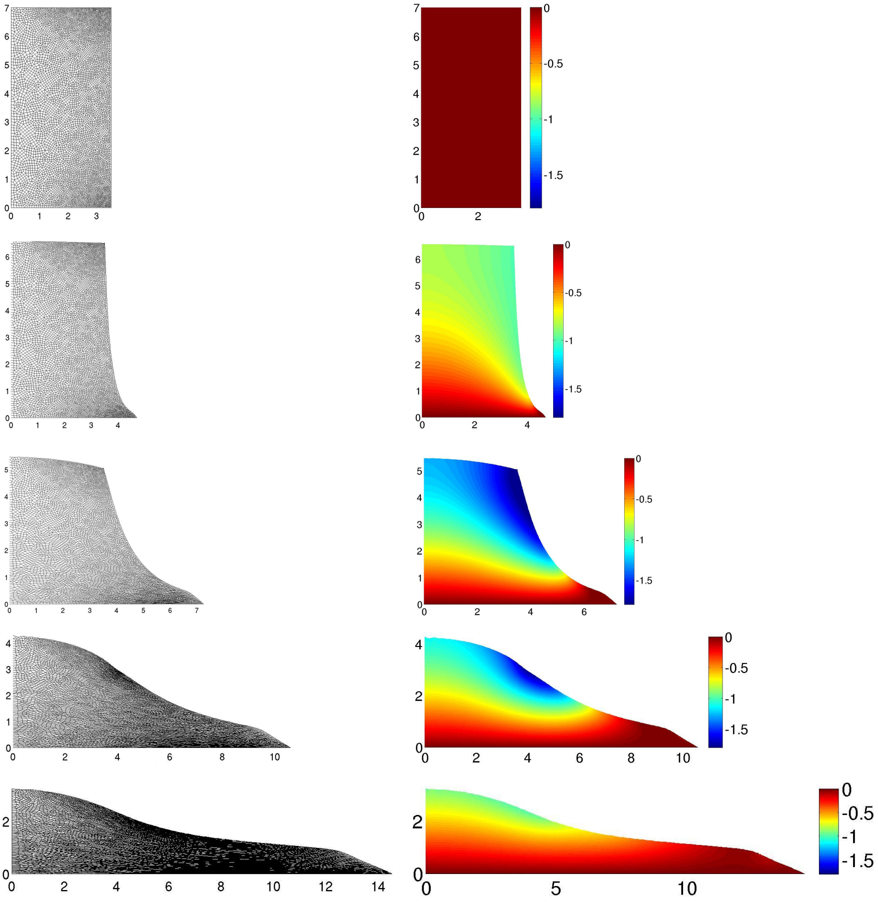

Figure 4.11: Broken dam: mesh and v_2 (m/s) at time t = 0, 1, 2, 3 and 4s.

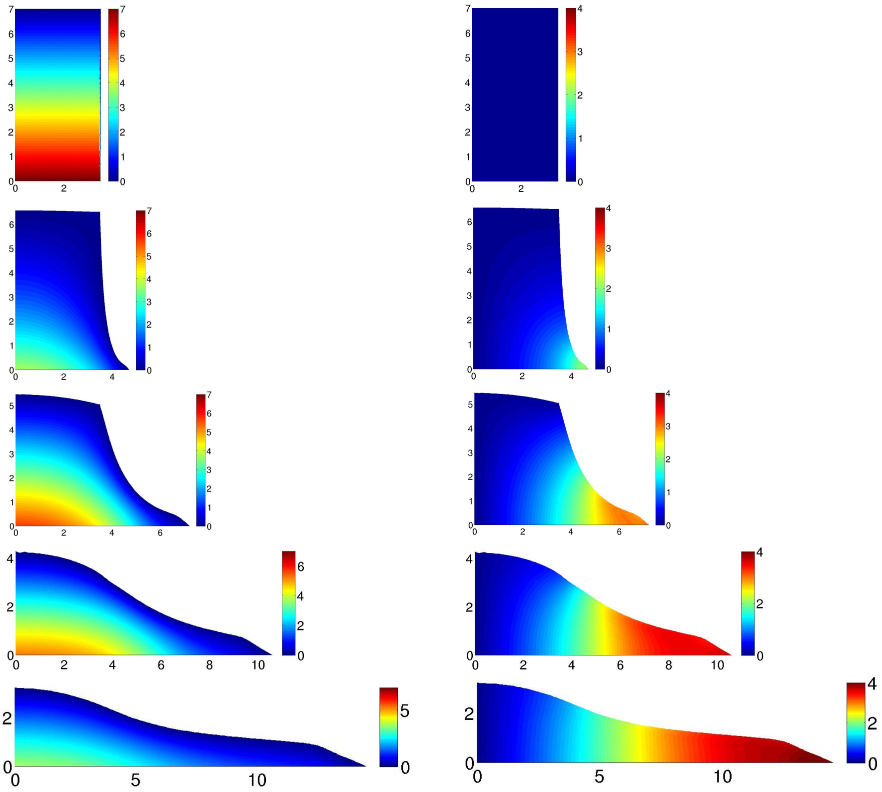

Figure 4.12: Broken dam: pressure and v_1 (m/s) at time t = 0, 1, 2, 3 and $4s$.

The numerical results are validated by the quantitative comparison with the experimental measurements obtained for the early stages of this experiment. The dimensionless position x/2H (where 2H = 3.5, is the initial length of the dam) of the liquid front along the bottom of the cavity, versus the dimensionless time $t\sqrt{g/H}$ is compared in figure (4.13). The horizontal position reached by the waterfront corresponds well with the experimental measurements and the numerical results obtained by the multicomponent fluid flow model.

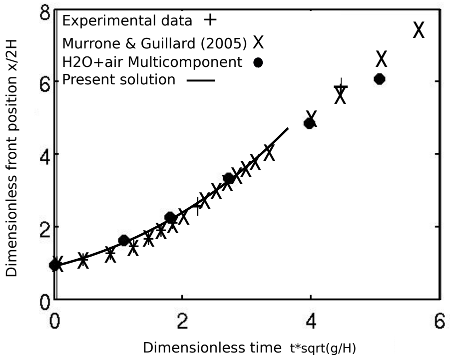

Figure 4.13: Broken dam: comparison of the numerical results.

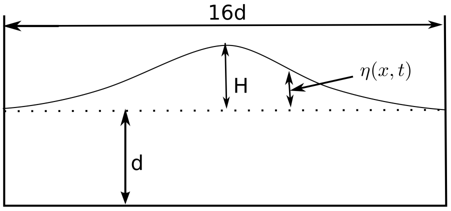

Figure 4.14: Solitary wave propagation: problem description

4.5.3 Solitary wave propagation

This numerical problem is extensively studied by many authors in the past to check the accuracy of the flow model for free surface problems [16,66,144,175]. The problem consists of the motion of a viscous incompressible fluid in a tank with three fixed walls (bottom and both vertical walls). The upper surface is free to deform. The gravitational force controls the motion of the wave. The model problem is presented by the figure (4.14). To model this problem the domain parameters are set as d = 10 and H = 2. The computational domain for this problem covers $-80 \leq x \leq 80$ in horizontal direction and $0 \leq y \leq \eta$. Where η represents the initial profile of the wave at free surface and is given by

$$\eta = d + H\ sech^2\left(\sqrt{\frac{3H}{4d^3}}x\right) \tag{4.22}$$

The computational mesh consists 5276 unstructured quadrangle elements with 5560 nodes. The mesh is more refined near the free surface. Fluid density and viscosity are assumed constant and set to 1 kg/m^3 and 1 kg/ms respectively. A gravitational acceleration of magnitude 9.8 m/s^2 acts vertically in the downward direction. The initial conditions for this problem are taken from the approximations given by Laitone [58]. More precisely, the initial conditions are given as

$$v_1 = \sqrt{gd}\left(\frac{H}{d}\right) sech^2\left(\sqrt{\frac{3H}{4d^3}}x\right) \tag{4.23}$$

$$v_2 = \sqrt{\frac{3g}{d}}\left(\frac{H}{d}\right)^{\frac{3}{2}} y\ sech^2\left(\sqrt{\frac{3H}{4d^3}}x\right) tanh\left(\sqrt{\frac{3H}{4d^3}}x\right) \tag{4.24}$$

At all walls of the container the free-slip boundary conditions are prescribed and at the free surface, the traction free condition is imposed. As regards the boundary conditions for mesh velocity, there are several options. Usually, it is preferred to move the mesh only in the normal direction of the flow. However, in this simulation, both the tangential and normal components of the mesh velocity are assigned. The time step used to perform this simulation is set to 0.001s.

Temporal evolution of the wave travelling is shown in the figure (4.15). The wave reaches to the right vertical wall at t = 7.6 s and stops its motion to the right and begins to move towards left. The simulation is continued until the water wave reaches to its initial position at x=0. The reflected wave takes approximately the same time to travel back to its initial position. Figure (4.16) shows the horizontal component of velocity at various times. The maximum run-up height of the right wall is 14.4 and can be computed from the following analytical relation

$$\frac{R_{max}}{d} = 2\left(\frac{H}{d}\right) + \frac{1}{2}\left(\frac{H}{d}\right)^2 + O\left(\frac{H}{d}\right) \tag{4.25}$$

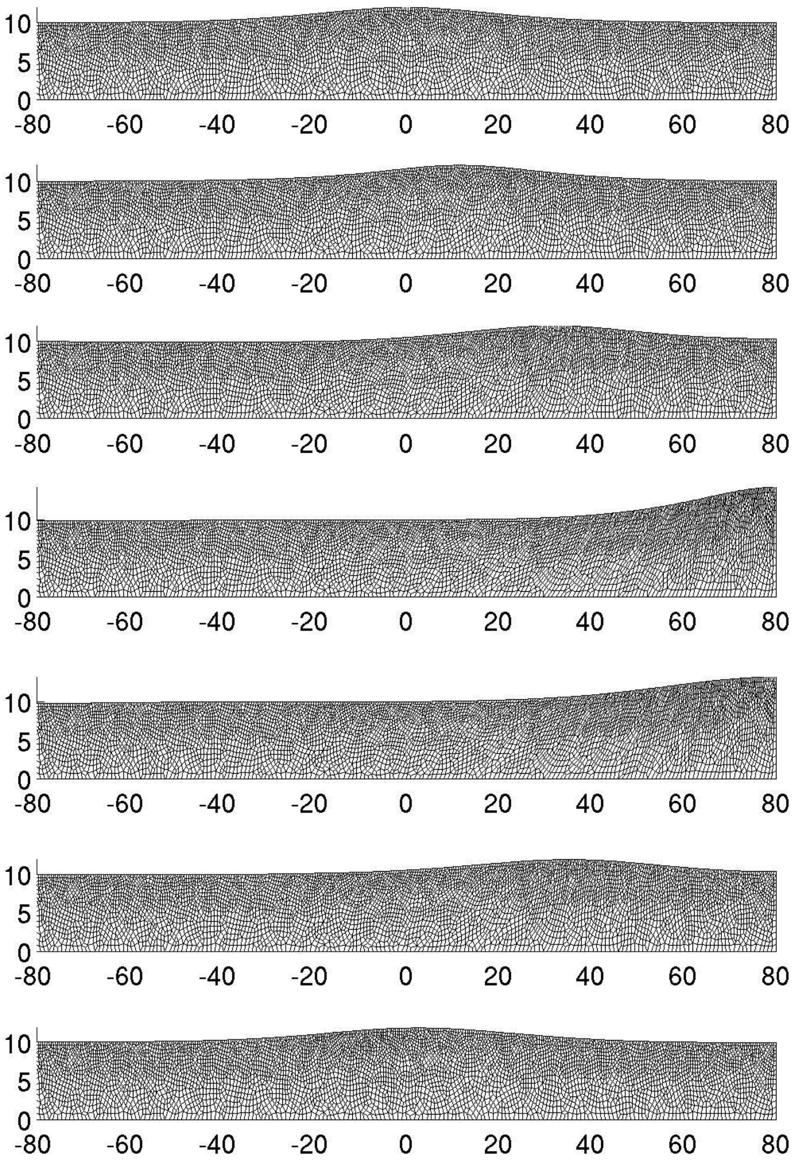

Figure 4.15: Solitary wave propagation: temporal evolution of mesh (from top) at time t = 0, 1, 3, 5, 7.6, 9, 12 and 15 s.

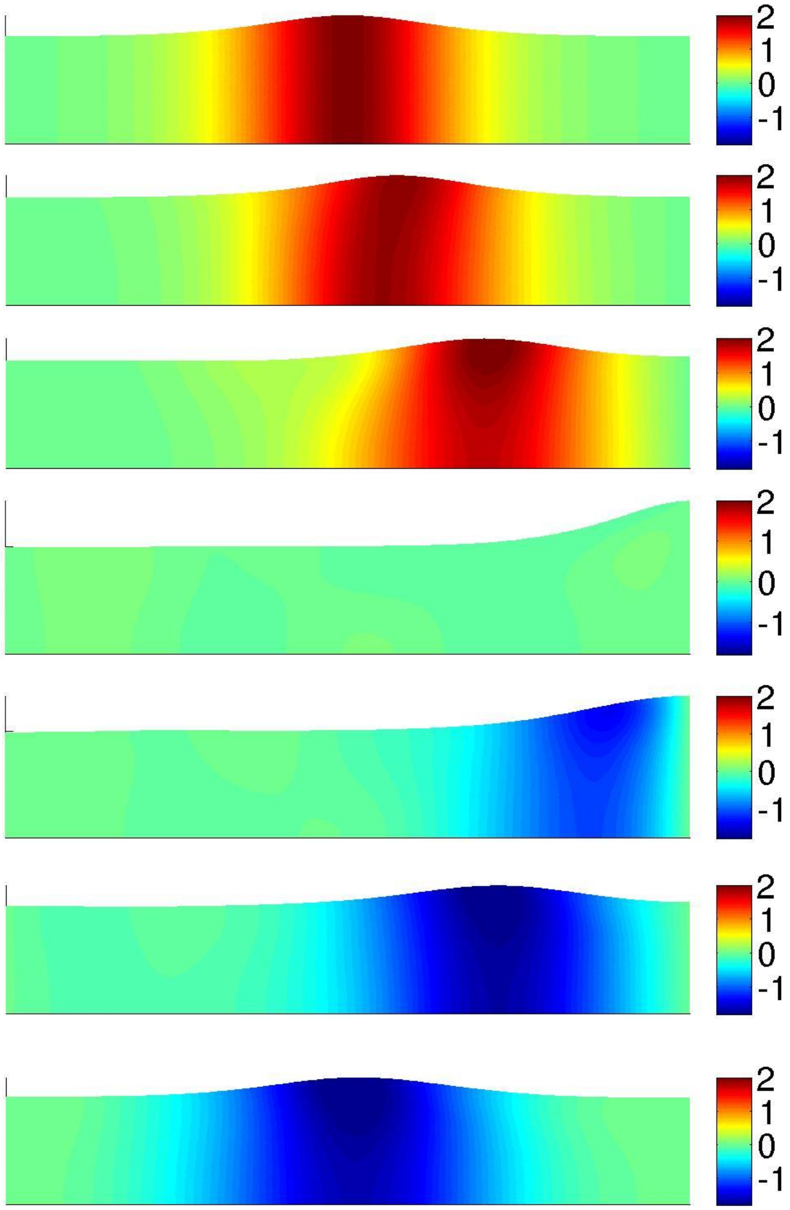

Figure 4.16: Solitary wave propagation: the horizontal velocity (m/s) (from top) at t = 0, 1, 3, 7.6, 9, 12 and 15 *s*.

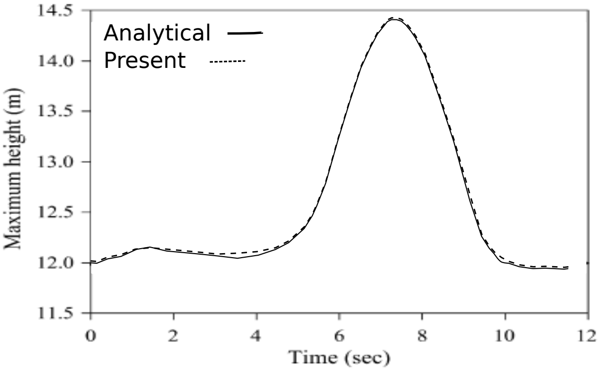

Figure 4.17: Solitary wave propagation: comparison of numerical results with analytical one.

The computed maximum run-up height is compared with the analytical one in figure (4.17). The numerical and analytic results are identical. Thus, verifying that the numerical model works well for the free surface flow problems.

Chapter 5

Structural mechanics

Introduction

This chapter covers the numerical technique to solve the structural mechanics equations. Sections 5.1 and 5.2 present the strong and weak form of the boundary value problem. In section 5.3 the linear viscoelastic model is presented. Sections 5.4 and 5.5 describe the spatial and time discretization of the problem respectively. Section 5.6 presents the linear elastodynamics as the limiting case of linear visco-elastodynamics. In section 5.7, the numerical scheme is verified on three problems.

5.1 Strong form

The strong form of structural mechanics equations is given by

$$\rho \ddot{\boldsymbol{u}} = \boldsymbol{\nabla} \cdot \boldsymbol{\sigma} + \rho \boldsymbol{f} \qquad \text{in } \ \Omega \times (0, T) \tag{5.1}$$

$$\begin{aligned} \boldsymbol{u} &= \boldsymbol{g} && \text{on } \ \Gamma_D \times (0,T) \\ \boldsymbol{\sigma} \cdot \boldsymbol{n} &= \boldsymbol{t} && \text{on } \ \Gamma_N \times (0,T) \\ \boldsymbol{u} &= \boldsymbol{u}_0 && \text{at } \ t = 0 \\ \dot{\boldsymbol{u}} &= \dot{\boldsymbol{u}}_0 && \text{at } \ t = 0 \end{aligned}$$

where Γ_D and Γ_N are the Dirichlet and the Neumann parts of the boundary domain respectively with $\Gamma = \Gamma_D \cup \Gamma_N$ and $\Gamma_D \cap \Gamma_N = \phi$. $\boldsymbol{f}$ is the body force. $\boldsymbol{g}$ and $\boldsymbol{t}$ are prescribed boundary displacements and tractions on Dirichlet and Neumann boundary parts respectively. $\boldsymbol{u}_0$ and $\dot{\boldsymbol{u}}_0$ are the given initial displacement and velocity respectively. ρ is the specified density.

5.2 Weak formulation

The trial space $\mathcal{S}$ and the weighting space $\mathcal{V}$ are defined as

$$\mathcal{S}_t = \{\boldsymbol{u}(.,t) \mid \boldsymbol{u}(\boldsymbol{x},t) \in \boldsymbol{H}^1(\Omega),\ \boldsymbol{u}(\boldsymbol{x},t)|_{\Gamma_D} = \boldsymbol{g}(\boldsymbol{x},t)\} \tag{5.2}$$

and

$$\mathcal{V} = \{\boldsymbol{w} \mid \boldsymbol{w} \in \boldsymbol{H}^1(\Omega),\ \boldsymbol{w}|_{\Gamma_D} = 0\} \tag{5.3}$$

The definition of trial function space varies as a function of time because the boundary conditions can evolve in time. The variational formulation of the problem is obtained by multiplying the equation (5.1) by a weighting function and integrating over the domain: given $\boldsymbol{f} : \Omega \rightarrow \mathbb{R}$, $\boldsymbol{g} : \Gamma_D \rightarrow \mathbb{R}$ and $\boldsymbol{t} : \Gamma_N \rightarrow \mathbb{R}$ find $\boldsymbol{u} \in \mathcal{S}$ such that for all $\boldsymbol{w} \in \mathcal{V}$

$$\int_\Omega \boldsymbol{w}\rho\ \ddot{\boldsymbol{u}}\ d\Omega - \int_\Omega \boldsymbol{w}\boldsymbol{\nabla} \cdot \boldsymbol{\sigma} - \int_\Omega \boldsymbol{w}\rho\ \boldsymbol{f}\ d\Omega = 0 \tag{5.4}$$

Integrating by parts the second term of the above expression and using the Gauss theorem to transform the volume integral into a surface integral, we obtain

$$\int_\Omega \boldsymbol{w}\rho\ \ddot{\boldsymbol{u}}\ d\Omega + \int_\Omega \epsilon(\boldsymbol{w}) \colon \boldsymbol{\sigma}\ d\Omega - \int_\Gamma \boldsymbol{w}\ \boldsymbol{t}\ d\Gamma - \int_\Omega \boldsymbol{w}\rho\ \boldsymbol{f}\ d\Omega = 0 \tag{5.5}$$

5.3 Linear-viscoelastic model

As defined in (2.58) and (2.62) for linear viscoelastic model the stress is modelled as the sum of instantaneous and historical contributions.

$$\boldsymbol{\sigma}(t) = \mathbb{C}_\infty \boldsymbol{\epsilon}(t) + \sum_{i=1}^{n} \boldsymbol{\sigma}_i(t) \tag{5.6}$$

$$\boldsymbol{\sigma}_i(t) = \int_0^t \mathbb{C}_i e^{\left(\frac{s-t}{\tau_i}\right)} \frac{d\boldsymbol{\epsilon}(s)}{ds} ds \tag{5.7}$$

The solution of the viscoelastic model is performed on discretized time levels t_k. Assuming that all solutions are available up to time t_n, the aim is to compute the solution for time t_{n+1}. A solution of the general form requires the summation over all previous time steps for each new time. By using the generalised Maxwell model the solution can be written in the form of a recursion formula in which each new solution is computed by a simple update of the previous solution. If t_{n+1} and t_n are the current and previous time steps and step size is defined as $\Delta t = t_{n+1} - t_n$.

$$\boldsymbol{\sigma}_i(t_{n+1}) = \int_0^{t_{n+1}} \mathbb{C}_i e^{\left(\frac{s-t_{n+1}}{\tau_i}\right)} \frac{\partial \boldsymbol{\epsilon}(s)}{\partial s} ds \tag{5.8}$$

$$= e^{-\left(\frac{\Delta t}{\tau_i}\right)} \int_0^{t_n} \mathbb{C}_i e^{\left(\frac{s-t_n}{\tau_i}\right)} \frac{\partial \boldsymbol{\epsilon}(s)}{\partial s} ds + \int_{t_n}^{t_{n+1}} \mathbb{C}_i e^{\left(\frac{s-t_{n+1}}{\tau_i}\right)} \frac{\partial \boldsymbol{\epsilon}(s)}{\partial s} ds \tag{5.9}$$

$$= e^{-\left(\frac{\Delta t}{\tau_i}\right)} \boldsymbol{\sigma}_i(t_n) + \int_{t_n}^{t_{n+1}} \mathbb{C}_i e^{\left(\frac{s-t_{n+1}}{\tau_i}\right)} \frac{\partial \boldsymbol{\epsilon}(s)}{\partial s} ds \tag{5.10}$$

$$= e^{-\left(\frac{\Delta t}{\tau_i}\right)} \boldsymbol{\sigma}_i(t_n) + \mathbb{C}_i \left(\frac{1 - e^{-\left(\frac{\Delta t}{\tau_i}\right)}}{\frac{1}{\tau_j}} \right) \left(\frac{\boldsymbol{\epsilon}(t_{n+1}) - \boldsymbol{\epsilon}(t_n)}{\Delta t} \right) \tag{5.11}$$

Substituting (5.11) in (5.6) the stress at time t_{n+1} is given by

$$\boldsymbol{\sigma}(t_{n+1}) = \mathbb{C}_\infty \boldsymbol{\epsilon}(t_{n+1}) + \sum_{i=1}^{n} \left[e^{-\left(\dfrac{\Delta t}{\tau_j}\right)} \boldsymbol{\sigma}_i(t_n) + \mathbb{C}_i \left(\frac{1 - e^{-\left(\frac{\Delta t}{\tau_j}\right)}}{\frac{1}{\tau_j}} \right) \left(\frac{\boldsymbol{\epsilon}(t_{n+1}) - \boldsymbol{\epsilon}(t_n)}{\Delta t} \right) \right] \tag{5.12}$$

$\mathbb{C}$ is the elastic tensor matrix. For isotropic material, it has the form

$$\mathbb{C} = \frac{E}{(1+\nu)(1-2\nu)} \begin{bmatrix} 1-\nu & 1 & 1 & 0 & 0 & 0 \\ 1 & 1-\nu & 1 & 0 & 0 & 0 \\ 1 & 1 & 1-\nu & 0 & 0 & 0 \\ 0 & 0 & 0 & \dfrac{1-2\nu}{2} & 0 & 0 \\ 0 & 0 & 0 & 0 & \dfrac{1-2\nu}{2} & 0 \\ 0 & 0 & 0 & 0 & 0 & \dfrac{1-2\nu}{2} \end{bmatrix} \tag{5.13}$$

Here E is the elastic modulus and ν is the Poisson's ratio. The strain vector $\boldsymbol{\epsilon}(\boldsymbol{u})$ and weighted strain vector $\boldsymbol{\epsilon}(\boldsymbol{w})$ are defined as

$$\boldsymbol{\epsilon}(\boldsymbol{u}) = \begin{bmatrix} u_{1,1} \\ u_{2,2} \\ u_{3,3} \\ u_{2,3} + u_{3,2} \\ u_{3,1} + u_{1,3} \\ u_{1,2} + u_{2,1} \end{bmatrix} \qquad \boldsymbol{\epsilon}(\boldsymbol{w}) = \begin{bmatrix} w_{1,1} \\ w_{2,2} \\ w_{3,3} \\ w_{2,3} + w_{3,2} \\ w_{3,1} + w_{1,3} \\ w_{1,2} + w_{2,1} \end{bmatrix} \tag{5.14}$$

5.4 Space discretization

To write the weak formulation of the problem into a system of algebraic equations, the Galerkin's method is used. The semi-discrete approach has been followed. Let $\mathcal{S}^h \subset \mathcal{S}$ and $\mathcal{V}^h \subset \mathcal{V}$ be the finite dimensional subspaces. The trial function $\boldsymbol{u}^h \in \mathcal{S}^h$ and weighting function $\boldsymbol{w}^h \in \mathcal{V}^h$ are defined as

$$\boldsymbol{u}^h = \sum_a N_a u_a \qquad \boldsymbol{w}^h = \sum_a N_a w_a \tag{5.15}$$

The above can be written in matrix notations

$$\boldsymbol{u}^h = \boldsymbol{N}\boldsymbol{u} \qquad \boldsymbol{w}^h = \boldsymbol{N}\boldsymbol{w} \tag{5.16}$$

Where

$$\boldsymbol{N} = \begin{bmatrix} N_a & 0 & 0 \\ 0 & N_a & 0 \\ 0 & 0 & N_a \end{bmatrix} \tag{5.17}$$

The strain vector $\boldsymbol{\epsilon}(\boldsymbol{u}^h)$ and weighted strain vector $\boldsymbol{\epsilon}(\boldsymbol{w}^h)$ can be written in the form

$$\boldsymbol{\epsilon}(\boldsymbol{u}^h) = \boldsymbol{B}\boldsymbol{u} \tag{5.18}$$

$$\boldsymbol{\epsilon}(\boldsymbol{w}^h) = \boldsymbol{B}\boldsymbol{w} \tag{5.19}$$

where

$$\boldsymbol{B} = \begin{bmatrix} N_{a,1} & 0 & 0 \\ 0 & N_{a,2} & 0 \\ 0 & 0 & N_{a,3} \\ 0 & N_{a,3} & N_{a,2} \\ N_{a,3} & 0 & N_{a,1} \\ N_{a,2} & N_{a,1} & 0 \end{bmatrix} \tag{5.20}$$

Substitution of $\boldsymbol{u}^h$ and $\boldsymbol{w}^h$ in equation (5.5) results in the semi-discrete Galerkin formulation: find $\boldsymbol{u}^h \in \mathcal{S}^h$ such that for all $\boldsymbol{w}^h \in \mathcal{V}^h$

$$\int_\Omega \boldsymbol{w}^h \rho\, \ddot{\boldsymbol{u}}^h \, d\Omega + \int_\Omega \epsilon(\boldsymbol{w}^h) : \boldsymbol{\sigma} \, d\Omega - \int_\Gamma \boldsymbol{w}^h \, \boldsymbol{t}^h \, d\Gamma - \int_\Omega \boldsymbol{w}^h \rho \, \boldsymbol{f}^h \, d\Omega = 0 \tag{5.21}$$

Substituting (5.12), (5.18) and (5.19) in (5.21) one obtains

$$\boldsymbol{\sigma}(t_{n+1}) = \mathbb{C}\boldsymbol{B}\boldsymbol{u}(t_{n+1}) + \sum_{i=1}^{n} \left[e^{-\left(\frac{\Delta t}{\tau_i}\right)} \boldsymbol{\sigma}_i(t_n) + a_i \mathbb{C}\boldsymbol{B}\big(\boldsymbol{u}(t_{n+1}) - \boldsymbol{u}(t_n)\big) \right] \tag{5.22}$$

$$= \Big(1 + \sum_{i=1}^{n} a_i\Big)\mathbb{C}\boldsymbol{B}\boldsymbol{u}(t_{n+1}) - \Big(\sum_{i=1}^{n} a_i\Big)\mathbb{C}\boldsymbol{B}\boldsymbol{u}(t_n) + \sum_{i=1}^{n} e^{-\left(\frac{\Delta t}{\tau_i}\right)} \boldsymbol{\sigma}_i(t_n) \tag{5.23}$$

where

$$a_i = \frac{1 - e^{-\left(\frac{\Delta t}{\tau_i}\right)}}{\frac{\Delta t}{\tau_i}} = 1 - \frac{1}{2!}\left(\frac{\Delta t}{\tau_i}\right) + \frac{1}{3!}\left(\frac{\Delta t}{\tau_i}\right)^2 - \frac{1}{4!}\left(\frac{\Delta t}{\tau_i}\right)^3 \dots \tag{5.24}$$

The matrix form of Galerkin formulation given by equation (5.21) is

$$\boldsymbol{M}\ddot{\boldsymbol{u}}(t_{n+1}) + \boldsymbol{M}_2\boldsymbol{u}(t_{n+1}) - \boldsymbol{M}_1\boldsymbol{u}(t_n) + \boldsymbol{V}_h(t_{n+1}) - \boldsymbol{F}(t_{n+1}) = 0 \quad (5.25)$$

Where $\boldsymbol{u}(t_{n+1})$ and $\boldsymbol{u}(t_n)$ are the vectors of nodal displacements at current and previous time steps. $\boldsymbol{M}$ is the mass matrix and defined as

$$\boldsymbol{M} = \int_\Omega \boldsymbol{N}^T \rho \boldsymbol{N} d\Omega \quad (5.26)$$

$\boldsymbol{M}_2$ is the tangent stiffness matrix and defined as

$$\boldsymbol{M}_2 = \boldsymbol{K} + \boldsymbol{M}_1 \quad (5.27)$$

where

$$\boldsymbol{K} = \int_\Omega \boldsymbol{B}^T \mathbb{C} \boldsymbol{B} d\Omega \quad (5.28)$$

$$\boldsymbol{M}_1 = \int_\Omega \left(\sum_{i=1}^{n} a_i \right) \boldsymbol{B}^T \mathbb{C} \boldsymbol{B} d\Omega \quad (5.29)$$

Here $\boldsymbol{M}_1$ is the history stiffness matrix. $\boldsymbol{V}_h$ is the history vector at current time step and defined as

$$\boldsymbol{V}_h = \int_\Omega \boldsymbol{B}^T \left[\sum_{i=1}^{n} e^{-\left(\frac{\Delta t}{\tau_i}\right)} \boldsymbol{\sigma}_i(t_n) \right] d\Omega \quad (5.30)$$

$\boldsymbol{\sigma}_i(t_n)$ can be computed in terms of previous history and deformations as follow

$$\boldsymbol{\sigma}_i(t_n) = e^{-\left(\frac{\Delta t}{\tau_i}\right)} \boldsymbol{\sigma}_i(t_{n-1}) + a_i \mathbb{C} \boldsymbol{B} \Big(\boldsymbol{u}(t_n) - \boldsymbol{u}(t_{n-1}) \Big) \tag{5.31}$$

$\boldsymbol{F}$ is the external force vector and defined as the sum of body forces and boundary tractions.

$$\boldsymbol{F} = \int_\Omega \boldsymbol{N}^T \rho \boldsymbol{f}^h d\Omega + \int_\Gamma \boldsymbol{N}^T \boldsymbol{t}^h d\Gamma \tag{5.32}$$

5.5 Generalized α time integration method

The semi discrete system of equations (5.25) can be solved with variety of techniques [196]. For linear and nonlinear transient dynamics, a variant of the Newmark-Beta time integrator is used. The method is known as the generalized alpha method and is proposed by Chung and Hulbert [92]. Let the time interval $[0, T]$ is partitioned into subintervals. A time step $\Delta t = t_{n+1} - t_n$ is defined. Denoting $\boldsymbol{a}_n \approx \ddot{\boldsymbol{u}}(t_n)$, $\boldsymbol{v}_n \approx \dot{\boldsymbol{u}}(t_n)$ and $\boldsymbol{u}_n \approx \boldsymbol{u}(t_n)$, The iterations are performed within each time step, n, in order to find $(\boldsymbol{u}_{n+1}, \boldsymbol{v}_{n+1}, \boldsymbol{a}_{n+1})$. At the beginning of each time step the iterative counter i is set to 0 and the unknowns are initialized by the predictors. Two general choices of the predictor are:

Constant velocity predictor

$$\boldsymbol{v}^0_{n+1} = \boldsymbol{v}_n \tag{5.33}$$

$$\boldsymbol{a}^0_{n+1} = \frac{\gamma - 1}{\gamma} \boldsymbol{a}_n \tag{5.34}$$

$$\boldsymbol{u}^0_{n+1} = \boldsymbol{u}_n + \Delta t \ \boldsymbol{v}_n + \frac{(\Delta t)^2}{2} \Big[(1 - 2\beta) \boldsymbol{a}_n + 2\beta \boldsymbol{a}^0_{n+1} \Big] \tag{5.35}$$

Zero acceleration predictor

$$\boldsymbol{a}_{n+1}^{0} = 0 \tag{5.36}$$

$$\boldsymbol{v}_{n+1}^{0} = \boldsymbol{v}_n + (1-\gamma)\Delta t\ \boldsymbol{a}_n \tag{5.37}$$

$$\boldsymbol{u}_{n+1}^{0} = \boldsymbol{u}_n + \Delta t\ \boldsymbol{v}_n + (1-2\beta)\frac{(\Delta t)^2}{2}\boldsymbol{a}_n \tag{5.38}$$

The constant velocity predictor is preferred for fluid-structure interaction problems and the zero acceleration predictor is preferred for linear analysis. There are also other possibilities. For any choice, $\boldsymbol{u}_{n+1}$, $\boldsymbol{v}_{n+1}$ and $\boldsymbol{a}_{n+1}$ must satisfy the Newmark formulas

$$\boldsymbol{u}_{n+1} = \boldsymbol{u}_n + \Delta t\ \boldsymbol{v}_n + \frac{(\Delta t)^2}{2}\Big[(1-2\beta)\boldsymbol{a}_n + 2\beta\boldsymbol{a}_{n+1}\Big] \tag{5.39}$$

$$\boldsymbol{v}_{n+1} = \boldsymbol{v}_n + \Delta t\big[(1-\gamma)\boldsymbol{a}_n + \gamma\boldsymbol{a}_{n+1}\big] \tag{5.40}$$

where Δt is the time step. In multi-corrector phase, for iterates $i = 0, 1, \ldots, i_{max}$ the nodal solution is defined at the intermediate time levels as

$$\boldsymbol{u}_{n+\alpha_f}^{i} = \boldsymbol{u}_n + \alpha_f\big(\boldsymbol{u}_{n+1}^{i} - \boldsymbol{u}_n\big) \tag{5.41}$$

$$\boldsymbol{v}_{n+\alpha_f}^{i} = \boldsymbol{v}_n + \alpha_f\big(\boldsymbol{v^i}_{n+1} - \boldsymbol{v}_n\big) \tag{5.42}$$

$$\boldsymbol{a}_{n+\alpha_m}^{i} = \boldsymbol{a}_n + \alpha_m\big(\boldsymbol{a}_{n+1}^{i} - \boldsymbol{a}_n\big) \tag{5.43}$$

where α_f, α_m, β and γ are real-valued parameters that define the method and chosen based on the stability and accuracy. Chung and Hulbert [92] showed that the second-order accuracy in time is attained if

$$\gamma = \frac{1}{2} - \alpha_f + \alpha_m \qquad \text{and} \qquad \beta = \frac{1}{4}(1 - \alpha_f + \alpha_m)^2 \tag{5.44}$$

while unconditional stability can be attained if

$$\alpha_m \geq \alpha_f \geq \frac{1}{2} \tag{5.45}$$

This work sets $\alpha_f = \alpha_m = \gamma = \frac{1}{2}$ and $\beta = \frac{1}{4}$. The intermediate values defined in equations (5.41)-(5.43) are used to compute the residual of the equation (5.25)

$$\boldsymbol{R}^i_{n+1} = \boldsymbol{M}\boldsymbol{a}^i_{n+\alpha_m} + \boldsymbol{M}_2\boldsymbol{u}^i_{n+\alpha_f} - \boldsymbol{M}_1\boldsymbol{u}^i_n + \boldsymbol{V}_h(t_{n+1}) - \boldsymbol{F}(t_{n+1}) \tag{5.46}$$

The residual is used to calculate a correction to the acceleration term by solving

$$\boldsymbol{M}^*\Delta\boldsymbol{a} = -\boldsymbol{R}^i_{n+1} \tag{5.47}$$

where $\boldsymbol{M}^*$ can be chosen in an implicit/explicit way. Explicitly $\boldsymbol{M}^*$ can be considered as lumped mass matrix and implicitly $\boldsymbol{M}^*$ is defined as

$$\boldsymbol{M}^* = \frac{d\boldsymbol{R}^i_{n+1}}{d\boldsymbol{a}^i_{n+1}} \tag{5.48}$$

From equation(5.46) one obtains

$$\frac{d\boldsymbol{R}^i_{n+1}}{d\boldsymbol{a}^i_{n+1}} = \frac{\partial \boldsymbol{R}^i_{n+1}}{\partial \boldsymbol{a}^i_{n+\alpha_m}} \frac{\partial \boldsymbol{a}^i_{n+\alpha_m}}{\partial \boldsymbol{a}^i_{n+1}} + \frac{\partial \boldsymbol{R}^i_{n+1}}{\partial \boldsymbol{u}^i_{n+\alpha_f}} \frac{\partial \boldsymbol{u}^i_{n+\alpha_f}}{\partial \boldsymbol{u}^i_{n+1}} \frac{\partial \boldsymbol{u}^i_{n+1}}{\partial \boldsymbol{a}^i_{n+1}} \tag{5.49}$$

This can be written as

$$\boldsymbol{M}^* = \alpha_m \boldsymbol{M} + \alpha_f \beta (\Delta t)^2 \boldsymbol{M}_2 \tag{5.50}$$

After solving the linear system (5.47), in corrector, the iterates are updated as

$$\boldsymbol{a}^{i+1}_{n+1} = \boldsymbol{a}^i_{n+1} + \Delta \boldsymbol{a} \tag{5.51}$$

$$\boldsymbol{v}^{i+1}_{n+1} = \boldsymbol{v}^i_{n+1} + \gamma \Delta t \Delta \boldsymbol{a} \tag{5.52}$$

$$\boldsymbol{u}^{i+1}_{n+1} = \boldsymbol{u}^i_{n+1} + \beta (\Delta t)^2 \Delta \boldsymbol{a} \tag{5.53}$$

After each iteration, the residual is checked for convergence. If $\|\boldsymbol{R}^i_{n+1}\| \leq \epsilon \|\boldsymbol{R}^0_{n+1}\|$ for some predetermined tolerance ϵ, the solution is moved to the next time step. If not, then the exit iteration is performed. For implicit $\boldsymbol{M}^*$, usually, the convergence is reached in just one iteration. However, if the precision of the solution is approximate then additional iterations are performed.

5.6 Linear-elastodynamics

For linear-elastodynamics the solution is computed with only the current state of stress and strain.

$$\boldsymbol{\sigma}(t) = \boldsymbol{\sigma}_0(t) \tag{5.54}$$

The space discretization of displacement leads to the following matrix equation

$$\boldsymbol{M}\ddot{\boldsymbol{u}}(t_{n+1}) + \boldsymbol{K}\boldsymbol{u}(t_{n+1}) - \boldsymbol{F} = 0 \tag{5.55}$$

In the above equation, $\boldsymbol{M}$ and $\boldsymbol{K}$ are the mass and stiffness matrices defined in equations (5.26) and (5.28) respectively. In structural dynamics one often needs to consider the structural damping effects and work with the following system

$$\boldsymbol{M}\ddot{\boldsymbol{u}}(t_{n+1}) + \boldsymbol{C}\dot{\boldsymbol{u}}(t_{n+1}) + \boldsymbol{K}\boldsymbol{u}(t_{n+1}) = \boldsymbol{F} \tag{5.56}$$

Where $\boldsymbol{C}$ is the viscous damping matrix. The damping is often assumed to have one part proportional to the mass and another proportional to the stiffness. In the Rayleigh hypothesis, the damping matrix C is assumed to be

$$\boldsymbol{C} = a\boldsymbol{M} + b\boldsymbol{K} \tag{5.57}$$

where a and b are constants that depend on the material and are known as the Rayleigh damping parameters. The equation (5.56) can be solved by generalized-α time integration method with residual $\boldsymbol{R}^i_{n+1}$ and matrix $\boldsymbol{M}^*$ defined as

$$\boldsymbol{R}^i_{n+1} = \boldsymbol{M}\boldsymbol{u}^i_{n+1} + \boldsymbol{C}\boldsymbol{u}^i_{n+1} + \boldsymbol{K}\boldsymbol{u}^i_{n+1} - \boldsymbol{F} \tag{5.58}$$

$$\boldsymbol{M}^* = \alpha_m\boldsymbol{M} + \alpha_f\gamma\Delta t\boldsymbol{C} + \alpha_f\beta(\Delta t)^2\boldsymbol{K} \tag{5.59}$$

5.7 Numerical examples

In this section the numerical examples for linear elastodynamics are presented and are solved using generalized alpha method.

5.7.1 1-D impact of an elastic bar against a rigid wall

This benchmark illustrates the basic properties of the numerical solution obtained using the employed technique for problems of linear elastodynamics. Due to spurious high-frequency oscillations, 1-D impact linear elastodynamics problem is of particular interest. The problem is solved by the generalised alpha method. The impact of an elastic bar of the length $L = 4$ and the cross-section $A = 1$ is considered against a rigid wall (see Fig. 5.1). The Young's modulus and density are set to $E = 1$, and $\rho = 1$. As initial conditions, the $\boldsymbol{u}$ and $\boldsymbol{v}$ are set to zero. As boundary conditions on the left-hand side of the bar the displacement is set to $\boldsymbol{u} = t$, this corresponds to $\boldsymbol{v} = 1$. On the right-hand side, the displacement is set to zero, which corresponds to zero velocity. Due to boundary conditions, an elastic wave is generated and travels from left to right. After striking with the right end of the bar the wave is reflected back and move leftwards. For this simulation, a mesh is constructed of 100 elements. The time step is set to 0.001. Figure (5.2) shows the displacement of the propagating elastic wave through the bar at various times.

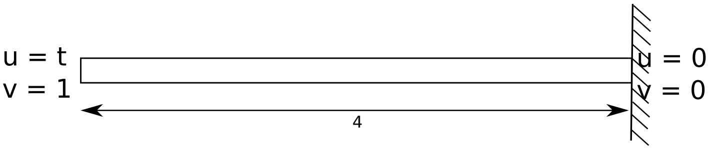

Figure 5.1: 1D impact of an elastic bar: Domain and boundary conditions.

The analytic solution of the problem for time $0 \leq t \leq L\rho/E$ is given as $\boldsymbol{u} = t - x$ for $t \geq x$ and $\boldsymbol{u} = 0$ for $t \leq x$; and $\boldsymbol{v} = 1$ for $t \geq x$ and $\boldsymbol{v} = 0$ for $t \leq x$. At the interface $x = 2$, a jump in velocity occurs. For time $4 \leq t \leq 8$ the solution is similar to that for $0 \leq t \leq 4$ with the difference that the elastic wave reflects from the right end and propagates to the left. For time $8 \leq t \leq 12$ the solution is the same as for time $0 \leq t \leq 4$ and so on. Figure (5.3) compares the numerical solution with the analytic one. A little

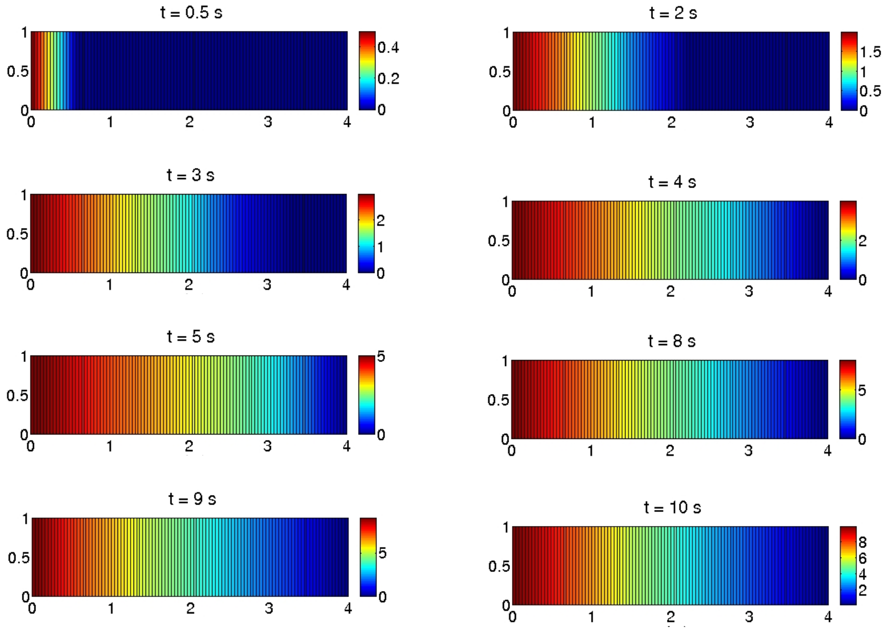

Figure 5.2: 1D impact of an elastic bar: Temporal evolution of displacement (m) in the bar.

divergence of velocity can be noticed from the velocity plot. The numerical results are without any filtering [26].

5.7.2 Uniaxial bar

In this test case a uniaxial bar, which is clamped at one end (fixed), and subjected to a traction at the other end is studied for an interval of time. The bar is depicted in figure 5.4. It is assumed that the bar is rigid with respect to bending (bending stiffness EI $\rightarrow \infty$) and only the longitudinal deformation u(x,t) is considered.

The length and width of the bar are 1.0 m and 0.01m respectively. The density is set to 1.0 kg/m^3 and elastic modulus is set to 1.0 Pa. The bar is discretized into 200 elements. On the left end of the bar the displacement is set to zero as the Dirichlet boundary condition and on the right end, the time-dependent load F(t) is set as Neumann boundary condition. F(t) is a

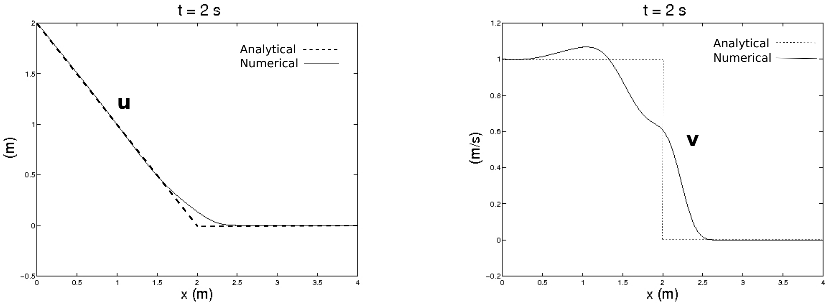

Figure 5.3: 1D impact of an elastic bar: The comparison of analytical and numerical solution of $\boldsymbol{u}$ (m) and $\boldsymbol{v}$ (m/s) at time $t = 2s$.

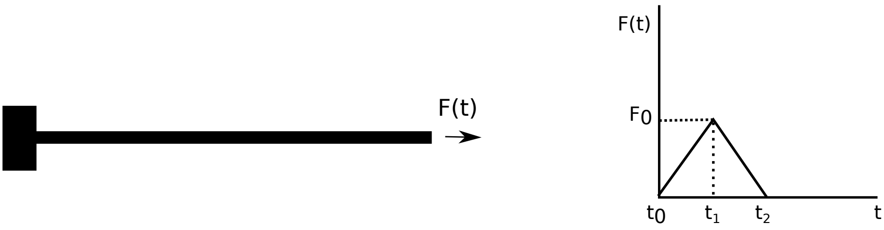

Figure 5.4: 1D uniaxial bar: The problem set up.

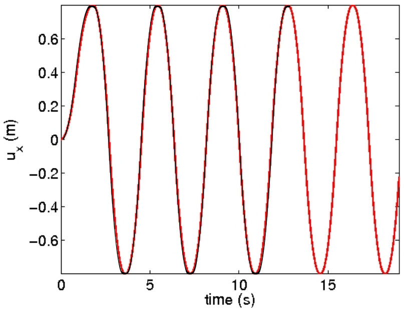

Figure 5.5: 1D uniaxial bar: The comparison of displacement (m) at the right end. The black and red colors are corresponding to the reference and current numerical simulation respectively.

triangular impulse, with a duration $t_2 = 1.75$.

$$F(t) = \begin{cases} \dfrac{t}{0.875} & \text{for} \qquad 0 \leq t < 0.875 \\ 2 - \dfrac{t}{0.875} & \text{for} \qquad 0.875 \leq t \leq 1.75 \\ 0 & \text{for} \qquad t > 1.75 \end{cases} \tag{5.60}$$

The total time span of observation is t = 20 s. The time step for the simulation is set to 0.005 s. A reference solution is computed using modal analysis and the Duhamel integral [176]. Figure (5.5) depicts the comparison of the transient displacement at the right end of the bar with the reference solution. Figure (5.6) shows the displacement at time t = 5.875 along the bar and compares it with the reference solution. As can be seen from the figures the numerical solution obtained from the current simulation well agrees with the reference solution.

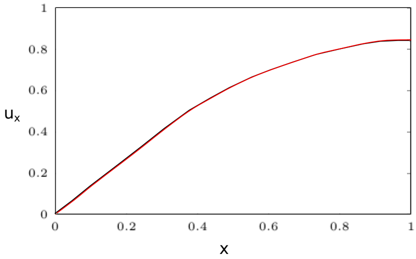

Figure 5.6: 1D uniaxial bar: The comparison of displacement (m) at time t = 5.875. The black and red colors are corresponding to the reference and current numerical simulation respectively.

5.7.3 2-D impact of an elastic bar against a rigid wall

This problem is a two dimensional version of the 1-D impact problem discussed in section 5.7.1. In contrast to the 1-D impact problem, compressional and shear elastic waves propagate in the 2-D case. The problem set up is taken from [10] in the following way. A bar of length 4 m and height 1 m is considered. Due to symmetry, the problem is solved for a half of the bar ABCD where AD is the axis of symmetry. Young's modulus is chosen to be $E = 1$, the density to be $\rho = 1$ and Poisson's ratio to be $\nu = 0.3$. The following boundary conditions are applied: along boundary AB, $u_n = t$ (it corresponds to velocity $v_n = v_0 = 1$) and $\tau_n = 0$; along boundaries BC and CD $\sigma_n = 0$ and $\tau_n = 0$; along boundary AD $u_n = 0$ and $\tau_n = 0$, where u_n, v_n and σ_n are the normal displacements, velocities and the tractive forces, respectively; τ_n are the tangential tractive forces. Initial displacements and velocities are zero; i.e., $u(x, y, 0) = v(x, y, 0) = 0$. The observation time is chosen to be t = 13. During this time the velocity pulse travels within the bar with multiple reflections from the ends of the bar and from the external surface BC.

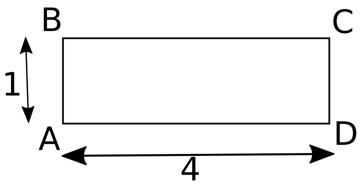

Figure 5.7: Impact 2D: The geometry of the domain.

The mesh is discretized into 6400 quadrilateral elements. The time step for the simulation is set to 0.001 s. The figure (5.8) shows the velocity distribution along the axis of symmetry AD at observation time t = 13. The comparison shows that the obtained results are very similar to the one reported in [10]. It is worth mentioning that the results are without any filtering and damping coefficients. The suitable choice of damping coefficients can effectively reduce the fluctuation in velocity.

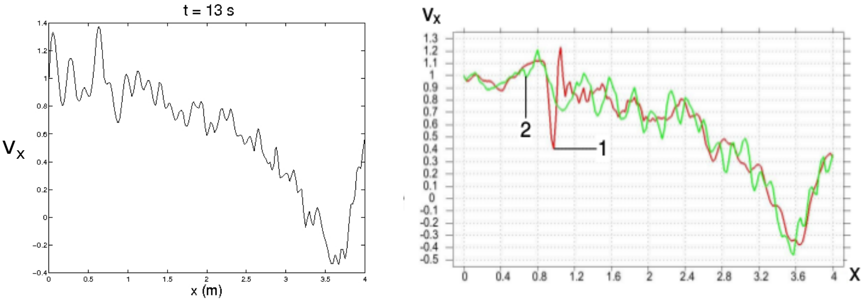

Figure 5.8: Impact 2D: The comparison of velocity (m/s) at time t = 13 s along the axis of symmetry AD. Left panel show the velocity distribution obtained from the current simulation and the right panel shows the velocity obtained in [10].

Chapter 6

Volcanic applications

Introduction

This chapter presents numerical simulations for magma dynamics occurring in magma chambers. First of all, the model assumptions are discussed, followed by a description of the constitutive equations of the models employed to compute the physical properties of magma in section 6.1. Section 6.2 presents a case of natural convection driven by temperature contrast in magma. In section 6.3, two simulations are performed over different magmas to model the magma replenishment and mixing dynamics. Section 6.4 studies a case of magma replenishment and mixing dynamics during and after a seismic excitation. Finally, all results are discussed in section 6.5.

Magma chamber dynamics is characterised by highly non-linear and strongly time-dependent physical properties involving a large number of variables. The behaviour of the magma inside a chamber is strongly affected by pressure, temperature, volatile contents, physical properties of the melt, amount of crystals and bubbles suspending in the liquid melt. The domain size in particular the length of a chamber may vary from tens of meters to hundreds of kilometres. The magmatic system may be composed of several shallow magma chambers connected to a deeper reservoir or to each other through dikes. Geochemical and petrological studies suggest that in many cases magma residing in shallow chambers is recharged by the deeper source through dikes. Magma coming from depth can be of same composition and physical properties as the resident magma or different.

Magma ascent through volcanic dikes can be driven by buoyancy and/or overpressure [59]. In literature often magma replenishment is considered to be driven by the combination of buoyancy and pressure forces with pressure playing a dominant role. Such a refilling adds an excess mass in the shallow chamber which increases the overall overpressure and progresses towards an eruption. Nevertheless, there can also be the cases where magma ascent is driven by only buoyancy force without any overpressure. Understanding the physics of magma mixing arise due to pure buoyancy forces is interesting and has not been explored well in the literature. It is important to know the outcomes of such a magma mixing driven by only buoyancy forces. The present work focuses on the numerical experimentation of magma dynamics solely due to buoyancy forces also known as natural convection. In the cases of natural convection the driving mechanism is density contrast which can be due to a difference in temperature and/or composition. However, both of these factors are interlinked. The thermal evolution of the magma determines how crystallisation proceeds, which in turn determines how composition and temperature evolve. In this study for simplicity the crystallisation process is not taken into account and the density contrast is set up by using different temperatures and magma compositions.

In this chapter three different cases of natural convection occurring inside a magma chamber are investigated. The first case investigates that what happens when a fresh hot magma enters from the bottom of the chamber. The resident and refilling magma are assumed to have the same composition but different temperature. The difference in temperature determines a density gradient, driving the convection. The second case studies the magma mixing and convection process between two chemically heterogeneous magmas. Two different kinds of magmas are placed in two chambers connected through a dike. In this case, the temperature of magmas are kept the same and particular emphasis is given on the convection driven by differences in composition. The third case investigates the resulting magma dynamics when a near-field seismic wave strikes with the chamber and shakes it. The duration of the interacting wave is 60 s. The flow dynamics during and after this period is studied. In this case the simulation setup is the same as in the second case with the addition of an external disturbance. This test case requires the movement of the magma chamber domain and associated changes in magma dynamics. The algorithm described in chapter 4 has been employed to couple magma dynamics and mesh motion.

In general model complexity involves a trade-off between simplicity and accuracy of the model. While added complexity usually improves the realism of a model, it can make the model difficult to understand and analyse, and can also pose computational problems including numerical instability. The computational cost of adding a huge amount of details effectively inhibits the usage of a model. Additionally, the uncertainty increases due to an overly complex system. It is therefore usually appropriate to make some approximations for the model. The model developed in this thesis and applied to simulate the chamber dynamics is based on some simplifying assumptions. Magma is assumed to have a Newtonian rheology. At low strain rate magma stresses are linearly proportional to the strain rate [174] but with an increase in strain rate the flow behaviour approaches a non-Newtonian behaviour. For the cases under consideration of this study the strain rate is quite low, this justifies the choice of a Newtonian rheology. For a large amount of crystals (> 30 vol%) the non-Newtonian behaviour occurs even at lower strain rates. To overcome this problem, magma is assumed to have no crystals. The magma is assumed to be in superliquidus conditions at the temperatures set up in the simulation cases.

The multicomponent flow mixture model used for the simulations is homogeneous. The phase transition of components is controlled by the local physical properties of the mixture. Liquid and gas phase are assumed to move with same velocity (i.e. mechanical equilibrium). The model takes into account only the mechanical mixing and the chemical reaction between different magmas is not considered. In the literature, mixing without chemical reaction among components is referred as mingling. However, here the word mixing is used throughout the text. The detailed study of the mixing of two magmas at chemical level is not under the scope of the current work. The present model is in 2-D. The bi-dimensionality of the present model assume that the thickness of the chamber is negligible in comparison to the length and the breadth. Though this is a major assumption in the modelling of magma dynamics inside an ellipsoidal chamber, which can not be represented by an ellipse on a plane in 2-D, the general idea of the overall dynamics can be well attained. A 3-D simulation increases the number of grid elements and hence the computation time. In order to keep the computational efforts affordable the choice of numerical computation in 2-D are justified.

6.1 Constitutive model equations

For all the simulation cases studied in this chapter, magma is assumed as a fluid mixture of liquid oxides and volatiles. The velocity of magma inside the chambers may vary from 2 to 10 m/s. The sound speed of magma-gas mixtures may range from as low as 10 m/s for bubbly foam at shallow depths, up to 2500 m/s for magma below the CO_2 nucleation depth [126]. This determines a variable Mach number ($M = v/c$). Where v is the magma flow velocity and c is the local speed of sound in magma. Depending on the Mach number the flow regime can vary from incompressible to compressible. In general the flow of magma inside a chamber is incompressible ($M < 0.3$), however, the flow can be compressible if $M > 0.3$. Therefore, this variable regime is modelled by the Navier-Stokes equations for compressible flows. The compressible model is able to switch to incompressible if the change in density with respect to temperature and pressure in negligible. This is determined by the compressibility coefficients. The details are given in chapter 2 and chapter 3.

Only H_2O and CO_2 are considered as volatiles which can exsolve or dissolve in the melt according to local pressure, temperature and composition of magma. For the exsolution and dissolution of H_2O and CO_2 in the magmatic mixture, a saturation model [147] is used. The model is based on the thermodynamics equilibrium between gaseous and liquid volatile components. The following equilibrium equations are used in the model

$$p^G = p^L = p \qquad\qquad T^G = T^L = T$$

$$\phi_{H_2O} y_{H_2O} p = \gamma_{H_2O} x_{H_2O} f^{0l}_{H_2O} \qquad\qquad \phi_{CO_2} y_{CO_2} p = \gamma_{CO_2} x_{CO_2} f^{0l}_{CO_2}$$

$$y_{H_2O} + y_{CO_2} = 1$$

$$\frac{x^t_{H_2O} - y_{H_2O}}{y_{H_2O} - x_{H_2O}} = \frac{x^t_{CO_2} - y_{CO_2}}{y_{CO_2} - x_{CO_2}}$$

where p is pressure, T is temperature, ϕ is the fugacity coefficient in gas phase, f^{0L} is the fugacity in liquid phase in reference state, γ is the activity coefficient in liquid phase, y and x are mole fractions in gas and liquid phases respectively, and the superscripts G, L and t refer to gas phase, liquid phase and total mole fraction respectively.

The density of dissolved H_2O and CO_2 is computed as a function of pressure and temperature by the model of Burnham et al. [44]. The molar volume of H_2O and CO_2 are evaluated as a polynomial function of pressure p and temperature T in the following form.

$$MV = a_0 + a_1 T + a_2 T^2 + a_3 T^3 + p(a_4 + a_5 T + a_6 T^2) + p^2(a_7 + a_8 T) + a_9 p^3$$

where MV is the molar volume, $a_0, a_1, \ldots$ are the fitting parameters of the experimental data. The density is computed by dividing the molar mass by molar volume. The density of H_2O and CO_2 gas is computed by the ideal gas law.

$$p = \rho R T$$

where p is pressure, ρ is density, R is specific gas constant and T is temperature. For the range of pressure and temperature used in the simulations the ideal gas law best approximates the density of H_2O and CO_2 gas [171]. The density of the silicate melt is computed with the model given by Lange [158]. The molar mass and molar volume of silicate melt is computed as follows

$$\frac{1}{M} = \sum_i \frac{y_i}{M_i}$$

$$MV = \sum_i x_i MV_i$$

where index i runs for the number of oxides, M is molar mass, MV is molar volume, x is mole fraction and y is the mass fraction. The density of the magma mixture containing liquid oxides and volatiles (dissolved and exsolved) is computed by the homogeneous mixture model 2.32.

Unlike density for which first the densities of silicate melt and volatiles (dissolved and exsolved) are computed separately and after the density of the mixture is obtained, the viscosity is computed for the mixture of liquid oxides and dissolved volatiles by the model of Giordano et al. [48]. The non-Arrhenian viscosity η_l is modelled as

$$log \eta_l = A + \frac{B}{T - C}$$

where A, B and C are adjustable parameters, including the pre-exponential factor, pseudo-activation energy, and the temperature, respectively. Assuming the Newtonian behaviour of magma, the effect of non-deformable gas bubbles is accounted by the simplified form of Ishii and Zuber's model [125].

$$\eta = \eta_l / (1 - \phi_g)$$

where ϕ_g is the volume fraction of the gas. The above equation considers the fact that the viscosity of the gas phase is negligible with respect to the liquid phase at magmatic conditions. For the mixture of two or more magmas the overall viscosity of the mixture is computed with the homogeneous mixture model [161]. Sound speed, compressibility coefficients, chemical diffusivities, specific heats, thermal conductivity, internal energy and enthalpy are modelled by homogeneous mixture model 2.32. The chemical reactions between the components are neglected.

6.2 Case 1: Natural convection due to temperature contrast

The characteristic features of many lavas are that they are rich in crystals and display a range of disequilibrium features. Petrological observations indicate a wide diversity of mineral textures, mineral compositions, apparent temperatures and disequilibrium observed in orogenic igneous rocks [166]. This fact is interpreted as the evidence of the mixing of magmas of contrasting composition and origin [73, 131]. However, this can also be due to the convection within a magma body with a single composition. The mechanism of self-mixing in a convecting magma body heated from below explains this phenomenon. Different types of zoned plagioclase phenocrysts in basalt samples have been analysed for major and trace elements from near East Pacific Rise 13 degree N [79]. Different extents of MgO have been found in the evolved basalt magma. High MgO basalts are explained due to self-mixing crystallization. Larger plagioclase xenocrysts are found to be in textural disequilibrium with the Felsic microgranular enclave groundmass in the Mauá Pluton, SE Brazil [21]. The plagioclase xenocrysts show complex zoning patterns with partially resorbed An-rich cores (locally with patchy textures) surrounded by more sodic rims. A combination of trace element and Sr isotope data suggests a self-mixing. Differences in crystal abundance and glass composition of pumices have been identified from the 1991 Pinatubo eruption [100]. The samples show a stable bulk composition and the presence of crystals in crystal-poor dacite shows evidence of breakage, resorption and crystal dissolution. These features were interpreted as forming in response to pre-heating of the dacite magma by underlying, freshly intruded basaltic magma. The evidence for thermal disequilibrium for dacite has also been observed [167] which can be explained by self-mixing.

The numerical simulation presented in this section shows a case when an elliptical magma chamber is fed by fresh hot magma through a dike from some deeper source. The resident and the injected magma are assumed to have same chemical composition. The resulting system is a closed chamber which has two layers of stratified magma. The upper layer of resident magma is assumed to be cold with respect to the lower layer of fresh hot magma. The objective of this simulation is to study the self mixing which occurs with such setup and is relevant for magma chambers dynamics. The lighter (hotter) magma interpenetrates the cold (heavier) magma. In this dynamic process both magmas seek to reduce their combined potential energy. Flow is described in terms of a non-dimensionless parameter the Atwood number A.

$$A = \frac{\rho_2 - \rho_1}{\rho_2 + \rho_1} \tag{6.1}$$

The Atwood number characterises the instabilities in density stratified flows. In the above expression of Atwood number, ρ_2 and ρ_1 are the densities of heavier and lighter magmas.

6.2.1 Simulation set up

The geometry of the simulated system is an oblate elliptical chamber filled with basalt magma as shown in figure (6.2). The length of semi-major and semi-minor axes are 400 m and 100 m, respectively. The central point of the chamber is considered at the depth of 4100 m from the surface level. A computational mesh composed of 11227 unstructured elements is constructed for the elliptical chamber (Figure 6.1). The mesh resolution is good to capture all aspects of flow variables during the dynamical evolution.

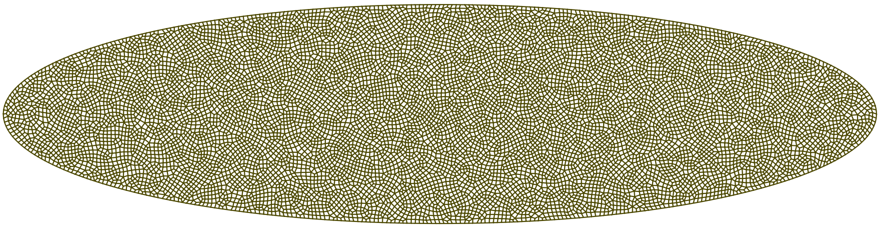

Figure 6.1: The computation mesh for the simulated case.

A slow injection of fresh hotter magma spreading at the base of the chamber is assumed. For the sake of simplicity, it is assumed that the upper 3/4-th of the chamber is filled with cool resident magma and the lower 1/4-th with the fresh hotter one. The interface between hot and cold magmas is set at a depth of 4150 m. Below the interface, the magma is assumed to have a temperature of 1320 K and above 1270 K. The density gradient between colder and hotter magma at the interface is 10, leading to a low value of the Atwood number $A = 0.003$. The interface is perturbed and set in the form of a sinusoidal wave.

$$y_{\text{interface}} = -4150 + a_0 \; sin\Big(\frac{\pi}{100}x\Big) \tag{6.2}$$

Where the amplitude a_0 of the sinusoidal wave is set to 10 m. As initial condition for pressure, a magma-static profile (hydrostatic profile for magma) is set. The composition of the basalt magma adopted in the simulation is reported in table 6.1. Magma is assumed to have 2 wt% of total H_2O and 0.5 wt% of total CO_2. As initial conditions, velocity is set to zero. No-slip and zero heat flux boundary conditions are applied on the chamber walls. Since there is the equation of state there is no need to fix the pressure at any point in the domain. The simulation is carried out for 1500 s with a time step of 0.01 s.

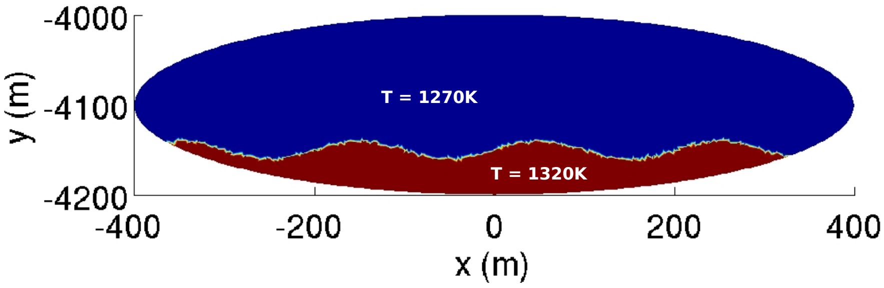

Figure 6.2: Schematic description of the domain geometry and the initial conditions set up for temperature. The red and blue colours represent the hot and cold magmas.

Major oxides									
SiO_2	TiO_2	Al_2O_3	Fe_2O_3	FeO	MnO	MgO	CaO	Na_2O	K_2O
48.40	1.67	17.80	1.86	8.36	0.18	5.53	10.20	3.87	2.11

Table 6.1: Basalt composition

6.2.2 Results

Figure (6.3) shows temporal evolution of temperature. Due to density contrast between hotter and colder magmas, the lighter magma pushes the heavier one up. Since this equilibrium is unstable to any disturbance or perturbation at the interface, the movement between hotter and colder magmas releases the gravitational potential energy, which is converted into kinetic energy. Within the first 50 seconds hotter and lighter magma start forming the spirals with a slightly upward velocity. Simultaneously, an equal volume of heavier magma is displaced downward. The temporal development of the flow leads to an instability of the interface, well known in the literature as Rayleigh-Taylor (RT) instability [136]. As the instability develops, downward-moving dimples are quickly magnified into sets of inter-penetrating RT fingers or plumes. During the initial stages of the Rayleigh-Taylor instability the perturbation amplitude is significantly smaller than the wavelength of the interface.

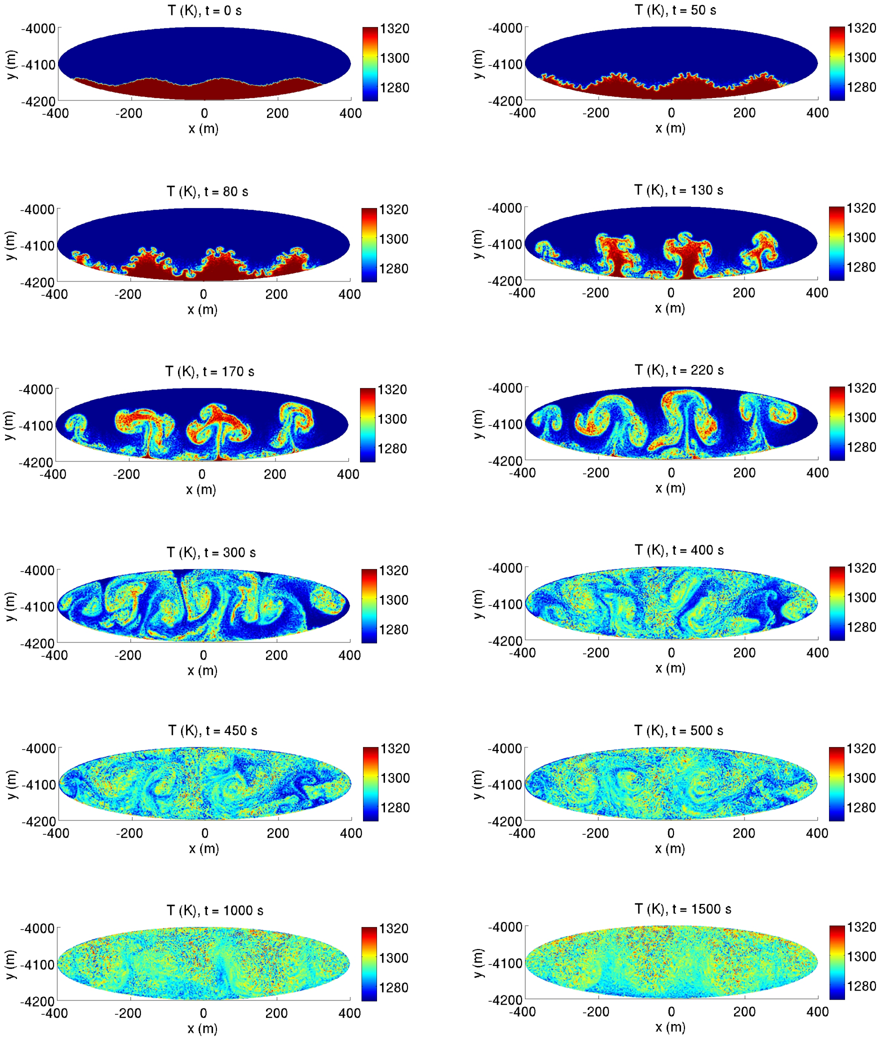

Figure 6.3: The temporal evolution of temperature (K) at various times.

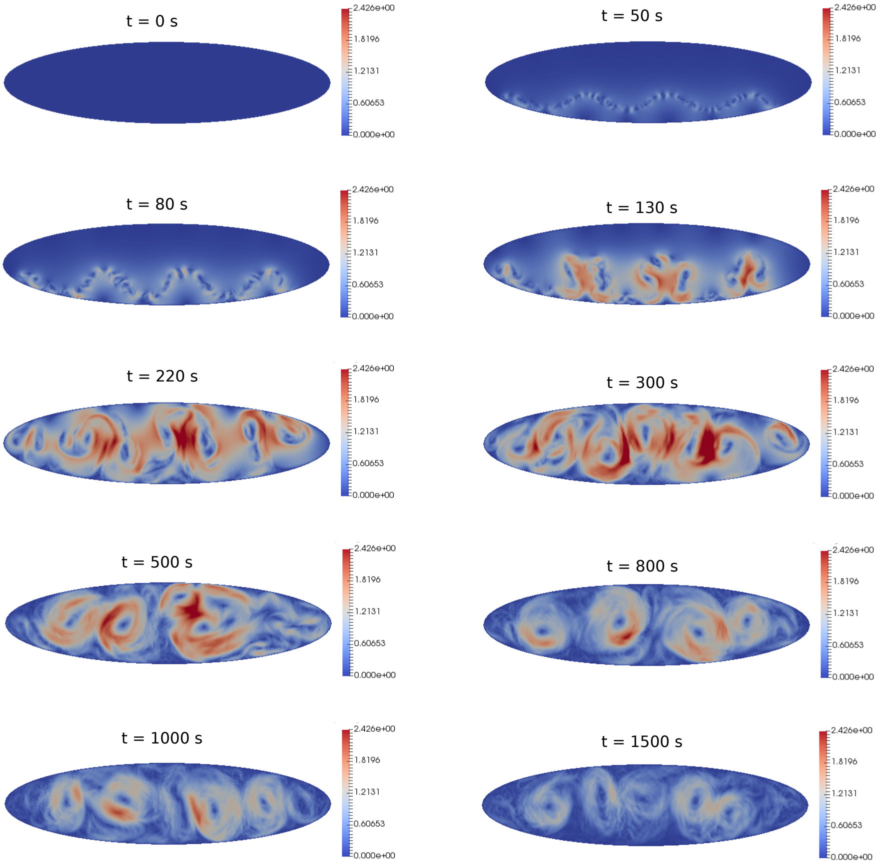

t = 0 s

t = 50 s

t = 80 s

t = 130 s

t = 220 s

t = 300 s

t = 500 s

t = 800 s

t = 1000 s

t = 1500 s

Figure 6.4: The temporal evolution of velocity (m/s) at various times

For subsequent times, the perturbation of the interface grows exponentially as

$$h(t) = h_0 e^{\sqrt{Agk}t}$$

Where h_0, k, g, A and t are the initial amplitude of the interface, wave number, gravitational acceleration, Atwood number and time, respectively. Beyond time t = 130 s the expanding spirals collide with each other and merge together. Due to initial interface profile which has four crests, the merged spirals evolve forming four big plumes (Figure 6.3 at t = 130, 170). The lighter magma continues to mix with the heavier magma through its rise and generates several counter-rotating vortices. After striking with the roof of the chamber the lighter magma spreads laterally. By time t = 550 s, the mixing of hotter and colder magmas gains a homogeneous texture. The simulation was run up to 1500 s.

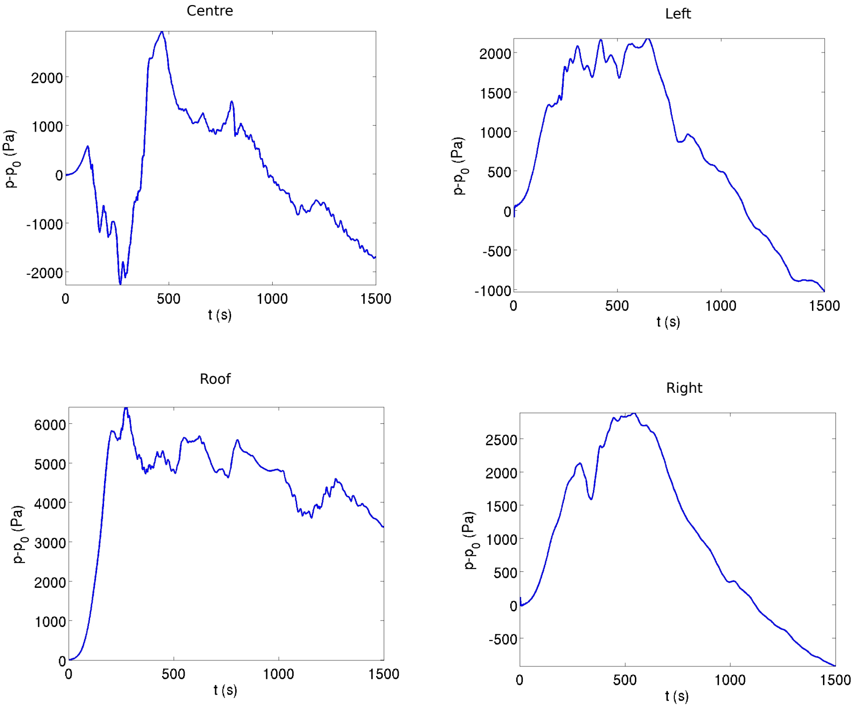

Figure 6.5: The temporal evolution of the overpressure (Pa) at the reference locations (centre, left, roof and right).

Figure (6.4) shows the absolute velocity of convecting magma at different times. Maximum velocity of the convective rolls reaches 2.426 m/s. At time t = 1500 s the maximum velocity reduces to 1.43 m/s. Figure (6.5) shows the temporal evolution of the overpressure. To analyse the pressure four locations have been chosen: the centre, the left, the right and the roof point of the chamber. The overpressure at the roof of the chamber reaches up to 6300 Pa. On left, right and centre of the chamber the maximum value of overpressure reaches 2200, 2940 and 2900 Pa respectively.

In order to see the effect of domain geometry on flow evolution, an irregular domain geometry (Figure 6.6) is used in the simulation with same setup. The results are similar to the elliptical chamber case. Figure (6.7) shows the temporal evolution of overpressure at specific locations (see points A, B, C and D in figure 6.6). At A, B, C and D the maximum value of the overpressure reaches to 3400, 4300, 6300 and 3200 Pa, respectively.

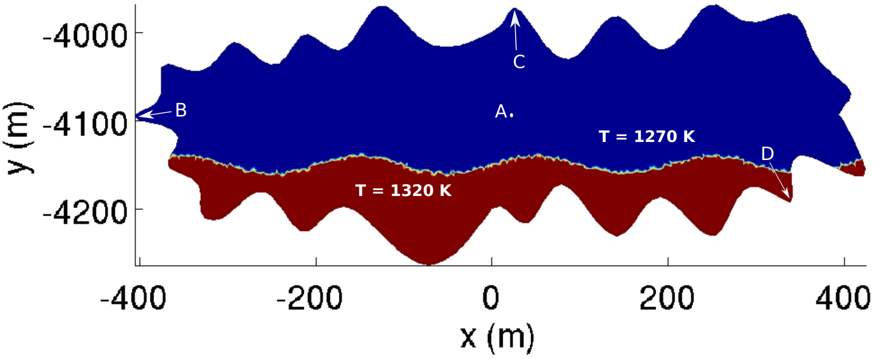

Figure 6.6: Schematic description of the irregular domain geometry, The points A, B, C and D are the reference points where the overpressure is computed.

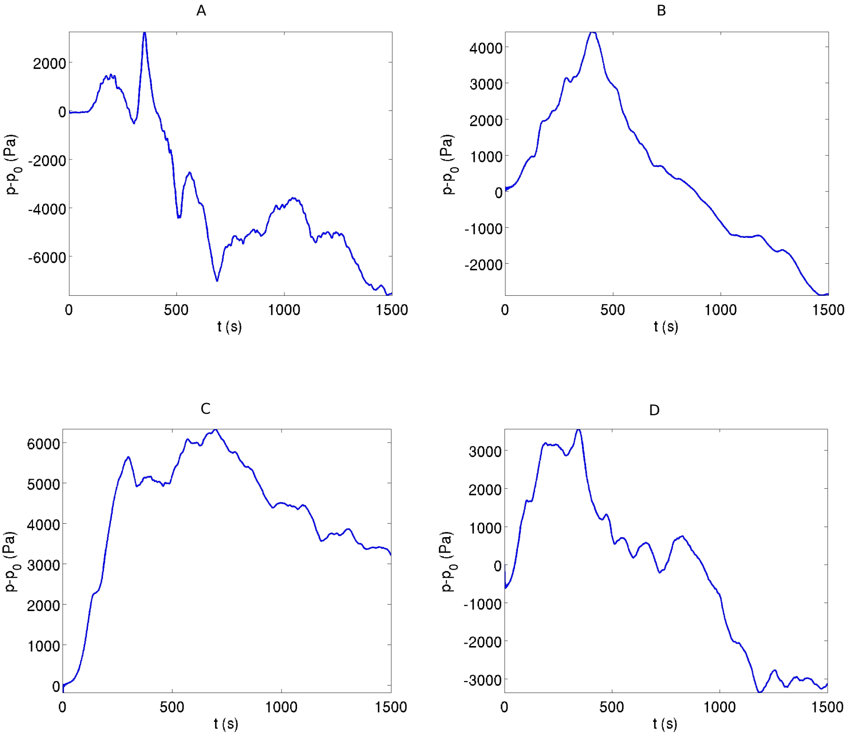

Figure 6.7: The temporal evolution of the overpressure (Pa) at the reference locations (A, B, C and D) of the irregular chamber.

6.3 Case 2: Magma chamber replenishment dynamics

There are evidences of feeding of shallow chamber by volatile-rich, less differentiated magma from the deeper system [34, 88] leading to an eruption [3, 49, 153, 164]. This section studies two simulation cases of natural convection in magma chambers. The simulations have been performed with the aim of understanding the dynamics of mixing and convection in the magma chamber caused by the density contrast between two heterogeneous magmas. The convection is driven by buoyancy. For both cases same domain set up is used. The simulated system is composed of a shallow magma chamber connected to a deeper chamber through a vertical dike (Figure 6.8). Thus, the system is an extended version of the setup used in the previous simulation. The shallow chamber is assumed to be much smaller in comparison to the deeper chamber. The density contrast is determined by the different compositions of magmas. Two simulations are performed. In the first simulation, the lower chamber and the dike are filled with shoshonite magma and the upper chamber is filled with phonolitic magma; in the second case the lower chamber and dike are filled with andesitic magma and the upper chamber is filled with dacitic magma. The geological setting of the first case is analogous of Campi Flegrei volcanic field and the second case is typical of a tectonic region of arc magmatism. The two systems are characterised by magmas with strongly different properties. A case similar to the first one has been modelled in [13]. In this work, the same domain and physical setup of [13] have been used. The evolution of mixing dynamics between shoshonite/phonolite and andesite/dacite magmas is compared.

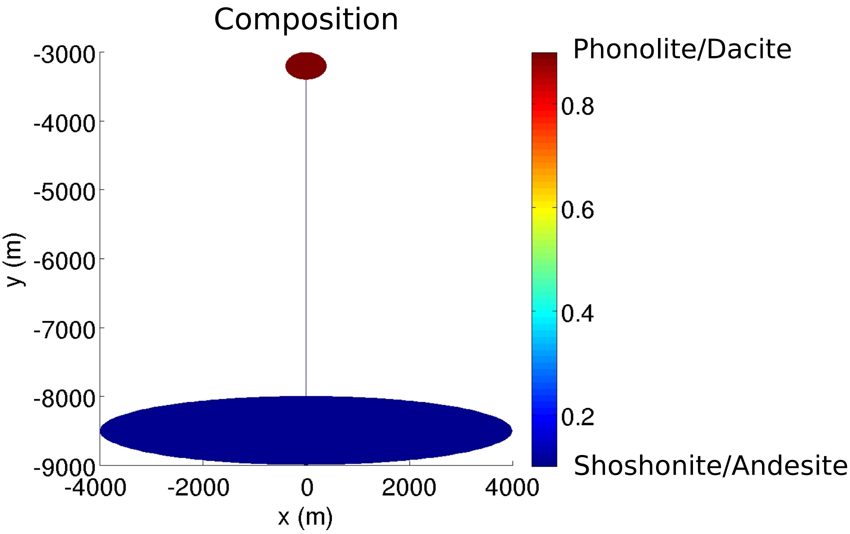

Figure 6.8: Sketch of the total geometry of the systems under consideration with composition.

6.3.1 Simulation set up

The domain geometry for the simulation is constructed in accordance to the recent available information on Campi Flegrei caldera. The seismic imaging and attenuation tomography indicate a shallow elliptical magma chamber at 3 km depth [89, 206]. Geophysical and geochemical studies indicate a deeper magma chamber at the depth of 8 km [18, 115]. In simulations the length of major and minor axis of the shallow chamber are set to 800 m and 400 m, respectively. The length of the major and minor axis of the deeper chamber are set to 8 km and 1 km, respectively. A vertical dike of width 20 m connects the upper chamber with the lower chamber. The temperature of both magmas is kept constant throughout the simulations, thus, excluding the effect of temperature on the convection process and considering that the energy is conserved. The assumption of isothermal system stems from the melt inclusion data of interacting magmas of Campi Flegrei, which have very similar composition [14]. The temperature difference between two magmas involved has often been found to be smaller than 10 % [156]. The isothermal assumption reduces the computational challenges. Density depends on pressure, temperature and composition. In order to set the initial value of density, the temperature is set to 1300 K for the Campi Flegrei case and 1180 K for the arc magmatism case.

	Major oxides									
	SiO_2	TiO_2	Al_2O_3	Fe_2O_3	FeO	MnO	MgO	CaO	Na_2O	K_2O
S	52.40	0.85	17.60	1.88	5.74	0.12	3.60	7.93	3.43	4.28
P	53.52	0.60	19.84	1.60	3.20	0.14	1.76	6.76	4.66	7.91
A	58.70	0.88	17.24	3.31	4.09	0.14	3.37	6.88	3.53	1.64
D	65.98	0.59	16.15	2.47	2.33	0.09	1.81	4.38	3.85	2.20

Table 6.2: Composition of magmas: Shoshonite (S), Phonolite (P), Andesite (A) and Dacite (D)

The initial conditions for magma consist of a magma-static pressure profile and zero velocities everywhere. The magma-static pressure derives from the assumption of equilibrium state with the lithostatic pressure of rock. As mentioned before, the two cases differ for the magma contained in the deeper and shallower reservoirs and in the connecting dike. In the Campi Flegrei case (shoshonite/phonolite) the deeper chamber and the dike contain gas-rich shoshonite with a total of 2 wt% of H_2O and a total of 1 wt% CO_2, and the shallower chamber contains degassed phonolite with a total of 1 wt% of H_2O and a total of 0.1 wt% of CO_2 [12, 14]. In the case of arc magmatism (andesite/dacite) the deeper chamber and the dike contain gas-rich andesite with a total of 4 wt% of H_2O and a total of 1 wt% CO_2, and the shallower chamber contains degassed dacite with a total of 3 wt% of H_2O and a total of 0.3 wt% CO_2. The compositions of magmas are reported in table 6.2. The interface between the two magmas is set at the depth of 20 m below the inlet of the shallow chamber [13]. Due to different compositions of magmas, a gravitationally unstable density difference appears at the level of interface. In Campi Flegrei case the density contrast is 160 kg/m^3, while in the volcanic arc case it is 210 kg/m^3 (Figure 6.9). The initial physical properties of two cases along the whole system are summarised in Table 6.3. On all boundaries no-slip boundary conditions are imposed.

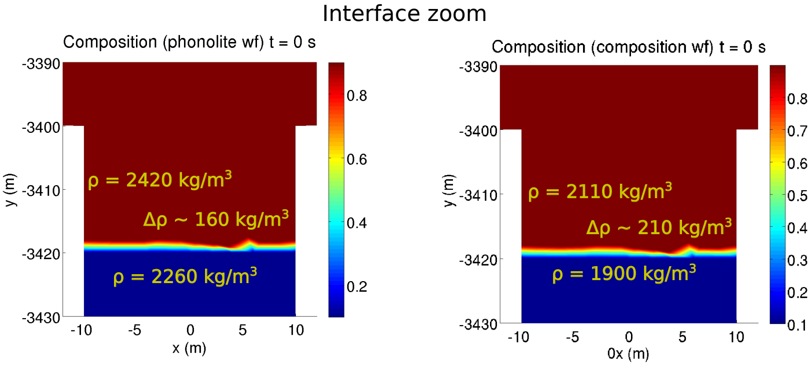

Figure 6.9: Initial conditions at the gravitationally unstable interface for shoshonite/phonolite in left panel, and andesite/dacite in right panel.

	Shoshonite-Phonolite	Andesite-Dacite
Density (kg/m^3)	2260 - 2420	1900 - 2310
Viscosity (Pas)	507 - 2800	3180 - 3.3×10^4
Compressibility (1/Pa)	(2.7 - 16) $\times10^{-10}$	(5.5 - 46) $\times10^{-10}$
CO$_2$ wt % in gas	0.81 - 0.909	0.34 - 0.62
Dissolved volatiles (wt %)	0.011 - 0.0192	0.0242 - 0.0346

Table 6.3: Comparison of initial physical properties of the Campi Flegrei and the volcanic arc cases.

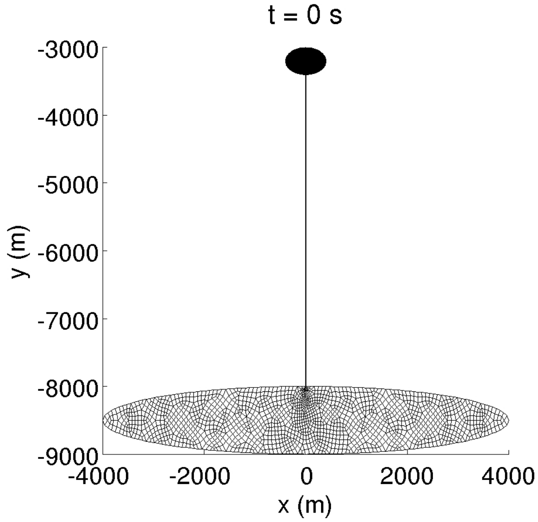

Figure 6.10: The computational mesh for the simulations.

The domain is discretized with unstructured quadrilateral elements and is shown in figure 6.10. Since in most cases the dikes reaching to the surface originate from the shallow chamber, more emphasis is given to the understanding of shallow magma chamber dynamics. The mesh is more refined in the shallower chamber and the dike. The average length of the side of an element in the shallow chamber is 12 m and in the dike is 3 m. In the deeper chamber, the mesh is coarser with an average element length of 30 m. For both cases, the simulation is carried out for 1100 s with a fixed time step of 0.01 s.

6.3.2 Results

The results for the simulation of shoshonite and phonolite magmas are shown in figures (6.11)-(6.17). Figure (6.11) illustrates the zoomed view of evolution of the composition for the earlier times. The system is gravitationally unstable because the shoshonite is lighter than the phonolite magma. Furthermore, in the simulation setup we consider that the shoshonite contains more gas content than the phonolite magma, which results in a further density contrast. This gravitationally unstable situation induces natural buoyancy due to which the lighter magma tends to move upwards. The interface sustains its equilibrium position only for few seconds. Starting from 10 s the interface starts destabilising and some part of phonolite magma pushes the interface level down. To compensate this change at the same time an equal amount of shoshonite move in upward direction. This movement is evident in figure (6.11) at time t = 30 s. Within 30-50 s the slow rising shoshonite magma acquires the form of a plume and reaches up to the base of the upper chamber penetrating through the phonolite magma. The heavier phonolite magma which was just above the interface continues to sink down in the dike and reaches up to 20 m below the level of the interface by the end of the simulation at time t = 1000 s. The outer layers of rising and sinking magmas interact and mix with the resident magmas. When plume enters in the upper chamber, its shape is similar to a blob. Soon after, as plume rises up along the chamber axis, the central part of the blob moves more rapidly than the sides leading to a significant deformation in the shape of the blob. The ascent of plume leaves a low-pressure area behind the plume, which is accumulated by the surrounding magma. In this region the mixing between magmas generates vortices and eventually plume acquires an ellipsoidal cap shape (Figure 6.12 at time t = 130 s). With further ascent, the shape becomes more and more convex and the resulting pattern is a thin film of plume head with two counter-rotating vortices on the sides. After around 120 s a second plume enters the chamber and joins the first plume in the middle, thickening the plume head and growing its size.

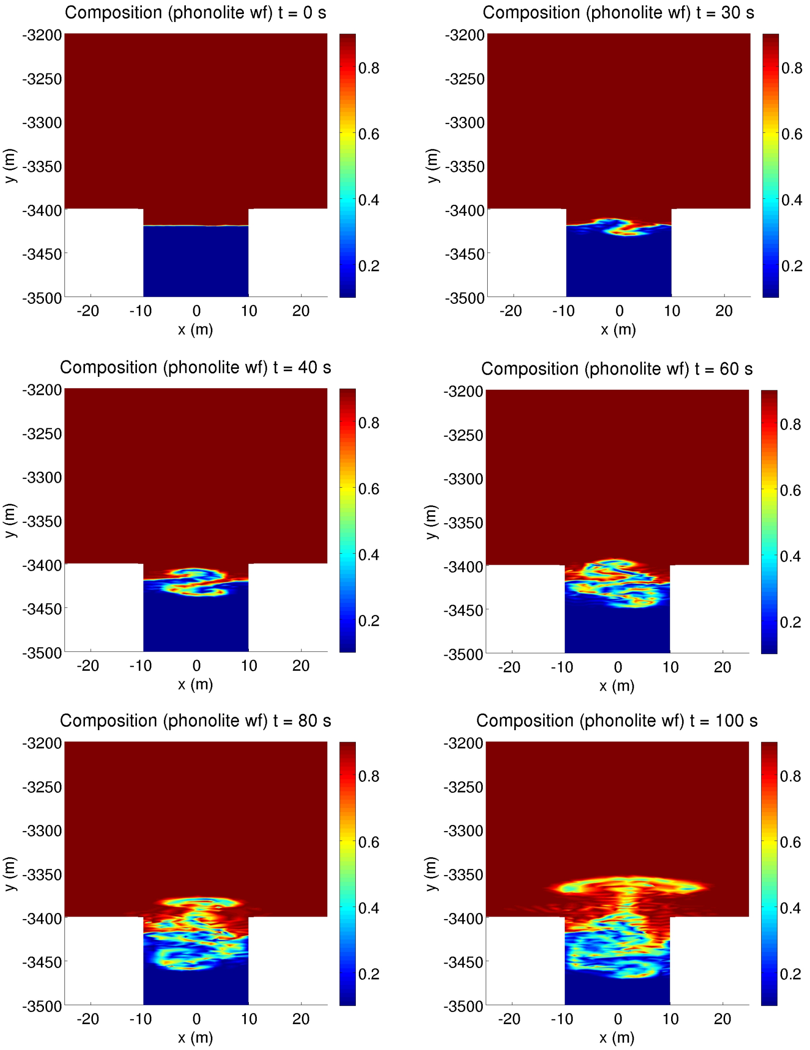
Composition (phonolite wf) t = 0 s

Composition (phonolite wf) t = 30 s

Composition (phonolite wf) t = 40 s

Composition (phonolite wf) t = 60 s

Composition (phonolite wf) t = 80 s

Composition (phonolite wf) t = 100 s

Figure 6.11: Initial phases of evolution of composition (phonolite wf) for the shoshonite-phonolite case.

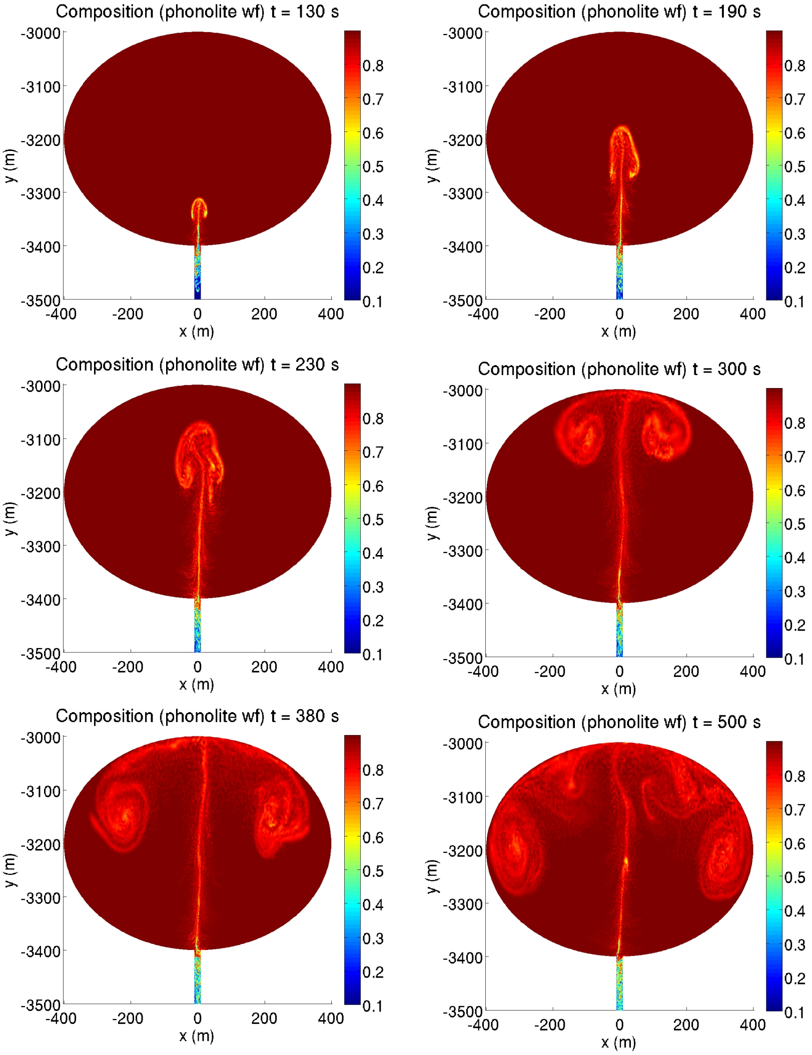

Composition (phonolite wf) t = 130 s

Composition (phonolite wf) t = 190 s

Composition (phonolite wf) t = 230 s

Composition (phonolite wf) t = 300 s

Composition (phonolite wf) t = 380 s

Composition (phonolite wf) t = 500 s

Figure 6.12: Intermediate phases of evolution of composition (phonolite wf) for the shoshonite-phonolite case.

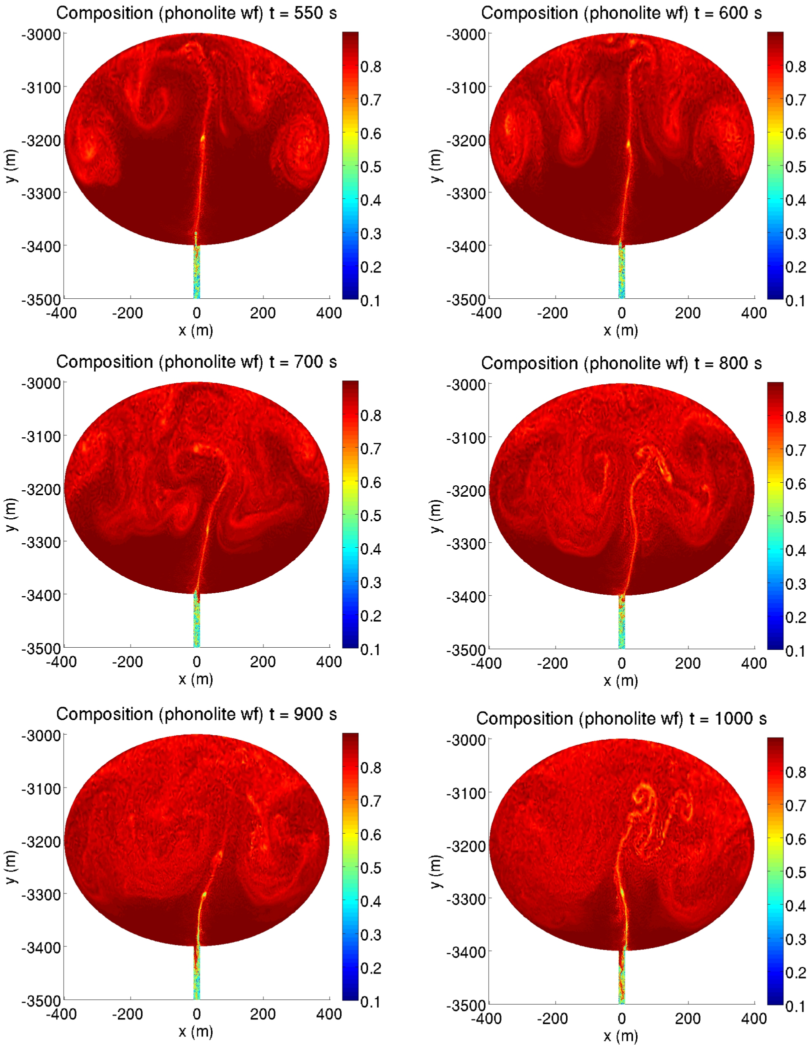

Composition (phonolite wf) t = 550 s

Composition (phonolite wf) t = 600 s

Composition (phonolite wf) t = 700 s

Composition (phonolite wf) t = 800 s

Composition (phonolite wf) t = 900 s

Composition (phonolite wf) t = 1000 s

Figure 6.13: Final (up to 1000 s) phases of evolution of composition (phonolite wf) for the shoshonite-phonolite case.

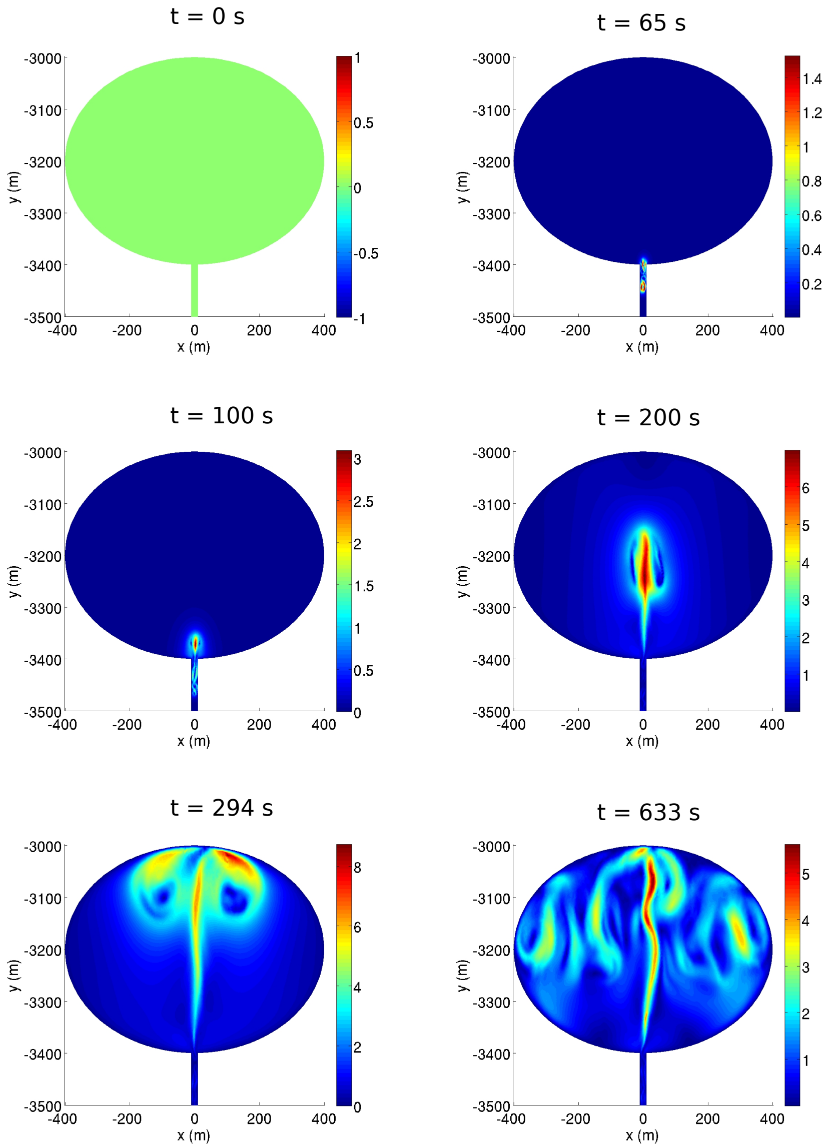

Figure 6.14: The temporal evolution of velocity (m/s) for shoshonite-phonolite case.

As plume ascends pressure decreases which results in an increase of exsolution of volatiles. The decrease in pressure supports the expansion of gases and therefore the plume expands more as it rises towards the roof of the chamber, resulting in a decrease of density of the plume. But at the same time the density of the outer layer of the plume increases due to mixing with the heavier phonolite. This results in a lower density in the central part of the plume and relatively higher density in the outer layer. The lower density of the rising plume with respect to the higher density of the surrounding magma supports the further rise.

The plume reaches the chamber roof at around 270 s and after that spreads laterally (Figure 6.12 at time t = 300 s). During the subsequent times a number of plumes enter the chamber and follows a similar chaotic path as the first plume. Resulting convection enhances the size of both primary vortices. The vortices continue to spread and move along the chamber walls due to gained momentum. The continuous supply of later plumes forms other two vortices near the chamber top at around t = 500 s. By time t = 1000 s almost 80 % of magma present in the chamber is involved in mixing (Figure 6.13). The sinking magma reaches up to 3.8 km depth. At this level phonolite magma loses its identity due to intense mixing. This implies that for later times magma entering in the upper chamber is not fresh any more.

Figure (6.14) shows the temporal evolution of the absolute velocity. The maximum velocity of sinking magma is about 1.5 m/s at t = 65 s. The rising plume gains more velocity as it enters and ascends in the upper chamber. This is due to pressure decrease and exsolution of volatiles, which has the tendency to move more rapidly than the pure melt. It is important to differentiate the velocity of the plume front and the central part of the plume. It is the central part of the plume which gains rapid growth of velocity rather than the front. The host magma continuously interacts with the plume front and try to oppose its motion. As a result the plume front moves much slower than the central part. Though the velocity of the central part of the plume increases significantly and reaches up to 9 m/s, there is a very little increment in the velocity of the plume front. It is observed that after a large perturbation of the interface at time t = 20 s, The rising magma moves with 1.5 m/s in the dike and reaches at the base of upper chamber at t = 50 s. After entering the upper chamber the plume front covers next 100 m (3400-3300 m depth) in 85

s. For the next 100 m (3300-3200 m depth) the vertical velocity of the plume front is 2.2 m/s and for next 100 m (3200-3100 m depth) the vertical velocity of the plume front reaches to 3 m/s. As plume approaches the chamber roof the expansion of vortices and the mixing with the surrounding magma reduces the rising motion. Consequently, to cover next 100 m (3100-3000 m depth) the plume front takes 60 s. As regards the velocity of the central part of the plume, it consistently increases through the rise of the plume and acquires its maximum value of 9 m/s at time t = 294 s (Figure 6.14).

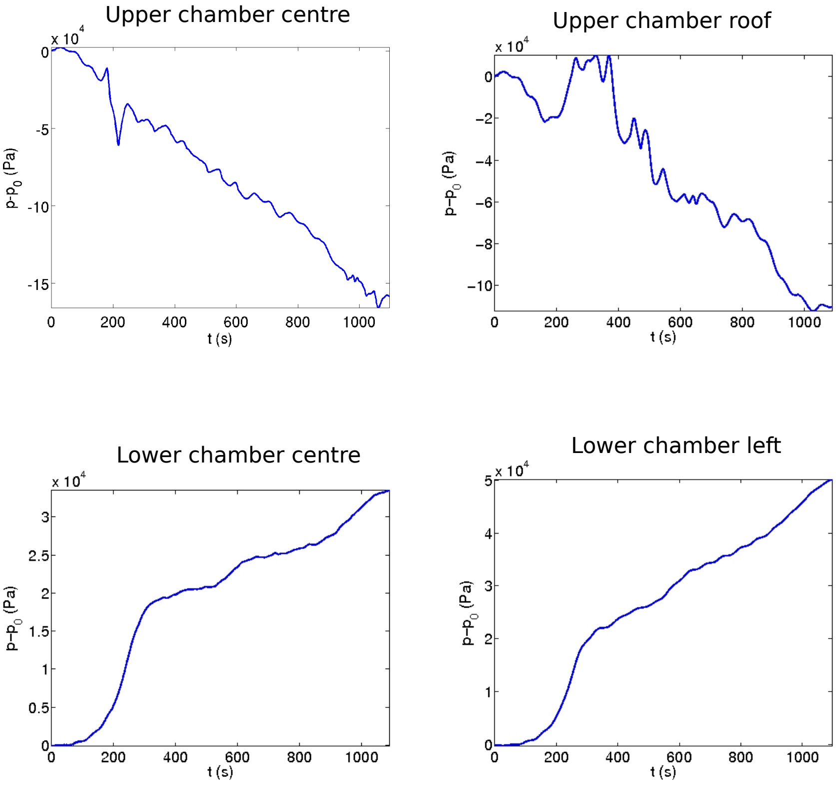

Figure 6.15: The temporal evolution of overpressure (Pa) at various locations for shoshonite-phonolite case.

Pressure is the most important variable in overall dynamics. From the very first moment the lighter magma in the process of rising generates a decompression wave which travels at the speed of about 800 m/s in the dike downwards and leaves the high-pressure area behind. The wave reaches the bottom chamber and reverses, moving upward in the dike. This is related to the starting of disturbance of the equilibrium. However, as magma starts moving the wave is stabilised and decompression is localised at the interface region. Four locations are chosen to analyse the pressure of overall system: the centre of the shallow chamber, the top point of the upper chamber, and, the centre and the left point of the bottom chamber. Figure (6.15) reports the temporal evolution of overpressure. From the beginning of the simulation the overpressure in the upper chamber shows a decreasing trend which is due to the decreasing density of the magma. Figure (6.16) shows the mass of the upper chamber and the dike. The mass of the upper chamber decreases with time whereas the dike gains additional mass. At the upper chamber roof, there is a slight increase in the overpressure during 250-320 s, which is due to the arrival of the plume. During this interval the rising plume tries to compress the magma along the chamber top, therefore, a hike in overpressure is seen for a short duration. The maximum value of overpressure reached on the roof of the upper chamber is 1×10^4 Pa. Every little hike in the profile of overpressure for the upper chamber corresponds to the arrival of new shoshonite magma batches. On the other hand the overpressure in the lower chamber continuously increases due to the sinking of the dense magma. Figure(6.17) shows the temporal evolution of overpressure (Pa), density (Kg/m^3), Gas vol fraction, wt of CO_2 gas in total gas, compressibility (1/Pa) and viscosity (Pas) along the system axis. Overall, the pressure in upper chamber decreases with the time which supports the exsolution of the volatiles. There is an increase of 0.01 vol % of the gas, mostly H_2O. Due to an increase in gas content the compressibility of magma increases in the upper chamber and decreases in the dike. The viscosity shows a decreasing trend in the upper chamber.

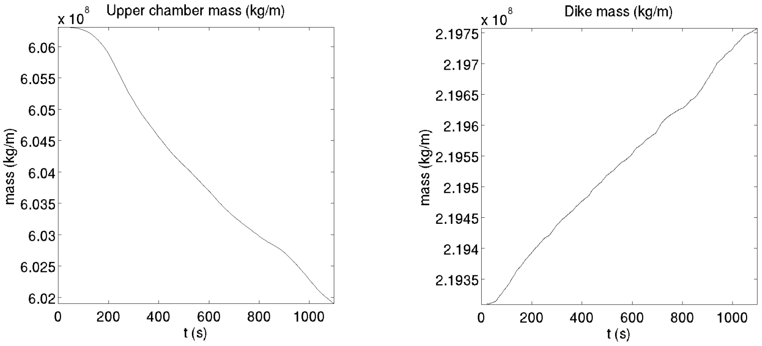

Figure 6.16: The temporal evolution of mass (Kg/m) in upper chamber and dike for shoshonite-phonolite case.

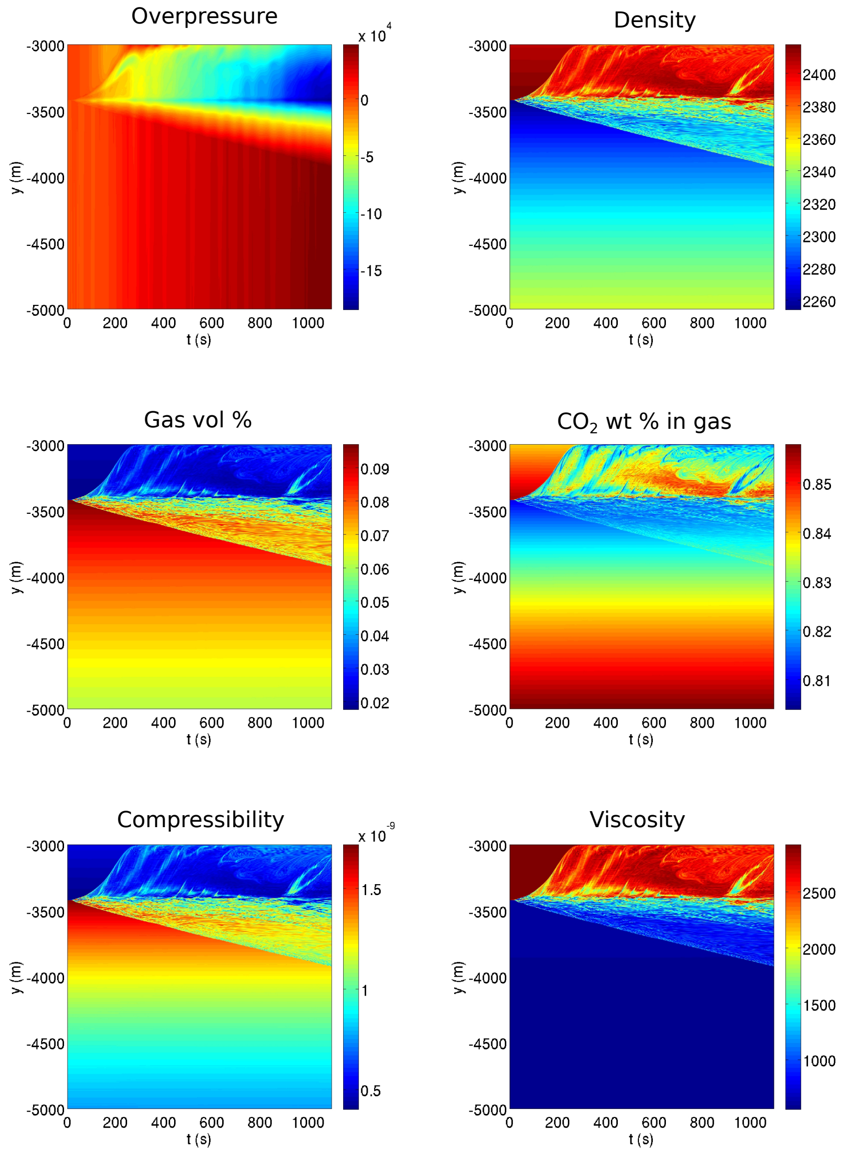

Figure 6.17: The temporal evolution of overpressure(Pa), density(Kg/m^3), Gas vol %, CO$_2$ wt % in gas, compressibility(1/Pa) and viscosity(Pas) along the system axis (3-5 km depth) for shoshonite-phonolite case.

The results for andesite/dacite simulation are shown in figures(6.18) - (6.20). The evolution is similar to the shoshonite/phonolite case, but due to the much higher viscosity of the upper chamber magma, the fluid-dynamics evolution is delayed. The high viscosity of the magma tries to restrain any kind of motion. As a result, the lighter magma takes 60 s to destabilise the interface. Figures (6.18)-(6.20) report the evolution of the interface from the initial interface destabilization, the upward rising of the lighter plume in the upper chamber, and its spreading and mixing with the resident magma. The strong effect of the high viscosity in preventing the rising and mixing of the plume in the upper chamber is clearly visible. The plume takes 170 s to reach the base of the upper chamber. As it was in the previous case, the dense magma sinks in the dike and lighter magma tends to rise up. In this case the host magma restricts the formation of vortices. As a result the andesite magma penetrates the dacite magma along a straight vertical line with extremely less mixing. As plume rises up the decrease in pressure causes the gas expansion and plume expands. Plume takes approximately 550 s to reach the top of the chamber. On the other hand the dacite magma sinks at a much slower rate and retains its signature in the dike. After 1000 s only 20-30 % of the magma in the upper chamber is involved in the mixing. In comparison to the previous simulation, in this case only a few number of small plumes enter in the upper chamber. The second large plume enters in the upper chamber around at t = 750 s and reaches the roof at t = 1020 s.

Again, in this case the velocity of the centre of the plume is higher than the front. The velocity increases as plume rises in the chamber. The maximum velocity of the central part of the rising plume reaches to 4.3 m/s with front moving at 1m/s. Similar to the previous case, the initial disturbance generates a decompression wave which travels downwards through the dike. The speed of the wave is 300 m/s, which is relatively low to the previous case. Figure(6.21) shows the overpressure at specific spots in upper and bottom chambers. The overpressure increases for first 170 s and then after shows a decreasing trend. In the overpressure profile of upper chamber centre there is a little spike at around t = 390 s. This is corresponding to the arrival of the plume. The plume front in the process of rising up try to compress the magma on its way makes a little hike in overpressure.

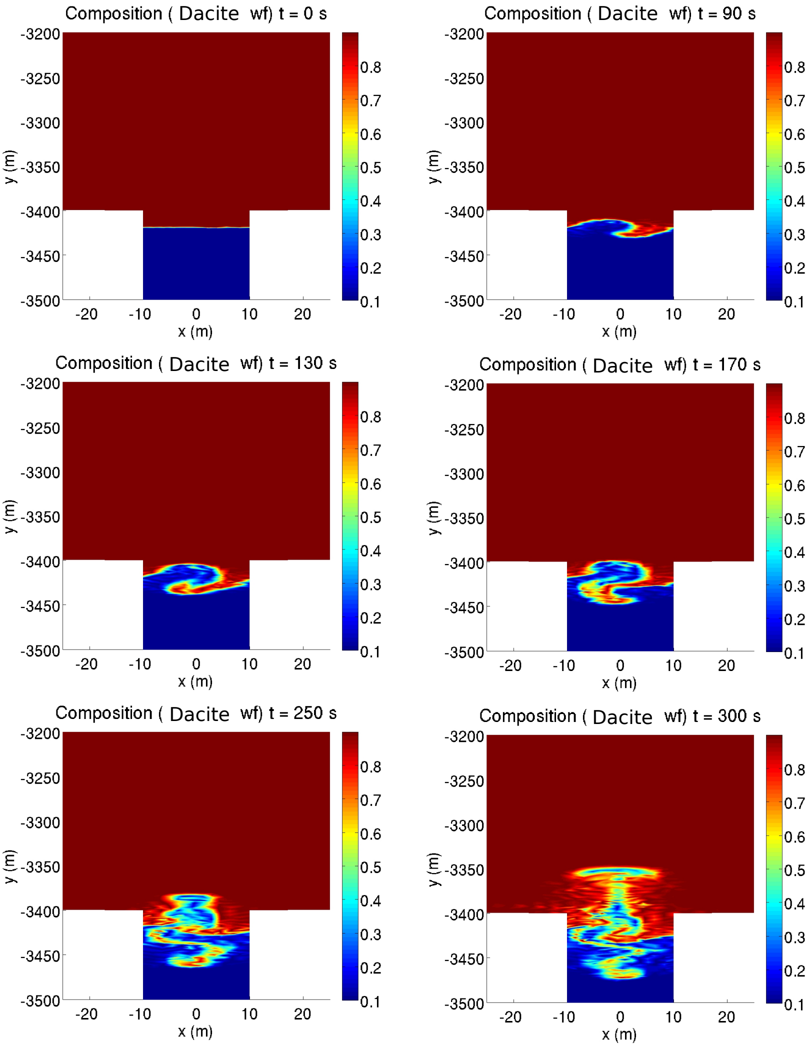

Figure 6.18: Initial phases of evolution of composition (dacite wf) for the andesite-dacite.

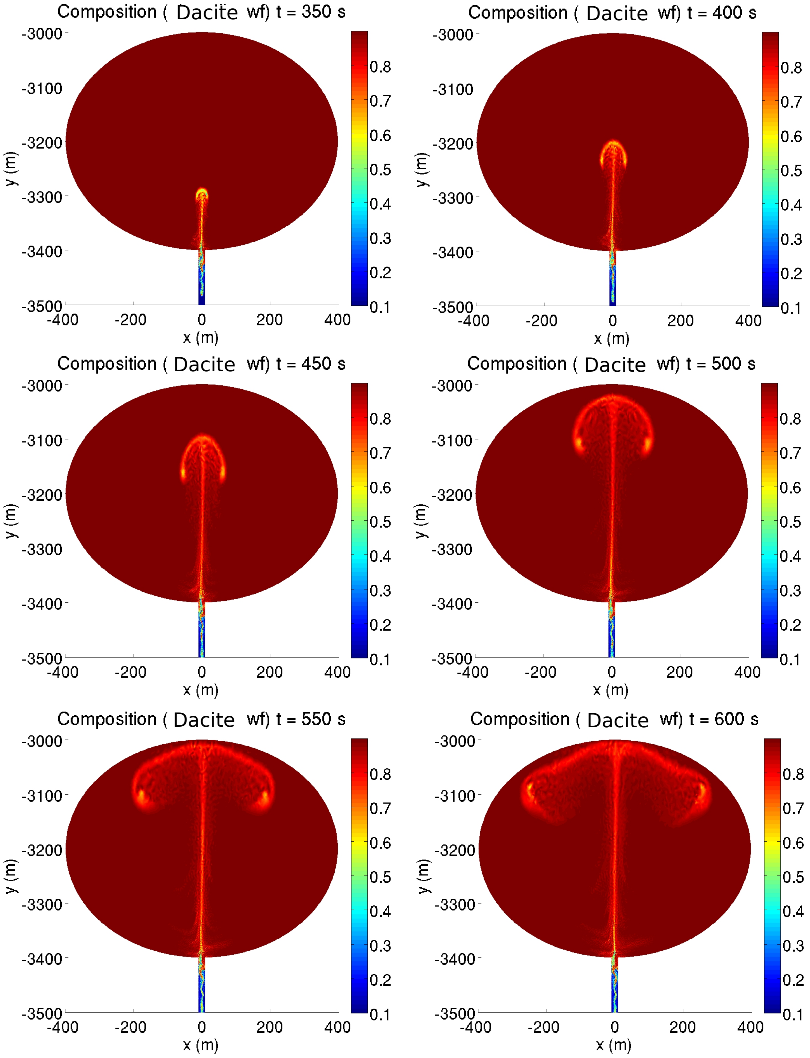

Figure 6.19: Intermediate phases of evolution of composition (dacite wf) for the andesite-dacite case.

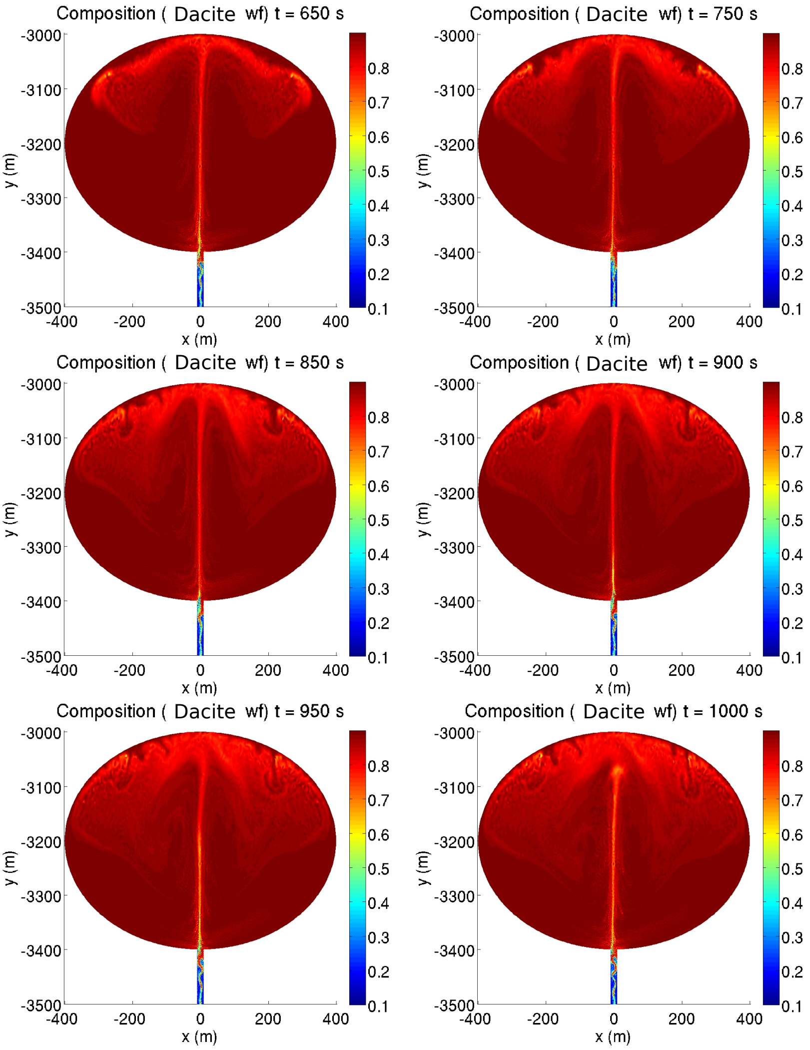

Figure 6.20: Final (up to 1000 s) phases of evolution of composition (dacite wf) for the andesite-dacite case.

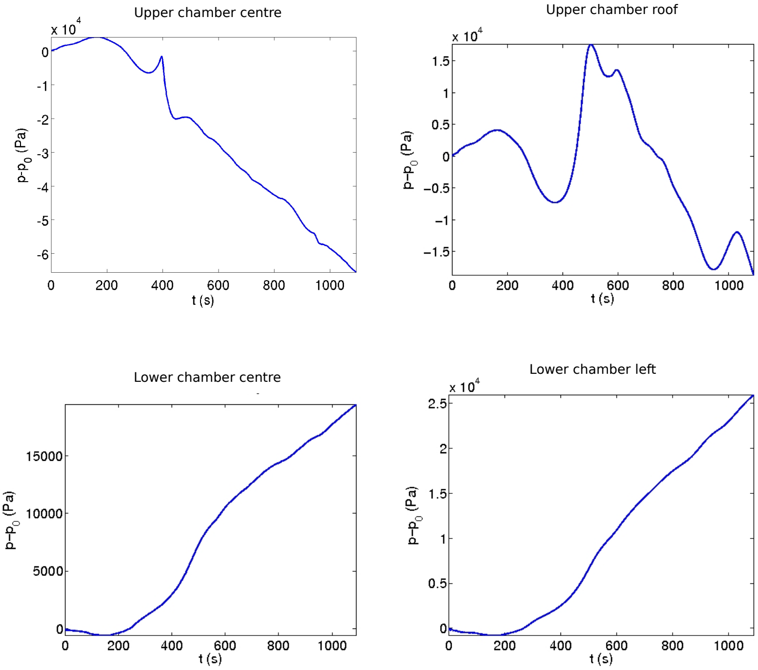

Figure 6.21: The temporal evolution of overpressure (Pa) at various locations for the andesite-dacite case.

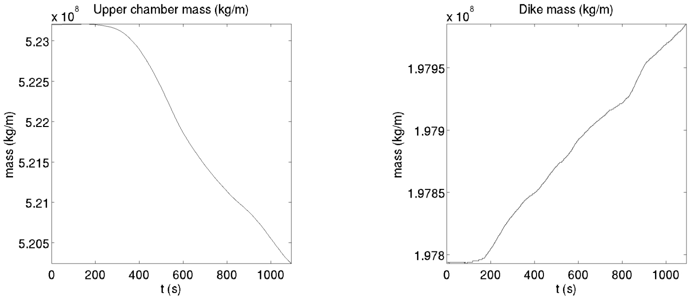

Figure 6.22: The temporal evolution of mass (Kg/m) in upper chamber and dike for the andesite-dacite case.

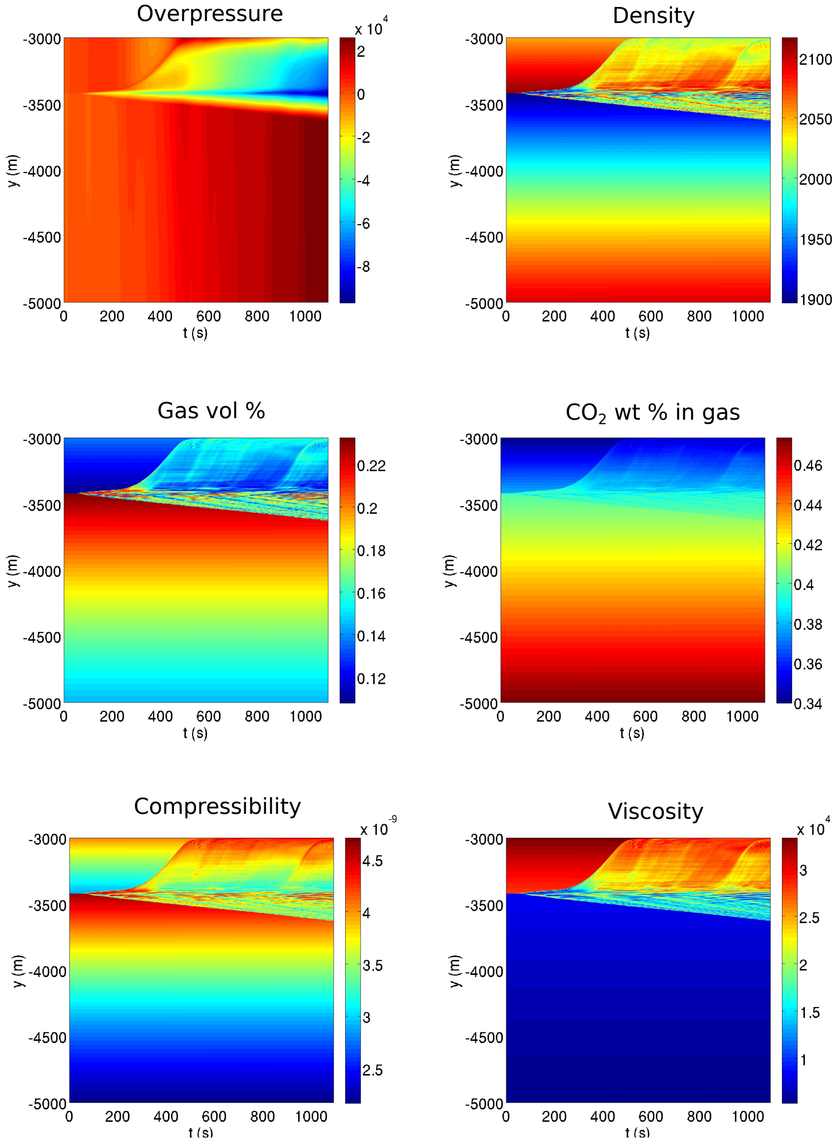

Figure 6.23: The temporal evolution of overpressure(Pa), density(Kg/m^3), Gas vol %, CO_2 wt % in gas, compressibility(1/Pa) and viscosity(Pas) along the system axis (3-5 km depth) for the andesite-dacite case.

Similar to the centre of the upper chamber on the roof there is an increase of overpressure for the first 170 s. The maximum value of overpressure at the roof of the upper chamber reaches to 1.7×10^4 Pa which is very close to the previous case. At time t = 1020 s there is a tiny increase of overpressure at the roof which is caused by the arrival of the second plume. The overpressure in lower chamber shows a general increasing trend which is due to the sinking of the dense magma in the dike. Figure(6.22) displays the mass of the upper chamber and the dike. Similar to the other case the mass of the upper chamber decreases and the mass of dike increases with time. Figure(6.23) reports the temporal evolution of overpressure (Pa), density (Kg/m^3), gas vol %, CO_2 wt % in gas, compressibility (1/Pa) and viscosity (Pas) along the system axis. The density of magma in upper chamber decreases with time as the lighter magma accommodate the place of denser magma. The average density of the magma in the upper chamber decreases by 150 Kg/m^3. The decrease in pressure cause the exsolution of the volatiles. As a result, almost 30 % of the magma has 0.05 vol % increment of the gas. The CO_2 increases by 0.01 wt %. Similar to the last case the compressibility increases and the viscosity decreases in the upper chamber.

6.4 Case 3: Influence of a near-field seismic wave on magma chamber dynamics

Earthquakes and volcanic eruptions usually occur at the meeting boundary of converging tectonic plates. Many people proposed correlations between large earthquakes and eruptions [25, 117]. Seismic swarms are often observed in the proximity of active volcanoes. This indicates that the seismic signals observed by monitoring networks at the surface of volcanoes can be directly related to the motion of magma taking place somewhere underneath. The magma intrusion may change the stress at active faults and trigger earthquakes [211]. Several models have been developed in the recent past to study the deformation induced by the magma dynamics [70, 118]. Further studies and the development of new models aimed at depicting the accurate deformation and strain as a result of applied magmatic forces are still an ongoing research field.

On the other hand, the earthquakes may influence the magma dynamics and the eruptive scenario [152]. Many studies suggest that the earthquakes preceded a large-scale change in magma dynamics and in some cases even eruptions [204, 210]. During his journey in Chile when an 8.5 magnitude earthquake struck in 1835, Charles Darwin reported that at least three volcanoes erupted there in the aftermath of the quake [36]. Eruptions also followed earthquakes in Chile in 1906 [169]. The most unambiguous case of triggering is the Kalapana, Hawai earthquake of November 29, 1975, with a magnitude of 7.2, which was immediately followed by a small and short-lived eruption at Kilauea volcano [160]. Another example of possible triggering occurred after the 9.5 magnitude earthquake on May 22, 1960, in Chile. Puyehue-Cordn Caulle in Central Chile, an inactive volcano for more than 25 years, erupted violently about 38 hours after the main shock [116]. On the contrary, there are also a number of cases where no eruption was recorded after a proximal earthquake. Chile 2010 is one among these examples in which no activity was observed after a magnitude of 8.8 earthquake struck [179]. Another case occurred in Japan where a magnitude 9.0 earthquake struck in 2011 and did not result in any eruption [170]. Although there are many evidences that the two phenomena can interact each other, the impact of the earthquake on magma dynamics has not been understood completely.

It is important to understand the triggering mechanisms quantitatively not only for the scientific interests but also for the mitigation of volcanic risks. Since a volcanic eruption requires a change in stress for permitting the migration of magma to the surface, the static stress change induced by an earthquake is considered to be a key issue of the triggering mechanism [65, 121, 203]. Understanding the internal dynamics preceded by an earthquake is crucial for hazard evaluation. High amplitude seismic waves passing through a magma reservoir may destabilise the system which was in a state of a semi-equilibrium prior to the arrival of seismic wave. The destabilisation can affect the mixing of meta-stable layers of magmas, with different composition, and can result in providing momentum to magma chamber dynamics.

The simulation cases presented in this section explore what can happen when a near-field earthquake strikes with a magmatic reservoir. The two simulation cases performed in the previous section are modelled under the condition of the passage of an earthquake. The main objective is to study the scenario of development of dynamics of magma in case if the magmatic system is shaken by some near-field earthquake. This work does not study the change in stress field induced by the seismic wave. In order to simplify the things, the rock dynamics is not accounted in the simulation cases. The seismic wave is not propagated from the source, rather the instantaneous displacements and velocities of the seismic wave are taken and applied to the magmatic system in order to shake it. The simulation results obtained after the strike of a near-field seismic wave are compared with the results of the simulations performed without an earthquake.

6.4.1 Simulation set up

The domain geometry and magma model are the same as were in the last two simulations. Two magma chambers filled with different magmas are connected by a dike. The same initial conditions are set. Since the aim of this study is to investigate the magma dynamics induced by a near-field seismic wave, the distance between the source of the earthquake and the magmatic system is assumed 15.5 km. The seismic wave data is taken from Petrolia/Cape Mendocino earthquake, 25-26 April 1992, of 7.2 magnitude of the Richter scale [20]. The setting of the hypocenter with respect to the system is reported in Figure (6.24). The distance between the source of the earthquake and the magmatic system is assumed 15.5 km. The Up and North-South components of the seismic wave are depicted in Figure (6.25).

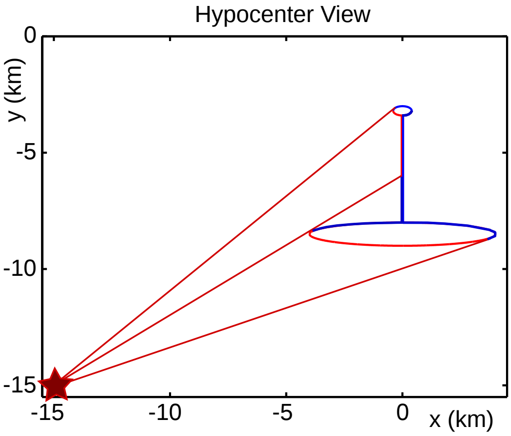

Figure 6.24: Position of the hypocenter with respect to the system.

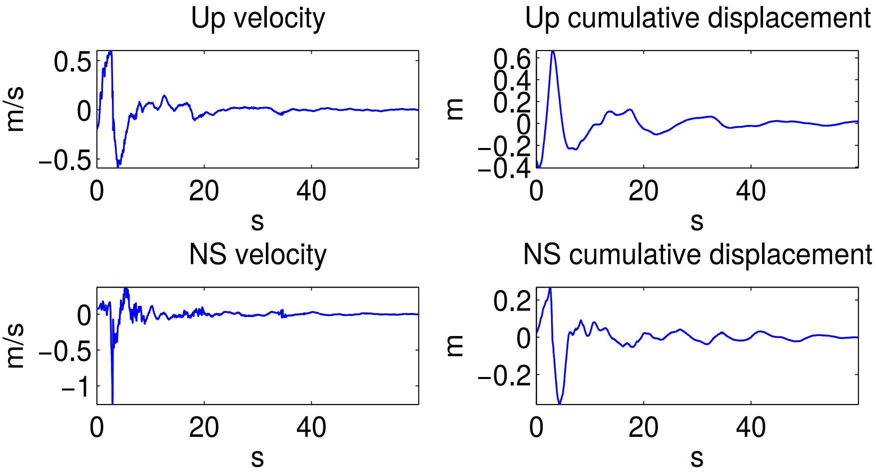

Figure 6.25: Up and North-South components of the seismic wave.

The simulations are performed over the same geometry and physical set up of magmas as were employed in the previous simulation. Magma static pressure and zero velocities are set as the initial conditions for the magma problem. For the simulation case, the magma chamber is assumed to be surrounded by an elastic thin (1 m) layer of rock. The absorption of the seismic wave by the rock between the source and the magmatic system is not considered in this study. This simulation requires coupling with the surrounding layer of rock. In order to do the coupling, the following initial and boundary conditions are applied. The initial conditions for the elastostatic mesh problem are set as zero deformation. The boundary conditions for the magma problem are set in the following way. Along the domain boundary where seismic wave strikes (boundary in red colour in Figure 6.24), the fluid velocity is set equal to the velocity of the seismic wave. On the remaining part of the domain boundary (boundary in blue colour in Figure 6.24), the fluid velocity is set equal to the velocity of deforming rock layer which is evaluated from the solution of the elastostatic problem. For the elastostatic problem, the boundary conditions are the seismic deformation on the boundary where seismic wave strikes (boundary in red colour in Figure 6.24) and the magma traction forces on the remaining part (boundary in blue colour in Figure 6.24).

6.4.2 Results

At time t = 0 s, the seismic wave strikes on the magmatic system boundary shown in red colour in Figure 6.24. The seismic wave interacts with the system for 60 s. The behaviour of the mixing of magma is similar to the shoshonite-phonolite case discussed in the previous section. The interface starts getting perturbed around at 12 s and at 50 s a plume of buoyant shoshonite reaches at the top of the dike and enters inside the upper chamber. From the base to the top of the upper chamber plume covers 70 m between 50-110 s, 110 m between 110-170 s, 120 m between 170-230 s and 100 m between 230-270 s. Thus, it takes approximately 220 s to reach from the bottom to the top of the upper chamber, covering a total distance of 400 m.

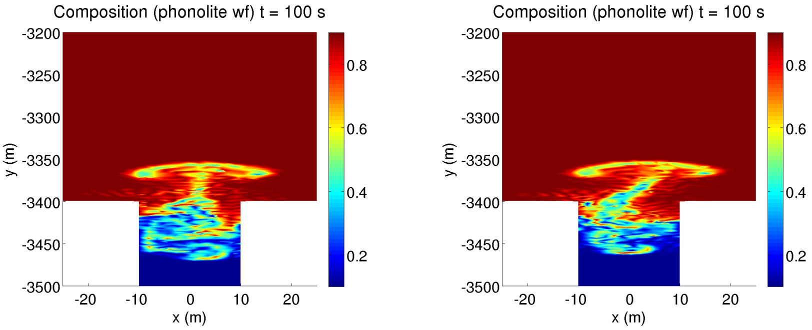

Figure 6.26: The comparison of the inclination of the rising plumes at time t = 100s. The left panel shows the case of shoshonite-phonolite discussed in the previous section and the right panel shows the present case (shoshonite-phonolite shaken by the seismic wave).

The only minor difference between the cases with and without the seismic wave is the inclination of the rising plumes. In the case of seismic wave, the rising plume is more deflected (see Figure 6.26). Whilst the plume of shoshonite invades the upper chamber, phonolite makes a passage in the dike and mix with the surrounding magma. The vertical motion of the rising and sinking magma is accompanied by the formation of a number of vortices which contribute further to magma mixing. In this case, the velocities fluctuate for the first 150 s. However, the magnitude of the velocity is the same as it was without seismic wave case. The plume reaches its maximum velocity of 8 m/s when it is near the roof of the upper chamber.

The sudden arrival of the wave generates a longitudinal overpressure wave which travels through the system from left to right and top to bottom. The speed of the generated wave is observed in the range of 750-1000 m/s. Figure (6.27) shows the temporal evolution of overpressure wave at the various locations in the domain.

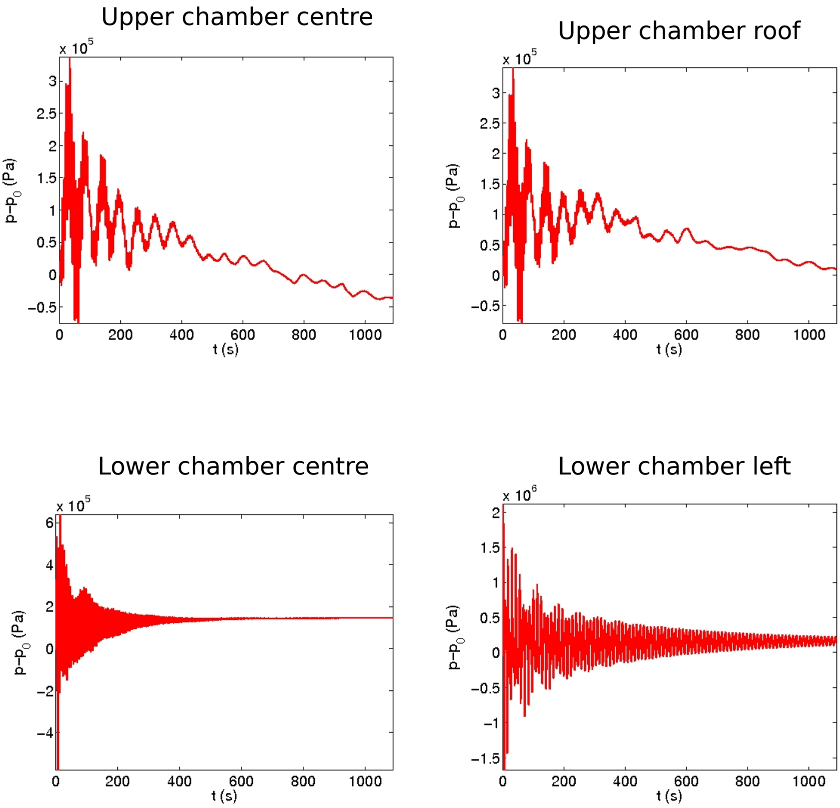

Figure 6.27: Overpressure (Pa) in the system at various locations for shoshonite-phonilte seismic wave case.

The seismic wave causes the fluctuation of overpressure in the domain. In the upper chamber, the maximum value of overpressure reaches to 3.5×10^5 (Figure 6.28). The wave lasts in the system for a longer time. The system is simulated up to 1100 s and observed that the wave is still present (see Figure 6.29). The amplitude of the wave decreases with time due to the viscosity of the magma. Since the seismic wave shakes the system only for first 60 s, the wave loses its energy proceeding in time. Eventually, after 500 s the wave almost dampens and there are minor fluctuations of overpressure, showing a decreasing trend. On the other hand, at the centre and on the left of the bottom chamber the maximum values of overpressure reaches to 6.3×10^5 Pa and 2.2 MPa respectively. Similar to the upper chamber, the wave lasts in the bottom chamber until the end of the simulation. The overpressure in the bottom chamber shows a general increasing trend. Figure (6.30) compares the overpressure along the system axis for seismically shaken case and without seismic wave case. In comparison to the upper and bottom chambers, there is a significant hike of overpressure in the dike. The maximum value of overpressure in the dike reaches 2.2 Mpa. However, for later times the wave continues to dampen and in the end, attains a similar profile of no seismic wave case.

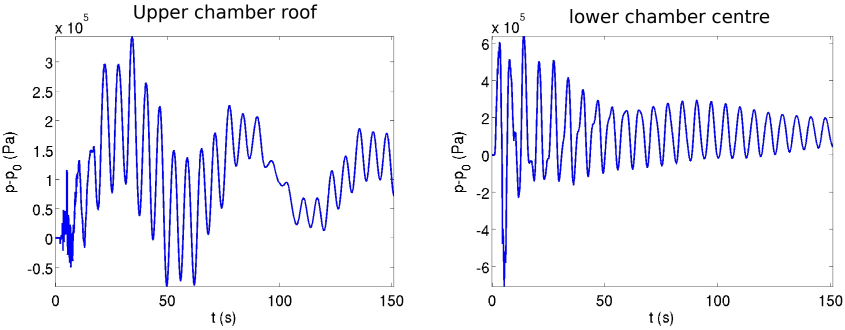

Figure 6.28: Zoom view of overpressure (Pa) at the upper chamber roof and at the centre of bottom chamber for first 150 s for shoshonite-phonilte seismic wave case.

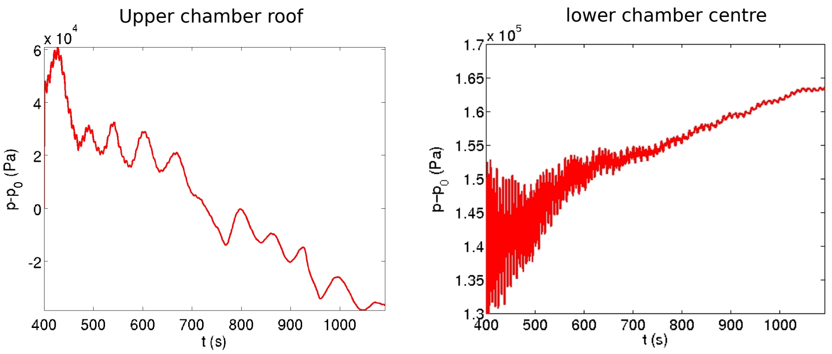

Figure 6.29: Zoom view of overpressure (Pa) at the upper chamber roof and at the centre of bottom chamber for 400-1100 s for shoshonite-phonilte seismic wave case.

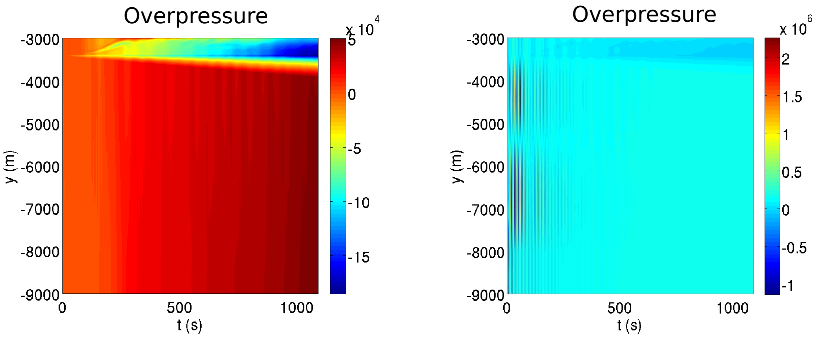

Figure 6.30: The comparison of overpressure (Pa) along the system axis. The left panel shows the case of shoshonite-phonolite discussed in the previous section and the right panel shows the present case (shoshonite-phonolite shaken by the seismic wave). The horizontal axis displays the time and the vertical axis displays the depth of the magmatic system along the central line.

Figure (6.31) reports the temporal evolution of the mass of the upper chamber and the dike. There is a disturbance in the mass for first few seconds whilst the seismic wave is striking with the system. In the upper chamber, this disturbance continues up to first 170 s while in the dike it lasts longer, up to 360 s. The general trend for the mass is similar to the case of no seismic wave. The upper chamber loses the mass and the dike gains proceeding in time.

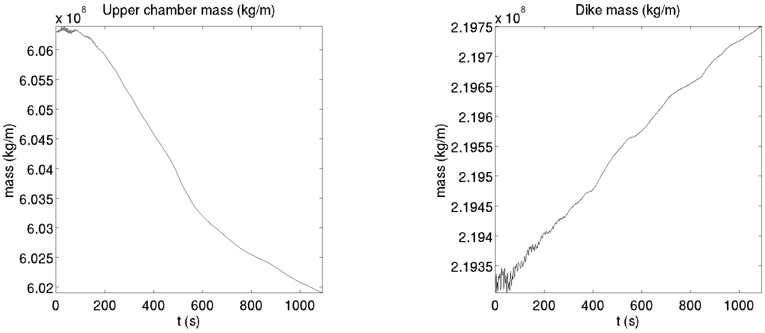

Figure 6.31: The temporal evolution of mass (Kg/m) in upper chamber and dike for the shoshonite-phonolite seismically shaken case.

The results of the andesite-dacite magmatic system shaken by a seismic wave are similar to the ones discussed in the previous section (the case without seismic wave) in the sense of mixing, magma motion as well as the physical variables such as density, viscosity etc. The only difference is the formation of pressure wave due to the seismic wave. The results for the overpressure are shown in Fig (6.32). In this case, due to a much higher viscosity of the magma, the pressure wave dampens quickly. The maximum overpressure at the roof of the chamber is reached to 6.2×10^5 Pa, while on the left part of the bottom chamber the maximum overpressure reaches to 2.9 MPa. Figure (6.33) compares the overpressure in the dike. The maximum value of overpressure in the dike reaches to 2.3 MPa.

The interaction of seismic wave with the system causes changes at the microscopic level, which is mainly seen only in the generation of overpressure wave. Macroscopically the evolution of the overall dynamics is similar to the case of no seismic wave. The density, gas vol fraction, CO_2 gas mass fraction, compressibility and the viscosity show exactly similar behaviour as was discussed in the previous section.

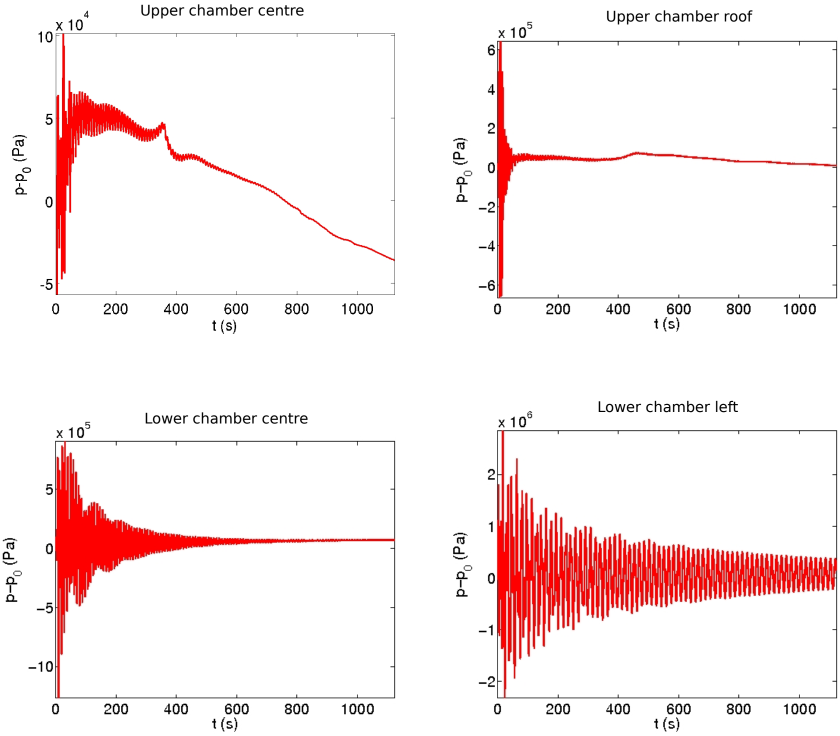

Figure 6.32: Overpressure (Pa) in the system at various locations for andesite-dacite seismic wave case.

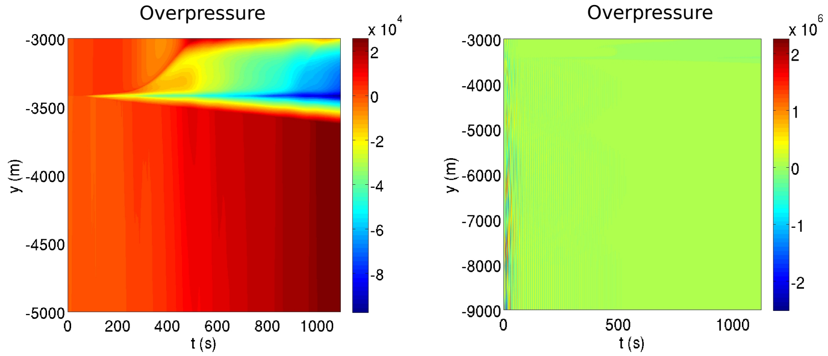

Figure 6.33: The comparison of overpressure (Pa) along the system axis. The left panel shows the case of andesite-dacite discussed in the previous section (3000 to 5000 m depth) and the right panel shows the present case (andesite-dacite shaken by a seismic wave). The horizontal axis displays the time and the vertical axis displays the depth of the magmatic system along the central line.

6.5 Discussion

The time scale of the processes occurring in a magma chamber can vary from a range of minutes to years. The occurrence of convection inside the magma chamber is a fundamental process. The convection can be either natural or forced. Hereby, natural convection is referred as the mechanism by which the magma motion is generated by density differences in magmas. It can be either due to different compositions of two magmas or due to temperature gradients. The forced convection can be caused by the excess forces of the bottom magmatic system which try to push the magma upwards. A numerical study is performed on natural convection cases taking place because of buoyancy forces. The model accounts in the most realistic conditions of magma mixing dynamics, in terms of local compressible/incompressible behaviour of the magma. The density and viscosity are modelled as a function of the composition of magma, temperature and pressure. The simulation results illustrate many interesting processes that occur during magma replenishment.

A number of forces come into play and the resulting scenario is a consequence of all the factors. Two principal forces acting and influencing the dynamics are viscosity and buoyancy. The viscosity opposes the motion while buoyancy supports. The simulation results show that the evolution of magma properties is non-linear and magmatic properties vary in space and time corresponding to the local conditions.

The time-scale of convection and mixing largely depends on the viscosity of the magma. Three different combinations are employed in the simulations; basalt-hot/basalt-cold, shoshonite/phonolite and andesite/dacite. Among these, basalt and shoshonite/phonolite are less viscous in comparison to andesite/dacite. The simulation results show that the mixing is faster and more efficient for the basalt and shoshonite/phonolite cases than the andesite/dacite case. In the case of basalt and shoshonite/phonolite, the convection starts around 30 s and mixing time scale is in the range of a few hours. In the case of andesite/dacite, the starting time of the convection is 60 s and by the end of 20 minutes, only a minor part of the magma is involved in the mixing process. This suggests that the mixing time scale for the andesite/dacite case can be in the range of tens of hours. In shoshonite/phonolite and andesite/dacite cases, denser magma continuously sinks in the dike and interact with the lighter one. As a result, after few minutes, the plumes coming from the dike are not of fresh magma. The density of the magmas in the shallow chamber decreases due to mixing with the lighter magmas of the plumes. This leads to a decrease in the density contrast between incoming and host magmas, and hence slows the mixing process. Also, due to viscous dissipation, the mixing slows down for the later times. It is important to notice that the present results are with the assumption that the magma has no crystals and the crystallisation does not occur. In contrast, often in magma chambers, the crystallisation occurs due to the loss of heat to the surrounding chamber rock, which results in an increase in viscosity of magma by orders of magnitude. In such cases, the magma can not be modelled as a Newtonian fluid and the non-Newtonian rheology must be considered. The ascent speed of a high viscous magma ($10^6 - 10^7$ Pas) can be as low as 5-20 m/day [166] and the mixing time scale can be of hundreds of years. The simulation cases studied here are with the assumption of the Newtonian rheology of the magma which restricts us to neglect the crystallisation. The results obtained in the current work are in agreement with [12, 13, 43].

In the first case of natural convection driven by the temperature contrast, the self-mixing between the hot and cold basalt magma is studied for 1500 s. The aim was to see the dynamical evolution during a self mixing event. According to the simulation set up, the value of Atwood number, A = $(\rho_h - \rho_l)/(\rho_h + \rho_l)$ at time t = 0 is 0.003, which indicates the hydrodynamic instabilities between density stratified magmas. The simulation is a particular situation in the closed domain when the magma is injected into a chamber and the Rayleigh-Taylor instability develops due to the density contrast. The cases in which the magma injection continues for a long time, the resulting scenario can be different. The current simulation results show that the diffusion among the hot and cold magmas generate the vortices, which tend to slow down at later times due to the viscous forces and approach to a stable equilibrium state. The velocity of the rotating vortices depends on the viscosity of the magma. The maximum velocity in the current simulation reached to 2.426 m/s which decreased to 1.43 m/s for the later time. As expected, the overpressure increases in the chamber by a magnitude of few kPa. The maximum hike in the overpressure is observed at the roof of the chamber by a magnitude of 6 kPa. The same simulation setup is applied to an irregular chamber to study the effect of the domain irregularities. The obtained results are found to be in a close resemblance to the elliptical case. This indicates that for such kind of self-mixing, the domain geometry does not have an effective influence on the dynamics.

In the second case, the magma mixing has been studied to track the dynamical evolution when magma coming from deeper source reaches a shallower chamber. It is important to note that here the only driving force is buoyancy. Two simulations are performed over two different magma combinations. The first one with shoshonite/phonolite magma took as reference the most recent reconstruction of a possible magmatic reservoir at Campi Flegrei (Italy) while the second one with andesite/dacite represented a case of arc magmatism. In both simulations, the same domain was used. The two simulations shared a common setup, a smaller shallower magma chamber containing degassed and more evolved magma, connected through a dike with a bigger deeper magma chamber filled with volatile-rich less evolved magma. The different compositions of magma determined a density contrast. The initial values of Atwood number for the shoshonite/phonolite and the andesite/dacite were

0.034 and 0.05 respectively. Even though the values of Atwood number were small as in the first case, they were still large enough to infer the instability between the two magmas at the interface. Infact, this is evident also from the values of Froude number.

$$Fr = v/\sqrt{gl} \tag{6.3}$$

which were approximately equal to 0.565 and 0.282 corresponding to maximum velocity reached for shoshonite/phonolite and andesite/dacite case respectively. In the above formula, v is the characteristic velocity, g is the gravity and l is the characteristic length. For the earlier times, the values of Froude number were even smaller representing that the small surface waves will move upstream with time. Note that the Froude number is analogous to the Mach number. A greater value of the Froude number indicates a greater resistance. In the simulation cases considered here, the density ratio ρ_l/ρ_g for shoshonite/phonolite and andesite/dacite magmas are low. Here, ρ_l and ρ_g are the densities of the liquid melt and the gas. As the density ratio are low for the small values of Atwood number, the relative velocity between the phases is very small and can be neglected. This justifies that the assumption of homogeneous multicomponent flow model is valid. The value of Archimedes Number has also been examined.

$$Ar = \rho L^3 g \Delta\rho/\mu^2 \tag{6.4}$$

For shoshonite/phonolite and andesite/dacite cases the values of Ar are 80355 and 498 respectively. The value of Ar which is greater than 1 for both cases indicates that the buoyancy forces are dominating over the viscous forces. However, for shoshonite/phonolite case a larger value of Ar suggests that the flow will be more rapid than the andesite/dacite case. This is evident from the simulation results that in the case of andesite/dacite the viscous forces play a crucial role in restraining the flow. As a result, a much less efficient convection dynamics emerges from the andesite/dacite case in comparison to the shoshonite/phonolite case.

The density contrast between the two magmas generates a destabilisation at the interface. The movement of the interface produced a decompression pressure wave travelling first downwards and then upwards. This was due to the response of the magmatic system towards the disturbance of equilibrium. The wave stabilised as the system got ready for its further dynamical evolution. As the plume of lighter magma entered from the dike into the upper chamber, two main features of the rising plume are observed. The plume accelerated during its rise in the upper chamber. The decompression caused the expansion of volatiles, which increased the rising velocity of the plume. The second interesting feature is the cap shape of the plume, which contributes to the formation of vortices. The two ends of the cap shape of the plume generate two small vortices which continue to broaden due to convection with the hosting magma. After striking the chamber roof the vortices spread along the walls of the chamber and interact with more magma, mixing and trying to equilibrate the density. The mixing between the magmas is strengthened with the arrival of subsequent fresh plumes which enter the shallow chamber after the primary one. Viscosity played a crucial role in restriction of convection as well as the entering of the subsequent plumes. For andesite/dacite case only a countable number of plumes enter in the upper chamber in comparison to the shoshonite/phonolite case. The maximum rising velocity is reached to a few meters per second.

In both simulation cases, pressure in the upper chamber decreases. This makes sense because low-density magma was entering into the chamber which makes the host dense magma to sink in the dike. In the upper chamber the mixing between the magmas of different densities lowers the overall density locally as well as globally. This in a result reduces the thermodynamic pressure which is the sum of magma static pressure and the dynamic pressure due to the motion of magma. As plume is rising up the magma static pressure is decreasing which induces the exsolution of volatiles and decreases the density. On one hand the increment in velocity due to the exsolved gas increases the dynamic pressure, whereas, on the other hand the decrease in density tends to decrease. The dynamic pressure increases during the rise of the plume but soon after as the plume strikes with the roof and spreads along the walls of the chamber, the velocity decreases as well as the density of the mixing magma, which overall reduces the thermodynamic pressure. In this model the thermodynamic pressure coincides with the mechanical pressure. The mechanical pressure for any parcel of the fluid can be written as

$$p_{mech} = p_{ther} - \Big(\lambda + \frac{2}{3}\mu\Big)\boldsymbol{\nabla}\cdot\boldsymbol{v} \tag{6.5}$$

here, p_{mech} and p_{ther} are the mechanical and thermodynamic pressure respectively. $\lambda + \frac{2}{3}\mu$ is the bulk viscosity. Although, $\boldsymbol{\nabla} \cdot \boldsymbol{v} \neq 0$ but by setting $\lambda = -2/3\mu$ according to Stoke's hypothesis, the bulk viscosity is set equal to zero in the model and hence the small difference between the thermodynamic and mechanical pressure is neglected. For the upper chamber, a general decreasing trend of the overpressure is attained. However, at the roof of the chamber, there is some increment in the overpressure, which is associated with the arrival of the plume. In both shoshonite/phonolite and andesite/-dacite cases, the maximum value of overpressure at the roof of the chamber is reached to $\approx 10^4$ Pa, which is not sufficient to rupture the wall rock. On the other hand, in the dike as well as in bottom chamber there is a profile of increasing overpressure. The rise of overpressure is little higher along the boundaries than the centre which is reasonable as the boundaries have less space to distribute the force in comparison to the centre. On the other hand, the sinking of dense magma increases the mass and the overpressure in the dike as well as in the bottom chamber. According to the simulation results, with such type of geometry and physical set up the influx of magma in the upper chamber is lower than the outflux, which is the main reason for the decrease of overpressure. However, a general hypothesis can not be set on the basis of the simulations performed here. It requires a large number of simulations and the parametric study, which was not in the scope of the current research work. It is very much likely that the different setup and domain geometry can lead to different results. The aim of these simulations was to understand the physics behind the processes with specified domain and model assumptions. The interesting point emerged from this study is the role of viscosity, which not only delays but also significantly affects the mixing and the convection.

Products of eruptions may be representative of the magma chamber state just prior to the eruptive event, despite the ejection processes can strongly influence the magmatic conditions of the chamber itself. However, petrological and chemical investigations show several cases where magma conditions in the chamber are clearly preserved [132, 157, 168]. The eruptive sequences of the 1915 Lassen Peak (California) [132], the AD 1640 and 1694 of Hokkaido-Komagatake Volcano (Japan) [157], and the Akagi Volcano (Japan) [168] show that mafic products were erupted at first, followed by mixed/mingled mafic to silic magma, ending with the silicic end-member. This could be interpreted as a stratified magma chamber with upper mafic and lower silicic regions, and an intermediate zone of mixed/mingled magma. This is in accordance with the simulations of the shoshonite/phonolite and andesite/dacite cases where the plume of less evolved magma rising from the feeding dike reached and accumulated at the top of the shallower magma chamber, giving rise to convection inside the chamber promoting mixing/mingling between the more evolved residing magma and the less evolved injected one.

In the third case, the effect of a near-field seismic wave on the evolution of magma chamber replenishment dynamics has been studied. Contrary to the previous case, where the dynamics was solely driven by the density contrast between two heterogeneous magmas, here an external disturbance is passed to the system in the form of a seismic wave. This study is of particular importance because there are ample pieces of evidence which reflect a correlation between the earthquakes and change in magma dynamics. The later could eventually culminate into an eruption. Much of the research on this topic has been focused on the stress change around the walls of the magma chamber, which can further be distinguished as the static stress change and the dynamic stress change. Possible effects of the seismic waves on volcanic behaviour have been proposed in the literature. Nevertheless, most of these are based on logical reasoning of the authors. The current simulations model the scenario numerically which allows examining the detailed features of the evolution of the magma dynamics. The real earthquake data of Petrolia/Cape Mendocino, 25-26 April 1992 has been used in the simulation. The hypocenter of the earthquake was assumed close to the magmatic system. This allowed us to neglect the attenuation of the seismic wave. The propagation of the seismic wave through the surrounding rock can be successfully computed by the viscoelastodynamics equations (see chapter2 and chapter5). But, since this step is not implemented in the computer code yet and the prime objective is to focus on the magma dynamics, the absorption of the seismic wave by rock is neglected. The wave data was applied to the magmatic system by the boundary conditions. The domain setup for the magmatic system was the same as the second case. The seismic wave impinged with the system at time t = 0. Though the strike of the wave produced some disturbance of velocities near the boundaries, the evolution of plume rise and convection was similar to the second case (without external excitation). The velocities were observed to fluctuate for the earlier times whilst the wave was shaking the chamber.

The impressive result obtained from the simulation is the appearance of the overpressure wave, which is generated due to disturbance caused by the seismic wave. Though the seismic wave shakes the chamber for 60 s, the longitudinal overpressure wave is still there even at 1500 s. The amplitude of the overpressure wave is observed to decrease in time due to the viscous dissipation and eventually seems to attain a smoother profile for later times. Nevertheless, the overpressure in the system is increased. In the upper chamber, it is one order of magnitude higher, whereas, in the dike and in the bottom chamber, it is two order of magnitude higher than the second case (without external excitation). The wave is more effective in the dike and on the left of the bottom chamber with an increase in overpressure up to 2.2 MPa. The seismic wave has negligible effect on other flow variables (density, viscosity etc.) These are the results when the seismic wave shook the system at the very early stage of mixing and convection. However, if there were already ongoing mixing which would increase the overpressure in the dike as well as in the bottom chamber (as was seen in the case without external excitation), the impinge of a seismic wave might increase the overpressure beyond a critical value. If there was a crack, for such overpressure it could be very likely to propagate further.

In [120] authors suggested that the small lateral distance and mechanical interaction between dike and fault could have triggered the slip observed on the fault during the North Mono-Inyo eruption sequence of 1350 A.D. after a series of strong earthquakes. The slip, in turn, could have reduced the horizontal confining pressure in a region near the southern tip of the fault. The presence of the main Inyo vents in this region suggests that the reduction in confining stress was sufficient to allow magma to propagate to the surface. Two volcanic eruptions in the Sumatra-Andaman arc were followed the disastrous M 9.3 earthquake of 26 December 2004. In [203] authors suggested that earthquake-induced decompression of the volcano magma systems leads to such eruptions. The earthquakes can promote eruptions by compressing the magma body at depth and opening suitably oriented near-surface conduits. Voiding the magma body in turns brings these same normal faults closer to Coulomb failure, promoting earthquakes. Such a coupling is strongest if the magma reservoir is a dike oriented normal to the regional extension axis, parallel to the Apennines, and the near-surface conduits and fissures are oriented normal to the Apennines. This preferred orientation suggests that the eruptions issuing from such fissures should be most closely linked in time to Apennine earthquake [37].

Chapter 7

Conclusion

7.1 Summary of contribution

The thesis presented a numerical algorithm to solve magma-rock interaction (fluid-structure interaction, FSI) problem. Magma was modelled as a multicomponent singe-phase compressible/incompressible fluid flow and rock was modelled as an elastic/viscoelastic structure. Governing Navier-Stokes equations for compressible fluid flow consist of mass conservation equation for each component and momentum and energy equations for the mixture of components. In order to obtain the incompressibility of the flow, two compressibility coefficients, volume expansivity, α_p and isothermal compressibility, β_T were defined and set equal to zero. A homogeneous mixture model was used in the algorithm. The mixture model evaluated the weighted average value of thermodynamic variables, where weights were respectively the mass fractions of the components in a given phase. The structural model for rock was based on the linear elastic/viscoelastic behaviour undergoing a small deformation. Elasticity and viscoelasticity respectively were modelled by the Hooke's law and the generalised Maxwell's model. The later wrote the stress relaxation function for elastic and inelastic parts in the form of a Prony series.

Based on the numerical techniques, two separate software programs have been developed for fluid and structure. The programs are written in C++ template metaprogramming language. The parallelization of the code is done by Open MPI library, allowing the code to run on multiple processors simultaneously. The meshes are generated by Gmsh software and are partitioned into a number of specified processes by pmetis software. The meshes are transformed into required format by a Matlab script. Sparse vectors and matrices arise from the assembly of elements are defined by the Epetra package from trilinos libraries. Linear set of equations is solved by an iterative block GMRES solver from BELOS package of trilinos. The postprocessing of the results is done with Matlab and ParaView.

The Navier-Stokes equations for the fluid flow were solved by the space-time Galerkin least square method. The proposed method was continuous in space and discontinuous in time. This allowed solving the flow problem independently for each time slab instead of solving a global problem over the whole time domain. The compressible flow equations were written in a vector form and transformed from conservative to pressure primitive variables. The transformed equations allowed to compute both compressible and incompressible flow in a unified way. Two stabilisation operators, least square and discontinuity capturing were defined to stabilise the numerical solution. The details of space-time finite element method were provided including the mapping, the weak formulation and the computation of unit time normal vector. Two discretization schemes, linear in time and constant in time were discussed and the computation of vectors and matrices were provided at the element level. The method was successfully validated on fixed domain single/multicomponent compressible and incompressible fluid flow benchmarks.

The numerical method was developed to deal with the moving domain problems which required the updation of the fluid mesh in response to the movement of the boundaries and the associated changes in the fluid flow. In moving domain problems, the space-time slab required the computation of the fluid mesh velocity. For this purpose, an elastic mesh deformation method was presented which computed the displacement and velocity of the fluid mesh nodes. In order to deal with the large distortion of the fluid mesh elements, Jacobian based stiffening approach was proposed. It increased the rigidity of the smaller elements than the larger ones, which allowed to move the mesh for larger deformation of the boundary as well as decreased the frequency of remeshing. The quality of the mesh was qualified by angle, length ratio, element area change and element shape change criteria. After testing the elastic mesh deformation method on two test cases, a segregated algorithm was developed to couple the mesh deformation with the fluid flow problem. The algorithm was validated on deforming body and free surface problems for both single and multicomponent fluid flows.

The structure mechanics equations were solved on the undeformed configuration by the semi-discrete finite element method. The spatial discretization was done by standard Galerkin method and time was discretised by the generalised α time integration method. Two different type of predictors were proposed: constant velocity and zero acceleration. The tangent matrix was computed in an implicit way. Linear elastodynamics was presented as a special case of viscoelastodynamics with only the elastic part and neglecting the inelastic part. The numerical scheme was tested on three benchmarks.

Segregated algorithms were proposed for one-way and two-way coupling. In two-way coupling algorithm, in the first step, the Navier-Stokes equations for multicomponent fluid flow were solved. From the fluid solution the traction forces were computed and applied to the structure problem as Neumann boundary conditions at the interface. In the second step, the structure equations were solved and displacement and velocity were computed. In the third step, the structural displacement was passed as Dirichlet boundary condition to the fluid mesh motion problem at the interface. The mesh motion problem was solved for the displacement and velocity of the fluid mesh nodes. Once the fluid mesh displacement was known, the space-time slab was formed and computations were performed for the next time step by passing the structural velocity to the fluid at the interface as Dirichlet boundary condition.

The developed algorithm was applied to study the natural convection occurring inside a magma chamber. The proposed model was based on some necessary assumptions including the Newtonian behaviour of magma, neglection of crystallisation and chemical reactions, and single phase and bi-dimensional flow of the magma. The physical models were discussed to compute the exsolution and dissolution of the volatiles, the density of volatiles and silicate melt, and the viscosity for the magma. A mixture model was used to compute the thermodynamic variables. Three different type of cases were investigated with magma combinations.

The first case investigated the Rayleigh-Taylor (RT) instability arise inside an elliptical chamber due to the mixing of hot and cold basalt magma. Numerical results showed that the RT fingers grow exponentially with time and the mixing time scale was in the range of a few hours. During mixing several convective cells appeared, moving at ≈ 2.4 m/s. The velocity of the convective cells decreased with time which indicated the slowing down of mixing. The overpressure increased due to mixing. The maximum value of overpressure 6300 Pa was reached at the top of the chamber. It was tested by a simulation that the irregular geometry does not influence the dynamics.

In the second case, two numerical simulations were performed to study the magma replenishment from a deeper source to a shallower magma chamber. The first simulation was done with the volatile rich shoshonite and degassed phonolite magmas, and the second simulation was performed over volatile rich andesite and degassed dacite magmas. The simulation results showed that the viscosity has a major influence on the convection and mixing efficiency. In Shoshonite/Phonolite (SP) case a large number of plumes entered inside the shallower chamber, while in Andesite/Dacite (AD) case very small number of the plumes arrived. Like basalt, the mixing time scale for SP was in the range of a few hours, whereas, for AD it was in the range of tens of hours. For SP the maximum velocity of the rising plumes reached up to 9 m/s while for AD it reached only 4.3 m/s. For SP and AD respectively, the maximum value of the overpressure reached at the top of the upper chamber was up to 1×10^4 and 1.7×10^4; in the dike up to 5×10^4 and 2.2×10^4; at the centre of the bottom chamber up to 3.4×10^4 and 1.9×10^4. In both cases the replenishment and mixing of the magmas decreased the overpressure in the shallow chamber and increased in the dike and the bottom chamber. The current results show that the replenishment driven by only buoyancy forces can produce a decompression in the shallower chamber. This can be an important factor in formation and collapse of a caldera.

The third case explored the influence of a near-field seismic wave on magma dynamics. The impact of a seismic wave was applied to the magma combinations employed in the second case. The simulation results showed a fluctuation of velocity for first 150 s, localised next to the boundary where the wave was striking. Though the wave impinged with the chamber only for first 60 s, the effect on the velocity lasted up to 150 s. The dynamics of plume rising, convection and mixing were not affected by the impact of seismic wave. The strike of seismic wave generated a longitudinal overpressure wave in the system which travelled with the magma sound speed. For SP and AD respectively, the maximum value of the overpressure, at the top of the upper chamber, was up to 3.5×10^5 and 6.2×10^5; in the dike up to 2.2×10^6 and 2.3×10^6; at the centre of the bottom chamber up to 6.3×10^5 and 1×10^6. In this case, the overpressure, in the upper chamber was about one order of magnitude higher than no seismic wave cases, while in the dike and in the bottom chamber it was about two order of magnitude higher. The overpressure wave damped with time due to viscous dissipation. Similar to the second case, the overpressure decreased in the shallow chamber and increased in the dike and bottom chamber.

7.2 Directions for future work

- In the current work, the details about the coupling between magma and rock have been provided. Two separate software programs for magma flow and rock dynamics have been developed and validated. The coupling between the two problems was not yet implemented in the software. This is the prime objective of the future work. The fully coupled code would be extremely important as well as useful. It would allow computing the synthetic signals for rock deformation subject to the magmatic forces applicable on the chamber walls. The comparison between the computed synthetic signals and recorded monitoring signals would help to understand the subsurface magma activity and the physical processes behind that.

- In the present work, in near-field seismic wave impact simulation, a smooth vertical dike was taken as the domain geometry. Following the results, which indicate that the seismic wave is more effective in the dike, the irregular geometry of a dike can cause a high overpressure, large enough to rupture the rock and propagate the cracks. Also, in the simulation, the seismic wave was hit to the system at the beginning of the convection. The shaking of an already ongoing magma mixing might produce completely different results. The effect of the irregular dike and the shaking of the chamber when the mixing has already started are two interesting factors that should be addressed in the future research.

- All the results presented in this thesis were based on 2D numerical simulations. For a realistic scenario of the magma dynamics, a 3D model is necessary. The extension of the present model into a 3D model has already been done and has been validated, but is not presented in the current thesis work. In future, it would be nice to explore that whether there is any difference in magma dynamics between a 2D and 3D computations.

- The present model is in general applicable to any kind of magma flow simulations but it will not be suitable for modelling the volcanic conduit dynamics in which the gas phase can rise through the moving liquid, generating slug flow as in Strombolian eruptions. In conduits, the exsolved gas can move much faster than the melt, in particular during the transient phase of an eruptive event. It requires a multiphase model to capture the accurate dynamics. However, once the slug is formed the current model can be applied to simulate the slug rising to the conduit. A global model which link the magma chambers with the conduit should be able to compute the multiphase multicomponent fluid flows. The future research should consider the development of multiphase multicomponent fluid flow model applicable to simulate the chamber and conduit flow dynamics simultaneously.

- Current work focused on the natural convection cases, in which the results showed a decrease of overpressure in the shallow chamber. This was associated to the mass outflux of the magma. There can be situations when the overpressure in the bottom system can cause more mass influx than outflux in the shallow chamber. In such cases, the dynamics will be driven by forced convection. In such cases, the overpressure in the shallow chamber can overcome the tensile strength of host rock and lead to an eruption. A further research is required to model the forced convection cases.

- As it was pointed out in the discussion that the crystallisation increases the viscosity, which ultimately strongly influences the dynamics. Therefore, the inclusion of crystallisation in the current model remains for the future work.

- Current developed model was based on the finite element method (FEM) that can be easily modified into extended finite element method

(XFEM). The XFEM is in particularly useful for the crack propagation modelling. The implementation of XFEM into the current model would be useful to model the dike propagation from magma chamber to the surrounding rock.

- From the numerical point of view, there is always a need of stabilised techniques so that the numerical method should be used for larger time steps. Further research is required to develop the optimised stabilisation operators for multicomponent fluid flows.

Appendix A

A.1 Definitions of vectors

Denoting

$$\left[\boldsymbol{Y_{n-1}}\right]_{(n-1)\times 1} = \begin{bmatrix} y_1 \\ y_2 \\ \vdots \\ y_{n-1} \end{bmatrix} \qquad \left[\boldsymbol{V_{n-1}}\right]_{(n-1)\times 1} = \begin{bmatrix} (g_1 - k)/T \\ (g_2 - k)/T \\ \vdots \\ (g_{n-1} - k)/T \end{bmatrix}$$

$$\left[\boldsymbol{v}\right]_{3\times 1} = \begin{bmatrix} v_1 \\ v_2 \\ v_3 \end{bmatrix} \qquad \left[\boldsymbol{\tau_i}\right]_{3\times 1} = \begin{bmatrix} \tau_{1i} \\ \tau_{2i} \\ \tau_{3i} \end{bmatrix} \qquad \left[\boldsymbol{b}\right]_{3\times 1} = \begin{bmatrix} b_1 \\ b_2 \\ b_3 \end{bmatrix}$$

$$\left[\boldsymbol{J^i_{n-1}}\right]_{(n-1)\times 1} = \begin{bmatrix} J^i_1 \\ J^i_1 \\ \vdots \\ J^i_{n-1} \end{bmatrix}$$

The vectors are given by

$$\left[\boldsymbol{U}\right]_{(n+4)\times 1} = \rho \begin{bmatrix} \boldsymbol{Y_{n-1}} \\ y_n \\ \boldsymbol{v} \\ e_t \end{bmatrix} \qquad \left[\boldsymbol{Y}\right]_{(n+4)\times 1} = \begin{bmatrix} \boldsymbol{Y_{n-1}} \\ p \\ \boldsymbol{v} \\ T \end{bmatrix} \tag{A.1}$$

$$\left[\boldsymbol{V}\right]_{(n+4)\times 1} = \begin{bmatrix} \boldsymbol{V_{n-1}} \\ (g_n - k)/T \\ \boldsymbol{v}/T \\ -1/T \end{bmatrix} \qquad \left[\boldsymbol{F}_i^a\right]_{(n+4)\times 1} = \begin{bmatrix} \rho v_i \boldsymbol{Y_{n-1}} \\ \rho v_i y_n \\ \rho v_i \boldsymbol{v} + \boldsymbol{\delta_i} p \\ \rho v_i e_t + v_i p \end{bmatrix} \tag{A.2}$$

$$\left[\boldsymbol{F}_i^d\right]_{(n+4)\times 1} = \begin{bmatrix} -\boldsymbol{J_i^{n-1}} \\ -J_i^n \\ \boldsymbol{\tau_i} \\ \tau_{ij} v_j - q_i - \sum_k J_i^k h_k \end{bmatrix} \qquad \left[\boldsymbol{\mathcal{F}}\right]_{(n+4)\times 1} = \rho \begin{bmatrix} \boldsymbol{0_{n-1}} \\ 0 \\ \boldsymbol{b} \\ \boldsymbol{b} \cdot \boldsymbol{v} + r \end{bmatrix} \tag{A.3}$$

A.2 Definitions of matrices

The matrix of partial derivatives of conservation variables $\boldsymbol{U}$ with respect to $\boldsymbol{Y}$ is defined as

$$\boldsymbol{A}_0(\boldsymbol{Y}) = \begin{bmatrix} \dfrac{\partial \rho \boldsymbol{Y}_{n-1}}{\partial \boldsymbol{Y}_{n-1}} & \dfrac{\partial \rho \boldsymbol{Y}_{n-1}}{\partial p} & \dfrac{\partial \rho \boldsymbol{Y}_{n-1}}{\partial \boldsymbol{v}} & \dfrac{\partial \rho \boldsymbol{Y}_{n-1}}{\partial T} \\ \dfrac{\partial \rho y_n}{\partial \boldsymbol{Y}_{n-1}} & \dfrac{\partial \rho y_n}{\partial p} & \dfrac{\partial \rho y_n}{\partial \boldsymbol{v}} & \dfrac{\partial \rho y_n}{\partial T} \\ \dfrac{\partial \rho \boldsymbol{v}}{\partial \boldsymbol{Y}_{n-1}} & \dfrac{\partial \rho \boldsymbol{v}}{\partial p} & \dfrac{\partial \rho \boldsymbol{v}}{\partial \boldsymbol{v}} & \dfrac{\partial \rho \boldsymbol{v}}{\partial T} \\ \dfrac{\partial \rho e_t}{\partial \boldsymbol{Y}_{n-1}} & \dfrac{\partial \rho e_t}{\partial p} & \dfrac{\partial \rho e_t}{\partial \boldsymbol{v}} & \dfrac{\partial \rho e_t}{\partial T} \end{bmatrix}$$

Individual terms in above matrix are defined as

$$\left[\frac{\partial \rho \boldsymbol{Y}_{n-1}}{\partial \boldsymbol{Y}_{n-1}}\right]_{(n-1)\times(n-1)} = \begin{bmatrix} y_1 C_1 + \rho & y_1 C_2 & \dots & y_1 C_{n-1} \\ y_2 C_1 & y_2 C_2 + \rho & \dots & y_2 C_{n-1} \\ \vdots & \vdots & \ddots & \vdots \\ y_{n-1} C_1 & y_{n-1} C_2 & \dots & y_{n-1} C_{n-1} + \rho \end{bmatrix}$$

$$\left[\frac{\partial \rho \boldsymbol{Y}_{n-1}}{\partial p}\right]_{(n-1)\times 1} = \rho \beta \boldsymbol{Y}_{n-1} \qquad \left[\frac{\partial \rho \boldsymbol{Y}_{n-1}}{\partial \boldsymbol{v}}\right]_{(n-1)\times 3} = \boldsymbol{0}$$

$$\left[\frac{\partial \rho \boldsymbol{Y}_{n-1}}{\partial T}\right]_{(n-1)\times 1} = -\rho\alpha \boldsymbol{Y}_{n-1} \qquad \frac{\partial \rho y_n}{\partial T} = -\rho\alpha y_n$$

$$\left[\frac{\partial \rho y_n}{\partial \boldsymbol{Y}_{n-1}}\right]_{1\times(n-1)} = \begin{bmatrix} y_n C_1 - \rho & y_n C_2 - \rho & \dots & y_n C_{n-1} - \rho \end{bmatrix}$$

$$\frac{\partial \rho y_n}{\partial p} = \rho\beta y_n \qquad \left[\frac{\partial \rho y_n}{\partial \boldsymbol{v}}\right]_{1\times 3} = \boldsymbol{0}^T$$

$$\left[\frac{\partial \rho \boldsymbol{v}}{\partial \boldsymbol{Y}_{n-1}}\right]_{3\times(n-1)} = \boldsymbol{v}\begin{bmatrix} C_1 & C_2 & \dots & C_{n-1} \end{bmatrix}$$

$$\left[\frac{\partial \rho \boldsymbol{v}}{\partial p}\right]_{3\times 1} = \rho\beta \boldsymbol{v} \qquad \left[\frac{\partial \rho \boldsymbol{v}}{\partial \boldsymbol{v}}\right]_{3\times 3} = \rho \boldsymbol{I}_3$$

$$\left[\frac{\partial \rho \boldsymbol{v}}{\partial T}\right]_{3\times 1} = -\rho\alpha \boldsymbol{v} \qquad \frac{\partial \rho e_t}{\partial T} = e_4^p$$

$$\left[\frac{\partial \rho e_t}{\partial \boldsymbol{Y}_{n-1}}\right]_{1\times(n-1)} = \begin{bmatrix} e_t C_1 + \rho e_1^n & e_t C_2 + \rho e_2^n & \dots & e_t C_{n-1} + \rho e_{n-1}^n \end{bmatrix}$$

$$\frac{\partial \rho e_t}{\partial p} = e_1^p \qquad \left[\frac{\partial \rho e_t}{\partial \boldsymbol{v}}\right]_{1\times 3} = \rho \boldsymbol{v}^T$$

Where

$$C_k = \rho^2\left(\frac{1}{\rho_n} - \frac{1}{\rho_k}\right) \qquad e_k^n = e_k - e_n$$

$$e_1^p = \rho\beta(h+k) - \alpha T \qquad e_4^p = -\rho\alpha(h+k) + \rho c_p$$

Here, α and β are the coefficients of isobaric expansion and isothermal compressibility. $\boldsymbol{I}_3$ is identity matrix.

The advective flux matrices $\boldsymbol{A}_{i,\boldsymbol{Y}}$ are defined as

$$\boldsymbol{A}_i(\boldsymbol{Y}) = \begin{bmatrix} \dfrac{\partial \rho v_i \boldsymbol{Y}_{n-1}}{\partial \boldsymbol{Y}_{n-1}} & \dfrac{\partial \rho v_i \boldsymbol{Y}_{n-1}}{\partial p} & \dfrac{\partial \rho v_i \boldsymbol{Y}_{n-1}}{\partial \boldsymbol{v}} & \dfrac{\partial \rho v_i \boldsymbol{Y}_{n-1}}{\partial T} \\[2ex] \dfrac{\partial \rho v_i Y_n}{\partial \boldsymbol{Y}_{n-1}} & \dfrac{\partial \rho v_i Y_n}{\partial p} & \dfrac{\partial \rho v_i Y_n}{\partial \boldsymbol{v}} & \dfrac{\partial \rho v_i Y_n}{\partial T} \\[2ex] \dfrac{\partial P_i}{\partial \boldsymbol{Y}_{n-1}} & \dfrac{\partial P_i}{\partial p} & \dfrac{\partial P_i}{\partial \boldsymbol{v}} & \dfrac{\partial P_i}{\partial T} \\[2ex] \dfrac{\partial Q_i}{\partial \boldsymbol{Y}_{n-1}} & \dfrac{\partial Q_i}{\partial p} & \dfrac{\partial Q_i}{\partial \boldsymbol{v}} & \dfrac{\partial Q_i}{\partial T} \end{bmatrix}$$

Where $P_i = \rho v_i(\boldsymbol{v} + \boldsymbol{\delta}_i p)$ and $Q_i = \rho v_i(e_t + v_i p)$. The individual terms in matrix are evaluated as

$$\left[\frac{\partial \rho v_i \boldsymbol{Y}_{n-1}}{\partial \boldsymbol{Y}_{n-1}}\right]_{(n-1)\times(n-1)} = v_i \left[\frac{\partial \rho \boldsymbol{Y}_{n-1}}{\partial \boldsymbol{Y}_{n-1}}\right]$$

$$\left[\frac{\partial \rho v_i \boldsymbol{Y}_{n-1}}{\partial p}\right]_{(n-1)\times 1} = v_i \left[\frac{\partial \rho \boldsymbol{Y}_{n-1}}{\partial p}\right]$$

$$\left[\frac{\partial \rho v_1 \boldsymbol{Y}_{n-1}}{\partial \boldsymbol{v}}\right]_{(n-1)\times 3} = \rho \boldsymbol{Y}_{n-1} \begin{bmatrix} 1 & 0 & 0 \end{bmatrix}$$

$$\left[\frac{\partial \rho v_2 \boldsymbol{Y}_{n-1}}{\partial \boldsymbol{v}}\right]_{(n-1)\times 3} = \rho \boldsymbol{Y}_{n-1} \begin{bmatrix} 0 & 1 & 0 \end{bmatrix}$$

$$\left[\frac{\partial \rho v_3 \boldsymbol{Y}_{n-1}}{\partial \boldsymbol{v}}\right]_{(n-1)\times 3} = \rho \boldsymbol{Y}_{n-1} \begin{bmatrix} 0 & 0 & 1 \end{bmatrix}$$

$$\left[\frac{\partial \rho v_i \boldsymbol{Y}_{n-1}}{\partial T}\right]_{(n-1)\times 1} = v_i \left[\frac{\partial \rho \boldsymbol{Y}_{n-1}}{\partial T}\right]$$

$$\left[\frac{\partial \rho v_i y_n}{\partial \boldsymbol{Y}_{n-1}}\right]_{1\times(n-1)} = v_i \left[\frac{\partial \rho y_n}{\partial \boldsymbol{Y}_{n-1}}\right] \qquad \frac{\partial \rho v_i y_n}{\partial p} = v_i \frac{\partial \rho y_n}{\partial p}$$

$$\left[\frac{\partial \rho v_1 y_n}{\partial \boldsymbol{v}}\right]_{1\times 3} = \rho y_n \begin{bmatrix} 1 & 0 & 0 \end{bmatrix}$$

$$\left[\frac{\partial \rho v_2 y_n}{\partial \boldsymbol{v}}\right]_{1\times 3} = \rho y_n \begin{bmatrix} 0 & 1 & 0 \end{bmatrix} \qquad \left[\frac{\partial \rho v_3 y_n}{\partial \boldsymbol{v}}\right]_{1\times 3} = \rho y_n \begin{bmatrix} 0 & 0 & 1 \end{bmatrix}$$

$$\frac{\partial \rho v_i y_n}{\partial T} = v_i \, \frac{\partial \rho y_n}{\partial T} \qquad \left[\frac{\partial P_i}{\partial \boldsymbol{Y}_{n-1}}\right]_{3\times (n-1)} = v_i \left[\frac{\partial \rho \boldsymbol{v}}{\partial \boldsymbol{Y}_{n-1}}\right]$$

$$\left[\frac{\partial P_1}{\partial p}\right]_{3\times 1} = \begin{bmatrix} \rho\beta v_1^2 + 1 \\ \rho\beta v_1 v_2 \\ \rho\beta v_1 v_3 \end{bmatrix} \qquad \left[\frac{\partial P_2}{\partial p}\right]_{3\times 1} = \begin{bmatrix} \rho\beta v_1 v_2 \\ \rho\beta v_2^2 + 1 \\ \rho\beta v_1 v_3 \end{bmatrix}$$

$$\left[\frac{\partial P_3}{\partial p}\right]_{3\times 1} = \begin{bmatrix} \rho\beta v_1 v_3 \\ \rho\beta v_1 v_2 \\ \rho\beta v_3^2 + 1 \end{bmatrix} \qquad \left[\frac{\partial P_1}{\partial \boldsymbol{v}}\right]_{3\times 3} = \begin{bmatrix} 2\rho v_1 & 0 & 0 \\ \rho v_2 & \rho v_1 & 0 \\ \rho v_3 & 0 & \rho v_1 \end{bmatrix}$$

$$\left[\frac{\partial P_2}{\partial \boldsymbol{v}}\right]_{3\times 3} = \begin{bmatrix} \rho v_2 & \rho v_1 & 0 \\ 0 & 2\rho v_2 & 0 \\ 0 & \rho v_3 & \rho v_2 \end{bmatrix} \qquad \left[\frac{\partial P_3}{\partial \boldsymbol{v}}\right]_{3\times 3} = \begin{bmatrix} \rho v_3 & 0 & \rho v_1 \\ 0 & \rho v_3 & \rho v_2 \\ 0 & 0 & 2\rho v_3 \end{bmatrix}$$

$$\left[\frac{\partial P_i}{\partial T}\right]_{3\times 1} = v_i \left[\frac{\partial \rho \boldsymbol{v}}{\partial T}\right] \qquad \left[\frac{\partial Q_i}{\partial \boldsymbol{Y}_{n-1}}\right]_{1\times (n-1)} = v_i \left[\frac{\partial \rho e_t}{\partial \boldsymbol{Y}_{n-1}}\right]$$

$$\frac{\partial Q_i}{\partial p} = v_i e_2^p \qquad \left[\frac{\partial Q_1}{\partial \boldsymbol{v}}\right]_{1\times 3} = \begin{bmatrix} e_3^p + \rho v_1^2 & \rho v_1 v_2 & \rho v_1 v_3 \end{bmatrix}$$

$$\left[\frac{\partial Q_2}{\partial \boldsymbol{v}}\right]_{1\times 3} = \begin{bmatrix}\rho v_1 v_2 & e_3^p + \rho v_2^2 & \rho v_2 v_3\end{bmatrix}$$

$$\left[\frac{\partial Q_3}{\partial \boldsymbol{v}}\right]_{1\times 3} = \begin{bmatrix}\rho v_1 v_3 & \rho v_2 v_3 & e_3^p + \rho v_3^2\end{bmatrix}$$

$$\left[\frac{\partial Q_i}{\partial T}\right]_{3\times 1} = v_i \left[\frac{\partial \rho e_t}{\partial T}\right]$$

Where $e_2^p = e_1^p + 1$ and $e_3^p = \rho e_t + p$

The diffusivity matrices $\boldsymbol{K}_{ij}$ are defined as

$$\left[\begin{array}{cc} \left[\boldsymbol{D_{ij}}\right]_{(n-1)\times(n-1)} & [\mathbf{0}]_{(n-1)\times 5} \\ \hdashline \left[\boldsymbol{d}\right]_{1\times(n-1)} & \\ [\mathbf{0}]_{3\times(n-1)} & [k_{ij}]_{5\times 5} \\ [\boldsymbol{hd}]_{1\times(n-1)} & \end{array}\right]$$

Where

$$\left[\boldsymbol{D_{ij}}\right]_{(n-1)\times(n-1)} = \mathbf{0} \qquad \text{if} \quad i \neq j$$

For $\quad i = j \qquad \left[\boldsymbol{D_{ij}}\right]_{(n-1)\times(n-1)} = \rho \begin{bmatrix} d_{11} & d_{12} & \dots & d_{(1)(n-1)} \\ d_{21} & d_{22} & \dots & d_{(2)(n-1)} \\ \vdots & \vdots & \ddots & \vdots \\ d_{(n-1)(1)} & d_{(n-1)(2)} & \dots & d_{(n-1)(n-1)} \end{bmatrix}$

$$\left[\boldsymbol{d}\right]_{1\times(n-1)} = \begin{bmatrix} d_{n1} & d_{n2} & \dots & d_{(n)(n-1)} \end{bmatrix}$$

$$\left[\boldsymbol{hd}\right]_{1\times(n-1)} = \boldsymbol{hd}(i) = \sum_{j=1}^{n} h_j d_{ji} \qquad\qquad i = 1, 2, \dots, n-1$$

Where d_{ji} is the diffusion coefficient between component j and i; h_j is the specific enthalpy of jth component.

$$k_{11} = \begin{bmatrix} 0 & 0 & 0 & 0 & 0 \\ 0 & \chi & 0 & 0 & 0 \\ 0 & 0 & \mu & 0 & 0 \\ 0 & 0 & 0 & \mu & 0 \\ 0 & \chi v_1 & \mu v_2 & \mu v_3 & \kappa \end{bmatrix} \qquad k_{12} = \begin{bmatrix} 0 & 0 & 0 & 0 & 0 \\ 0 & 0 & \lambda & 0 & 0 \\ 0 & \mu & 0 & 0 & 0 \\ 0 & 0 & 0 & 0 & 0 \\ 0 & \mu v_2 & \lambda v_1 & 0 & 0 \end{bmatrix}$$

$$k_{13} = \begin{bmatrix} 0 & 0 & 0 & 0 & 0 \\ 0 & 0 & 0 & \lambda & 0 \\ 0 & 0 & 0 & 0 & 0 \\ 0 & \mu & 0 & 0 & 0 \\ 0 & \mu v_3 & 0 & \lambda v_1 & 0 \end{bmatrix} \qquad k_{21} = \begin{bmatrix} 0 & 0 & 0 & 0 & 0 \\ 0 & 0 & \mu & 0 & 0 \\ 0 & \lambda & 0 & 0 & 0 \\ 0 & 0 & 0 & 0 & 0 \\ 0 & \lambda v_2 & \mu v_1 & 0 & 0 \end{bmatrix}$$

$$k_{22} = \begin{bmatrix} 0 & 0 & 0 & 0 & 0 \\ 0 & \mu & 0 & 0 & 0 \\ 0 & 0 & \chi & 0 & 0 \\ 0 & 0 & 0 & \mu & 0 \\ 0 & \mu v_1 & \chi v_2 & \mu v_3 & \kappa \end{bmatrix} \qquad k_{23} = \begin{bmatrix} 0 & 0 & 0 & 0 & 0 \\ 0 & 0 & 0 & 0 & 0 \\ 0 & 0 & 0 & \lambda & 0 \\ 0 & 0 & \mu & 0 & 0 \\ 0 & 0 & \mu v_3 & \lambda v_2 & 0 \end{bmatrix}$$

$$k_{31} = \begin{bmatrix} 0 & 0 & 0 & 0 & 0 \\ 0 & 0 & 0 & \mu & 0 \\ 0 & 0 & 0 & 0 & 0 \\ 0 & \lambda & 0 & 0 & 0 \\ 0 & \lambda v_3 & 0 & \mu v_1 & 0 \end{bmatrix} \qquad k_{32} = \begin{bmatrix} 0 & 0 & 0 & 0 & 0 \\ 0 & 0 & 0 & 0 & 0 \\ 0 & 0 & 0 & \mu & 0 \\ 0 & 0 & \lambda & 0 & 0 \\ 0 & 0 & \lambda v_3 & \mu v_2 & 0 \end{bmatrix}$$

$$k_{33} = \begin{bmatrix} 0 & 0 & 0 & 0 & 0 \\ 0 & \mu & 0 & 0 & 0 \\ 0 & 0 & \mu & 0 & 0 \\ 0 & 0 & 0 & \chi & 0 \\ 0 & \mu v_1 & \mu v_2 & \chi v_3 & \kappa \end{bmatrix}$$

Where, $\chi = \lambda + 2\mu$.

The source matrix $\boldsymbol{S}$ is defined as

$$\boldsymbol{S} = \begin{bmatrix} [\mathbf{0}]_{(n-1)\times(n-1)} & [\mathbf{0}]_{(n-1)\times 1} & [\mathbf{0}]_{(n-1)\times 3} & [\mathbf{0}]_{(n-1)\times 1} \\ 0 & 0 & 0 & 0 \\ [\mathbf{0}]_{3\times(n-1)} & [\mathbf{0}]_{3\times 1} & [\mathbf{0}]_{3\times 3} & \left[\dfrac{\rho \boldsymbol{b}}{T}\right]_{3\times 1} \\ [\mathbf{0}]_{1\times(n-1)} & 0 & [\rho \boldsymbol{b}^T]_{1\times 3} & \dfrac{\rho r}{T} \end{bmatrix}$$

The source matrix with Boussinesq-approximation is defined as

$$\boldsymbol{S} = \begin{bmatrix} [\mathbf{0}]_{(n-1)\times(n-1)} & [\mathbf{0}]_{(n-1)\times 1} & [\mathbf{0}]_{(n-1)\times 3} & [\mathbf{0}]_{(n-1)\times 1} \\ 0 & 0 & 0 & 0 \\ [\mathbf{0}]_{3\times(n-1)} & [\mathbf{0}]_{3\times 1} & [\mathbf{0}]_{3\times 3} & \left[\dfrac{-\rho \boldsymbol{b} \alpha (T - T_0)}{T}\right]_{3\times 1} \\ [\mathbf{0}]_{1\times(n-1)} & 0 & [\mathbf{0}]_{1\times 3} & 0 \end{bmatrix}$$

$\boldsymbol{V}_{,\boldsymbol{Y}}$ is evaluated as

$$\boldsymbol{V}_{,\boldsymbol{Y}} == \begin{bmatrix} \dfrac{\partial \boldsymbol{V}_{n-1}}{\partial \boldsymbol{Y}_{n-1}} & \dfrac{\partial \boldsymbol{V}_{n-1}}{\partial p} & \dfrac{\partial \boldsymbol{V}_{n-1}}{\partial \boldsymbol{v}} & \dfrac{\partial \boldsymbol{V}_{n-1}}{\partial T} \\ \dfrac{\partial V_n}{\partial \boldsymbol{Y}_{n-1}} & \dfrac{\partial V_n}{\partial p} & \dfrac{\partial V_n}{\partial \boldsymbol{v}} & \dfrac{\partial V_n}{\partial T} \\ \dfrac{\partial (\boldsymbol{v}/T)}{\partial \boldsymbol{Y}_{n-1}} & \dfrac{\partial (\boldsymbol{v}/T)}{\partial p} & \dfrac{\partial (\boldsymbol{v}/T)}{\partial \boldsymbol{v}} & \dfrac{\partial (\boldsymbol{v}/T)}{\partial T} \\ \dfrac{\partial (-1/T)}{\partial \boldsymbol{Y}_{n-1}} & \dfrac{\partial (-1/T)}{\partial p} & \dfrac{\partial (-1/T)}{\partial \boldsymbol{v}} & \dfrac{\partial (-1/T)}{\partial T} \end{bmatrix}$$

Where $V_n = \dfrac{g_n - k}{T}$. The individual terms of the matrix are as follows:

$$\left[\frac{\partial \boldsymbol{V}_{n-1}}{\partial \boldsymbol{Y}_{n-1}}\right]_{i,j} = RM_t\left(\frac{1}{M_n}-\frac{1}{M_j}\right)+\frac{R}{y_i}\delta_{ij} \qquad i,j=1,2,\ldots,n-1$$

$$\left[\frac{\partial \boldsymbol{V}_{n-1}}{\partial p}\right]_{(n-1)\times 1} = \frac{R}{p}(1,1,\ldots,1)^T$$

$$\left[\frac{\partial \boldsymbol{V}_{n-1}}{\partial \boldsymbol{v}}\right]_{(n-1)\times 3} = \frac{-1}{T}\begin{bmatrix} v_1 & v_2 & v_3 \\ v_1 & v_2 & v_3 \\ \vdots & \vdots & \vdots \\ v_1 & v_2 & v_3 \end{bmatrix}$$

$$\left[\frac{\partial \boldsymbol{V}_{n-1}}{\partial T}\right]_{(n-1)\times 1} = \frac{|\boldsymbol{v}|^2}{2T^2}(1,1,\ldots,1)^T$$

$$\left[\frac{\partial V_n}{\partial \boldsymbol{Y}_{n-1}}\right]_{1,j} = RM_t\left(\frac{1}{M_n}-\frac{1}{M_j}\right)-\frac{R}{y_n} \qquad j=1,2,\ldots,n-1$$

$$\frac{\partial V_n}{\partial p}=\frac{R}{p} \qquad \left[\frac{\partial V_n}{\partial \boldsymbol{v}}\right]_{1\times 3} = \frac{-1}{T}\boldsymbol{v}^T$$

$$\frac{\partial V_n}{\partial T}=\frac{|\boldsymbol{v}|^2}{2T^2}$$

$$\left[\frac{\partial(\boldsymbol{v}/T)}{\partial\boldsymbol{Y}_{n-1}}\right]_{3\times(n-1)} = \mathbf{0} \qquad \left[\frac{\partial(\boldsymbol{v}/T)}{\partial p}\right]_{3\times 1} = \mathbf{0}$$

$$\left[\frac{\partial(\boldsymbol{v}/T)}{\partial\boldsymbol{v}}\right]_{3\times 3} = \frac{1}{T}\boldsymbol{I}_3 \qquad \left[\frac{\partial(\boldsymbol{v}/T)}{\partial T}\right]_{3\times 1} = \frac{-1}{T^2}\boldsymbol{v}$$

$$\left[\frac{\partial(-1/T)}{\partial\boldsymbol{Y}_{n-1}}\right]_{1\times(n-1)} = \mathbf{0} \qquad \frac{\partial(-1/T)}{\partial p} = 0$$

$$\left[\frac{\partial(-1/T)}{\partial\boldsymbol{v}}\right]_{1\times 3} = \mathbf{0} \qquad \frac{\partial(-1/T)}{\partial T} = \frac{1}{T^2}$$

Where, M_i is the molar mass of ith component and M_t is the total molar mass. $\boldsymbol{V}_{,\boldsymbol{U}}$ is defined as $\boldsymbol{V}_{,\boldsymbol{U}} = \boldsymbol{V}_{,\boldsymbol{Y}}\boldsymbol{Y}_{,\boldsymbol{U}}$; where, $\boldsymbol{Y}_{,\boldsymbol{U}} = \boldsymbol{U}_{,\boldsymbol{Y}}{}^{-1}$.

A.3 Third order predictor multi-corrector algorithm

Third order predictor multi-corrector algorithm used to solve the non-linear systems of equations is given as below:

```
Given $n_{step}$ and $i_{max}$
(Initialize)
 set $\boldsymbol{Y}^2_{(0)}$

 (Time steps)
 For $n = 0, 1, \ldots, n_{step} - 1$

        (Predictor)
        $\boldsymbol{Y^2}^{(0)} = \boldsymbol{Y^1}^{(0)} = \boldsymbol{Y}^2_{(0)}$

        Set $\Delta t$
        (Multi-corrector loop)
        For $i = 0, 1, \ldots, i_{max} - 1$

                Form $R^{2(i)}\left(\boldsymbol{Y^2}^{(i)}, \boldsymbol{Y^1}^{(i)}, \boldsymbol{Y^2}_{(n)}\right)$
                Form $M^{(i)}\left(\boldsymbol{Y^2}^{(i)}, \boldsymbol{Y^1}^{(i)}\right)$
                Solve for $\Delta\boldsymbol{Y^2}^{(i)}$:

                $M^{(i)}\Delta\boldsymbol{Y^2}^{(i)} = -R^{2(i)}$
                update $\boldsymbol{Y^2}^{(i+1)} = \boldsymbol{Y^2}^{(i)} + \Delta\boldsymbol{Y^2}^{(i)}$
                If $i = i_{max}$, Exit the loop

                Form $R^{1(i)}\left(\boldsymbol{Y^2}^{(i+1)}, \boldsymbol{Y^1}^{(i)}, \boldsymbol{Y^2}_{(n)}\right)$
                Form $M^{(i)}\left(\boldsymbol{Y^2}^{(i+1)}, \boldsymbol{Y^1}^{(i)}\right)$
                Solve for $\Delta\boldsymbol{Y^1}^{(i)}$:

                $M^{(i)}\Delta\boldsymbol{Y^1}^{(i)} = -R^{1(i)}$
                update $\boldsymbol{Y^1}^{(i+1)} = \boldsymbol{Y^1}^{(i)} + \Delta\boldsymbol{Y^1}^{(i)}$
        (end multi-corrector loop)
```

```
    $\boldsymbol{Y^2}_{(n+1)} = \boldsymbol{Y^2}^{(i+1)}$
  (end time steps)
Exit
```

A.4 First order predictor multi-corrector algorithm

First order predictor multi-corrector algorithm used to solve the non-linear systems of equations is given as below:

```
Given $n_{step}$ and $i_{max}$
(Initialize)
 set $\boldsymbol{Y}^2_{(0)}$

(Time steps)
For $n = 0, 1, \ldots, n_{step} - 1$

        (Predictor)
        $\boldsymbol{Y^2}^{(0)} = \boldsymbol{Y}^2_{(0)}$

        Set $\Delta t$
        (Multi-corrector loop)
        For $i = 0, 1, \ldots, i_{max} - 1$

                Form $R^{2^{(i)}}\left(\boldsymbol{Y^2}^{(i)}, \boldsymbol{Y^1}^{(i)}, \boldsymbol{Y^2}_{(n)}\right)$
                Form $M^{(i)}\left(\boldsymbol{Y^2}^{(i)}, \boldsymbol{Y^1}^{(i)}\right)$
                Solve for $\Delta\boldsymbol{Y^2}^{(i)}$:

                $M^{(i)}\Delta\boldsymbol{Y^2}^{(i)} = -R^{2^{(i)}}$
                update $\boldsymbol{Y^2}^{(i+1)} = \boldsymbol{Y^2}^{(i)} + \Delta\boldsymbol{Y^2}^{(i)}$
                If $i = i_{max}$, Exit the loop

        (end multi-corrector loop)
  $\boldsymbol{Y^2}_{(n+1)} = \boldsymbol{Y^2}^{(i+1)}$
(end time steps)
Exit
```

Bibliography

[1] A. Esmaeeli and G. Tryggvason, "A front tracking method for computations of boiling in complex geometries," Int. J. Multiphase Flow, vol. 30, pp. 1037–1050, 2004.

[2] A. Folch, J. Fernández, J. Rundle, and J. Martí, "Ground deformation in a viscoelastic medium composed of a layer overlying a half-space: a comparison between point and extended sources," Geophys. J. Int., vol. 140, pp. 37–50, 2000.

[3] A. Folch and J. Marti, "The generation of overpressure in felsic magma chambers by replenishment," Earth Planet Sci Lett, vol. 163, pp. 301–314, 1998.

[4] A. Folch, J. Martí, R. Codina, and M. Vazquez, "A numerical model for temporal variations during explosive central vents eruptions," J. Geophys. Res., vol. 103, pp. 20,883–20,899, 1998.

[5] A. Folch, M. Vazquez, R. Codina, and J. Martí, "A fractional-step finite-element method for the navier-stokes equations applied to magma-chamber withdrawal," Comput. Geosci., vol. 25, no. 3, pp. 263–275, 1999.

[6] A. Folch, R. Codina, and J. Martí, "Numerical modeling of magma withdrawal during explosive caldera-forming eruptions," J. Geophys. Res., vol. 106, pp. 16,163–16,176, 2001.

[7] A. Gudmundsson, "Emplacement of dikes, sills and crustal magma chambers at divergent plate boundaries," Tectonophysics, vol. 176, pp. 257–275, 1990.

[8] ——, "The mechanics of large volcanic eruptions," Earth-Science Reviews, vol. 163, pp. 72–93, 2016.

[9] A. Gudmundsson, "How local stresses control magma-chamber ruptures, dyke injections, and eruptions in composite volcanoes," Earth-Science Reviews, vol. 79, pp. 1–31, 2006.

[10] A. Idesman et al., "Benchmark problems for wave propagation in elastic materials," Comput Mech, vol. 43, pp. 797–814, 2009.

[11] A. Longo, M. Barsanti, A. Cassioli, and P. Papale, “A finite element galerkin/least squares method for computation of multicomponent compressible incompressible flows,” Computers and fluids, vol. 67, pp. 57–71, 2012.

[12] A. Longo, M. Vassalli, P. Papale, and M. Barsanti, “Numerical simulation of convection and mixing in magma chambers replenished with CO_2-rich magma,” Geophys Res Lett, vol. 33, no. L21305, pp. 1–6, 2006.

[13] A. Longo and P. Papale et al., “Magma convection and mixing dynamics as a source of ultra-long-period oscillations,” Bull. Volcanology, vol. 74, no. 4, pp. 873–880, 2012.

[14] A. Mangiacapra et al., “The deep magmatic system of the campi flegrei caldera (italy),” Geophys Res Lett, vol. 35, no. L21304, pp. 1–6, 2008.

[15] A. Masud, “Effects of mesh motion on the stability and convergence of ale based formulations for moving boundary flows,” Computational Mechanics, vol. 38, no. 4–5, pp. 430–439, 2006.

[16] A. Masud and T.J.R. Hughes, “A space-time galerkin/least-squares finite element formulation of the navier-stokes equations for moving domain problems,” CMAME, vol. 146, no. 1–2, pp. 91–126, 1997.

[17] A. Murrone and H. Guillard, “A five equation reduced model for compressible two phase flow problems,” Journal of Computational Physics, vol. 202, no. 2, pp. 664–698, 2005.

[18] A. Zollo et al., “Seismic reflections reveal a massive melt layer feeding campi flegrei caldera,” Geophysical Research Letters, vol. 35, p. L12306, 2008.

[19] A.A. Johnson and T.E. Tezduyar, “Mesh update strategies in parallel finite element computations of flow problems with moving boundaries and interfaces,” CMAME, vol. 119, pp. 73–94, 1994.

[20] A.A. Velasco et al., “Recent large earthquakes near cape mendocino and in the gorda plate: Broadband source time functions, fault orientations, and rupture complexities,” Journal of Geophysical Research, vol. 99, pp. 711–728, 1994.

[21] Adriana Alves et al., “Microgranitic enclaves as products of self-mixing events: a study of open-system processes in the mauá granite, sao paulo, brazil, based on in situ isotopic and trace elements in plagioclase,” J Petrology, vol. 50, pp. 2221–2247, 2010.

[22] A.F. Trial, F.J. Spera, J. Greer, and D.A. Yuen, “Simulations of magma withdrawal from composizionally zoned bodies,” J. Geophys. Res., vol. 97, pp. 6713–6733, 1992.

[23] Alain Burgisser and George W. Bergantz, “A rapid mechanism to remobilize and homogenize highly crystalline magma bodies,” Nature, vol. 471, pp. 212–215, 2011.

[24] A.N. Brooks and T.J.R. Hughes, "Streamline upwind/petrov-galerkin formulations for convection dominated flows with particular emphasis on the incompressible navier-stokes equations," CMAME, vol. 32, pp. 199–259, 1982.

[25] A.T. Linde and I.S. Sacks, "Triggering of volcanic eruptions," Nature, vol. 395, pp. 888–890, 1998.

[26] A.V. Idesman, Finite element modeling of linear elastodynamics problems with explicit time-integration methods and linear elements with reduced dispersion. Comparative study of different finite element techniques used for elastodynamics. COMPDYN 2013, V. Plevris (eds.), 2013.

[27] B. Chouet, P. Dawson, and M. Martini, "Shallow-conduit dynamics at stromboli volcano, italy, imaged from waveform inversions." Geol. Soc. London. Special Publication, vol. 307, pp. 57–84, 2008.

[28] B. Chouet, P. Dawson, M.R. James, and S.J. Lane, "Seismic source mechanism of degassing bursts at kilauea volcano, hawaii: results from waveform inversion in the 10-50 s band," Journal of Geophysical Research, vol. 115, no. Article number B09311, 2010.

[29] B. Hubner, E. Walhorn, and D. Dinkler, "A monolithic approach to fluid structure interaction using space time finite elements," CMAME, vol. 193, pp. 2087–2104, 2004.

[30] B.C. Haimson, F. Rummel, , and , "Hydrofracturing stress measurements in the iceland research drilling project drill hole at reydarfjordur, iceland," J. Geophys. Res., vol. 87, pp. 6631–6649, 1982.

[31] B.R. Shin, "Numerical analysis of unsteady cavitating flow by a homogeneous equilibrium model," 2001.

[32] C. Annen and R.S.J. Sparks, "Effects of repetitive emplacement of basaltic intrusions on the thermal evolution and melt generation in the crust," Earth and Planetary Science Letters, vol. 203, pp. 937–955, 2002.

[33] C. Farhat, C. Degand, B. Koobus, and M. Lesoinee, "Torsional springs for two-dimensional dynamic unstructured fluid meshes," Comp. Meth. Appl. Mech. Engrg., vol. 163, pp. 231–245, 1998.

[34] C. Fourmentraux et al., "Crystal fractionation, magma step ascent and syn-eruptive mingling: the averno 2 eruption (phlegraean fields, italy)," Contributions to Mineralogic and Petrology, vol. 163, pp. 1121–1137, 2012.

[35] C. Johnson, U. Nävert, and J. Pitkäranta, "Finite element methods for linear hyperbolic problems," CMAME, vol. 45, no. 1–3, pp. 285–312, 1984.

[36] C. Lomnitz, "Major earthquakes of chile: A historical survey, 1535-1960," Seismological Research Letters, vol. 75, pp. 368–378, 2004.

[37] C Nostro, "Two-way coupling between vesuvius eruptions and southern apennine earthquakes, italy, by elastic stress transfer." J Geophys Res, vol. 103, pp. 24 487–24 504, 1998.

[38] C.F. Miller and J.S. Miller, "Contrasting stratified plutons exposed in tilt blocks, eldorado mountains, colrado river rift, nv, usa," LITHOS, vol. 61, pp. 209–224, 2002.

[39] C.L. Merkle, J.Z. Feng, and P.E.O. Buelow, "Computational modeling of the dynamics of sheet cavitation," 1998.

[40] Claes Johnson, "Discontinuous galerkin finite element methods for second order hyperbolic problems," CMAME, vol. 107, pp. 117–129, 1993.

[41] C.M. Klaij, J.J.W. van der Vegt, and H. van der Ven, "Space-time discontinuous galerkin method for the compressible navier-stokes equations," J. Comp.Phys., vol. 217, no. 2, pp. 586–611, 2006.

[42] C.M. Oldenburg, F.J. Spera, D.A. Yuen, and G. Sewell, "Dynamic mixing in magma bodies: Theory, simulations and implications," J. Geophys. Res., vol. 94, pp. 9215–9236, 1989.

[43] C.P. Montagna et al., "Timescales of mingling in shallow magmatic reservoirs," Geological Society, London, Special Publications, vol. 422, pp. 1–10, 2015.

[44] C.W. Burnham, J.R. Holloway, and N.F. Davis, "Thermodynamic properties of water to 1,000°c and 10,000 bars," Geological Society of America Special Papers, vol. 132, pp. 1–96, 1969.

[45] C.W. Hirt and B.D. Nichols, "Volume of fluid (vof) method for the dynamics of free boundaries," J. Comp. Phys., vol. 39, pp. 201–225, 1981.

[46] D. Barkley, M.G.M. Gomes, and R.D. Henderson, "Three-dimensional instability in flow over a backward-facing step," J Fluid Mech., vol. 473, pp. 167–190, 2002.

[47] D. Dingwell, "Recent experimental progress in the physical description of silicic magma relevant to explosive volcanism," Geological society London special Publications, vol. 145, pp. 9–26, 1998.

[48] D. Giordano, J.K. Russel, and D.B. Dingwell, "Viscosity of magmatic liquids: a model," Earth and Planetary Science Letters, vol. 271, pp. 123–134, 2008.

[49] D. Snyder, "Thermal effects of the intrusion of basaltic magma into a more silicic magma chamber and implications for eruption triggering," Earth Planet Sci Lett, vol. 175, pp. 257–273, 2000.

[50] D.A. Mayne, A.S. Usmani, and M. Crapper, "h-adaptive finite element solution of high rayleigh number thermally driven cavity problem," International Journal of Numerical Methods for Heat and Fluid Flow, vol. 10, no. 6, pp. 598–615, 2000.

[51] D.C. Wan, B.S.V. Patnaik, and G.W. Wei, "A new benchmark quality solution for the buoyancy-driven cavity by discrete singular convolution," Numerical Heat Transfer Part B: Fundamentals: An International Journal of Computation and Methodology, vol. 40, no. 3, pp. 199–228, 2001.

[52] D.D. Pollard and A.M. Johnson, "Mechanics of growth of some laccolithic intrusions in the henry mountains, utah, ii. bending and failure of overburden layers and sill formation," Tectonophysics, vol. 18, pp. 311–354, 1973.

[53] D.J. Torres and J.U. Brackbill, "The point-set method: Front-tracking without connectivity," J. of Comp. Phys., vol. 165, pp. 620–644, 2000.

[54] D.R. Lynch, "Unified approach to simulation on deforming elements with application to phase change problems," J. Comput. Phys., vol. 47, pp. 387–411, 1982.

[55] D.S. Miller and R.B. Smith, "P and s velocity structure of yellowstone volcanic field from local earthquakeand controlled source tomography," J. Geophysical Research, vol. 104, no. B7, pp. 15 105–15 121, 1999.

[56] E. Bavier, M. Hoemmen, S. Rajamanickam, and H. Thornquist, "Amesos2 and belos: Direct and iterative solvers for large sparse linear systems," Scientific Programming, vol. 20, no. 3, pp. 241–255, 2012.

[57] E. Erturk and C. Gokcol, "Fourth order compact formulation of navier-stokes equations and driven cavity flow at high reynolds numbers," Int J Numer Methods Fluids, vol. 50, pp. 421–436, 2006.

[58] E. Laitone, "The second approximation to cnoidal and solitary waves," J. Fluid Mech., vol. 9, pp. 430–444, 1960.

[59] E. Rivalta et al., "A review of mechanical models of dike propagation: Schools of thought, results and future directions," Tectonophysics, vol. 638, pp. 1–42, 2015.

[60] E.M. Anderson, "The dynamics of formation of cone sheets, ring dykes and caldron subsidences," Proceedings of the Royal Society of Edinburgh, vol. 56, pp. 128–163, 1936.

[61] B. A. et al., "Experimental and theoretical investigation of backward-facing step flow," J Fluid Mech., vol. 127, pp. 473–496, 1983.

[62] F. Rispoli and R. Saavedra, "A stabilized finite element method based on sgs models for compressible flows," CMAME, vol. 196, pp. 652–664, 2006.

[63] F. Shakib and T.J.R. Hughes, "A new finite element formulation for computational fluid dynamics: Ix. fourier analysis of space-time galerkin/least-squares algorithms," CMAME, vol. 87, pp. 35–58, 1991.

[64] F. Shakib, T.J.R. Hughes, and Z. Johan, “A new finite element formulation for computational fluid dynamics: X. the compressible euler and navier-stokes equations,” CMAME, vol. 89, no. 1–3, pp. 141–219, 1991.

[65] F. Wang et al., “Influence of the march 11, 2011 mw 9.0 tohoku-oki earthquake on regional volcanic activities,” Chinese Sci. Bull., vol. 56, pp. 2077–2081, 2011.

[66] Fabián Duarte, Raúl Gormaz, and Srinivasan Natesan, “Arbitrary lagrangian eulerian method for navier stokes equations with moving boundaries,” CMAME, vol. 193, pp. 4819–4836, 2004.

[67] F.H. Harlow and J.E. Welch, “Numerical calculation of time-dependent viscous incompressible flow of fluid with free surface,” Pys. Fluids, vol. 8, pp. 2182–2189, 1965.

[68] F.J. Spera, C.M. Oldenburg, U.R. Christensen, and M. Todesco, “Simulation of convection in the system $KAlSi_2O_6$-$CaMgSi_2O_6$: Implications for compositionally zoned magma bodies,” Am. Mineral., vol. 80, pp. 1188–1207, 1995.

[69] F.J. Spera, D.A. Yuen, J.C. Greer, and G. Sewell, “Dynamics of magma withdrawal from stratified magma chambers.” Geology, vol. 14, pp. 723–726, 1986.

[70] G. Currenti et al., “Elasto-plastic modeling of volcano ground deformation,” Earth Planet. Sci. Lett., vol. 296, pp. 311–318, 2010.

[71] G. Hauke, “Simple stabilizing matrices for the computation of compressible flows in primitive variables,” CMAME, vol. 190, pp. 6881–6893, 2001.

[72] G. Hauke and T.J.R. Hughes, “A unified approach to compressible and incompressible flows,” CMAME, vol. 113, no. 3–4, pp. 389–396, 1994.

[73] G. Heiken et al., “Eruptions at chaos crags, lassen volcanic national park, california,” J. Volcanol. Geotherm. Res., vol. 7, pp. 443–481, 1980.

[74] G. Hauke and T.J.R. Hughes, “A comparative study of different sets of variables for solving compressible and incompressible flows,” CMAME, vol. 153, no. 1–2, pp. 1–44, 1998.

[75] G.A. Davis and O.O. Bendiksen, “Unsteady transonic two-dimensional euler solutions using finite elements,” AIAA Journal, vol. 31, pp. 1051–1059, 1993.

[76] G.J. Le Beau, S.E. Ray, S.K. Aliabadi, and T.E. Tezduyar, “Supg finite element computation of compressible flows with the entropy and conservation variables formulations,” CMAME, vol. 104, pp. 397–422, 1993.

[77] G.J. Le Beau and T.E. Tezduyar, “Finite element computation of compressible flows with the supg formulation,” In Advances in Finite Element Analysis in Fluid Dynamics, vol. 123, pp. 21–27, 1991.

[78] G.M. Hulbert and T.J.R. Thomas, "Space-time finite element methods for elastodynamics:formulations and error estimates," CMAME, vol. 66, pp. 339–363, 1987.

[79] GuoLiang Zhang et al., "Periodical mixing of morb magmas near east pacific rise 13 degree n: evidence from modeling and zoned plagioclase phenocrysts," Sci. China Ser. D-Earth Sci, vol. 51, pp. 1786–1801, 2008.

[80] G.W. Bergantz, "On the dynamics of magma mixing by reintrusion: implications for pluton assembly process," J. Struct. Geology, vol. 22, no. 9, pp. 1297–1309, 2000.

[81] H. Nguyen and J. Reynen, "A space-time least-square finite element scheme for advection diffusion equations," CMAME, vol. 42, no. 3, pp. 331–342, 1984.

[82] H. Rymer, J. Cassidy, C.A. Locke, and J.B. Murray, "Magma movements in etna volcano associated with the major 1991-1993 lava eruption: evidence from gravity and deformation," Bull. Volcanol., vol. 57, pp. 451–461, 1995.

[83] H. Van der Ven and J.J.W. Van der Vegt, "Space-time discontinuous galerkin finite element method with dynamic grid motion for inviscid compressible flows. ii. efficient flux quadrature," CMAME, vol. 191, pp. 4747–4780, 02.

[84] Helene Le Mevel et al., "Magma injection into a long-lived reservoir to explain geodetically measured uplift: Application to the 2007-2014 unrest episode at laguna del maule volcanic field, chile," JOGR, vol. 121, pp. 6092–6108, 2016.

[85] H.G. Matthies and J. Steindorf, "Partitioned strong coupling algorithms for fluid-structure interaction," Computers and Structures, vol. 81, pp. 805–812, 2003.

[86] H.G. Matthies and J. Steindorf, "Partitioned but strongly coupled iteration schemes for nonlinear fluid-structure interaction," Computers and Structures, vol. 80, pp. 1991–1999, 2002.

[87] Hiroki Michioka and Ikuro Sumita, "Rayleigh-taylor instability of a particle packed viscous fluid: Implications for a solidifying magma," GEOPHYSICAL RESEARCH LETTERS, vol. 32, no. L03309, pp. 1–4, 2005.

[88] I. Arienzo et al., "Isotopic evidence for open system processes within the campanian ignibrite (campi flegrei - italy) magma chamber," Bullettin of Volcanology, vol. 71, pp. 285–300, 2009.

[89] I. Arienzo et al., "The feeding system of agnano-monte spina eruption (campi flegrei, italy): dragging the past into present activity and future scenarios," Chemical Geology, vol. 270, pp. 135–147, 2010.

[90] J. Batina, "Unsteady euler algoithm with unstructured dynamic mesh for complex-aircraft aerodynamic analysis," AIAA Journal, vol. 29, no. 3, pp. 327–333, 1991.

[91] J Browning, "Cooling-dominated cracking in thermally stressed volcanic rocks," Geophysical Research Letters, vol. 43, pp. 8417–8425, 2016.

[92] J. Chung and G.M. Hulbert, "A time integration algorithm for structural dynamics with improved numerical dissipation: The generalized alpha method," J. Appl. Mech, vol. 60, no. 2, pp. 371–375, 1993.

[93] J. Degroote, K. Bathe, and J. Vierendeels, "Performance of a new partitioned procedure versus a monolithic procedure in fluid-structure interaction," Computers and Structures, vol. 87, pp. 793–801, 2009.

[94] J. Du et al., "A simple package for front tracking," J. Comput. Phys., vol. 213, pp. 613–628, 2006.

[95] J. FernÃ¡ndez, J.M. Carrasco, J.B. Rundle, and V. Arana, "Geodetic methods for detecting volcanic unrest: a theoretical approach," Bull. Volcanol., vol. 60, pp. 534–544, 1999.

[96] J. Glimm et al., "Front tracking in two and three dimensions," Comput. Math. App., vol. 35, pp. 1–11, 1998.

[97] J. Hickey and J. Gottsmann, "Benchmarking and developing numerical finite element models of volcanic deformation," Journal of Volcanology and Geothermal Research, vol. 280, pp. 126–130, 2014.

[98] J. Hron and S. Turek, "A monolithic fem/multigrid solver for an ale formulation of fluid-structure interaction with applications in biomechanics," Lecture Notes in Computational Science and Engineering, vol. 53, pp. 146–170, 2006.

[99] J. Keskar and D.A. Lyn, "Computations of a laminar backward-facing step flow at re = 800 with a spectral domain decomposition method," Int J Numer Methods Fluids, vol. 29, no. 4, pp. 411–427, 1999.

[100] J. S. Pallister et al., "A basalt trigger for the 1991 eruptions of pinatubo volcano," Nature, vol. 356, pp. 426–428, 1992.

[101] J.A. Sethian and P. Smereka, "Level set methods for fluid interfaces," Annu. Rev. Fluid. Mech., vol. 35, pp. 341–372, 2003.

[102] J.B. Rundle, "Viscoelastic-gravitational deformation by a rectangular thrust fault in a layered earth," Journal of Geophysical Research, vol. 87, pp. 7787–7796, 1982.

[103] J.C. Jaeger, "Thermal effects of intrusions," Reviews of Geophysics, vol. 2, pp. 443–466, 1964.

[104] J.C. Jaeger, "The cooling of irregularly shaped igneous bodies," American Journal of Science, vol. 259, pp. 721–734, 1961.

[105] J.H. Dieterich and R.W. Decker, "Finite element modelling of surface deformation associated with volcanism," Journal of Geophysical Research, vol. 80, pp. 4094–4102, 1975.

[106] J.J. Sudirham, J.J.W. Van der Vegt, and R.R.J. Van Damme, “Space-time discontinuous galerkin method for advection-diffusion problems on time-dependent domains,” Appl. Numer. Math., vol. 56, no. 12, pp. 1491–1518, 2004.

[107] J.J.W. Van der Vegt and H. Van der Ven, “Space-time discontinuous galerkin finite element method with dynamic grid motion for inviscid compressible flows. part i. general formulation,” J. Comp. Phys., vol. 182, pp. 546–585, 2002.

[108] K. Baba and M. Tabata, “On a conservative upwind finite element scheme for the convective diffusion equations,” R.A.I.R.O., Analyse Numérique, vol. 27, pp. 277–282, 1981.

[109] K. Mogi, “Relations between eruptions of various volcanoes and the deformations of the ground surfaces around them,” Bulletin of the Earthquake Research Institute, vol. 36, pp. 99–134, 1958.

[110] K. Stein, T.E. Tezduyar, and R. Benney, “Mesh moving techniques for fluid-structure interactions with large displacements,” ASME, vol. 70, pp. 1–6, 2003.

[111] K. Takizawa and T.E. Tezduyar, “Space-time fluid structure interaction methods,” Math. Models Methods Appl. Sci., vol. 22, no. Suppl. 2, p. 49 pages, 2012.

[112] K.E. Jansen, “A stabilized finite element method for computing turbulence,” CMAME, vol. 174, pp. 299–317, 1999.

[113] K.U. Hess and D. Dingwell, “Viscosities of hydrous leucogranitic melts: a non-arrhenian model,” Am. Mineral, vol. 80, pp. 94–108, 1996.

[114] L. Catabriga, A.L.G.A. Coutinho, and T.E. Tezduyar, “Compressible flow supg parameters computed from element matrices,” Communications in Numerical Methods in Engineering, vol. 21, pp. 465–476, 2005.

[115] L. De Siena, E. Del Pezzo, and F. Bianco, “Seismic attenuation imaging of campi flegrei caldera: architecture and temporal evolution,” Journal of Geophysical Research, vol. 115, pp. 1–18, 2010.

[116] L.E. Lara, J.A. Naranjo, and H. Moreno, “Rhyodacitic fissure eruption in southern andes (cordón caulle; 40.5Â°s) after the 1960 (mw:9.5) chilean earthquake: a structural interpretation,” Journal of Volcanology and Geothermal Research, vol. 138, pp. 127–138, 2004.

[117] M. Alam and M. Kimura, “Statistical analysis of time-distance relationship between volcanic eruptions and great earthquakes in japan,” Earth Planets and Space, vol. 56, pp. 179–192, 2004.

[118] M. Battaglia, P.F. Cervelli, and J.R. Murray, “dmodels: a matlab software package for modeling crustal deformation near active faults and volcanic centers,” J. Volcanol. Geotherm. Res., vol. 254, pp. 1–4, 2013.

[119] M. Bonafede, M. Dragoni, and F. Quareni, “Displacement and stress field produced by a centre of dilatation and by a pressure source in a visco-elastic half-space: application to the study of ground deformation and seismic activity at campi flegrei, italy.” Geophys. J. R. astr. Soc, vol. 87, pp. 455–485, 1986.

[120] M. Bursik et al., “A volcanotectonic cascade: Activation of range front faulting and eruptions by dike intrusion, mono basin-long valley caldera, california,” Journal of Geophysical Research, vol. 108, no. B8, 2393, pp. 1–12, 2003.

[121] M. Diez et al., “Evidence for static stress changes triggering the 1999 eruption of cerro negro volcano, nicaragua and regional aftershock sequences,” Geophys. Res. Lett., vol. 32, no. L04309, pp. 1–4, 2005.

[122] M. Dragoni and C. Manganesi, “Displacement and stress produced by a pressurized, spherical magma chamber, surrounded by a viscoelastic shell,” Physics of the Earth and Planetary Interiors, vol. 56, pp. 316–328, 1989.

[123] M. Tabata, “Symmetric finite element approximations for convection-diffusion problems,” Theoretical and Applied Mechanics, vol. 33, pp. 445–453, 1985.

[124] M. Tabata, “Some applications of the upwind finite element method,” Theoretical and Applied Mechanics, vol. 27, pp. 277–282, 1979.

[125] M. Ishii and N. Zuber, “Drag coefficient and relative velocity in bubbly, dropletor particulate flows,” AiChE Journal, vol. 25, pp. 843–855, 1979.

[126] M. Miksis and L. Ting, “Wave propagation in a bubbly liquid with finite-amplitude asymmetric bubble oscillations.” Physica of fluids, vol. 29, pp. 603–618, 1986.

[127] M. Poland, M. Hamburger, and A. Newman, “The changing shapes of active volcanoes: history, evolution, and future challenges for volcano geodesy,” Journal of Volcanology and Geothermal Research, vol. 150, pp. 1–13, 2006.

[128] M. Pólner, J.J.W. van der Vegt, and R.M.J. van damme, “Analysis of stabilization operators for galerkin least-squares discretizations of the incompressible navier-stokes equations,” CMAME, vol. 195, no. 9-12, pp. 982–1006, 2006.

[129] M. Pólner, L. Pesch, and J.J.W. van der Vegt, “Construction of stabilization operators for galerkin least-squares discretizations of compressible and incompressible flows,” CMAME, vol. 196, no. 21–24, pp. 2431–2448, 2007.

[130] M. Tabata, “A finite element approximation corrresponding to the upwind finite differencing,” Memoirs of Numerical Mathematics, vol. 4, pp. 47–63, 1977.

[131] M.A. Clynne, “A complex magma mixing origin for rocks erupted in 1915, lassen peak, california,” J. Petrol., vol. 40, pp. 105–132, 1999.

[132] ——, “A complex magma mixing origin for rocks erupted in 1915, lassen peak, california,” Journal of Petrology, vol. 40, pp. 105–132, 1999.

[133] Malte Braack and Gert Lube, “Finite elements with local projection stabilization for incompressible flow problems,” Journal of Computational Mathematics, vol. 27, no. 2–3, pp. 116–147, 2009.

[134] Mark Hoemmen, “A communication-avoiding, hybrid-parallel, rank-revealing orthogonalization method,” IEEE International Parallel and Distributed Processing Symposium, pp. 966–977, 2011.

[135] M.C. Lai and Z. Li, “A remark on jump conditions for the three-dimensional navier-stokes equations involving an immersed moving membrane,” Appl. Math. Letters, vol. 14, pp. 149–154, 2001.

[136] M.J. Andrews and D.B. Spalding, “A simple experiment to investigate two-dimensional mixing by rayleigh-taylor instability,” Phys. Fluids, vol. A, no. 2, pp. 922–927, 1990.

[137] Mónika Polner, “Galerkin least-squares stabilization operators for the navier-stokes equations, a unified approach,” Ph.D. dissertation, Department of Applied Mathematics, Universiteit Twente, 2005.

[138] M. Tabata, “Uniform convergence of the upwind finite element approximation for semilinear parabolic problems,” Journal of Mathematics of Kyoto University, vol. 18, pp. 327–351, 1978.

[139] M.W. Gee, U. Kuttler, and W.A. Wall, “Truly monolithic algebraic multigrid for fluid-structure interaction,” Int. J. Num. Meth. Eng., vol. 85, pp. 987–1016, 2010.

[140] N. Barral, E. Luke, and F. Alauzet, “Two mesh deformation methods coupled with a changing-connectivity moving mesh method for cfd applications,” Procedia Engineering 23rd International Meshing Roundtable, vol. 82, pp. 213–227, 2014.

[141] N. Dumont, O. Simonin, and C. Habchi, “Numerical simulation of cavitating flows in diesel injectors by a homogeneous equilibrium modeling approach,” 2001.

[142] O. Hassan, E.J. Probert, and K. Morgan, “Unstructured mesh procedures for the simulation of three dimensional transient compressible inviscid flows with moving boundary components,” Int. J. Num. Meth. Fluids, vol. 27, pp. 41–55, 1998.

[143] O. Karaoglu et al., “Numerical modelling of triple-junction tectonics at karliova, eastern turkey, with implications for regional magma transport,” Earth and Planetary Science Letters, vol. 452, pp. 157–170, 2016.

[144] O.C. Zienkiewicz, R.L. Taylor, and P. Nithiarasu, The finite element method for fluid dynamics, 6th ed. ELSEVIER, 2006.

[145] P. Causina, J.F. Gerbeaua, and F. Nobile, "Added-mass effect in the design of partitioned algorithms for fluid-structure problems," CMAME, vol. 194, pp. 4506–4527, 2005.

[146] P. Jamet, "Galerkin-type approximations which are discontinuous in time for parabolic equations in a variable domain," SIAM J. of Numerical Analysis, vol. 15, no. 5, pp. 912–928, 1978.

[147] P. Papale, R. Moretti, and D. Barbato, "The compositional dependence of the saturation surface of $H_2O + CO_2$ fluids in silicate melts," Chemical Geology, vol. 229, pp. 78–95, 2006.

[148] P. Segall, Earthquake and Volcano Deformation. Princeton: Princeton University Press, 2010.

[149] Patricia M. Gregg et al., "Catastrophic caldera-forming eruptions ii: The subordinate role of magma buoyancy as an eruption trigger," JOGR, vol. 305, pp. 100–113, 2015.

[150] P.M. Davis, "Surface deformation due to inflation of an arbitrarily oriented triaxial ellipsoidal cavity in an elastic half space, with reference to kilauea volcano, hawaii," Journal of Geophysical Research, vol. 91, pp. 7429–7438, 1986.

[151] P.M. Gresho and D.K. Gartling et al., "Is the steady viscous incompressible two-dimensional flow over a backward-facing step at re = 800 stable?" Int J Numer Methods Fluids, vol. 17, no. 6, pp. 501–541, 1993.

[152] P.W. Lipman et al., Ground deformation associated with the 1975 magnitude-7.2 earthquake and resulting changes in activity of Kilauea Volcano, Hawaii, U. S. Geological Survey, Reston, VA, United States, 1985.

[153] R. Bateman, "The interplay between crystallization, replenishment and hybridization in large felsic magma chambers," Earth Sci Rev, vol. 39, pp. 91–106, 1995.

[154] R. Löhner and C. Yang, "Improved ale mesh velocities for moving boundaries," Comm. Num. Meth.Eng., vol. 12, pp. 599–608, 1996.

[155] R. Scardovelli and S. Zaleski, "Interface reconstruction with least-square fit and split eulerian lagrangian advection," Int. J. Numr. Methods Fluid, vol. 41, pp. 1–32, 2003.

[156] R. Sparks et al., "Magma mixing: a mechanism for triggering acid explosive eruptions," Nature, vol. 267, pp. 315–318, 1977.

[157] R. Takahashi et al, “Formation of a compositionally reverse zoned magma chamber: Petrology of the ad 1640 and 1694 eruptions of hokkaido-komagatake volcano, japan,” Journal of Petrology, vol. 54, pp. 815–838, 2013.

[158] R.A. Lange, “The effects of H_2O, CO_2 and F on the density and viscosity of silicate melts,” Reviews of Mineralogy, vol. 30, pp. 331–369, 1994.

[159] R.A. Schultz, “Limits on strength and deformation properties of jointed basaltic rock masses,” Rock Mech. Rock Eng., vol. 28, pp. 1–15, 1995.

[160] R.C. Jachens and G.P. Eaton, “Geophysical observations of kilauea volcano, hawaii, 1. temporal gravity variations related to the 29 november, 1975, m = 7.2 earthquake and associated summit collapse,” Journal of Volcanology and Geothermal Research, vol. 7, pp. 225–240, 1980.

[161] R.C. Reid, J. Prausnitz, and T. Sherwood, The McGraw Hill.properties of Gases and Liquids. New York: McGraw Hill. 3rd edn., 1977.

[162] R.S.J. Sparks et al., “The fluid dynamics of evolving magma chambers,” Phi. Trans. of the Royal society, vol. 310, pp. 511–534, 1984.

[163] S. Biswas, A. Esmaeeli, and G. Tryggvason, “Comparison of results from dns of bubbly flows with a two-fluid model for two-dimensional laminar flows.” Int. J. Multiphase Flow, vol. 31, pp. 1036–1048, 2005.

[164] S. Blake, “Volcanism and dynamics of open magma chambers,” Nature, vol. 289, pp. 783–785, 1981.

[165] S. Bower and A.W. Woods, “Control of magma volatile content and chamber depth on the mass erupted during explosive volcanic eruptions,” J. Geophys. Res., vol. 102, no. 10,273–10,290, 1997.

[166] S. Couch et al., “Mineral disequilibrium in lavas explained by convective self-mixing in open magma chambers,” Nature, vol. 411, pp. 1037–1039, 2001.

[167] S. Nakada et al., “Petrology of the 1991-1995 eruption at unzen: effusion pulsation and groundmass crystallisation,” J. Volcanol. Geotherm. Res., vol. 89, pp. 173–196, 1999.

[168] S. Umino et al, “Multistage magma mixing revealed in phenocryst zoning of the yunokuchi pumice, akagi volcano, japan,” Journal of Petrology, vol. 39, pp. 101–124, 1998.

[169] ScienceDaily, “Large earthquakes trigger a surge in volcanic eruptions,” University of Oxford, 2009.

[170] Shinji Toda et al., “Widespread seismicity excitation throughout central japan following the 2011 m=9.0 tohoku earthquake and its interpretation by coulomb stress transfer,” Geophysical Research Letters, vol. 38, no. L00G03, pp. 1–5, 2011.

[171] Simone Colucci et al., "A thermodynamical model for the surface tension of silicate melts in contact with H_2O gas," Geochimica et Cosmochimica Acta, vol. 175, pp. 113–127, 2016.

[172] S.K. Aliabadi, S.E. Ray, and T.E. Tezduyar, "Supg finite element computation of compressible flows with the entropy and conservation variables formulations," CMAME, vol. 104, no. 3, pp. 397–422, 1993.

[173] S.K. Aliabadi and T.E. Tezduyar, "Space-time finite element computation of compressible flows involving moving boundaries and interfaces," CMAME, vol. 107, no. 1–2, pp. 209–223, 1993.

[174] S.L. Webb and D.B. Dingwell, "Non-newtonian rheology of igneous melts at high stresses and strain-rates: experimental results for rhyolite, andesite, basalt and nephelinite," J.Geophys. Res., vol. 95, pp. 15 695–15 701, 1990.

[175] S.M. Zandi, B. Boroomand, and S. Soghrati, "Exponential basis functions in solution of incompressible fluid problems with moving free surfaces," Journal of Computational Physics, vol. 231, pp. 505–527, 2012.

[176] S.Rao, Mechanical vibrations. Addison-Wesley Longman, 1986.

[177] T. Chacón Rebollo and M. Gómez Mármol, "A high order term-by-term stabilization solver for incompressible flow problems," IMA J Numer Anal, vol. 33, pp. 974–1007, 2012.

[178] T. Kuritani, "Magmatic differentiation examined with a numerical model considering multicomponent thermodynamic and momentum, energy and species trasport," Lithos, vol. 74, no. 3–4, pp. 117–130, 2004.

[179] T. Lay et al., "Teleseismic inversion for rupture process of the 27 february 2010 chile (mw 8.8) earthquake," Geophysical Research Letters, vol. 37, no. L13301, pp. 1–5, 2010.

[180] T. Masterlack, "Magma intrusion and deformation predictions: sensitivities to the mogi assumptions," Journal of Geophysical Research, vol. 112, no. Article No. B06419, 2007.

[181] T. Masterlark et al., "Magma intrusion and deformation predictions: Sensitivities to the mogi assumptions," JOGR, vol. 112, no. B06419, pp. 1–17, 2007.

[182] ——, "Volcano deformation source parameters estimated from insar: Sensitivities to uncertainties in seismic tomography," JOGR, vol. 121, pp. 3002–3016, 2016.

[183] T. Menand, K.A. Daniels, and P. Benghiat, "Dyke propagation and sill formation in a compressive tectonic environment," Journal of Geophysical Research, vol. 115, no. Article No. B08201, pp. 1–12, 2010.

[184] T. Nakayama and M. Mori, “An eulerian finite element method for time-dependent free surface problems in hydrodynamics,” Int. J. Num. Meth. Fluids, vol. 22, pp. 175–194, 1996.

[185] T. Nishimura and B. Chouet, “A numerical simulation of magma motion, crustal deformation, and seismic radiation associated with volcanic eruptions.” Geophys. J. Int., vol. 153, no. 99–718, 2003.

[186] T.B. Helenbrook, “Mesh deformation using the biharmonic operator,” Int. J. Numer. Meth. Engng, pp. 1–30, 2001.

[187] T.E. Tezduyar, “Calculation of the stabilization parameters in finite element formulations of flow problems.” Applications of Computational Mechanics in Structures and Fluids, pp. 1–19, 2005.

[188] T.E. Tezduyar and M. Behr, “A new strategy for finite element computations involving moving boundaries and interfaces- the deforming-spatial-domain/space-time procedure: I. the concept and the preliminary numerical tests,” CMAME, vol. 94, pp. 339–351, 1992.

[189] T.E. Tezduyar, M. Behr, S. Mittal, and A.A. Johnson, “Computation of unsteady incompressible flows with the stabilized finite element methods-space-time formulations, iterative strategies and massively parallel implementations,” New Methods in Transient Analysis, vol. 143, pp. 7–24, 1992.

[190] T.E. Tezduyar, S. Sathe, J. Pausewang, M. Schwaab, J. Christopher, and J. Crabtree, “Interface projection techniques for fluid-structure interaction modeling with moving mesh methods,” Computational Mechanics, vol. 43, no. 1, pp. 39–49, 2008.

[191] T.E. Tezduyar, S. Sathe, R. Keedy, and K. Stein, “Space-time finite element techniques for computation of fluid-structure interactions,” CMAME, vol. 195, no. 17–18, pp. 2002–2027, 2006.

[192] T.E. Tezduyar, “Computation of moving boundaries and interfaces and stabilization parameters,” I.J. for Numerical Methods in Fluids, vol. 43, no. 5, pp. 555–575, 2003.

[193] T. Tezduyar, “Stabilized finite element formulations for incompressible flow computations,” Advances in applied mechanics, vol. 28, pp. 1–44, 1992.

[194] T.J. Baker, “Mesh modification for solution adaptation and time evolving domains,” in 7th International Conference on Numerical Grid Generation in Computational Field Simulations, 2000.

[195] T.J. Barth, “Numerical methods for gasdynamic systems on unstructured meshes,” Notes in Computational Sci. and Eng., 1998.

[196] T.J.R. Hughes, Linear static and dynamic finite element analysis. Dover, 2000.

[197] T.J.R. Hughes, L.P. Franca, and G.M. Hulbert, “A new finite element formulation for computational fluid dynamics: Viii. the galerkin/least-squares method for advective-diffusive equations,” CMAME, vol. 73, pp. 173–189, 1989.

[198] T.J.R. Hughes, L.P. Franca, and M. Mallet, “A new finite element formulation for computational fluid dynamics: I. symmetric forms of the compressible euler and navier-stokes equations and the second law of thermodynamics,” CMAME, vol. 54, no. 2, pp. 223–234, 1986.

[199] T.J.R Hughes, L.P. Franca, and M. Mallet, “A new finite element formulation for computational fluid dynamics: Vi. convergence analysis of the generalized supg formulation for linear time-dependent multidimensional advective-diffusive systems,” CMAME, vol. 63, no. 1, pp. 97–112, 1987.

[200] T.J.R. Hughes, M. Mallet, and A. Mizukami, “A new finite element formulation for computational fluid dynamics: Ii. beyond supg,” CMAME, vol. 54, pp. 341–355, 1986.

[201] T.J.R. Hughes and T.E. Tezduyar, “Finite element methods for first-order hyperbolic systems with particular emphasis on the compressible euler equations,” CMAME, vol. 45, pp. 217–284, 1984.

[202] T.J.R. Hughes and T.E. Tezduyar, “Finite element formulations for convection dominated flows with particular emphasis on the compressible euler equations,” In Proceedings of AIAA 21st Aerospace Sciences Meeting, AIAA Paper, pp. 83–125, 1983.

[203] T.R. Walter and F. Amelung, “Volcanic eruptions following m $\geq$ 9 megathrust earthquakes: Implications for the sumatra-andaman volcanoes,” Geology, vol. 35, pp. 539–542, 2007.

[204] T.R. Walter and F. Amelung, “Volcano-earthquake interaction at mauna loa volcano, hawaii,” Journal of Geophyiscal Research, vol. 111, no. B05204, pp. 1–17, 2006.

[205] U. Ghia, K.N. Ghia, and C.T. Shin, “High-re solution for incompressible flow using the navier stokes equations and the multigrid method,” J. Comput. Phys., vol. 48, no. 3, pp. 387–411, 1982.

[206] V. Di Renzo et al., “The magmatic feeding system of the campi flegrei caldera: architecture and temporal evolution,” Chemical Geology, vol. 281, pp. 227–241, 2011.

[207] V. Maronnier, M. Picasso, and J. Rappaz, “Numerical simulation of free surface flows,” Journal of Computational Physics, vol. 155, pp. 439–455, 1999.

[208] V. Venkatakrishnan and D.J. Mavriplis, “Implicit method for the computation of unsteady flows on unstructured grids,” AIAA, vol. 127, pp. 380–397, 1996.

[209] W. Degruyter and C. Huber, "A model for eruption frequency of upper crustal silicic magma chambers," Earth and Planetary Letters, vol. 403, pp. 117–130, 2014.

[210] W. Marzocchi et al., "Modeling the stress variations induced by great earthquakes on the largest volcanic eruptions of the 20th century," Journal of Geophysical Research B: Solid Earth, vol. 107, no. ESE 13, pp. 1–8, 2002.

[211] W. Thatcher, J.C. Savage, and , "Triggering of large earthquakes by magma-chamber inflation, izu peninsula," Japan, Geology (Boulder), vol. 10, pp. 637–640, 1982.

[212] X.D. Li and N.E. Wiberg, "Structural dynamic analysis by a time-discontinuous galerkin finite element method," I. J. for Numerical Methods in Engineering, vol. 39, no. 12, pp. 2131–2152, 1996.

[213] Y. Bazilevs, K. Takizawa, T.E. Tezduyar, M.C. Hsu, N. Kostov, and S. McIntyre, "Aerodynamic and fsi analysis of wind turbines with the ale-vms and st-vms methods," Arch Computat Methods Eng, vol. 22, no. supp02, p. 1230002 [62 pages], 2012.

[214] Y. Rouizi, Y. Favennec, J. Ventura, and D. Petit, "Numerical model reduction of 2d steady incompressible laminar flows: Application on the flow over a backward-facing step," J of Computational Physics, vol. 228, no. 6, pp. 2239–2255, 2009.

[215] Y.C. Chang, T.Y. Hou, B. Merriman, and S. Osher, "A level set formulation of eulerian interface capturing methods for incompressible fluid flows," J. Comp. Phys.,, vol. 124, pp. 449–464, 1996.